Multi-Scale Modeling of the Neural Control of Respiration

A Thesis

Submitted to the Faculty

of

Drexel University

by

Bartholomew James Bacak

in partial fulfillment of the

requirements for the degree

of

Doctor of Philosophy

March 2016

Dedications

To my friends and family, thank you for the support throughout the years.

(With particular thanks to my mother)

Acknowledgements

I would first like to express my sincerest gratitude to my advisor, Dr. Ilya Rybak, for the years he's dedicated to my scientific development. It is only through his guidance that I was able to complete the work in this dissertation. I would also like to thank Drs. Yaroslav Molkov, Jonathan Rubin, and Jeffrey Smith for their mentorship and collaboration on various aims of this work. In addition to Drs. Molkov and Smith, my committee members, Drs. Kimberly Dougherty, Vitaliy Marchenko, Uri Hershberg, and Simon Giszter, have provided invaluable feedback and I am grateful for their time and efforts.

I would like to take this opportunity to thank the many friends and colleagues who have offered support and guidance throughout my time at Drexel and the University of Pittsburgh. My undergraduate professors Drs. Sanjeev Shroff and Larry Shuman, as well as my undergraduate research advisor, Dr. Henry Zeringue, who taught me the fundamentals of engineering and inspired me to pursue an MD/PhD program. I would like to thank all past and present members of the Rybak lab: Drs. Natalia Shevtsova, Sergey Markin, Jessica Ausborn, Patrick Jasinski, TaeGyo Kim, Khaldoun Hamade, and Simon Danner. I would also like to thank Jane Clifford, the director of the MD/PhD program, as well as the administration of the Neurobiology and Biomedical Engineering departments – Joy, Kathy, Janet, Natalia, and the many other staff and faculty members – I would be years behind schedule without your assistance.

The past seven years would not have been as enjoyable or memorable without the companionship of the friends I've made in medical and graduate school. Thank you to Luke Mitchell, John Lee, and Simon Danner – in twenty years I expect to associate graduate

school with the time we spent lifting weights, cooking sausages, and passionately arguing about topics of which we know little beyond the Wikipedia introduction. I thank Lauren Salami for patiently dealing with my stresses, complaints, and poor grammar. Finally, I am forever indebted to my brother, sister, and parents for their love and support throughout my life. I am truly fortunate, thank you.

Table of Contents

List of Tables

List of Illustrations

a

Abstract

Multi-Scale Modeling of the Neural Control of Respiration
Bartholomew J. Bacak
Ilya A. Rybak, Ph.D.

The generation of respiration in mammals begins in the lower brainstem where groups of neurons, that together comprise the respiratory central pattern generator (CPG), interact to produce a motor output that controls breathing. The pre-Bötzinger complex (pre-BötC) in the ventrolateral respiratory column (VRC) is believed to be a major contributor to rhythmic inspiratory activity that interacts with other neural compartments within the VRC as well as with other brainstem areas, including the pons. Though there has been a substantial push to understand the exact cellular and network mechanisms operating within the pre-BötC, as well as the way it is incorporated into the larger respiratory network, there is still much to be resolved. The overarching goal of the work presented in this dissertation is to contribute to our understanding of the neural control of respiration at several hierarchical levels. It is my hope that better insight into the complexities of these multiscale neural control mechanisms will provide a more complete framework for understanding various respiratory pathologies, and ultimately guide the development of novel therapies that will improve patient outcomes.

I applied techniques from the fields of mathematics and computer science to develop computational models that reproduced results from electrophysiological recordings (done by our collaborators) and generated verifiable predictions. The scale of my modeling work encompasses the interaction of neurons in a single population, several interconnected populations of neurons that encompass the core of the mammalian

respiratory network, and an integration of the respiratory network into a larger control system that includes afferent feedback loops. At each level I address specific, but related, topics that add to the general understanding of the neural control of respiration.

The aims of my thesis address specific issues at each of the scales mentioned above. These issues may be summarized as follows: (i) the characteristic rhythmic bursting behavior observed in the pre-BötC, which was studied at the cellular levels with a particular interest in how this behavior impacts respiratory rhythmogenesis; (ii) a respiratory network connectome that defines interactions between several populations of neurons that together form the VRC, which produces an alternating pattern of inspiration, post-inspiration and expiration, and, how such a pattern may be affected by changes in chemical environment, e.g. elevated carbon dioxide or diminished oxygen concentrations; and (iii) the role of afferent feedback to the VRC, from the pons and lungs, which was studied in the context of respiratory phase switching mechanisms.

Chapter I: Introduction

A. Neural control of respiration

Respiration, or the cyclical uptake of oxygen and removal of carbon dioxide, occurs approximately once every four seconds, for the duration of human life. Like many physiological processes, it is easy to take respiration for granted, particularly when considering the robust regulatory mechanisms employed by our bodies to ensure continued and effective gas exchange. Respiration will, and typically does, occur without any conscious input, but failure to generate a respiratory rhythm is the final symptom of several neurodegenerative diseases. Therefore, it is unsurprising that a basic understanding of the neural circuitry controlling respiration has been an area of intense research during the last century. The following sections will provide an overview of the mechanics of respiration, its neural origins, and the finely tuned control mechanisms needed to maintain mammalian respiratory rhythms.

A-1. Overview of mammalian respiration

During inhalation, air enters the body through the mouth or nose and converges at the pharynx, together these structures make the upper airway. The upper airway gives way to the conducting airways where the pharynx meets the trachea. Below the trachea, airways begin to branch, increasing the contact area of air and vessel walls. The first, and largest diameter, branches are the bronchi, followed by the bronchioles and terminal bronchioles. There are 23 branch points between the trachea and the alveolar sacs, the final 7 of which encompass the respiratory bronchioles, the alveolar ducts, and the alveoli. The alveoli are the terminal portion of the respiratory tract and have a combined surface area of 70 m^2 [1]. Ultimately, gas exchange occurs between the alveoli and the surrounding pulmonary capillaries. These capillaries bring blood rich in carbon dioxide and low in oxygen to the alveoli, where, via simple diffusion, oxygen moves into the capillaries and carbon dioxide enters the alveoli. Carbon dioxide is then expelled during expiration while oxygen is carried throughout the body.

During respiration, the movement of air, into and out of the thoracic cavity, follows pressure gradients created by the muscles of respiration. When the thoracic cavity expands in volume its pressure decreases and air enters the lungs. Contraction of the diaphragm accounts for 75% of the chest cavity's increase in volume during quiet inspiration [1]. The external intercostal muscles also contribute to the increased thoracic volume during inspiration and, in absence of diaphragmatic contraction, are able to produce sufficient expansion for resting ventilation. When breathing becomes more labored, neck muscles, such as the scalene and sternocleidomastoid muscles, raise the thoracic cavity and enable deeper inhalations. Early in the inspiratory phase, abductors of the upper airways must contract to open the glottis and pull the vocal folds apart.

Air is pushed out of the lungs when the thoracic cavity passively contracts after the inspiratory expansive phase. The decrease in thoracic volume increases the pressure, relative to the atmosphere, and air moves out. During forced expiration lung volume is further decreased by contraction of the internal intercostal muscles and various anterior abdominal muscles, e.g. rectus abdominus, transverse abdominus, and the external and internal oblique muscles. These muscles pull the ribcage down and inward, thus increasing the volume of expelled air.

Spinal motor neurons in the ventral horn of the cervical, thoracic, and upper lumbar cord innervate the muscles of respiration described above. The phrenic nerve exits the spinal cord at C3-C5 and innervates the diaphragm. External and internal intercostal muscles are innervated by neurons from the thoracic ventral horn, and abdominal muscles receive innervation from motorneurons originating in the thoracic and upper lumbar cord regions [2]. The nucleus ambiguous, in the ventrolateral medulla, contains several pools of motor neurons that innervate the laryngeal and pharyngeal muscles. Also in the ventrolateral medulla is the facial motor nucleus which innervates the nasalis muscle and other facial muscles involved in the initial entry of air to the mouth and nasal cavity. In addition, the genioglossus muscle, which, when contracted, assists in enlarging the upper airway, is innervated by motor neurons arising from the hypoglossal nucleus [2].

A-2. Respiratory rhythm generating circuits in the medulla

The respiratory cycle in mammals consists of two major phases: inspiration and expiration. Expiration is further comprised of two phases, post-inspiration and a second phase of expiration [3], [4]. These respiratory phases can be recognized in the integrated activities of the phrenic (PN, defining inspiratory phase) and cranial nerves (e.g., the central vagus nerve expressing activity during both inspiration and postinspiration). The rhythm and coordinated motor pattern that causes breathing in mammals is generated by a respiratory central pattern generator (CPG) located in the medulla [3], [5], [6]. Medullary respiratory neurons are organized into bilaterally symmetrical groups referred to as the dorsal respiratory group (DRG) and the ventral respiratory column (VRC). Neurons in the DRG and VRC are further classified by their locations and the timing of their discharge with respect to the respiratory cycle (e.g. inspiratory (I) neurons are found in the pre-Bötzinger complex (pre-BötC) of the VRC).

Dorsal Respiratory Group

The dorsal respiratory group is located in the nucleus of the tractus solitaries (NTS), and respiratory neurons were first identified there in the 1950's [7]. I-α and I-β neural populations in the DRG are active during inspiration and can be distinguished by their activity during suppression of lung inflation. Specifically, I-α neurons neurons show an increase in activity during lung suppression, while I-β neurons demonstrate decreased activity [8], and both populations project to the phrenic motor neurons [9]. A third population of neurons in the DRG, namely, the pump cells, receives afferent axonal input from pulmonary stretch receptors (I-β neurons receive this input as well), via the vagus nerve, exciting the pump cells and providing phasic, respiratory-modulated activity [10]–[12]. The pump cells are thought to drive the Hering-Breuer reflex (discussed in Chapter I: A-5), because of the results of microinjection of pharmacological blockers and lesioning studies [12]–[15]. The connectivity between the DRG, VRC, and pontine respiratory groups is a topic of this thesis and further information can be found in Chapter V.

Ventral Respiratory Column

The ventral respiratory column (VRC) contains the core circuitry needed to generate a respiratory rhythm. The main regions of the VRC will be discussed starting with the caudal ventral respiratory group (cVRG) and moving rostral to the retrotrapezoidal nucleus (RTN), see Figure I-1.

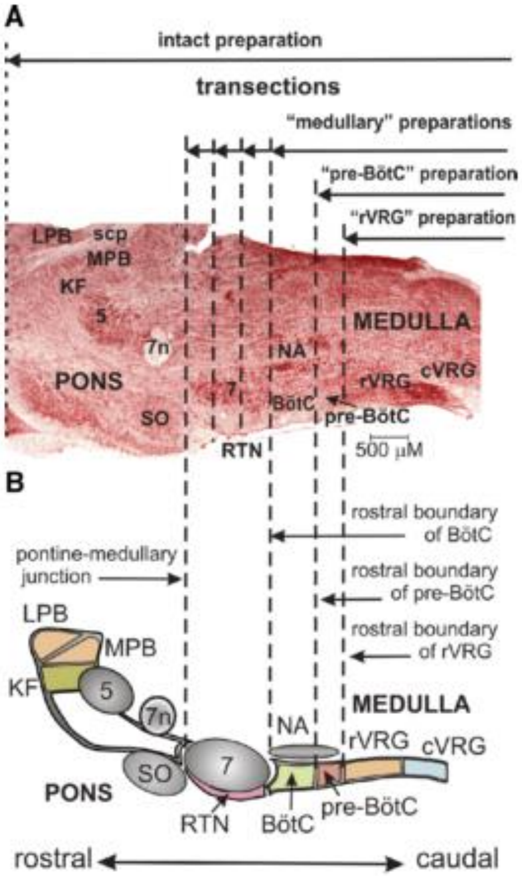

Figure I-1. Intact representation of the neural respiratory network, from [16]. (A) A parasagittal section of the brainstem with neutral red stain. (B) Schematic representation of the respiratory-related structures in the brainstem.

The cVRG and rostral ventral respiratory group (rVRG) contain pre-motor neurons for phrenic, abdominal, and central vagus motor neurons, though it is unlikely that this list is exhaustive. The cVRG has bulbospinal pre-motor neurons that project primarily to expiratory motor neurons, such as the abdominal nerve [17]. The rVRG also contains bulbospinal premotor neurons, but projects primarily to inspiratory motor neurons [16], [18]–[22]. In addition, because of elevated c-fos expression after exposure to elevated CO_2, some have speculated that the rVRG may be a site of central chemoreception [22].Smith et al. first described a sub-region of the VRC putatively responsible for generating the inspiratory rhythm, named the pre-Bötzinger complex (pre-BötC) [23]. In this study, inspiratory rhythm generation ceased after removal of a slice containing the pre-BötC [23]. Furthermore, when a 500 µm thick medullary slice containing the pre-BötC was excised from the brainstem, an inspiratory rhythm (in this case, hypoglossal nerve activity) comparable to those observed in intact brainstem preparations was recorded. Following this initial publication, the pre-BötC became the target of many studies that confirmed and further explored the pre-BötC's role in respiratory rhythm generation [20], [24], [25]. The pre-BötC's intrinsic rhythmicity extends beyond rhythm generation in a slice, and it was shown that rhythmic bursting activity occurred even when the pre-BötC was isolated from a slice, in so called "pre-BötC islands," see [26] for initial publication of this experimental preparation. Moreover, some individual pre-BötC neurons in these slices continued generating rhythmic bursting after synaptic connections were blocked, i.e. endogenous bursting, see [25]–[28]. In these studies, bursting in slices was typically induced by the increasing the concentration of extracellular potassium, K_{out}, from its physiological level of 3-4 mM up to 8-9 mM [27]–[30]. This elevation of K_{out} was usually applied for a necessary increase in neuronal excitability (neuronal membrane depolarization) *in vitro* to compensate for a lack of external excitatory drives operating in more intact systems *in vivo*. It should be noted here that the mechanisms underlying the endogenous rhythmicity in the pre-BötC are an area of intense debate. The neuron models used in this dissertation rely on the persistent sodium current for their rhythmicity, however, several other currents have been implicated in this behavior and are discussed more extensively in Chapter II.

Several groups have attempted to determine the connectivity of the pre-BötC using anatomical (e.g. antidromic stimulation, viral neuronal tracing, calcium imaging, etc.) as well as functional (e.g. qualitative changes following transections, ablations, drug application, etc.) methods. Presently, there are several proposed connectivity schematics, however, there is significant disagreement over the existence and importance of various connections. The topic of the pre-BötC's connectivity will be addressed throughout this dissertation using computational modeling alongside experimental work, particularly in Chapters III-V.

Rostral to the pre-BötC is the Bötzinger complex (BötC), containing mostly expiratory related neurons [3], [31]–[34]. Recordings from the BötC revealed neurons that were active immediately following inspiration (post-inspiratory, i.e. post-I neurons) and others that had increasing activity during expiration (augmenting-expiratory, aug-E neurons) [16], [18], [19], [35], [36]. Together, the BötC and pre-BötC comprise the core circuitry of the respiratory CPG, and they generate respiratory oscillations defined by the intrinsic biophysical properties of the neurons involved as well as the architecture of network interactions between neural populations within and between the pre-BötC and BötC.

Rostral to the BötC is the parafacial respiratory group (pFRG), that lies within, or overlapping, the retrotrapezoid nucleus (RTN) [37]–[39], and they are often referred to together as the RTN/pFRG. This region was first discovered by Smith et al. via retrograde labeling from the VRC [40]. Several studies indicate that RTN/pFRG oscillations drive abdominal motor (AbN) activity. The AbN is typically active during the expiratory phase, and, in particular, plays a critical role in forced, or active, expiration. The activity of the RTN/pFRG seems to drive AbN activity primarily in the pre-inspiratory (or late-expiratory, late-E) phase of expiration when CO_2 is elevated (hypercapnic conditions) [20], [41]–[43].

This sensitivity to CO_2 is supported by several studies that found chemosensitive characteristics in the RTN/pFRG region of the medulla [22], [44]–[48]. The work presented in Chapters III and IV of this dissertation will examine the role of the RTN/pFRG in altered chemical environments, specifically hypercapnia and hypoxia, as well as in the presence of opioid agonists. The purpose of this work is to better understand how the RTN/pFRG participates in the generation of a respiratory rhythm through interactions with other VRC compartments.

A-3. Additional neural populations in the brainstem contributing to the respiratory rhythm

Pontine involvement in respiratory rhythm generation was first observed in 1887 by Marckwald, who demonstrated that lesioning the pons and then cooling the vagus nerve caused a transformation from eupnea to apneusis (a pattern characterized by significantly prolonged inspiratory duration) [49]. Later, Lumsden challenged the necessity of vagal cooling (or removal), and instead posited that only removal of the pons was needed to induce apneusis [50]. Although subsequent studies have shown only an increase in inspiratory duration following a chronic pontine lesion in vagi intact animals [51]–[55], it is widely agreed that the pons plays a critical role in the generation and maintenance of eupneic breathing and this role is dramatically altered by hypoxic conditions [36], [56]–[60]. Several populations of neurons in the dorsolateral (dl) and ventrolateral (vl) pons, as well as the intertrigeminal region (ITR), send axonal projections to the VRC to modulate the respiratory rhythm [16], [18], [19], [61]–[64]. Additionally, the pons contains the locus coeruleus and pedunculopontine tegmental nuclei, both of which can effect breathing and may participate in adaptation of the respiratory rhythm [64]–[66].

The dl pons contains the Kölliker-Fuse nucleus (KF) and the parabrachial (PB) complex. There are many nuclei in the KF and PB regions of the dl pons, and the specific functions tend to vary by species [64], therefore I will refer to this area simply as the dl pons. Arguably the most notable function of the dl pons is the inspiration-expiration phase transition, often referred to as the inspiratory off-switch (IOS) [3], [18], [63], [64]. Stimulation of the dl pons causes a premature termination of inspiration, i.e. a sharp inspiration-expiration phase transition [3], [63], similar to the IOS promoted by the Hering-Breuer reflex (see Chapter I: A-5). The activity patterns of inspiratory (I) and inspiratory-expiratory (IE) neurons in the dl pons can be either phasic and tonic [63], [64], [67]–[73]. The source of phasic activity in the dl pons is still unknown, but numerous models and experimental studies suggest that input from the medullary CPG is required for phasic activity in the pons [18], [60], [63], [64], [74], [75]. This phasic activity exists in intact animals, but is minimal, however, it has been shown that inhibition of the NTS, or removal of vagal input to the NTS, causes a strong facilitation in the phasic activity of dl pontine neurons [60], [63], [72], [73], [76]. This evidence pointed to the NTS as a strong inhibitor of phasic dl pons activity. Interestingly, Feldman and Cohen demonstrated that this inhibition had little effect on the tonic discharges of dl pontine neurons, and it was thus suggested that this inhibition may therefore be presynaptic [72], [73].

The vl pons is not as well characterized as the dl pons. However, neurons in the A5 region of the vl pons have been recorded with expiratory modulated activity, typically post-inspiratory and middle-late expiratory [57], [77] and localized application of glutamate to

A5 has been shown to prolong the expiratory phase [78]. Moreover, several studies have uncovered reciprocal connections between A5 and neurons of the respiratory CPG in the ventrolateral medulla [79]–[81]. In addition, it has been speculated that intra-pontine connections exist between the dl and vl regions [82], possibly through ITR interneurons [64].

A-4. In vitro characterization of respiratory rhythm following progressive transections

The previous two sections introduced the key sub-populations of the brainstem respiratory network, the connectivity of which is a central focus of this dissertation. Though there has been extensive work performed using antidromic stimulation, viral tracing, and calcium imaging (see [21], [81], [83]–[86]) to understand the respiratory CPG's connectivity, elucidating the importance of known connections is an ongoing task. To address this issue, Smith et al., 2007 performed serial transections on an *in vitro* spinal cord preparation and used the qualitative changes to posit functional connections that were tested in a computational model [16], [19].

The specific transections performed by Smith et al. are highlighted in Figure I-1. The intact preparation included the pons and medulla, and produced the three-phased rhythm characteristic of eupneic breathing (see Figure I-2A and Figure I-3A). The specific phases of this rhythm include the inspiratory phase (early-I and pre-I neurons in the pre-BötC, and ramp-I neurons in the rVRG), post-inspiration (post-I neurons in the BötC), and augmented expiration (aug-E neurons in the BötC), see Figure I-3A. The activity of these medullary CPG neurons is reflected in the output of inspiratory motor neurons (hypoglossal and phrenic nerves) and the inspiratory-expiratory central vagus nerve, see Figure I-2A. Note that the hypoglossal nerve activity precedes the phrenic nerve suggesting pre-I neurons in the pre-BötC are pre-motor for hypoglossal activity, whereas the early-I and ramp-I neurons of the pre-BötC and rVRG, respectively, are likely pre-motor for phrenic nerve activity.

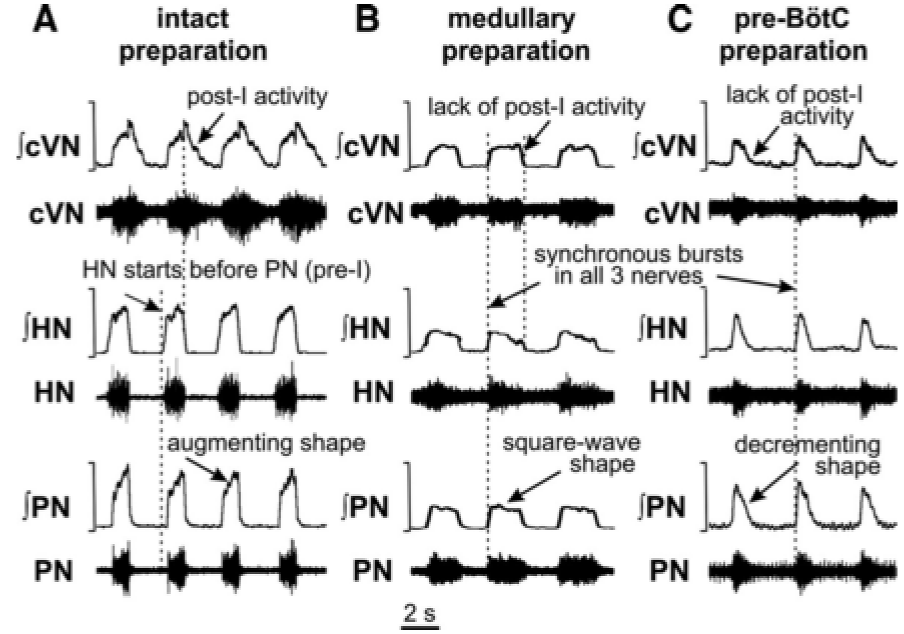

Figure I-2. Activity patterns of central vagus (cVN), hypoglossal (HN), and phrenic (PN) nerves recorded with suction electrodes, adapted from [16]. Raw recordings are below integrated activity for each nerve. (A) Intact preparation containing pons and medulla. (B) Following transection at ponto-medullary junction, i.e. medullary preparation, no post-I activity is observed. (C) Preparation with removal of medulla rostral to pre-BötC.

Transection of the pons produced a two-phased rhythm with comparable durations of inspiration and expiration (see Figure I-2B and Figure I-3B). In Figure I-3B the activity of post-I neurons in the BötC is eliminated and the aug-E neuron now comprises the entire expiratory phase. The onset of pre-BötC neurons is now closer in temporal proximity and this is reflected in the onset of hypoglossal and phrenic nerve activity. Finally, after removal of the medulla, rostral to the pre-BötC (i.e. pre-BötC preparation, in see Figure I-2C and Figure I-3C), only the inspiratory phase remains. Notably, the activity in early-I pre-BötC neurons has ceased, and only the pre-I pre-BötC and ramp-I rVRG neurons remain active. This suggests: (i) some form of internal rhythmicity and (ii) pre-I pre-BötC neurons likely project to the rVRG pre-motor neurons as well as directly to the hypoglossal nerve.

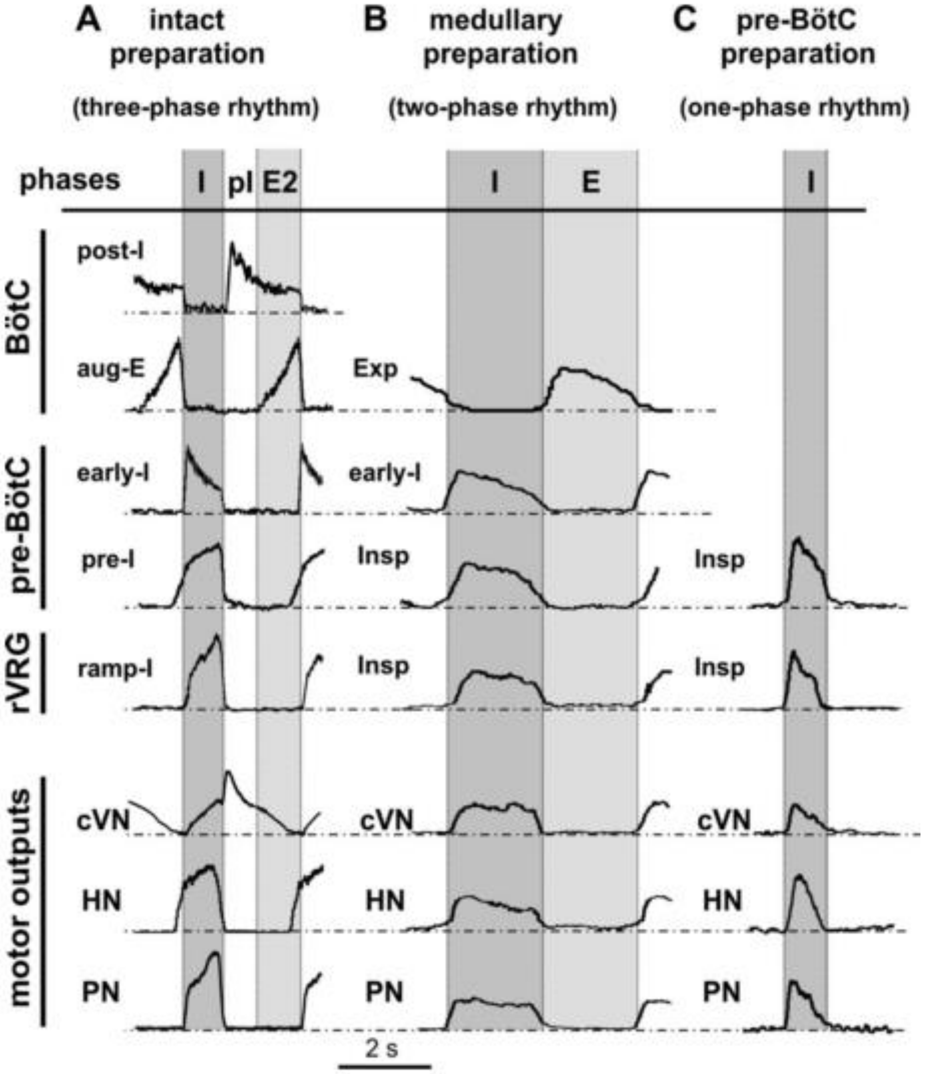

Figure I-3. Activity patters within multiple respiratory compartments, adapted from [16]. Individual neurons were recorded in several compartments and traces represent cycle-triggered waveforms for the groups of cells recorded. (A) Intact preparation showing three-phase rhythm. (B) Preparation with pons removed, shows two-phase rhythm. (C) Preparation with removal of medulla rostral to the pre-BötC, shows one-phase, inspiratory rhythm.

These transection studies inspired modeling studies by the Rybak group, aimed at elucidating the VRC connectivity responsible for these qualitative changes [35], [61]. Models used in these studies employed qualitatively similar network architectures that included pre-BötC, BötC, and pontine compartments with pre-I (excitatory) and early-I (inhibitory) neurons in the pre-BötC compartment and post-I (inhibitory) and aug-E (excitatory) neurons in the BötC compartment (note: the Rybak et al., 2007 model had a more complex framework to account for motorneuron activity), see Figure I-4.

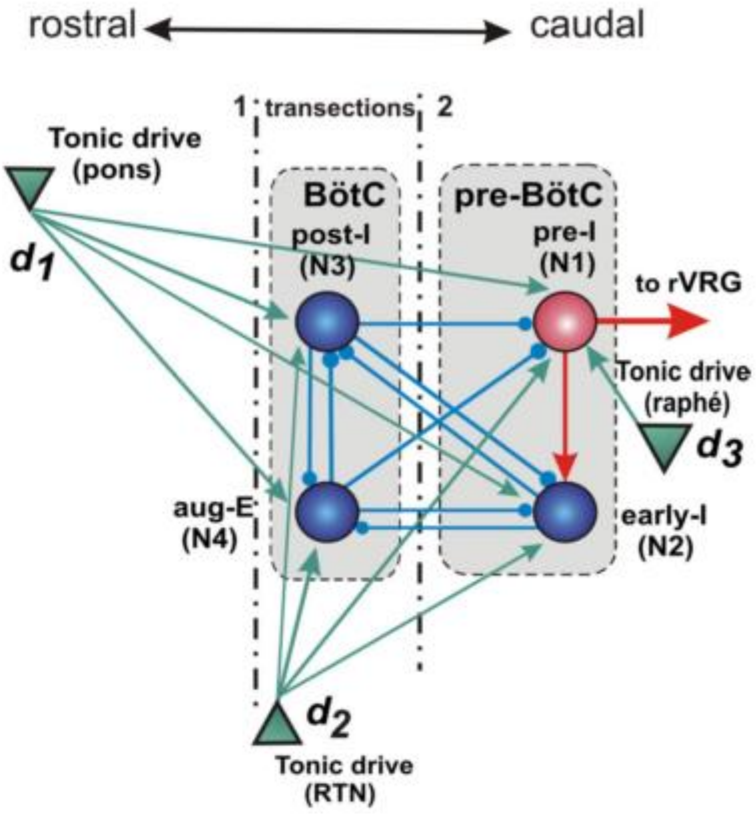

Figure I-4. Adapted schematic of simplified VRC model, published in [35]. Model includes an excitatory pre-I population (red circle), inhibitory populations (blue circles), and tonic drives (green triangles). Transection experiments from [16] were simulated by progressive removal of drives, i.e. to simulate the medullary preparation d_1=0 and to simulate the pre-BötC preparation, d_2=0.

Moving rostral to caudal, the tonic pontine drive supplied the post-I neurons only source of excitation, therefore, transection of the pons (d_1=0 in the model) silenced the post-I neurons. When intact, the expiratory neurons of the BötC exist in a state of mutual, but asymmetric, inhibition where the post-I escapes from early-I inhibition and thus begins the expiratory phase by inhibiting the aug-E neuron. As the post-I neuron adapts, the aug-E neuron is released and, as its activity grow, it inhibits the inspiratory pre-BötC neurons, thus prolonging the expiratory phase. When inhibition from the BötC is no longer sufficient to suppress the pre-BötC neurons, the pre-I neurons activate and excite the early-I neurons. In the intact configuration there is a latency between pre-I and early-I activation created by stronger inhibition to the early-I neurons from inhibitory BötC neurons, this addresses the latency between pre-I and early-I, as well as hypoglossal and phrenic nerves, seen experimentally (Figures I-2A, I-3A).

To simulate transection of the pons, d_1 was set to zero, and post-I activity ceased. Without the post-I neuron, the expiratory phase included only aug-E activity (hence the two-phased rhythm). Moreover, this weakened the expiratory side of the half-center interactions between BötC and pre-BötC, resulting in an extended duration of inspiration. Moreover, the loss of inhibition from the post-I to the early-I reduced the latency between pre-I and early-I activation at the onset of inspiration, comparable to Figure I-2B and Figure I-3B. Finally, removal of the medullary compartments rostral to the pre-BötC was simulated by setting d_2 to zero and thus removing all drive to the BötC compartment and the early-I neuron. In this simulation, the pre-I neuron continued to generate a rhythm due to its persistent sodium dependent rhythmicity.

These experimental and modeling studies established the rostral to caudal framework of the VRC. This framework forms the basis of many subsequent models and has been supported by several experimental studies, see [17], [36], [41], [63], [87]–[89].

The connectivity presented in this section will be expanded on in Chapters III-V of this dissertation.

A-5. Afferent feedback to the brainstem respiratory network

Many systems are in place to regulate the respiratory rhythm, in this section modulation caused by changes in lung inflation, pH, and the partial pressures of O_2 and CO_2, will be discussed. Chemoreception in the periphery occurs primarily in parenchymal lobules located above the bifurcation of the common carotid (carotid bodies) and along the superior portion of the aortic arch (aortic bodies). These receptors sense decreases in arterial partial pressure of O_2 (P_aO_2) and pH, and increases in P_aCO_2, and project to the NTS via cranial nerve IX (carotid bodies) and X (aortic bodies) to modulate the respiratory rhythm. Though these chemoreceptors are quick to respond to changes in the peripheral chemical environment, they do not have as strong an influence on the respiratory rhythm as the central chemoreception system, with an unappreciable effect at P_aO_2 levels above 40 mmHg [2].

Currently, existing models of the respiratory CPG rely on tonic drives from various brainstem compartments, including the raphe, locus ceruleus, and the RTN [16]–[19], [35], [62], [63], [88]. Some of the most critically involved tonic drives include areas that are often implicated in chemosensation, including the NTS and Raphe (see [90], [91]), and the RTN [22], [45], [46]. This dissertation will focus particularly on the role of the RTN in chemosensation, and its subsequent modulation of the respiratory rhythm. However, it should be noted that there exists an opposing concept to the paradigm of distinct chemoreceptive populations [48]. Specifically, the Guyenet group has posited that chemosensation is not a phenomenon reliant on specialized neurons outside the respiratory CPG, but could instead be an emergent phenomenon of the neurons participating in the generation of a respiratory rhythm, including BötC and pre-BötC neurons [92]. Some studies support the hypotheses drawn by the Guyenet group and have shown that respiratory CPG neurons either exhibited hyperpolarization or depolarization in response to a decrease in pH [93], that acidification of the pre-BötC resulted in an increase in breathing frequency [94], and that acidification of the rVRG caused an increase in phrenic nerve amplitude [95].

While it is not the purpose of this dissertation to argue against the concept of a respiratory CPG with intrinsic chemosensitivity, it is important to point out that the Guyenet group seems to be in agreement that the RTN possesses the properties needed to be considered a central respiratory chemoreceptor. Namely, the RTN: (i) increases firing rate *in vivo* when P_aCO_2 is increased, (ii) this response is caused by a direct decrease in pH sensed by these cells, and (iii) this response stimulates breathing [91], [96]. Our use of the RTN in a computational model, explored in detail in Chapter III and IV does not seem to contradict the criteria put forward by the Guyenet group. Moreover, the concept of chemosensitivity being an emergent property of respiratory CPG neurons does not directly contradict any of the work presented in this dissertation.

Unlike central chemoreception, the respiratory reflexes originating from the airways have a long history with relative agreement across groups [12], [97]–[99]. There are several receptors in the airways, each eliciting specific responses. Rapid adapting receptors (RARs) augment breathing, initiate cough, and increase airway secretion [100]–[102]; bronchopulmonary C fibers induce rapid breathing, bronchoconstriction, vasodilation, and bradycardia [99], [103]–[105]; and other receptor types have been identified, though their purpose has yet to be identified, see neuroepethelial bodies [99], [106] and slow adapting deflation receptors [107]. However, the slow adapting receptors (SARs) that underlie the Hering-Breuer reflex (HBR), as well as brondodilation and tachycardia, will be the focus of the remaining portion of this section and Chapter V of this thesis.

First identified by Josef Breuer and Edwald Hering in 1868, the HBR is initiated by SARs in the lungs and promotes the termination of inspiration while facilitating expiration [108], [109]. SARs are mechanoreceptors that exhibit phasic activity tracking lung inflation and deflation. Like all airway receptors, SARs send axons to the middle and caudal portions of the NTS via the vagus nerve [110]–[112]. Specifically, SARs project to the ipsilateral NTS at the rostrocaudal level of the area postrema [100]–[102], [113]. At least two cell types are known to receive monosynaptic input from SARs, these include I-β [114] and pump cells [10], [100], [115], [116]. These NTS cells exhibit phasic activity mirroring the SARs, and therefore long inflation and deflation, however, the I-β cells have a tonic drive that the pump cells are lacking [12], [114]. The pump cells are thought to be the primary initiator of the HBR and therefore have extensive projections to the respiratory CPG. The connectivity of the NTS's pump cells, the VRC, and pons is the topic of Chapter V of this dissertation.

B. Computational modeling of neural processes

The purpose of computational neuroscience is to explain the brain's generation and control of behaviors using computational models [117]. These models are used to address one or more of the following questions: (i) what is happening? (ii) how does the brain do this? (iii) why does the brain do this? A purely descriptive model (i), also known as a phenomenological or statistical model, summarizes experimental observations without explaining the mechanisms at play [118]. The results of a regression analysis are an example of a descriptive model, providing a relationship between two variables, which are often, though not necessarily, a system's input and output. Mechanistic models (ii) attempt to explain how a system works. A purely mechanistic model, that is also perfectly correct, will reproduce the experimentally observed output for the entire set of possible inputs. Finally, interpretive models (iii) are used to provide a reason for the observed activity and/or the mechanisms employed to produce that activity. These models often use mechanistic models and apply some novel perturbation that could demonstrate a benefit for the system to operate in a particular way.

The computational models in this paper were built with the intention of developing mechanistic explanations for breathing behavior. To validate a model we first demonstrate that the model reproduces experimentally observed activity. To separate our particular model from the infinite set of network architectures and/or mathematical formalizations that could reproduce experimental findings, we generate experimentally testable predictions. That said, a confirmed prediction does not guarantee that our model is correct. Indeed, many network configurations could likely produce the initial observations and the proposed predictions - a "problem" common to all applications of the scientific method.

Model predictions in this dissertation can be categorized by scale such that there are sub-cellular, cellular, and system level predictions. At the sub-cellular scale, predictions address the intrinsic properties of the neuron. In this work, sub-cellular predictions focus on the currents required to provide neurons with intrinsic rhythmicity. Predictions made at the cellular level concern the interactions of neurons in a single population. For example, we can identify a network parameter, e.g. probability of connections between neurons or strength of this connection, and vary this parameter to predict how a biological system might behave under analogous circumstances. The largest hierarchal scale is the system level, which I define as several interacting populations of neurons. The presence or absence of an interaction between populations, the nature of the interaction (e.g. pre-synaptic, excitatory, etc.), and the strength of an interaction can all be system level predictions. The majority of predictions made in this work are system level predictions.

B-1. Introduction to computational models of neurons

Application of dynamical systems theory to model biological, and specifically neural, processes began over a century ago. The difference in ionic concentrations on either side of a lipid bilayer creates an electrical potential that can change when ions traverse this bilayer via various channels. This phenomenon is analogous to an electrical circuit, where the lipid bilayer, or membrane, is represented by a capacitor and the various ion channels may be modeled as variable resistors connected in parallel. Indeed, many computational models of neuronal action potentials model the neuron in just this way, see Figure I-5 for a circuit diagram representation of the Hodgkin-Huxley model of a neuron.

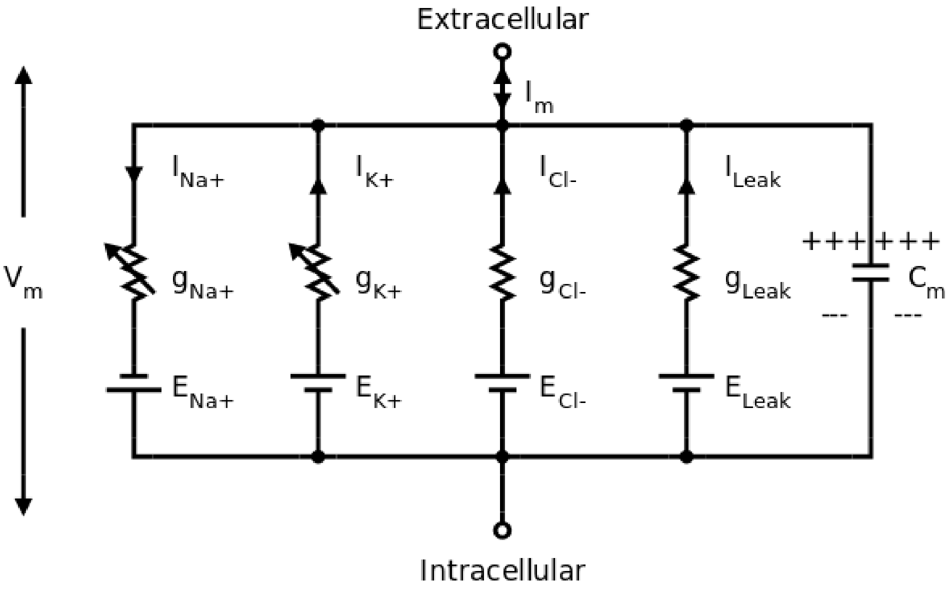

Figure I-5. Electrical circuit equivalent of a Hodgkin-Huxley computational model. The voltage (V_m) across a membrane is dependent on the capacitive properties of the membrane (C_m) and the conductances of the various ionic channels (g_x). Adapted from [119].

Conductance-based models are often used to make biophysically realistic models of neurons. More simplistic models, e.g. the integrate and fire [120] and FitzHugh-Nagumo models [121], [122], are often selected for situations calling for extensive mathematical analysis or large-scale network simulations. However, the work in this dissertation will employ only conductance-based models modified from the canonical Hodgkin-Huxley model [123], [124].

There are, broadly speaking, two types of models I wish to use in this dissertation: (i) spiking neurons that are integrated into networks of neurons (Sections B-2, 3), and (ii) activity-based, or reduced, formalizations (Section B-4), and each model type has unique features and advantages. It should be emphasized that, in this section, I am simply presenting a general form of these models. I applied slight variations to perform the simulations presented in this document and these variations will be addressed in the methods sections of each specific chapter.

B-2. Model of a spiking neuron

The model of a single, spiking pre-BötC neuron, used in Chapters II, III, and V, represents an extension of previous conductance-based models [125]–[127]. The neuron's membrane potential (V) is defined using the differential equation:

$$C \cdot \frac{dV}{dt} = -I_{Na} - I_{NaP} - I_K - I_L - I_{Syn}, \qquad (I\text{-}1)$$

where C is the membrane capacitance, V is membrane potential, and I_x represents the various currents described below:

$$I_{Na} = \bar{g}_{Na} \cdot m_{Na}^3 \cdot h_{Na} \cdot (V - E_{Na}); \qquad (I\text{-}2)$$

$$I_{NaP} = \bar{g}_{NaP} \cdot m_{NaP} \cdot h_{NaP} \cdot (V - E_{Na}); \qquad (I\text{-}3)$$

$$I_K = \bar{g}_{Kdr} \cdot n^4 \cdot (V - E_K); \qquad (I\text{-}4)$$

$$I_L = g_L \cdot (V - E_L); \qquad (I\text{-}5)$$

$$I_{Syn} = g_{Syn} \cdot (V - E_{Syn}), \qquad (I\text{-}6)$$

where: $\bar{g}_{Na}$, $\bar{g}_{NaP}$, and $\bar{g}_K$ are maximal conductances for the fast sodium, persistent sodium, and potassium delayed rectifier currents, respectively; g_L and g_{Syn} are the leakage and synaptic conductances, respectively; m_{cur} and h_{cur} (where the index, cur, identifies either Na or NaP) represent the activation and inactivation gating variables for the corresponding voltage-gated sodium channels whose dynamics are described by the following equations:

$$\tau_{h,cur}(V)\cdot\frac{dh_{cur}}{dt}=h_{\infty,cur}(V)-h_{cur}; \tag{I-7}$$

$$\tau_{m,cur}(V)\cdot\frac{dm_{cur}}{dt}=m_{\infty,cur}(V)-m_{cur}, \tag{I-8}$$

where the voltage dependent inactivation, $h_{\infty,cur}$, and the voltage dependent activation, $m_{\infty,cur}$, have voltage dependent time constants, $\tau_{h,cur}$ and $\tau_{m,cur}$, respectively. These voltage dependent gating functions for the sodium currents, I_{NaP} and I_{Na}, are governed by the following equations, first described by [125]:

$$h_{\infty,cur}(V)=\left(1+\exp\left\{(V-V_{h,cur})/k_{h,cur}\right\}\right)^{-1}; \tag{I-9}$$

$$m_{\infty,cur}(V)=\left(1+\exp\left\{(V-V_{m,cur})/k_{m,cur}\right\}\right)^{-1}; \tag{I-10}$$

$$\tau_{h,cur}(V)=\tau_{h,cur,\max}/\cosh\left\{(V-V_{h,\tau,cur})/k_{h,\tau,cur}\right\}; \tag{I-11}$$

$$\tau_{\mathrm{m},cur}(V)=\tau_{\mathrm{m},cur,\max}/\cosh\left\{(V-V_{m,\tau,cur})/k_{m,\tau,cur}\right\}. \tag{I-12}$$

The voltage dependent activation, *n*, of the delayed rectifier potassium current, I_K, follows the same general form as the other currents activations:

$$\tau_{\mathrm{n}}(V)\cdot\frac{dn}{dt}=n_{\infty}(V)-n, \tag{I-13}$$

and obeys the voltage dependent functions described by [128]:

$$n_{\infty}(V)=k_1(V)/\left(k_1(V)+k_2(V)\right); \tag{I-14}$$

$$\tau_n(V)=\left(k_1(V)+k_2(V)\right)^{-1}; \tag{I-15}$$

$$k_1(V)=n_A\cdot\left(n_{AV}+V\right)/\left(1-\exp\left\{-\left(n_{AV}+V\right)/n_{Ak}\right\}\right); \tag{I-16}$$

$$k_2(V)=n_B\cdot\exp\left\{-\left(V+n_{BV}\right)/n_{Bk}\right\}. \tag{I-17}$$

The reversal potentials, E_{Na} and E_K in equations (*I-2)-(I-4*), for *Na* and *K* ions, may be calculated with the Nernst equation:

$$E_{ion} = \frac{R \cdot T}{F} \cdot \ln \frac{[Ion]_{out}}{[Ion]_{in}}, \qquad (I\text{-}18)$$

where R is the universal gas constant, T is the temperature in Kelvin, and F is Faraday's constant.

B-3. Modeling networks of neurons

The models used in Chapters II, III, and V were models of networks of spiking neruons similar to what was described in the previous section. To "connect" neurons within a population we used the following formalization:

$$g_{syn} = g_{dr} + g_{net}(t), \qquad (I\text{-}19)$$

where g_{dr} specifies an external drive applied to the system, and g_{net} describes afferent inputs from neurons in the population (it should be noted that equation (*I-19*) technically exists, separately, for both excitatory and inhibitory synaptic inputs, but I am using a general form here for brevity). g_{net} is equal to zero at rest, and increases when a spike is received. If a neuron, j, transmits a spike to a neuron, i, there is an increase in the synaptic conductance, $\bar{g} \cdot w_{ji}$ ($\bar{g}$ defines the increase in synaptic conductance produced by a single spike and w_{ji} is a synaptic weight from neuron j to i) of neuron i that obeys the formalization below:

$$g_{net}(t) = \bar{g} \cdot \sum_{j(j \neq i)} w_{ji} \cdot \sum_{t_{kj} < t} e^{-(t - t_{kj})/\tau_{syn}}. \qquad (I\text{-}20)$$

where τ_{syn} defines the synaptic time constant and t_{kj} emulates synaptic delay by defining the time at which the falling edge of the k-th action potential reaches -10mV. To explain how populations are connected in my models, assume that a given population A receives an input (either excitatory or inhibitory) from a population B. Then, based on a weighting coefficient that defines the strength of connection between populations A and B, we assume that every neuron in population B sends an input to every neuron in population A, with a strength based on the afore mentioned coefficient.

B-4. Activity-based model

To perform certain qualitative analyses I use a reduced, activity-based, non-spiking neuron model with two dynamical variables. This model was adapted from a reduced model of a population of intrinsically bursting neurons first developed by Rubin et. al [35], [88], [129]. Endogenous bursting in these neurons was suggested to involve the persistent sodium current, I_{NaP}, previously described in equation (*I-3*), with burst termination based on the slow inactivation of this current. This model is capable of generating bursting activity in a wide range of neuronal excitation and burst frequencies, and exhibited a reduction of burst amplitude when the frequency increased. Similar to the Rubin et al. models, our formulation for each center includes an explicit representation of I_{NaP}:

$$C \cdot \dot{V} = -I_{NaP} - I_L, \qquad (I\text{-}21)$$

where C is the membrane capacitance, I_{NaP} represents the persistent sodium current, and I_L is the leak current. The currents in equation (*I-21*) are described identically to the currents in the previous section, i.e. equations (*I-3*) and (*I-5*).

The output of each neuron describing its activity, or normalized firing rate, is transformed from its membrane potential by a piecewise linear function *f(V)*, changing between 0 and 1 such that:

$$f(V) = \begin{cases} 0, \text{ if } V < V_{\min} \\ (\mathrm{V} - \mathrm{V}_{\min}) / (V_{\max} - V_{\min}), \text{ if } V_{\min} \le V < V_{\max}, \\ 1, \text{ if } V \ge V_{\max} \end{cases} \qquad (I\text{-}22)$$

where V_{min} and V_{max} define the threshold and saturation voltages, respectively.

The model described in this section is somewhat incomplete. There may be up to two additional currents used to describe excitatory and inhibitory connections between neurons and, in Chapter IV an additional adaptive current was used. However, detailed descriptions of these neurons are provided in their respective chapters.

B-5. Previous computational models of the respiratory network

To my knowledge, the first published computational model of the respiratory network was by Rubio in 1967 [130]. This model employed a Volterra-type integral equation that could, under specific parameter sets, provide a stable limit-cycle that represented a respiratory rhythm. Similar conceptual models extended this work and accounted for possible firing patterns seen experimentally [131]–[133]. Just prior to the first publication of the pre-BötC, Duffin published a model of mutual inhibiton from the BötC to the putative inspiratory region [133]. This concept was expanded upon greatly by the Rybak group in a series of three publications [61], [134], [135]. The initial model was the first to employ biophysically realistic neurons, as well as multiple cell types, see Figure I-6. Despite being developed after the discovery of the pre-BötC, this model did not incorporate any pacemaker properties.

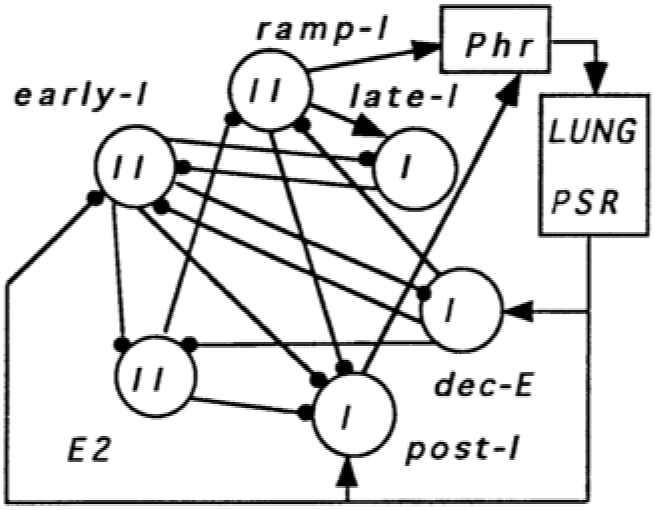

Figure I-6. Schematic of respiratory CPG from [135].

The first model of the respiratory network with intrinsically rhythmic, pacemaker neurons was published by Butera et al. in 1999 [125], [126]. The formalization of neurons in these models closely mirrors the ones we use in our spiking neuron models, see Chapter I: B-1, and was used by Rybak et al., 2003 to make a biophysically realistic model of the pre-BötC [136]. This model of the pre-BötC has been the fundamental kernel of many respiratory models published by the Rybak group [16]–[19], [62], [63], [127], as well as several models presented in this dissertation. The integration of the pre-BötC neurons with other medullary and pontine neurons was discussed in Chapter I: A-4. Further development of the pre-BötC (Chapter II), and its integration with the RTN/pFRG oscillator (Chapters III, IV), the pons (Chapters III, IV, and V), and the DRG (Chapter V) will be the focus of this dissertation.

C. Techniques of mathematical analysis

C-1. Overview

The computational models presented in this thesis are all non-linear systems, meaning that they do not satisfy the superposition principle. This principle states that linear systems have homogeneity and additivity, and these are defined, for variables x and y and scalar a, as follows:

$$F(a \cdot x) = a \cdot F(x)\,; \tag{I-23}$$

$$F(x \cdot y) = \cdot F(x) + F(y)\,. \tag{I-24}$$

equation (*I-23*) defines homogeneity and (*I-24*) defines additivity. Linear systems are typically easier to analyze than non-linear ones. However, using only linear systems would significantly limit the number of physical processes one could model. The need for non-linear systems, and an appreciation of their dynamics, underlies the mathematical fields of bifurcation theory and qualitative analysis. The following two sections will introduce these analytical tools and their application to computational models of neurons.

C-2. Bifurcation theory

To understand a broad range of dynamics produced by our models, we used a technique involving the construction of Poincaré sections to create bifurcation diagrams [137]. Various Poincaré sections could be constructed depending on the circumstance. However, as an example, assume we wish to create the bifurcation diagram shown in Figure I-7, where a neuron's interspike interval is calculated as a function of applied current (i.e. external drive). In this example drive is the bifurcation parameter and the Poincaré section was constructed by locating instances of a neuron's potential crossing a chosen threshold, typically -35 mV, in a specified direction. The time between these instances is the interspike interval. Such bifurcation diagrams show qualitative changes in the system's behavior as the parameters were varied. However, the time interval separating changes in drive must be sufficiently large to allow the system to closely converge to its steady state prior to the calculation of interspike intervals.

In this specific example, there is a bistability revealed in the bifurcation diagram in Figure I-7. When drive is increased the interspike interval is depicted with red dots, and then drive is decreased and interspike interval is depicted with green dots. The bistable region in occurs when drive = [0.3, 0.34] and the system could either exhibit bursting (i.e. several interspike intervals) or tonic spiking (one interspike interval). This behavior indicates a chaotic system, or, more informatively, a system whose state is dependent on the initial conditions. Similar observations have been made with *in vitro* preparations that demonstrate switching between quiescence and bursting behavior when a small transient current pulse is applied [138]. The *in silico* parallel creates two stable regions of attraction and applying an external drive can perturb the system away from one region and towards the other [139].

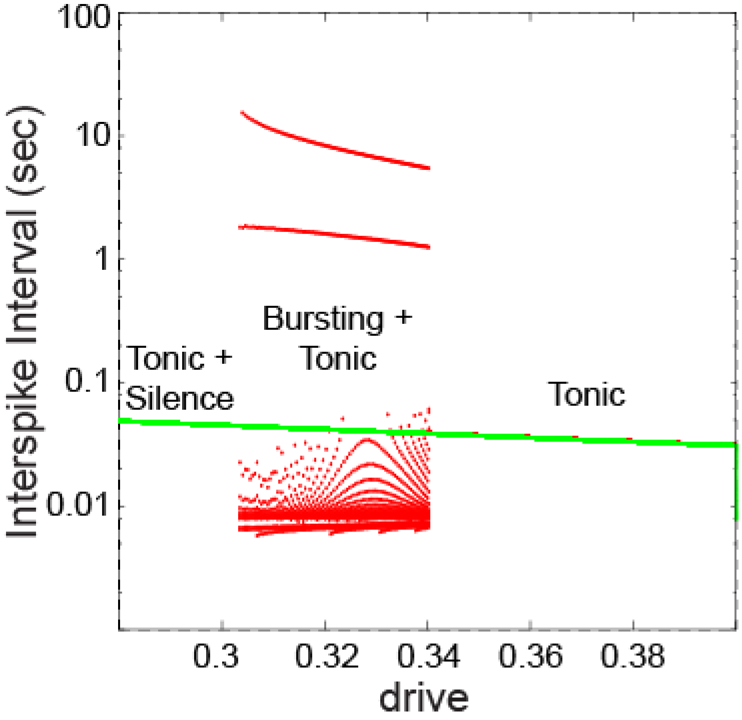

Figure I-7. One-dimensional bifurcation diagram showing interspike interval as a function of external drive. Red dots correspond to interspike intervals calculated when drive was increased, whereas green dots show the interspike interval with decreasing drive.

Two-dimensional bifurcation diagrams have different bifurcation parameters on the *x*- and *y*-axis. Using an example analogous to Figure I-7, drive and extracellular potassium concentration (K_{out}) could both be bifurcation parameters, and the qualitative nature of the interspike interval, i.e. silence, bursting, tonic spiking of a neuron, could be depicted with shading, see Figure I-8. In this example the regions of bursting are shaded black.

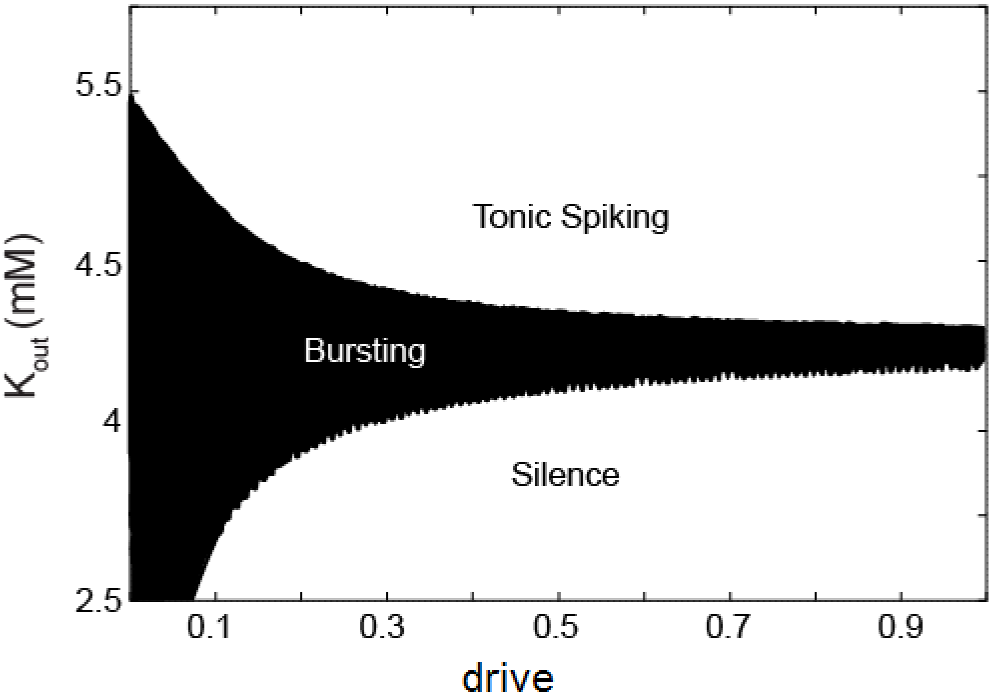

Figure I-8. Two-dimensional bifurcation diagram in the (K_{out}, drive)-plane. Bursting is calculated using the method described for one-dimensional bifurcation diagrams.

C-3. Fast-slow timescale decomposition

Bifurcation diagrams provide us with a picture of a broad range of system behaviors. However, further analysis is required to answer why a particular qualitative transition (e.g. from silence to bursting to tonic spiking, in a neuron, see Figures I-7, I-8), occurred. The technique of fast-slow timescale decomposition enables us to answer such a question. Using the example of a neuron that transitions from silence, bursting, to tonic spiking when K_{out} is increased, for a fixed value of drive (e.g. drive=0.5, Figure I-8), we can exploit the timescale difference between this neuron's fast and slow variables, note: though no parameter values were given for the simulations performed above, they closely resemble the parameters of pre-BötC neurons described in Chapters II, III, and V.

Specifically, the time constants for V, h_{Na}, m_{Na}, m_{NaP}, n, and h_{NaP} are such that the slower variable, h_{NaP}, may be treated as a fixed parameter of the five-dimensional fast subsystem with dynamical variables: V, h_{Na}, m_{Na}, m_{NaP}, and n. The equilibrium solutions, or critical points, of the fast subsystem were projected into (h_{NaP}, V) and formed the slow-manifold as h_{NaP} was varied, see Figure I-9, blue curve. The slow-manifold had a cubic shape with three branches. The lower and middle branches are connected by a point which is the lower knee (LK) of the slow-manifold. From right to left, along the slow-manifold, critical points become unstable at a Hopf bifurcation point (HB, blue circle), with periodic orbits emerging (red lines represent the extrema of the voltage on the emerging periodic orbit). The h_{NaP}-nullcline, calculated when the first derivative of h_{NaP} = 0, see equation. (*I-7*), is represented by a black dashed line, and the solution to the full system is depicted by a trajectory drawn with a solid black line.

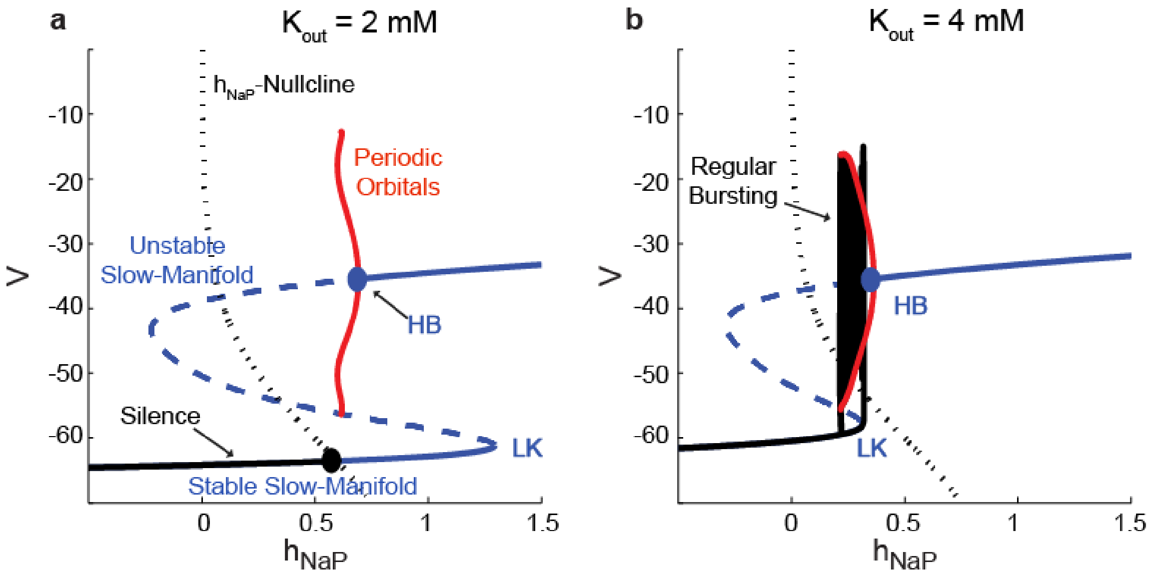

Figure I-9. Fast-slow analysis of transitions between silence and bursting. The slow-manifold is depicted by solid and dashed blue line when the critical points are stable and unstable, respectively. When the slow-manifold loses its stability (at the solid blue circle representing the location of the Hopf bifurcation), a periodic orbit emerges and its minimal and maximal V-coordinates are depicted with red lines. The h_{NaP}-nullcline is represented by a dashed black line. The solid black line represents the neuron's trajectory in (h_{NaP}, V). (A) Silence occurred when the neuron reached a stable critical point. (B) Bursting occurred by a homoclinic bifurcation.

Fast-slow decomposition methods reveal the mechanisms underpinning silence and bursting in this model of a neuron. Silence occurs when the low potential branch of the slow-manifold intersects the h_{NaP}-nullcline, creating a stable fixed point where the trajectory converges (black solid black circle). Increasing K_{out} causes a transition to bursting behavior via a saddle-loop (homoclinic) bifurcation in the fast subsystem that occurs when the HB is positioned to the left (lower h_{NaP}-coordinates) than the LK of the slow-manifold.

D. Specific Aims

D-1. Specific Aim 1 - Chapter II

This aim focuses on computational and theoretical investigations of neuronal activity arising in the pre-Bötzinger complex (pre-BötC), a medullary region generating the inspiratory phase of breathing in mammals. A progressive increase of neuronal excitability in medullary slices containing the pre-BötC produces mixed-mode oscillations (MMOs) characterized by large amplitude population bursts alternating with a series of small amplitude bursts. Using two different computational models, I demonstrated that MMOs emerge within a heterogeneous excitatory neural network because of progressive neuronal recruitment and synchronization. The MMO pattern depends on the distributed neuronal excitability, the density and weights of network interconnections, and the cellular properties underlying endogenous bursting. Critically, the latter should provide a reduction of spiking frequency within neuronal bursts with increasing burst frequency and a dependence of the after-burst recovery period on burst amplitude. This work highlights a novel mechanism by which heterogeneity naturally leads to complex dynamics in rhythmic neuronal populations.

D-2. Specific Aim 2 - Chapter III

I modeled the network level dynamics, specifically the phase switching between inspiration and expiration, of the pre-BötC and other populations relevant to respiratory rhythmogenesis. I incorporated chemosensitive elements that reproduced experimental findings in hypercapnic and hypoxic environments, specifically the emergence of abdominal nerve activity at the end of expiration (late-E) during hypercapnia that transitioned to biphasic (late-E and early-inspiration) pattern in hypoxic conditions. The computational model I used is a well-established model of the mammalian respiratory network, first proposed by [16]. I extended this model by adding a chemosensitive retrotrapezoidal nucleus/parafacial respiratory group (RTN/pFRG) that became increasingly active, at integer ratios relative to the respiratory rhythm, as carbon dioxide levels rose. I hypothesized that the RTN/pFRG entrains the respiratory CPG as carbon dioxide levels rise. Specific connections between the RTN-pFRG and BötC/pre-BötC were predicted based on the results of this modeling study.

D-3. Specific Aim 3 - Chapter IV

I developed a simplified model of the network proposed in Specific Aim 2, containing interacting pre-BotC and RTN/pFRG oscillators, that was used to understand, from a dynamical systems perspective, the mechanisms underlying the observed behaviors in the larger model and experimentally. I demonstrated that the dynamics governing the interactions of the core respiratory CPG and the RTN/pFRG may be explained in terms of release and escape mechanisms used in previous dynamical systems studies of the respiratory system [35]. Moreover, intrinsic rhythmicity of the RTN/pFRG was demonstrated to be essential to the observations made in Specific Aim 2, as well as experimentally.

D-4. Specific Aim 4 - Chapter V

I incorporated the network developed in Specific Aim 2 into a systems-level model of the respiratory network in the VRC with afferent feedback from the pons and lungs (via pulmonary stretch receptors). I focused on the respiratory phase switching, i.e. switching from expiration to inspiration and from inspiration to expiration. The VRC respiratory network receives many afferent connections from other brainstem areas such as the RTN/pFRG (Specific Aim 2), the pons, and the nucleus tractus solitarii (NTS). In this study I hypothesized that phasic populations in the pons and the pulmonary stretch receptors (acting through the NTS), control phase switching in the VRC by projecting to key inspiratory and expiratory neuron populations in specific ways. Furthermore, removal of both afferent feedback loops caused a transition to an apneustic pattern of breathing, characterized by a dramatically lengthened inspiration.

E. Significance

Uncovering the mechanisms governing the generation and control of respiration in mammals could lead to a better understanding of several pathologies (e.g. Congenital central hypoventilation syndrome, sudden infant death syndrome, Rett's syndrome, central sleep apnea, etc.) and provide key insights that would aid in clinical interventions. My long-term goal is to develop a complete connectome of the respiratory network and it's interaction with other physiological systems, as well as to cultivate a rich understanding of the sub-cellular, cellular, network, and system level dynamics that underlie respiratory motor outputs.

In addition to the direct impact this work may have within the field of neural control of respiration, the results may also add to our understanding of more general concepts in neuroscience as well as the field of computational biology. The first aim of this dissertation, for example, was designed to improve our understanding of the mechanisms that underlie rhythmic bursting. This bursting behavior is not limited to respiratory neurons, and our work may lend insight to neuroscientists that study bursting in other areas, e.g. the locomotor CPG. Moreover, we will develop several novel computational models that will be thoroughly described, and made available, for other researchers to use. These models could be modified to study a broad range of physiological systems.

Chapter II: Mixed-mode oscillations and population bursting in the pre-Bötzinger complex

The following section was adapted from the following submitted manuscript: B. J. Bacak, T. G. Kim, J. E. Rubin, J. C. Smith, I. A., Rybak, “Mixed-mode oscillations and population bursting in the pre-Bötzinger complex.,” *Submitted to eLife.* Dec. 2015.

A. Introduction

Mixed-mode oscillations (MMOs) represent rhythmic behaviors of dynamical systems characterized by an alternation between large amplitude (LA) and small amplitude (SA) oscillations [140] and have been observed in many physical, chemical, and biological systems, including a variety of neural structures. The latter include populations of neurons in the entorhinal cortex [141], [142], hippocampal neurons [143], dopaminergic neurons [144], neurons of the medullary pre-Bötzinger complex [145], [146] vibrissa motoneurons [147] and spinal motoneurons [148] in rats.

Theoretical investigations of MMOs typically focus on the mechanisms by which MMOs emerge from a complex interplay of multiple distinct time scales in the nonlinear processes governing a system’s activity. In this work, we introduce and explain a novel alternative paradigm for the generation of MMOs. The key element in the mechanism that we present is that a network of coupled oscillators can generative repetitive MMOs based on heterogeneity within the network. The importance of this paradigm for neural systems relates to central pattern generators (CPGs) that can intrinsically generate rhythmic activity controlling different motor behaviors such as breathing and locomotion. Heterogeneity in the quantitative features of the neurons involved is likely a ubiquitous property of such circuits [126], and thus our work predicts that MMO patterns should be attainable in a wide range of brain structures with rhythmic activity depending on mechanisms for neuronal synchronization. Furthermore, predictions that follow from the existence of this MMO-generation mechanism should be of similarly widespread relevance.

For concreteness, the present study focuses on computational models of a neuron population in a particular brain area, the pre-Bötzinger complex (pre-BötC), where MMOs have been previously observed [149]. The pre-BötC is a medullary region representing an excitatory kernel circuit of the respiratory CPG in mammals that is critically involved in generating the inspiratory phase of respiration [16], [23], [36], [150]. The pre-BötC can generate rhythmic bursting activity *in vitro*, in medullary slices containing this structure [25], [28], [30] and even in isolated "islands" extracted from these slices (Figure II-1A). This rhythmic activity is typically induced by elevating the extracellular concentration of potassium ($[K^+]_{out}$) up to 7-9 mM, which putatively increases neuronal excitability [25], [27], [28], [30], [151], [152]. Pre-BötC neurons project to the hypoglossal nuclei containing motor neurons, the activity of which can be recorded in rhythmically active slices from the hypoglossal (XII) nerve (see Figure II-1, panels A, B, and C1). Simultaneous optical recordings from individual neurons and XII output have shown that bursts in the XII root represent the synchronized activity of pre-BötC neurons ([25]; Figure II-1C1,C2) and the amplitude of XII bursts clearly depends on the number of pre-BötC neurons involved. Interestingly, a progressive increase in $[K^+]_{out}$ in slices containing the pre-BötC evokes complex population MMOs characterized by amplitude modulation, with large amplitude

(LA) bursts alternating with a series of small amplitude (SA) bursts [145], [146] (see Figure II-1A, bottom).

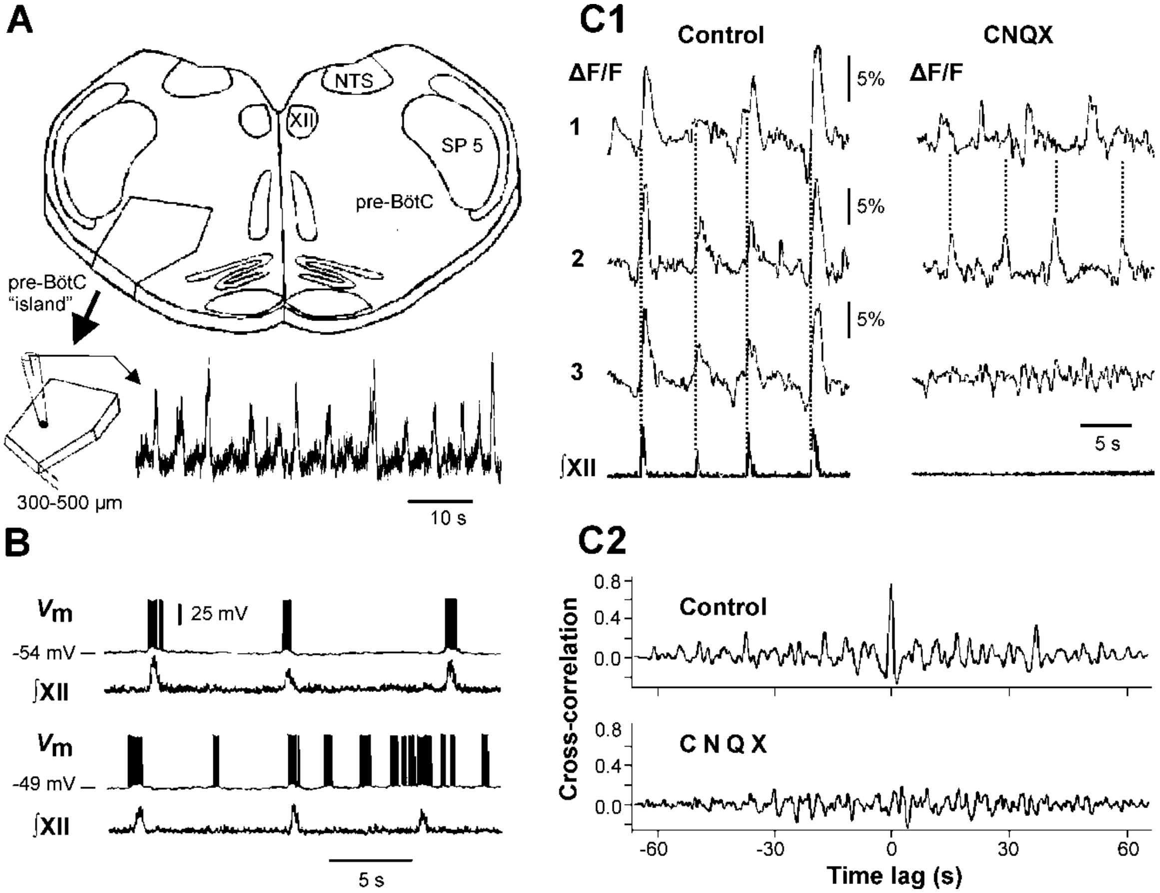

Figure II-1. Mixed mode and endogenous oscillations in the pre-Bötzinger complex *in vitro*. (A) Top: medullary slice showing "pre-BötC island" (shaded dark gray) and labeled structures: XII, hypoglossal motor nucleus; NTS, nucleus tractus solitarius; SP 5, spinal trigeminal tract. Bottom: Excised pre-BötC island with extracellular recording from the pre-BötC that demonstrates MMOs (i.e. interleaved large and small amplitude bursts). Modified from [26]. (B) Intracellular recording from pre-BötC neurons with resting membrane potential of -54 mV (top trace) and -49 mV (bottom trace). The corresponding integrated hypoglossal motor output (∫XII) is shown below each neuronal recording. In the top trace, each neuronal burst coincided with the activity in the hypoglossal motor output. At the more depolarized baseline potential, bursting occurred at higher frequency and several ectopic bursts did not correspond to ∫XII output. (C1) Optical recording from pre-BötC neuron activity (Ca^{2+} imaging). Left: three inspiratory neurons (1-3) show synchronized Ca^{2+} activities (ΔF/F) and corresponding ∫XII output (synchronization marked with dotted lines). Right: Application of CNQX (6-cyano-7-nitroquinoxaline-2,3-dione, blocking fast glutamatergic synaptic transmission, 50 μM) caused a loss of bursting in ∫XII and neurons 1 and 2 showed desynchronized bursting activity (see dotted lines). (C2) Cross-correlograms for neurons 1 and 2 in C1. The loss of a peak at 0 time lag after CNQX indicates loss of synchronization. B and C1-2 were adapted from [25].

To theoretically investigate the mechanisms underlying these MMOs, we developed and analyzed two models: (a) a computational model of a network of 100 neurons, described in the Hodgkin-Huxley style, with bursting properties defined by the persistent (slowly inactivating) sodium current (I_{NaP}) incorporated in each neuron, with sparse excitatory synaptic interconnections, and with randomly distributed neuronal parameters, and (b) a simplified model consisting of three mutually excitatory non-spiking neurons that allowed us to apply qualitative analytical methods for understanding key system behaviors. Our simulations and analysis suggest that neurons with low excitability, which generate low frequency bursting with high intra-burst spike frequency, recruit LA bursts by synchronizing the activity of many neurons in the network and therefore play a critical role in the generation of MMOs. Our simulations and analysis of these models provide important insights into how heterogeneity of neural excitability and other network features contribute to the generation of rhythmic activities in neuron populations that are key components of central pattern generators in vertebrates.

B. Methods

B-1. Description of single neuron in the large-scale population model

In the large-scale population model all neurons were modeled in the single-compartment Hodgkin-Huxley style, in accordance with our previous models [16], [18], [19], [136],

[153]. For each neuron, the membrane potential, *V*, was described by the following differential equation:

$$C\frac{dV}{dt} = -I_{Na} - I_{NaP} - I_K - I_L - I_{SynE}\,, \tag{\textit{II-1}}$$

where *C* is membrane capacitance. The following ionic currents were included in the model: fast sodium (I_{Na}); persistent, slowly inactivating sodium (I_{NaP}); delayed-rectifier potassium (I_K); leak (I_L); and excitatory synaptic (I_{SynE}). These currents were described as follows:

$$I_{Na} = \bar{g}_{Na} \cdot m_{Na}^3 \cdot h_{Na} \cdot (V - E_{Na}); \tag{\textit{II-2}}$$

$$I_{NaP} = \bar{g}_{NaP} \cdot m_{NaP} \cdot h_{NaP} \cdot (V - E_{Na})\;; \tag{\textit{II-3}}$$

$$I_K = \bar{g}_K \cdot m_K^4 \cdot (V - E_K)\;; \tag{\textit{II-4}}$$

$$I_L = \bar{g}_L \cdot (V - E_L); \tag{\textit{II-5}}$$

$$I_{SynE} = g_{SynE} \cdot (V - E_{SynE}), \tag{\textit{II-6}}$$

where $\bar{g}_x$ terms (with index *x* denoting the particular current) represent maximal conductances; g_{SynE} denotes the conductance of the excitatory synaptic current to the neuron (see below); E_x is the current's reversal potential; and m_x and h_x are dynamic variables describing current *x* activation and inactivation, respectively. Activation and inactivation kinetics obey the following equations:

$$\tau_{mx}(V)\,\frac{dm_x}{dt} = m_{x\infty}(V) - m_x\,, \tag{\textit{II-7}}$$

$$\tau_{hx}(V)\,\frac{dh_x}{dt} = h_{x\infty}(V) - h_x, \tag{\textit{II-8}}$$

where $m_{x\infty}(V)$ and $h_{x\infty}(V)$ define steady-state voltage-dependent activation and inactivation, respectively, and $\tau_{mx}(V)$ and $\tau_{hx}(V)$ are the corresponding voltage-dependent time constants (see Table II-1). Equations (*II-1*)-(*II-8*) were used for each neuron in the population, with all variables indexed by a numerical subscript specifying the identity of each neuron.

B-2. Interaction between neurons

We considered only excitatory synaptic connections between neurons. The excitatory synaptic conductance was zero at rest and was increased when each excitatory input occurred, such that

$$g_{SynEi} = \bar{g}_{SynE} \cdot \sum_{j} w_{ji} \cdot \sum_{t_{kj}<t} \exp[-(t - t_{kj}) / \tau_{SynE}], \qquad (II\text{-}9)$$

where w_{ji} is the synaptic weight from neuron j to neuron i, $\bar{g}_{SynE}$ is the maximal synaptic conductance, τ_{SynE} is the synaptic time constant, t_{kj} is the time of the k-th spike from neuron j, and each term in the sum is evaluated for $t > t_{kj}$.. That is, each new spike from neuron j increases the excitatory synaptic conductance of neuron i by $\bar{g}_{SynE} \cdot w_{ji}$. The probability of each connection (p) was set *a priori*, where in a network of N neurons, pN represents the mean number of neurons with which an individual neuron would form synapses. To form a network, a random number generator was used to determine whether or not each possible synaptic connection among neurons was actually present.

B-3. Simulations

Neuronal heterogeneity within the population was generated with Gaussian distributions for the leak reversal potential (E_L) (defining neuronal excitability) and the maximal conductance of the persistent sodium current ($\bar{g}_{NaP}$). The means and variances of these parameter distributions, as well as all other parameters used in the large-scale model, are provided in Table II-1.

Initial conditions for neuronal membrane potentials and variables defining currents' activation and inactivation were randomly distributed within physiologically realistic ranges for each variable. To rule out chaotic behaviors, simulations were repeated with redistributed initial conditions for each parameter set. Finally, results were only considered following an initial simulation period of 20 seconds to minimize the likelihood of transient dynamics.

All simulations were performed using the simulation package NSM 3.0, developed at Drexel University by S. N. Markin, I. A. Rybak, and N. A. Shevtsova. Differential equations were solved using the exponential Euler integration method with a step size of 0.1 ms.

Table II-1. Steady-state functions for voltage-dependent activation and inactivation of ionic channels and other parameter values of the large-scale model.

Ionic channels	
Fast sodium (*Na*)	$m_{Na\infty}(V) = 1/(1+\exp(-(V+43.8)/6))$; $\tau_{mNa}(V) = 0.25/\cosh(-(V+43.8)/14.0)$ ms; $h_{Na\infty}(V) = 1/(1+\exp((V+67.5)/10.8))$; $\tau_{hNa}(V) = 8.46/\cosh((V+67.5)/12.8)$ ms; $\bar{g}_{Na}$ = 170 nS.

Persistent sodium (*NaP*)	$m_{NaP\infty}(V) = 1/(1+\exp(-(V+47.1)/3.1))$; $\tau_{mNaP}\left(V\right) = 1/\cosh\left(-(V+47.1)/6.2\right)$ ms; $h_{NaP\infty}(V) = 1/(1+\exp((V+60)/9))$; $\tau_{hNaP}\left(V\right) = 6000/\cosh\left((V+60)/9\right)$ ms; $\bar{g}_{NaP}$ = 5.0 ± 0.5 nS.
Delayed-rectifier potassium (*K*)	$m_{K\infty}(V) = \alpha_{K\infty}/(\alpha_{K\infty}+\beta_{K\infty})$; $\tau_{mK}(V) = 1/(\alpha_{K\infty}+\beta_{K\infty})$ ms, where $\alpha_{K\infty} = 0.01\cdot(V+45)/(1-\exp(-(V+45)/5))$; $\beta_{K\infty} = 0.17\cdot\exp(-(V+49)/40)$; $\bar{g}_{K}$ = 180 nS.
Leak (*L*)	$\bar{g}_{L}$ = 2.5 nS.
Neuron parameters	
Reversal potentials	E_{Na} = 60.0 mV, E_{K} = -94.0 mV, E_{SynE} = -10.0 mV, E_{L}= -62.0 ± 0.93 mV.
Membrane capacitance	*C*= 36.2 pF.
Synaptic/network parameters	
Synaptic connections	$\bar{g}_{SynE}$ = 0.05 nS, τ_{SynE} = 5 mS, *wij* = *w*, varied [1, 5], *p* = varied [0.09, 0.4]; Spike threshold = -35.0 mV.

B-4. Reduced model formalization

Mathematical analysis of the large-scale model was prevented by its high dimensionality (100 neurons, each with several differential equations per neuron). However, a preliminary analysis of the simulation results suggested that a minimal neural network could be used to reproduce the development of MMOs caused by the clustering of neurons with similar excitabilities. We therefore developed a reduced network consisting of three neurons simulated by an "activity-based,” non-spiking, model with different excitability defined by the E_L value for each neuron. In this reduced formalization, a neuron's activity represents the aggregate activity of a distinct cluster in the large-scale model. Such reductive neuron models were previously used to simulate and analyze the behavior of larger models of respiratory networks, including the pre-BötC [35], [88].

Each neuron is described by one "fast" dynamic variable, V, that governs changes in a neuron's membrane potential and obeys the following differential equation:

$$C \cdot \frac{dV_i}{dt} = -I_{NaPi} - I_{Li} - I_{SynEi}, \tag{II-10}$$

where $i = \{1,2,3\}$ is the index corresponding to the neuron's number shown in Figure II-5A1 and C is membrane capacitance. This reduced model excluded the fast sodium (I_{Na}) and potassium (I_K) currents included in the large-scale model. However, similar formalizations of the persistent (slowly inactivating) sodium (I_{NaP}), leak (I_L), and excitatory synaptic (I_{SynE}) currents were used:

$$I_{NaPi} = \bar{g}_{NaP} \cdot m_{NaP\infty i}(V_i) \cdot h_{NaPi} \cdot (V_i - E_{Na}); \tag{II-11}$$

$$I_{Li} = \bar{g}_L \cdot (V_i - E_{Li}); \tag{II-12}$$

$$I_{SynEi} = \sum_{\substack{j=1 \\ j \neq i}}^{3} (w_{ji} \cdot f(V_j)) \cdot \bar{g}_{SynE} \cdot (V_i - E_{SynE}), \tag{II-13}$$

where for $x \in \{NaP, L, SynE\}$, $\bar{g}_x$ is the maximal conductance and E_x is the channel's reversal potential, respectively. E_L was uniformly distributed in the range [-54.5, -63.5] mV to produce the specific behaviors observed in the uncoupled case (Figure II-5B1). The excitatory synaptic current in equation (*II-13*) includes inputs to neuron i from neurons j, each of which is the product of a fixed connection weight, $w_{ji} = w$ and a piecewise linear function, $f(V)$:

$$f(V) = \begin{cases} 0, \text{ if } V < V_{\min} \\ (\mathrm{V} - \mathrm{V}_{\min}) / (V_{\max} - V_{\min}), \text{ if } V_{\min} \le V < V_{\max} \\ 1, \text{ if } V \ge V_{\max} \end{cases}, \qquad (II\text{-}14)$$

where V_{min} and V_{max} define the voltages at which threshold and saturation occur, respectively.

An activity level (or normalized firing rate) for each neuron is implicitly associated with the value of its voltage, and the function $f(V)$ represents an output signal corresponding to that activity level.

The activation of the persistent sodium current, I_{NaP}, is described by the voltage-dependent steady state gating variable, $m_{NaP\infty}$:

$$m_{NaP\infty}(V) = \left(1 + \exp\left\{(V - V_{mNaP}) / k_{mNaP}\right\}\right)^{-1}. \qquad (II\text{-}15)$$

I_{NaP} activation is considered instantaneous. The “slow” dynamical variable in the reduced model, h_{NaP}, represents inactivation of the persistent sodium current and is governed by the following equation:

$$\tau_{hNaP}(V) \cdot \frac{dh_{NaP}}{dt} = h_{NaP\infty}(V) - h_{NaP}, \qquad (II\text{-}16)$$

where $h_{NaP\infty}$ and $\tau_{NaP\infty}$ describe the voltage-dependent steady-state and time constant for inactivation, respectively:

$$h_{NaP\infty}(V) = \left(1 + \exp\left\{(V - V_{hNaP}) / k_{hNaP}\right\}\right)^{-1}; \qquad (II\text{-}17)$$

$$\tau_{hNaP\infty}(V) = \tau_{hNaP\max} / \cosh\left\{(V - V_{\tau hNaP}) / k_{\tau hNaP}\right\}. \qquad (II\text{-}18)$$

The variables V_{xNaP} and k_{xNaP} for $x \in \{m,h,\tau h\}$ in equations *(II-15), (II-17),* and *(II-18)* represent the gating variable’s half-activation voltage and slope, respectively.

All parameters of the reduced model are specified in Table II-2. The distribution of E_L was first set manually to match the large-scale model and then optimized by calculating a series of iterative one-dimensional bifurcation diagrams. The robustness of a given regime (for example, the ***LE*** period branches marked “1:X” in Figure II-6A) was determined by the range of connection weights across which the ***LE*** period maintained an integer ratio to the ***HE*** period. Simulations were performed and visualized using custom C^{++} scripts and gnuplot, respectively.

Table II-2. Parameter values for the reduced model

Ionic channels	
Persistent sodium (*NaP*)	V_{mNaP}=-40.0 mV, k_{mNaP}=-6 mV; V_{hNaP}=-59.0 mV, k_{hNaP}=10.0 mV; $V_{\tau hNaP}$=-59.0 mV, $k_{\tau hNaP}$=20.0 mV, $\tau_{hNaPmax}$=5000 ms; $\bar{g}_{NaP}$ =5.0 nS.
Leak (*L*)	$\bar{g}_L$ =2.8 nS.
Synaptic Current (*SynE*)	$\bar{g}_{SynE}$ =0.1 nS.
Neuron parameters	
Potentials	E_{Na}=50.0 mV; E_{L1}=-54.5 mV, E_{L2}=-59.0 mV, E_{L3}=-63.5 mV; E_{SynE}=-10.0 mV.
Membrane capacitance	*C*=20 pF.
Synaptic/network parameters	
Synaptic connections	w_{ij}= *w*, varied [0, 5]
Parameters of output function, *f(V)*	V_{min}=-50 mV, V_{max}=0.0 mV.

B-5. Time-scale decomposition in the reduced model

The complete range of a neuron's dynamics, as a function of E_L, was investigated with time-scale decomposition in the (V,h_{NaP})-plane (Figure II-5B3). When projected into the (V,h_{NaP})-plane, the dynamical variables, V and h_{NaP}, had steady states or "nullclines" (sets of points for which the right-hand sides of equations (*II-10*) and (*II-16*), respectively, were set to zero). Some possible positions of the cubic V-nullclines are depicted by a gray band in Figure II-5B3. The upper and lower boundaries of the band correspond to the lowest and highest values of E_L that produced bursting, respectively. That is, the intersection of the V- and h_{NaP}-nullclines created a fixed point for the system that, when stable, denotes the point where solutions converge. There were two possible stable fixed points in our model for each neuron: (i) along the left branch of the V-nullcline (silence), and (ii) on the right branch of the V-nullcline, creating a state of constant depolarization (the activity-based analog to tonic spiking). When E_L was intermediate to values that produced silence and tonic behavior, the h_{NaP}-nullcline intersected the V-nullcline's middle branch, creating an unstable fixed point with a stable periodic orbit, or oscillation (Figure II-5B3, red trace), that encompassed the local maximum and minimum of the V-nullcline (Figure II-5B3, blue curve). The presence of a stable periodic orbit corresponded to endogenous bursting in these neurons.

Each periodic orbit has two "slow" components located close to the neuron's V-nullcline and governed by the neuron's h_{NaP} (slow) dynamics, and two "fast components" connecting between V-nullcline branches and governed by the neuron's V (fast) dynamics. During the slow components, the neuron could be silent or at rest when its trajectory was traveling up the left branch of its V-nullcline corresponding to an absence of spike generation, and it could be active or depolarized when its trajectory was traveling down the right branch of its V-nullcline, corresponding to spike generation. While at rest, a neuron in the bursting regime slowly "recovered," with its trajectory rising to higher h_{NaP}-coordinates until it reached the left knee (or fold) of the V-nullcline (a bursting neuron, shown in Figure II-5B3, red trace). At the left knee, a neuron's trajectory moved rightward in the (V,h_{NaP})-plane under the fast dynamics to approach the right branch of the V-nullcline, corresponding to activation of the neuron. Once active, the neuron's trajectory traveled downward, to lower h_{NaP}–coordinates, along the right branch of the V-nullcline until it reached the right knee (fold) of the V-nullcline, which caused a leftward jump in the (V,h_{NaP})-plane corresponding to burst termination (Figure II-5B3, red trace). Similarly, a neuron with a stable fixed point could have slow transient dynamics and be in a rest (active) state as its trajectory traveled along the left (right) branch of its V-nullcline.

When a neuron became more excitable, either by an increase in E_L or in its excitatory inputs, the right-hand side of its voltage equation was altered, causing a change in the position of its V-nullcline, to a location downward and to the right of the original in the (V,h_{NaP})-plane. Such a change could cause the neuron's fixed point to switch from one branch of its V-nullcline to another, yielding a transition from silence to bursting to tonic spiking, depending on fixed point location.

C. Results

C-1. Computational modeling of a network of pre-BötC neurons with sparse excitatory synaptic interconnections

Intracellular recordings from individual pre-BötC neurons in rhythmically active slices show a range of resting membrane potentials and other quantitative properties among individual neurons [30], [145], [154], [155]. Neurons with more negative resting membrane potentials usually generate bursting activity that is fully consistent with, and reflected in, XII output activity, whereas neurons with less negative resting membrane potentials demonstrate higher burst frequencies and often generate "ectopic" busts not reflected in the XII output (see example in Figure II-1B). Pharmacological blockade of synaptic transmission within the pre-BötC by 6-cyano-7-nitroquinoxaline-2,3-dione (CNQX) results in a reduction and desynchronization of neuronal activity within the pre-BötC, with no activity in the hypoglossal output (see example in Figure II-1C1,C2).

In light of these experimental findings, we modeled the pre-BötC as an excitatory network consisting of 100 neurons described in the Hodgkin-Huxley style, with sparse excitatory synaptic interconnection between neurons. The intrinsic bursting prosperities of these neurons were based on the persistent (slowly inactivating) sodium current I_{NaP} [30], [125]–[127], [136], [153], [156]–[158] see Chapter II: B**)**. To account for neuronal heterogeneity, we distributed the reversal potential of the leak current, E_L, across the population (see Chapter II: B). In the absence of coupling (when all weights of connections were set to zero), the population contained silent neurons, as well as neurons with bursting and tonic activities (Figure II-2A1). Figure II-2A2 presents the raster plot of neuronal activity in the same population, in which neurons were sorted in order of increasing (from bottom to top) excitability (defined by the assigned E_L). This figure shows that neurons with the most negative E_L values were silent (neurons with ID numbers from 1 to 49), neurons with intermediate E_L exhibited bursting activity with burst frequency increasing with E_L (neurons 50-94), and neurons with greatest E_L displayed tonic spiking (neurons 95-100). The lack of network interactions resulted in asynchronous neuronal activity and the corresponding integrated population histogram lacked phasic modulation (Figure II-2A3).

The patterns of population activity and integrated output dramatically changed when relatively weak and sparse excitatory synaptic connections among neurons were incorporated in the model (Figure II-2B1-B3). The raster plot of the same sorted neurons in this coupled case (Figure II-2B2) shows the presence of overlapping clusters (sub-populations) of neurons with synchronized bursting, which generate MMOs characterized by alternating LA and SA population bursts (Figure II-2B3).

Figure II-3 shows another example of our simulations, including "uncoupled" (panel A1) and coupled (panel B1) cases for sorted neurons of the same populations and the integrated population activity for the coupled case (panel C1). In both A2 and B2 panels we plotted the membrane potentials (V) of four selected representative neurons that in the uncoupled case exhibited (bottom-up): silence (trace 1), bursting with low burst frequency (trace 2), bursting with higher burst frequency (trace 3), and tonic spiking (trace 4). Also in these figures, the time course of the I_{NaP} inactivation variable (h_{NaP}) of each neuron, which defined the burst recovery period, was superimposed onto its V time course (red trace). An important feature of all neurons operating in bursting mode is illustrated in Figure II-3A3 (uncoupled case): while the burst frequency (blue curve) increased with the neuronal excitability (bottom-up), the spike frequency within the burst (red curve) changed in an inverse manner, i.e., decreased with increasing neuronal excitability. This reduction of spike frequency within the bursts in more excited neurons limited their ability to synchronize and recruit other neurons activity in the coupled case (see below).

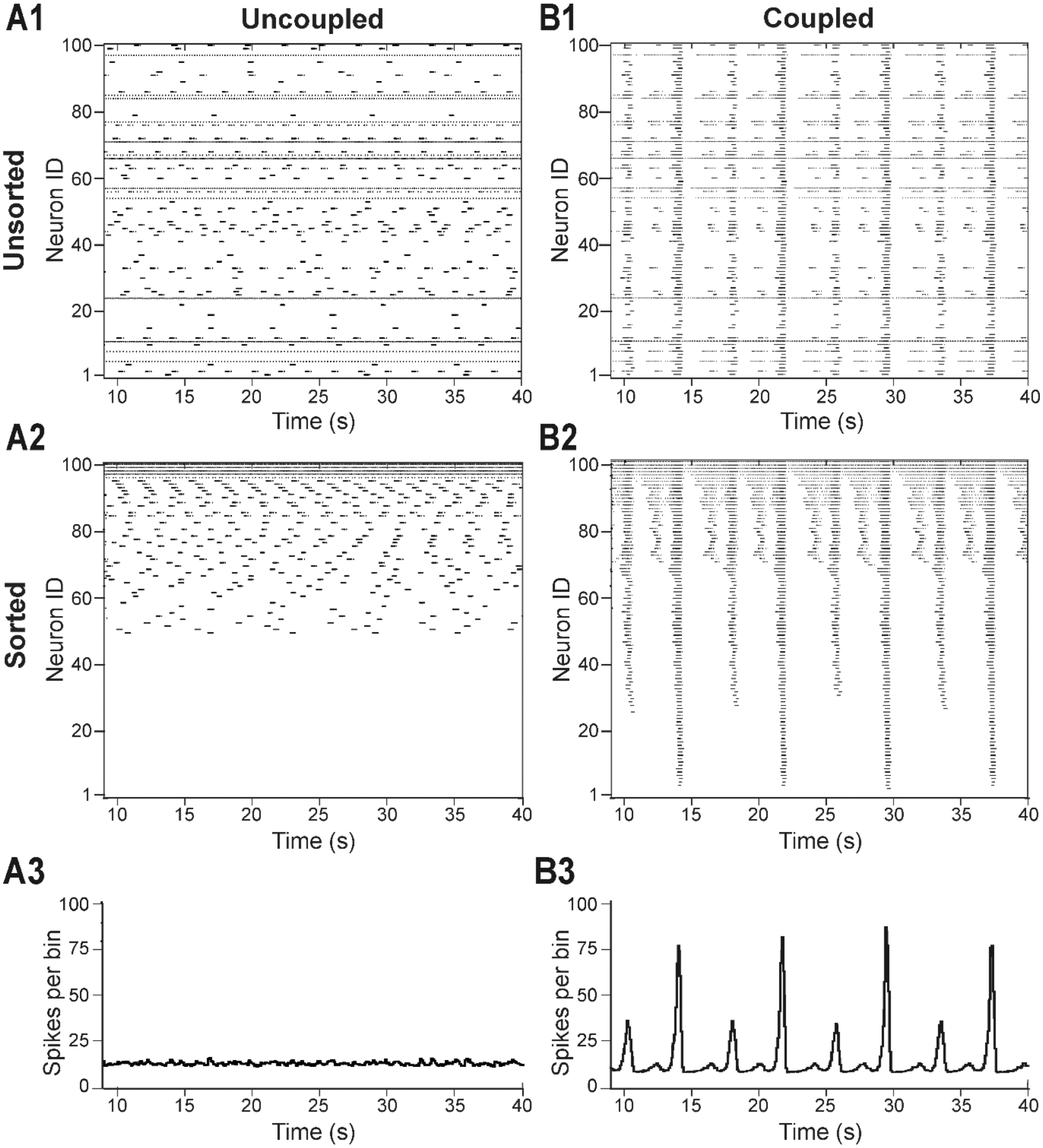

Figure II-2. Distribution of neural excitability in a sparsely connected network causes mixed mode oscillations. (A) Network simulation when excitatory interactions between neurons were removed (*w*=0, “uncoupled” network). (B) Simulation of network activity when *w*=2.5 and *p*=0.15. (A1), (B1) Unsorted raster plots depicting the timing of action potentials in neurons with randomly distributed E_L values. (A2), (B2) Raster plots were sorted by E_L values such that the lowest Neuron ID was assigned to the neuron with the most negative E_L. (A3), (B3) Histogram of population activity with 10ms bin size. No phasic component is observed in A3 due to the desynchronized bursting in the uncoupled population. B3 shows a typical MMO pattern including LA bursts alternating with SA bursts of varying amplitudes.

The pattern of population activity in a coupled network is shown in Figure II-3B1-B3,C1. Several clusters of neurons with synchronous bursting activity emerged dynamically in the population. Clusters differed by the number of the population bursts in which they participated (panel B1), which in turn defined the amplitude of integrated population bursts (panel C1). The same panels also show that several relatively small, distinct or partly overlapping clusters with synchronous bursts were formed by neurons with relatively high (less negative) E_L. These clusters generated a series of high-frequency SA bursts. Generation of low-frequency LA bursts involved synchronization of many neurons and included those with low excitability (most negative E_L) (Figure II-3B1,B2,C1).

Figure II-3C2 shows two insets from the raster plot in Figure II-3B1 that correspond to two SA bursts (left) and one LA burst (right). The neuronal clusters in these insets are colored as follows: spikes of neurons with default tonic spiking - yellow; spikes of neurons involved in SA bursts - light and dark green, light and dark blue, and purple, arranged in order of increasing excitability; spikes of neurons involved only in LA bursts - red.

The left inset (within the blue rectangle) in Figure II-3C2 and 3D1 depicts spikes in the raster plot corresponding to two SA bursts. Two clusters of high excitability neurons, colored by yellow and green, participated in both of these bursts. In addition, the blue cluster participated in the first, but not the second, SA burst, and a purple cluster participated in the second, but not the first, SA burst. The neurons belonging to the red cluster were only active during LA bursts (see right inset within the red rectangle).

To evaluate the role of different clusters in SA and LA bursts in both insets, we built integrated histograms showing the number of neurons, from each colored cluster, that were active within a 100 ms bin (Figure II-3D1). Note that the sub-population of low excitability neurons, colored red, do not contribute to SA bursts. Activation of this sub-population during the LA burst is marked by a black, dot-dashed, vertical line at about 32.7 seconds. This vertical line intersects with a black, dashed, horizontal line indicating a threshold for the activation of red neurons. This line intersects the two SA bursts demonstrating that, although the amplitudes of both SA bursts rose above the marked threshold for activation of the red sub-population in the LA burst, the latter neurons were not recruited in SA bursts (note the absence of the red neuron cluster in SA bursts) and hence the full LA burst did not develop. We further find that the sub-population of neurons with low excitability (colored red) cannot be recruited by other sub-populations (participating in SA bursts), and hence cannot generate LA bursts, until sufficient recovery of bursting capability in the low excitability neurons (defined by the I_{NaP} inactivation variable h_{NaP}) has occurred. This observation suggests that with fixed parameter values, even though the low excitability neurons do not burst when uncoupled, the generation of LA bursts and the durations of their interburst intervals (IBIs) are mostly defined by the operation of an intrinsic burst-supporting mechanism in the less excitable neurons, rather than by variations in the intensity of their recruitment by the activity of highly excitable neurons involved in SA bursts.

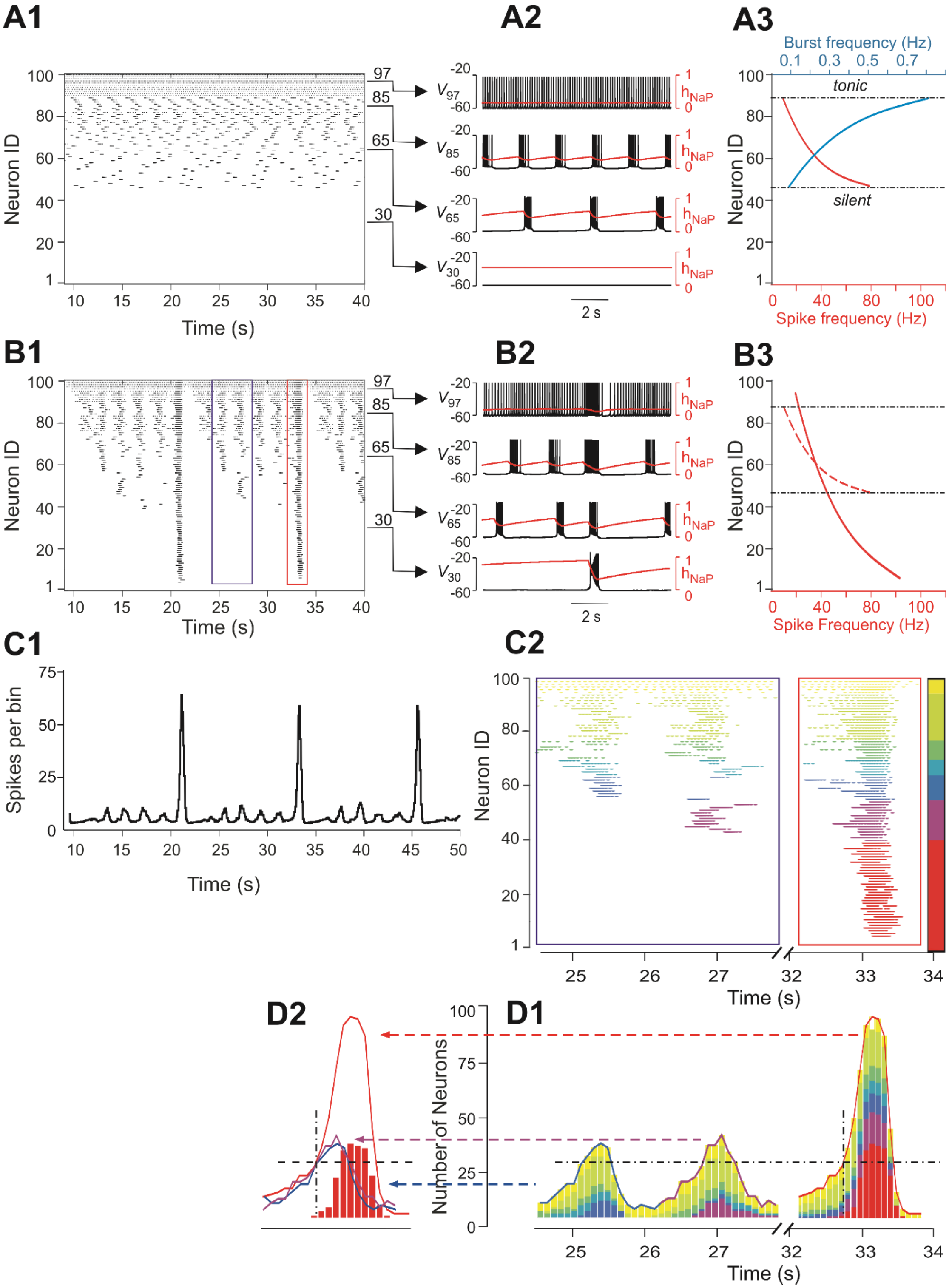

Figure II-3. Neurons with similar excitabilities activate in clusters within a heterogeneous network with sparse connectivity. (A) Simulation results for uncoupled network, w=0. (A1) Sorted raster plot showing silent (most negative E_L, lowest Neuron IDs), bursting, and tonic (least negative E_L, highest Neuron IDs) neurons. (A2) Endogenous activity of four individual neurons (Neuron IDs: 30, 65, 85 and 97) showing membrane potential (black) and inactivation, h_{NaP}, of the persistent sodium current (red). (A3) Burst frequencies (blue) and intra-burst spike frequencies (red) were calculated for each neuron in the uncoupled case. Boundaries separating bursting from silent and tonic neurons are marked (black, dot-dashed lines). (B) Simulation results for w=1.8 and p=0.15. (B1) Raster plot sorted by E_L (Neuron ID). Two SA bursts (blue rectangle) and one LA burst (red rectangle) were selected for the inset in C2. (B2) Membrane potential (black) and h_{NaP} are shown for the four neurons originally selected in A2. (B3) Spike frequency of neurons sorted by excitability in the coupled (w=1.8) case (the dashed red curve shows spike frequencies for the uncoupled (w=0) case in A3, for comparison). (C1) Histogram of population activity corresponding to B1. (C2) Insets depicting magnified raster plots from the selected bursts in B1. Colors were assigned to clusters from lowest excitability (***LE*** - red) to highest (yellow, tonic neurons). A cluster was defined as a group of neurons that participated in a unique set of bursts. (D1) The color-coding scheme from C2 was used in conjunction with a histogram depicting the number of active neurons within a 100 ms window. The vertical dot-dashed black line marks the time of onset of ***LE*** neuron activation in an LA burst and the horizontal dot-dashed line intersects this onset time to show the total number of neurons already active at the time of ***LE*** activation. The horizontal dot-dashed line is extended to the two SA bursts and demonstrates that ***LE*** activation failed despite the presence of a sufficient number of active neurons in the network. (D2) Comparison of number of neurons active over time from two SA bursts (purple and blue curves) and one LA burst (red curve). The intersection of the two dashed, black lines compares the SA and LA burst amplitudes when the ***LE*** neurons (red bars) first start to activate in an LA burst.

C-2. Parameter dependence of mixed mode oscillations (MMOs)

To study the dependence of MMOs on neuronal interactions within the network, we observed changes in the network activity when the weights and/or probability of synaptic connections were varied across simulations. Figure II-4A1,A2,A3 shows three heat maps that demonstrate quantal changes in MMO regimes defined by ratios of LA to SA bursts (e.g. 1:5, 1:4, etc.) as several key parameters were varied (Figure II-4A1,A2,A3). When either weights (Figure II-4A1,A2,B1) or probability of connections (Figure 4A1,A3,B2) were increased, the frequency of LA bursts increased and the number of SA bursts between successive LA bursts decreased. This corresponded to a progressive change in the quantal state of the network toward regimes with high LA to SA burst ratios.

Figure II-4B1 shows regimes observed when the probability of connections was fixed (p = 0.15) and only the weights of connections were varied. At the lowest weights (w = 1.0), only irregular SA bursts were observed because of insufficient neuronal synchronization (top trace, Figure II-4B1). Weights between 1.0 and 1.8 caused regimes characterized by low-frequency irregular LA bursts with irregular patterns of SA bursts (not shown). At a weight of 1.8, each LA burst emerged regularly following five SA bursts (second trace); no parameter sets produced stable regimes with more than five SA bursts per one LA burst. Further increases in weights caused a quantal increase of LA frequency and the corresponding reduction in the number SA bursts between LA bursts (traces 2-4), until strong enough weights yielded LA bursts only (trace 5). A similar trend is seen in Figure II-4B2 with increases in the probability of connections at a fixed value of synaptic weights (w = 1.8). Overall, for fixed connection weights, the availability of INaP in low excitability neurons still selects the cycles on which LA bursts occur during MMOs. Furthermore, our simulations showed increased IBIs following the LA bursts, relative to IBIs observed after SA bursts, in all instances of MMOs (Figure II-4B3,3C1, and 4B1,B2). In the next section, "Reduced model analysis of interburst intervals (IBIs)", we use a reduced model to explain these effects.

Finally, to study the dependence of MMOs on INaP, we varied the average maximal conductance for I_{NaP} ($\overline{g}_{NaP}$) and either weights (Figure II-4A2) or probability of connections (Figure II-4A3). The resulting heat maps show a qualitatively similar pattern where the ratio of LA to SA bursts decreases as $\overline{g}_{NaP}$ is reduced. Activity traces corresponding to $\overline{g}_{NaP}$ changes at fixed weights and probability of connections are shown in Figure II-4B3 (w = 3.0, p = 0.24,). At the typical value of $\overline{g}_{NaP}$ (5.0 nS), network activity consisted entirely of LA bursts (Figure II-4B3, top trace). When $\bar{g}_{NaP}$ was reduced, a decrease in LA burst frequency and an increase in SA burst count between LA bursts were observed (traces 2-4) until busting fully stopped at $\bar{g}_{NaP}$ = 3.2 nS (trace 5). Thus, while raising the weights or probability of synaptic connections can enhance the rate of LA burst generation in some parameter regimes, if there is insufficient availability of burst-supporting current, then the recruitment of low excitability neurons is precluded.

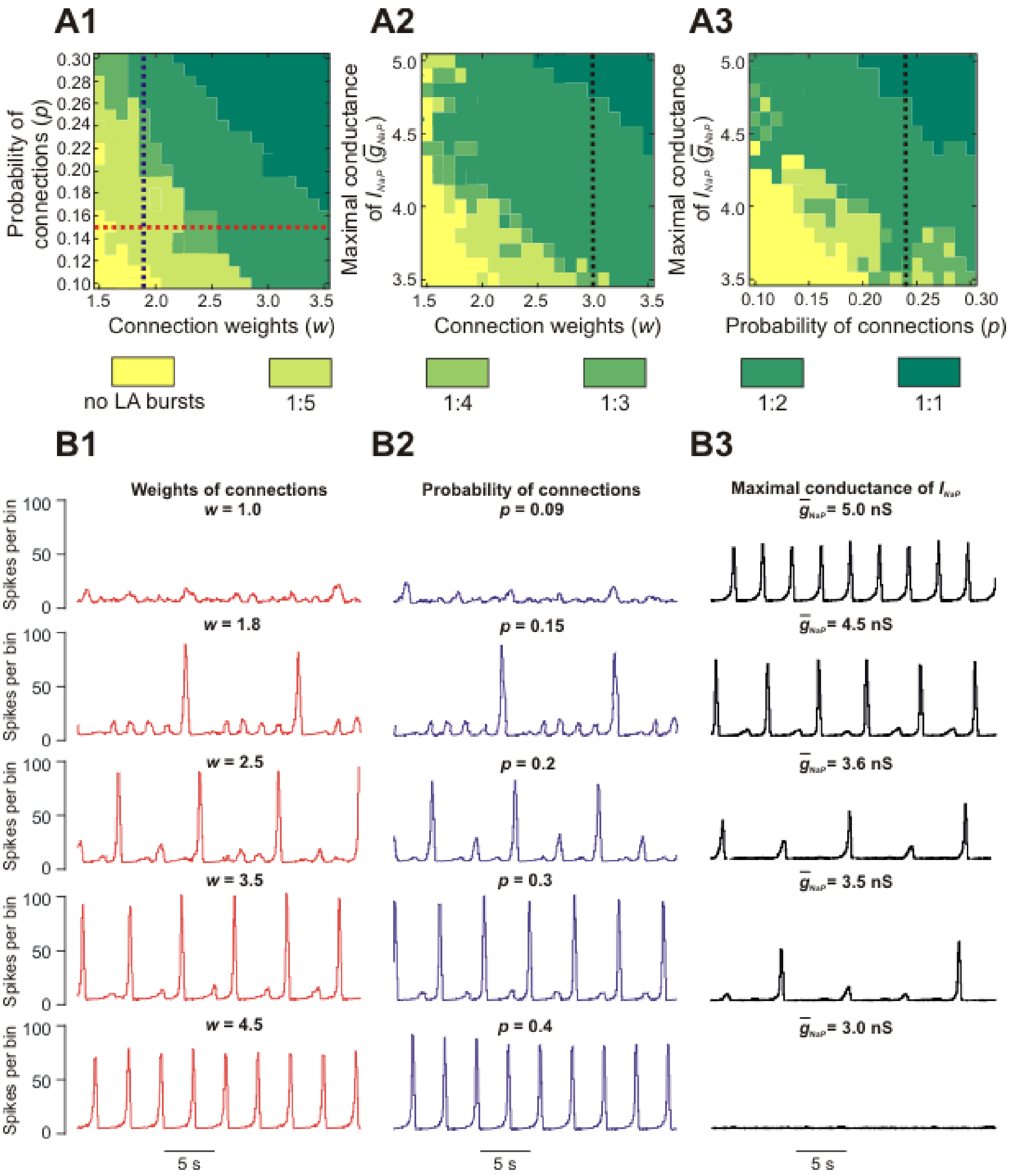

Figure II-4. Parameter dependence of mixed mode oscillations. (A1-A3) Heat maps depicting guantal changes in the ratio of LA to SA bursts, representing quantal MMO regimes calculated with variation of the connection weights (w), probability of connections (p), and maximal conductance of the persistent sodium channel ($\bar{g}_{NaP}$). In A1, w and p were iteratively varied at $\bar{g}_{NaP}$ = 5 nS. In A2, w and $\bar{g}_{NaP}$ were varied at p=0.24, and in A3, p and $\bar{g}_{NaP}$ were varied at w=3. (B1-B3) Histograms of population activity (spikes/10ms) were calculated as a parameter of interest was varied. In B1, w was varied between 1.0 and 4.5 at p=0.15 and $\bar{g}_{NaP}$ = 5 nS; these changes correspond to the horizontal red, dashed line in A1. Progressive increase of w caused the frequency of LA bursts to increase and the number of SA bursts between LA bursts to decrease. In B2, p was varied from 0.09 to 0.4 at w=1.8 and $\bar{g}_{NaP}$ = 5 nS; these changes correspond to the vertical blue, dashed line in A1. Similarly to changes of w, increasing p caused an increase in frequency of LA bursts and decrease in the number of SA bursts between LA bursts. In B3, $\bar{g}_{NaP}$ was decreased from 5.0 to 3.0 nS, with fixed values w=3.0 and p=0.24, corresponding to the black, dashed lines in A2 and A3, respectively. This progressive decrease caused a decline in LA burst frequency, and an emergence of SA bursts, until all network activity stopped at $\bar{g}_{NaP}$=3.0 nS.

C-3. MMOs in a reduced model

A reduced model was developed to allow qualitative mathematical analysis of the MMOs that we observed. The model consisted of three neurons with mutual excitatory synaptic interactions (see Figure II-5A1). It was considered that each model neuron represented a sub-population of spiking neurons with a particular level of excitability. Each neuron was described using a non-spiking, activity-based model [35], [88], [129]; see Chapter II: B). The behavior of each neuron was defined by two dynamical variables, the membrane voltage, V, and I_{NaP} inactivation, h_{NaP}. For each neuron we calculated a nonlinear output function, $f(V)$, which approximated the aggregate activity of a cluster of neurons in the original 100-neuron model. E_L values were distributed such that in the absence of coupling, neuron 1 (high excitability, ***HE***) engaged in high frequency bursting, neuron 2 (moderate excitability, ***ME***) engaged in low frequency bursting with no special frequency relation to the bursting of the ***HE*** neuron, and neuron 3 (low excitability, ***LE***) was silent; the three neurons' summed activity provided a representation of network output (Figure II-5B1,C1,D1,E1). For each simulation, in addition to voltage and summed activity time courses, we visualized the network trajectory as it evolved in ($h_{NaP,1}$, V_1, V_3)-space. Without coupling, this trajectory was cyclic, corresponding to the oscillations of the ***HE*** neuron 1 (i.e., of $h_{NaP,1}$, V_1) without changes in V_3 (Figure II-5B2).

In subsequent simulations, neurons in this model interacted through excitatory synaptic interconnections with the weights of connections increasing top-down in Figure II-5 from panels B1-B3 to panels E1-E3. Similarly to the previous model, when connection weights were progressively increased, the network underwent a series of regime transitions progressing from only SA bursts (Figure II-5B1,B2) to only LA bursts (Figure II-5E1,E2). The intermediate regimes (Figure II-5C1,C2 and 5D1,D2) are referred to as "quantal" and labeled as *1:N* if there were N-1 SA bursts between each pair of LA bursts; these correspond to the MMOs in the 100-neuron model described above. The periods of oscillations were calculated for all neurons as weights of connections were gradually increased (Figure II-5A), and these clearly distinguished the different quantal states observed. As in the previous model, LA bursts involved activation of all neurons and occurred exactly on the cycles when the ***LE*** neuron activated (Figure II-5C1,C2,D1,D2,E1,E2).

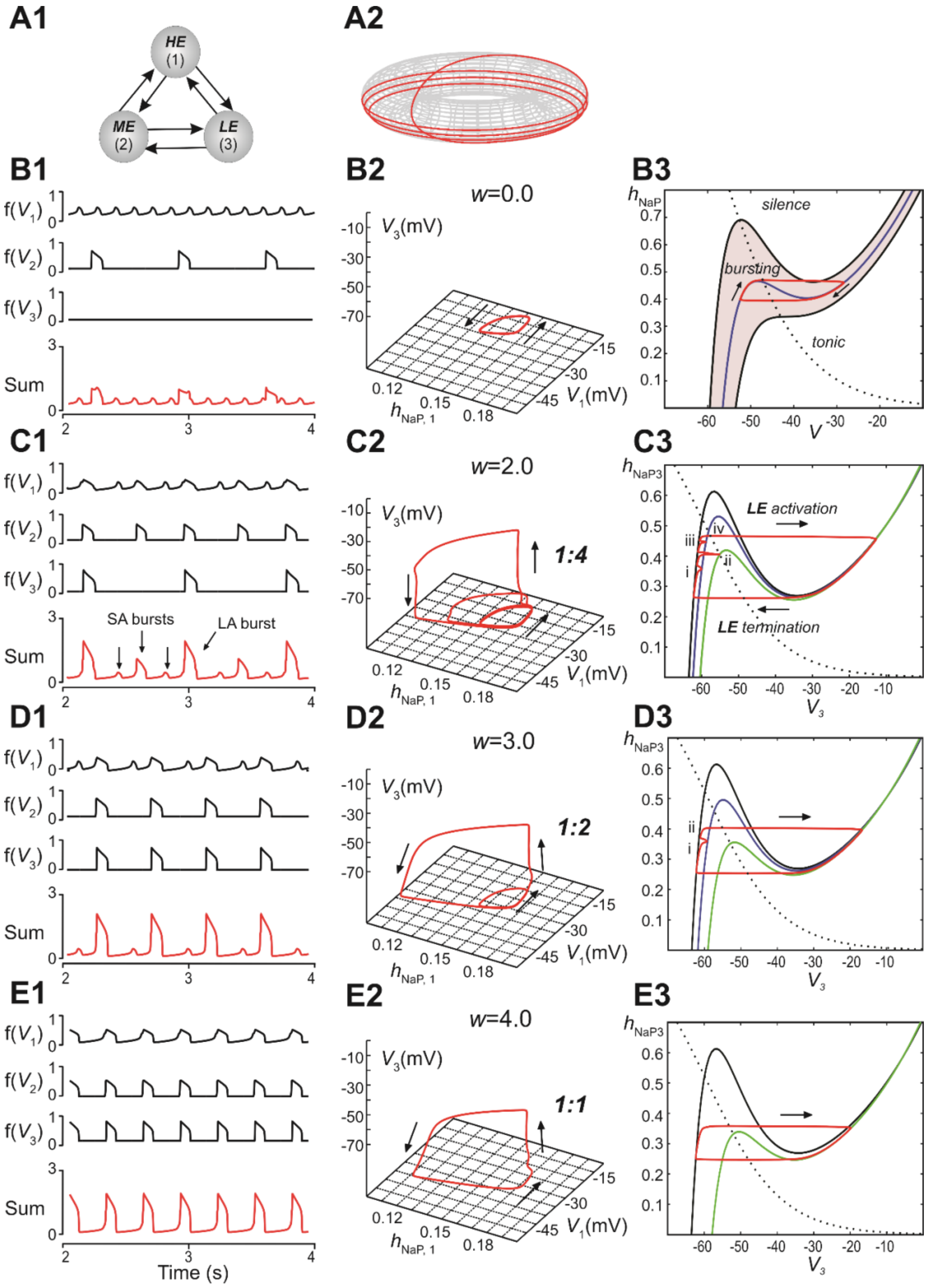

Figure II-5. Reproduction and analysis of mixed mode oscillations in a reduced model. (A1) Schematic of reduced model with mutual excitatory connections between all neurons. Indices correspond to (1) high-excitability (***HE***), (2) medium-excitability (***ME***), and (3) low-excitability (***LE***) neurons. (A2) 1:4 regime represented in toroidal state space (product of two cyclical variables). Four rotations around the larger cycle, corresponding to SA bursts, occur during a single rotation in the smaller cycle, corresponding to an LA burst. Adapted from [88]. (B) Simulation results when w=0. (B1) Output activity, f(V_i), was calculated for each neuron. The “Sum” trace depicts aggregate network output and is asynchronous when w=0 (uncoupled network). (B2) A trajectory (red trace) in the (h_{NaP1},V_1,V_3)-plane depicts endogenous ***HE*** oscillations (cyclical movement in the (h_{NaP1},V_1)-plane), and a silent ***LE*** neuron (no movement in V_3). (B3) In the (h_{NaP},V)-plane an endogenously bursting neuron’s trajectory (red trace) travels around the local minima and maxima of a V-nullcline (blue curve) that intersects the h_{NaP}-nullcline (black, dotted curve). A band of V-nullclines was calculated for the range of E_L values [-59.0, -53.8] mV where endogenous bursting occurred (gray band). E_L values above and below this range caused tonic activity and silence, respectively. (C) Simulation results when w=2. (C1) Output activity showed a pattern of three SA bursts between two LA bursts (1:4 quantal regime). LA bursts occurred when all three neurons were active, low amplitude SA bursts occurred when only the ***HE*** neuron was active, and higher amplitude SA bursts occurred when both ***HE*** and ***ME*** neurons were synchronously active. (C2) The system’s trajectory (red curve) projected into (h_{NaP1},V_1,V_3). Four rotations in (h_{NaP1},V_1) occurred (SA bursts) during with only a single rotation in (V_1,V_3), denoting an LA burst. (C3) The ***LE*** neuron’s trajectory (red curve) is projected into the (V_3,h_{NaP3})-plane. The h_{NaP3}-nullcline (black, dotted curve) intersects three V_3-nullclines:, the black nullcline curve corresponds to depicts the ***LE*** neuron's resting state (no excitatory input), and the blue and green nullcline curves correspond to excitatory inputs from the ***HE*** neuron and both ***HE*** and ***ME*** neurons, respectively. The ***LE*** neuron receives four inputs, marked (i)-(iv), while at rest. Only input (iv) corresponds with results in a successful ***LE*** activation, and therefore an LA burst. (D) Simulation results when w=3. (D1) Two SA bursts occurred between pairs of LA bursts (1:2 quantal regime). (D2) In (h_{NaP1},V_1,V_3) the trajectory makes two rotations in (h_{NaP1},V_1) during one rotation in (V_1,V_3). (D3) In (V_3,h_{Nap3}), the two inputs to the ***LE*** neuron ’s trajectory receives two excitatory inputs, occur at points marked (i) and (ii). Nullcline colors are consistent with B3. (E) Simulation results when w=4. (E1) Only LA bursts were observed (1:1 quantal regime). (E2) In (h_{NaP1},V_1,V_3), one revolution rotation occurs in (h_{NaP1},V_1) for each rotation in (V_1,V_3). (E3) The ***LE*** trajectory is projected into (V_3,h_{Nap3}) for the 1:1 regime. The ***LE*** neuron activates when it receives an excitatory input from the other neurons.

C-4. Analysis of the quantal nature of MMOs with the reduced model

The reduced model provided an explanation for the emergence of quantal MMOs. A key point was that for each neuron, when it was silent, there was a level of synaptic input that caused its activation. This level depended on the degree of I_{NaP} deinactivation in the neuron, quantified by h_{NaP}, as well as on its excitability. When one neuron was activated, it excited the other two neurons, and each of these could be activated if and only if the input it received was sufficiently large (cf. [159]). For the ***LE*** neuron, there were therefore discrete windows of opportunity for activation, corresponding to activation times of the other neurons. This idea can be visualized by considering the trajectory of the full system projected to the (V_3, $h_{NaP,3}$)-plane (Figure II-5B3,C3,D3,E3; see Chapter II: B, "time-scale decomposition in the reduced model"). When the ***LE*** neuron is not active, the trajectory evolves along the left branch of the cubic V_3-nullcline, corresponding to low V_3. The ***LE*** neuron is activated if the trajectory rises above the left knee, or local maximum, of the V_3-nullcline (analogously to the sample trajectory in Figure II-5B3).

Incoming synaptic excitation lowers the V_3-nullcline (Figure II-5C3,D3,E3), a well-known effect known as fast threshold modulation [160]; the amount of lowering depends on the input strength. In Figure II-5C3, three V_3-nullclines are shown: black corresponds to no input, blue to input from the ***HE*** neuron only, and green to input from the ***HE*** and ***ME*** neurons. If a synaptic input lowers the left knee below the current value of $h_{NaP,3}$, then the ***LE*** neuron is activated (e.g., Figure II-5C3, marked with "iv"). Therefore, the activation of the ***LE*** neuron depends on the recovery of $h_{NaP,3}$ when input arrives, and hence on the rate of recovery of $h_{NaP,3}$ relative to the frequency of input arrival. For example, in Figure II-5C3, an SA burst involving only the ***HE*** neuron occurs when the trajectory is at position "i". Since the trajectory is below the knee of the blue nullcline, the ***LE*** neuron does not activate. An SA burst involving the ***HE*** and ***ME*** neurons occurs when the trajectory is at "ii". Again, ***LE*** neuron activation fails, because the trajectory is below the knee of the green nullcline. A failure similar to the first occurs at "iii". Finally, when the ***HE*** and ***ME*** neurons activate with the trajectory at "iv", the green nullcline becomes relevant, the trajectory is above the knee, and the ***LE*** neuron activates, yielding an LA burst.

When synaptic weights were increased, the correspondingly larger excitatory input moved the V_3-nullcline to lower $h_{NaP,3}$ values, allowing activation of the ***LE*** neuron with less recovery time (increase of $h_{NaP,3}$) and hence with fewer input cycles. Figure II-5D3 shows one ***SA*** burst without ***LE*** neuron activation (“I”) and one cycle with ***LE*** neuron activation (“ii”), while in Figure II-5E3, the ***LE*** neuron can activate the first time it receives excitation. In all cases, a discrete number of activations of the ***HE*** and ***ME*** neurons is needed before $h_{NaP,3}$ recovers to a level from which the ***LE*** neuron can activate (Figure II-5C3,D3,E3), which gives rise to the quantal nature of the MMO patterns (Figure II-6A).

A change in the excitability of the ***LE*** neuron alone could alter the V_3-nullclines (for all input levels) and hence change the frequency of the LA cycles within each quantal MMO rhythm without any change in the overall oscillation frequency of the 3-neuron population (data not shown). On the other hand, an increase in the excitability of the ***HE*** neuron alone caused an increase of the SA burst frequency. Since the time between SA cycles became shorter, there was less recovery of the ***LE*** neuron per cycle, such that more SA cycles occurred between LA cycles and the overall LA frequency remained approximately constant (data not shown).

C-5. Reduced model analysis of interburst intervals (IBIs)

Another feature of the MMOs observed in our large-scale model is that IBIs were longer after LA bursts than after SA bursts. This property was seen in the reduced model as well (Figure II-5C1,D1, and see the multiple values of the period for the ***HE*** neuron within each quantal regime in Figure II-6A). The reduced framework elucidates the mechanism underlying this feature. When some neurons are activated, the active neurons excite each other. Each active neuron's variables evolve along the right branch of its *V*-nullcline, and activation ends when they reach the right knee, or local minimum, of this nullcline (see Figure II-5B3, red trace). Stronger excitation pushes a neuron's *V*-nullcline, including its right knee, to lower h_{NaP} values and hence causes the active phase to end with more I_{NaP} inactivation (i.e., lower h_{NaP}-coordinate). Thus, a longer recovery period is needed before subsequent activation of the leading neuron. On LA cycles, all neurons excite each other, which causes a maximal lowering of *V*-nullclines and subsequently yields the longest IBIs.

The difference in post-burst recovery times is evident in the ***HE*** neuron's trajectory when the 1:2 regime is simulated (*w*=3.0, see Figure II-6B). The different-size loops shown in (V_1, h_{NaP1}) correspond to SA and LA bursts, respectively, and therefore have different maximal V_1 and minimal h_{NaP1} values, defined by positions of the V_1-nullcline during ***HE*** activation. The SA bursts occur due to the ***HE*** neuron's intrinsic rhythmicity. When the ***ME*** and ***LE*** neurons excite the ***HE***, the V_1-nullcline moves to lower h_{NaP1} and V_1 values (lowest green nullcline, Figure II-6B). This movement extends the active phase by pushing the right knee of the V_1-nullcline down. As ***ME*** and ***LE*** neuron activity adapts, excitation gradually decreases (green band, Figure II-6B) but nonetheless, when excitation from ***ME*** and ***LE*** neurons is removed, the ***HE*** neuron returns to the left branch of the V_1-nullcline at much lower h_{NaP1} values than following an SA burst. Therefore, the time it takes the ***HE*** neuron to recover, following an LA burst, is longer than the recovery following an SA burst.

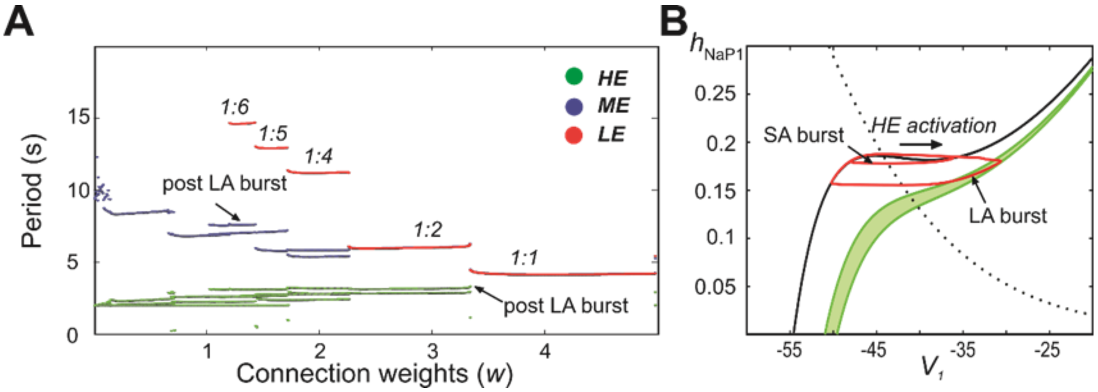

Figure II-6. Emergence of quantal regimes and analysis of interburst intervals. (A) The burst period of each neuron was continuously calculated as the connection weights (w) were increased and neuronal periods on each cycle were plotted. LA bursts occurred at w>1.4 (***LE*** emergence, red dots). The quantal regime was determined by the ratio of ***LE*** and ***HE*** periods. Transitions between stable regimes, i.e. bifurcations, occurred when the ***LE*** period “jumped” to progressively lower integer ratios of the ***HE*** period. The ***ME*** and ***HE*** neurons had longer periods following LA bursts than SA bursts. This phenomenon creates multiple branches in the ***ME*** and ***HE*** periods for a given quantal regime (see the pair of ***HE*** period branches at w=3 in the 1:2 quantal regime, for example). (B) The ***HE*** neuron's trajectory (red curve) is projected into the (h_{NaP1},V_1)-plane when w=3.0 (1:2 regime). Distinct oscillations arise in the ***HE*** neuron's trajectory for SA and LA bursts. The black V_1-nullcline governs ***HE*** activity when it is endogenously bursting during an SA burst. The green V_1-nullclines govern ***HE*** activity during network-wide activation (LA burst) and are depicted as a band because of the progressive decay of output from ***LE*** and ***ME*** neurons (resulting from the decrease in f(V) as their voltages decreased, see equation (*II-14*)) following LA burst onset.

C-6. Effects of reduced neuronal excitability and interconnections

To investigate the dependence of MMO regimes on excitability (E_L) we proportionally reduced excitability in all neurons. Quiescence could be induced in the ***LE*** and ***ME*** neurons after decreasing all excitabilities by 8% (Figure II-7A). The frequency of the ***HE*** neuron decreased, and this produced low frequency SA bursts with no LA bursts. A similar regime of only SA bursts could be produced by decreasing weights of neuronal interconnections (Figure II-7B). In the example shown, both the ***HE*** and ***ME*** neurons participated in the SA bursts. No change occurred in the frequency of the ***HE*** and ***ME*** neurons (Figure II-7B).

The phase diagram in Figure II-5B3 can be used to explain the effects of reduction in neuronal excitability and connection weights. Changing excitability moved the *V*-nullclines corresponding to the unexcited, or resting, state of a neuron. For an uncoupled neuron, increasing E_L caused progressive transitions from silence, to bursting, to tonic behavior. The transitions between these behaviors occurred when the fixed point (intersection of the neuron's *V*- and h_{NaP}-nullclines) moved from the *V*-nullcline's left branch (silence), to its middle branch (bursting), to its right branch (tonic). When excitability was decreased in a coupled network (Figure II-7A), the fixed points of the ***ME*** neuron moved to the left branch of the *V*-nullcline (the ***LE*** neuron's fixed point was already on the left branch, corresponding to the quiescence of the ***LE*** neuron in the uncoupled case, see Figure II-5B1). This decreased excitability increased the amplitude of excitation required to induce bursting in these neurons, and thus the low amplitude ***HE*** neuron's phasic excitation was insufficient.

When synaptic weights were changed (Figure II-5B3,C3,E3) only the *V*-nullclines corresponding to the presence of phasic excitation (from other neurons in the network) were altered. Thus, the intrinsic dynamics of each neuron stayed the same under changes in weights, such that the ***HE*** and ***ME*** neurons both remained able to activate. With decreased synaptic weights, however, we again found that synaptic excitation could no longer recruit the ***LE*** neuron (cf Chapter II: C-4).

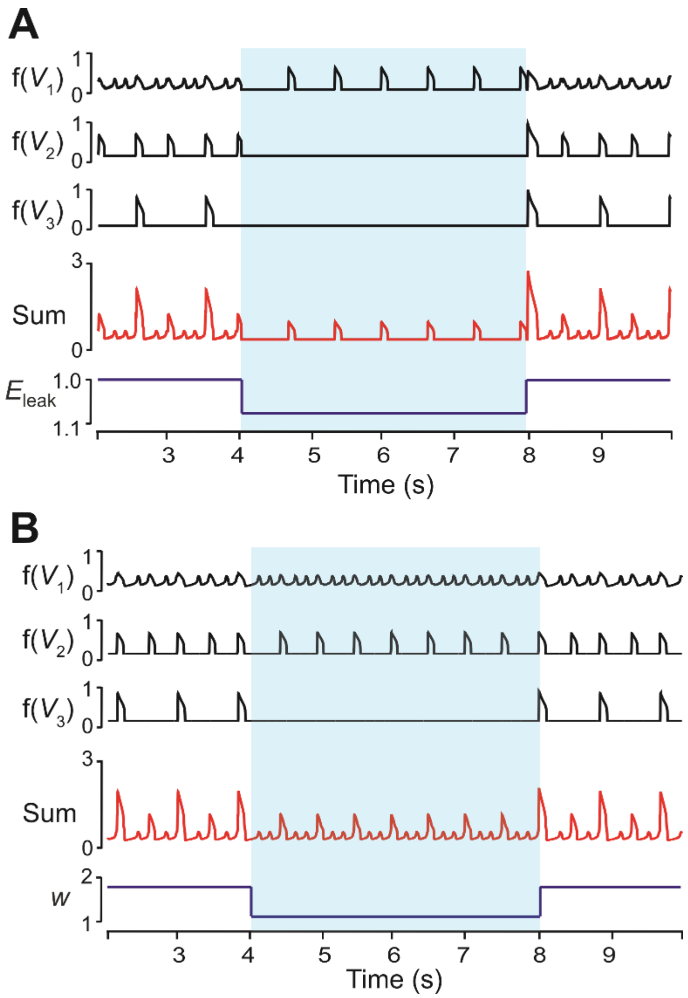

Figure II-7. Modulation of excitability and connection weights alters reduced model activity pattern. (A) Output levels, $f(V_i)$, for all three neurons with $w=1.7$. A transient decrease of 10% in E_L was implemented between 4 and 8 seconds (blue shaded region), causing the 1:5 quantal regime to transition to a regime with only ***HE*** active. (B) Output levels, $f(V_i)$, for all three neurons with $w=2.0$, producing the 1:4 quantal regime. A transient reduction of w by 50% between 4 and 8 seconds (blue shaded region) caused a loss of LA bursts. Resulting SA bursts featured activation of ***HE*** alone (lower amplitude SA bursts) or synchronized ***HE*** and ***ME*** activity (higher amplitude SA bursts).

D. Discussion

D-1. MMOs in heterogeneous populations of coupled excitatory neurons

We have presented and explored a novel, network-based mechanism for the emergence of MMOs, featuring repetitive alternations of SA and LA bursts of activity, in a heterogeneous population of neurons coupled via sparse excitatory synaptic interactions. In this form of MMOs, the time intervals between bursts are on a similar time scale regardless of whether an SA or an LA burst has just occurred, yielding quantal patterns of SA and LA events, although precise IBI durations actually depend on the amplitude of preceding bursts, and hence IBIs following LA bursts are longer than those following SA bursts (Figure II-6A). These MMOs appear to be a natural, perhaps inevitable, behavior of heterogeneous neural networks with excitatory coupling that can be expected to emerge widely in the nervous system, in which the rate of recovery of high excitability neurons dictates the period of subsequent events, while the recovery of low excitability neurons determines which subsequent events become LA bursts. LA bursts correspond to synchronous activation of most neurons in the network and occur when the least excitable neurons in the network can be recruited. Furthermore, feedback from these least excitable to the more excitable neurons is essential for synchronizing the network during LA bursts.

D-2. Relation to MMOs in previous theoretical and modeling studies

MMOs have been reported in a variety of neural systems [141]–[144], [147], [148]. The computational and mathematical analysis of these patterns has focused on mechanisms that emerge from the separation of time scales typically found within neural dynamics, between voltages and fast gating and synaptic kinetics on one hand and slower gating, synaptic, and ionic concentration kinetics on the other. Within the corresponding MMOs, SA oscillations occur during a delayed transition between two different attractors for the fast dynamics and are often relatively high frequency events that emerge after a quiescent period, whereas the actual transitions between attractors yield LA events [140].

Our present work deals with a very different form of MMOs where different oscillation amplitudes correspond to the participation of different numbers of neurons from within a network. In these MMOs, even within SA events, there is a complete transition between different attracting states (hyperpolarized and depolarized) for the fast voltage dynamics, although only some variables in the network are involved in this transition. The MMOs that we studied here depend critically on the synaptic interactions leading to the emergence of neuronal clusters with synchronous bursting activity, whereas the other described classes of MMOs mainly arise from intrinsic dynamics even in single neurons. Therefore, we observed a transition through a range of quantal MMO regimes as synaptic parameters were varied (Figure II-4A,B, 5, and 6). Furthermore, LA bursts are gained, as parameters are varied, by conversion of particular SA bursts, arising roughly evenly between pairs of LA bursts, into LA bursts (reminiscent of period-doubling), whereas in time-scale-based MMOs, transitions involve the less radical loss or gain of individual SA oscillations occurring just before each LA burst.

The previous analyses closely related to this novel form of MMO were presented in two earlier papers, both motivated by the pre-BötC in the respiratory brainstem. In one study, synchrony could emerge in a group of modeled neurons with heterogeneous excitability, coupled with synaptic excitation [159]. It was noted that, starting in a 1:1 regime, weakening synaptic strengths could cause less excitable neurons to skip some cycles. In the other previous work, the reduced neuron models were used to investigate quantal recruitment of normally-silent late-expiratory neurons under hypercapnia [88]. However, the model was not a heterogeneous excitatory network but rather consisted of several distinct neuronal populations coupled with a combination of excitation and inhibition, and the quantal effects observed involved only the single expiratory population, without any clustering or other alterations in other neurons' behaviors.

D-3. Generation of MMOs: the role of endogenous bursting properties of neurons

In the present work, we first studied MMOs in a large-scale neuron population consisting of 100 neurons modeled in the Hodgkin-Huxley style, which were coupled through sparse excitatory synaptic connections. All neurons in the model were capable of endogenous generation of rhythmic bursting activity (Figure II-2A2) within a particular range of excitability (their resting membrane potential, defined by E_L; see Figure II-2A1,A2 and 3A1,A2). This intrinsic neuronal bursting was based on a persistent (slowly inactivating) sodium current, I_{NaP}, characterized by fast sub-threshold activation and slow inactivation, both voltage-dependent [125], [126], [136], [156]. Although there is ongoing debate concerning the exact mechanisms responsible for endogenous bursting in the pre-BötC *in vitro* [21], [28], [146], [153], [154], [157], [158], [161]–[163], I_{NaP} has been found in pre-BötC neurons and the rhythmic bursting activity in the pre-BötC could be abolished by pharmacological blockade of this current [136], [149], [155], [156], [161]. Therefore, the inclusion of I_{NaP} in our models can be considered reasonable. Following the previous computational models of pre-BötC neurons [125], [126], [136], [153], [156], [158], the I_{NaP} inactivation variable, h_{NaP}, evolved with a large time constant and its slow dynamics defined a slow neuronal “recovery", i.e. gradual depolarization in the post-activity phase (red traces in Figure II-3A2).

The reversal potential of the leak current (E_L) was randomly distributed across neurons in the network to provide a range of excitabilities and subsequent behaviors. This combination of distributed neuronal excitability with slow voltage-dependent recovery provided two important characteristics of neurons within the population:

(1) With an increase of excitability in intrinsically bursting neurons, the frequency of bursts increased, whereas the spike frequency within the bursts decreased (Figure II-3A3); such a reciprocal effect of neuronal excitability on the burst vs. spike frequency arose because with higher burst frequencies (reduced IBIs), there was less time for recovery (deinactivation).

(2) Neurons with lower excitability required more time for recovery and could not be involved in high-frequency oscillations.

These two key features of the large-scale model were preserved in our reduced model, in which the spike frequency within the burst was explicitly represented by the amplitude of neuronal output. Therefore, this amplitude decreased with the increasing neuronal excitability (from ***LE*** to ***HE*** neurons), and the slow recovery of ***LE*** neurons (defined by the voltage-dependent time constant for h_{NaP3}), was greater than the recovery of ***HE*** neurons, and prevented the ***LE*** neuron from participation in higher frequency synchronized bursts (Figure II-5).

Although these key features in both our models are the direct result of I_{NaP} kinetics, they actually are not specific for the I_{NaP}-dependent bursting mechanism analyzed herein. Instead, they represent a common feature of most known cellular bursting mechanisms, in which the post-burst recovery time depends on the neuronal activity within the bursts and vice versa. For example, in the case of intrinsic bursting mechanisms based on Ca^{2+}-dependent potassium ($I_K(Ca^{2+})$), Ca^{2+}-activated nonspecific (I_{CAN}), or Na^+-dependent potassium ($I_K(Na^+)$ currents, involving intracellular accumulation of Ca^{2+} or Na^+ ions, a functionally similar slow recovery is usually connected with operation of either the Ca^{2+} or Na+/K+ pumps [153], [157], [158], [164]–[168]. Therefore the two key features formulated above, which are critical for generation of network-based MMOs, appear to represent common properties of populations of intrinsically bursting neurons with distributed excitability that extend across many different bursting mechanisms. This conclusion clearly contradicts a recently published opinion [163] that previous computational models reproducing the MMOs observed in the pre-BötC [126], [127] are not valid because the neuronal bursting in these models is critically dependent on slow deactivation kinetics of I_{NaP}.

To evaluate the potential role of I_{NaP} in the considered MMOs, we used our large-scale model to investigate the transition of the population activity pattern during progressive suppression of I_{NaP} in all neurons (Figure II-4A3,B2,B3). A regime with only LA bursts was selected as a starting point for this study (top trace). When I_{NaP} conductance ($\bar{g}_{NaP}$) was suppressed, the frequency of LA bursts decreased and an MMO regime emerged (Figure II-4B3, traces 2 and 3) until eventually only SA bursts remained and then activation completely ceased. We consider this result as a prediction for future experimental study, suggesting that a progressive suppression of I_{NaP} in the pre-BötC, *in vitro*, by its specific blocker, riluzole, should cause a transitional MMO regime before abolishing rhythmicity completely.

D-4. Generation of MMOs: effects of changing connections and neuronal excitability

When the weights of excitatory connections were progressively increased in our large-scale model, a succession of stable network rhythms, or “regimes”, were observed (Figure II-4A1,B1,B2). Low weights of connections produced only SA bursts in the network’s activity (top trace in Figure II-4B1), intermediate weights caused MMOs (traces 2-4), and strong weights produced regimes with only LA bursts (bottom trace). Similar regimes emerged when the probability of connections was increased at fixed weights of connections (Figure II-4B2). In all of these cases, the overall frequency of burst events remained similar; what changed was the frequency with which those bursts were of large amplitude.

Similar transformations in the integrated pattern occurred when weights of interconnections were increased in the reduced model (Figure II-5). In contrast, reduction of either the general neuronal excitability (Figure II-7A) or weights of connections (Figure II-7B) could cause ***LE*** neurons to remain silent, leading to an integrated pattern with only SA bursts present (Figure II-7A,B). These simulation results may provide a reasonable explanation for the transformation of MMOs observed during application of cadmium (Cd^{2+}) in a medullary slice exhibiting MMOs [146]. In these experiments, Cd^{2+} application abolished LA bursts whereas SA oscillations persisted. We therefore suggest that the effects of Cd^{2+}, a blocker of calcium currents, could either attenuate neuronal excitability or reduce excitatory synaptic interconnections within the pre-BötC, as seen in our simulations (Figure II-7A,B). However, more experimental investigations, particularly regarding frequency changes following Cd^{2+} exposure, are needed to distinguish these possibilities.

D-5. The frequency of output pre-BötC oscillations is defined by properties of neurons with the lowest excitability

The analysis of neuronal “clustering” of our large-scale model showed that groups of neurons with different excitability participated either in SA and LA bursts or only in LA bursts (see Figure II-3B1,B2,C1,C2,D1,D2). Specifically, neurons with relatively high excitability (E_L), and therefore with the high burst frequency (***HE*** neurons), participated in some SA and all LA bursts, whereas neurons with the lowest excitability and the lowest burst frequency (***LE*** neurons) participated only in LA bursts. Importantly, since ***LE*** neurons had the highest spike frequency (Figure II-3B3) within the bursts, they could provide the strongest excitatory synaptic inputs to other neurons, resulting in the network-wide synchronization underlying the generation of LA bursts. It is also interesting to note that ***LE*** neurons could fail to activate even when receiving excitatory inputs of sufficient strength (see intersection of dashed lines in Figure II-3D1), if the time from the last LA burst was insufficient for the recovery of ***LE*** neurons. This suggests that a mechanism intrinsic to the ***LE*** neurons and connected with their slow recovery is critically involved in the generation of LA bursts, defining their IBIs and the output burst frequency.

Our reduced model exhibited a similar dependence on ***LE*** neuron recovery, which could be confirmed by analysis using time-scale decomposition in the (V,h_{NaP})-plane (Figure II-5C3,D3,E3). This analysis showed that whether or not an excitatory input could recruit the ***LE*** neuron and induce an LA burst depended on the relative sizes of two quantities: (a) the h_{NaP}-coordinate of the ***LE*** neuron at the time of input (longer periods of recovery, or inactivity, led to higher h_{NaP}-coordinates) and (b) the h_{NaP}-coordinate of the left knee of the V_3-nullcline corresponding to the excitatory input (stronger inputs induced lower h_{NaP}-coordinates). Successful ***LE*** neuron activation occurred when (a) was greater than (b), as at point (iv) in Figure II-5C3**,** and activation failed when (b) was greater than (a), as at (i)-(iii) in Figure II-5C3. When weights were increased, the V_3-nullcline was shifted to lower h_{NaP} values, which allowed the ***LE*** neuron to activate with less recovery.

Interestingly, based on this analysis and previous work [158], we can infer that the strong mutual excitation, that occurs during an LA burst, is responsible for the pause in activity of the tonic spiking neurons after an LA burst in the large-scale model (Figure II-3B2). Both the prolonged IBI and the pause in tonic spiking after LA bursts rely on the synaptic excitation from the full collection of neurons in the network, and thus their presence can be taken as evidence that the least excitable neurons in the network are not recipients of feed-forward inputs but rather participate in the recurrent network structure.

D-6. Burstlets, bursts, and separate sub-networks for rhythm and pattern generation

The emergence of MMOs in the pre-BötC have been recently studied *in vitro* in the medullary slices from neonatal mice [146]. These MMOs were artificially evoked at a moderate level of neuronal excitability produced by elevation of $[K^{+}]_{out}$ to 5-6 mM and were characterized by a series of SA bursts ("burstlets") alternating with single LA bursts that, in contrast to the burstlets, were able to trigger the "inspiratory" rhythmic bursts in the hypoglossal motor output and hence defined the frequency of output oscillations. The emergence of MMOs in the pre-BötC in these conditions allowed Feldman and Kam to propose a novel "burstlet concept" of inspiratory rhythm generation that "fundamentally breaks with the burst hypothesis" [163]. According to this concept, "rhythm- and pattern-generating functions common to all CPGs are assumed to be segregated" so that the rhythm and the pattern are generated by "separable microcircuits" and "distinct mechanisms" [146], [163], similar to that in a previous model of the spinal locomotor CPG suggesting the existing separate circuits for rhythm generation and pattern formation [169], [170]. In this interpretation, the role of intrinsic bursting mechanisms in neurons generating the LA bursts in the pre-BötC is fully disregarded, and the lack of these bursts on the top of each burstlet (SA bursts) is considered as equivalent to the non-resetting spontaneous deletions (missing bursts) observed during fictive locomotion in the spinal cord.

Our computational study does not support the interpretation of MMOs in the pre-BötC as indicative of separate rhythm- (burstlets) and pattern- (bursts) generating sub-networks. The results of our present modeling study instead suggest that a single, inseparable population of coupled excitatory neurons incorporating endogenous neuronal oscillators with distributed excitability can reproduce, and is sufficient to explain, the coexistence of burstlets and bursts in population rhythmic activity (i.e., the MMOs described in this work). We implemented a sparse network connectivity pattern that reflects experimental data more completely than previous models [127], [153] and precludes the existence of separable sub-networks. In the models of the locomotor CPG in the spinal cord mentioned above, the pattern formation circuits did not affect the rhythm generator circuits, but just responded 1:1 to the rhythm-generating input, unless accidental perturbations happened, changing the excitability of the pattern formation network and producing deletions [169], [170]. In contrast, in the interconnected single network considered here, the activity of low-excitable neurons involved in generation of low frequency LA bursts (attributed to the "pattern generating circuits") synchronize the entire population activity, explicitly defining its output frequency ("rhythm"). Therefore, the intrinsic properties of these low-excitable neurons, specifically the temporal characteristics of their recovery (see Figure II-5D1,D2 and 6B), but not deletions of unknown origin, define the output frequency of rhythm generator that interacts with other circuits to shape the CPG activity pattern.

E. Summary of predictions

Sub-cellular level predictions: Both models presented in this chapter had persistent sodium (I_{NaP}) dependent intrinsic rhythmicity. The model of 100 Hodgkin-Huxley neurons used a more detailed description of I_{NaP} than the reduced model formalization. Interestingly, a major implication of the reduced modeling results was that the current did not need to be I_{NaP}, per se. Rather, intrinsic rhythmicity itself was the critical element. In fact, neurons in the reduced model were simple relaxation oscillators that were able to produce MMOs. This suggestion is critical given the controversial nature of I_{NaP}'s role in respiratory rhythmogenesis.

Cellular level predictions: The predictions at this level involved changes between quantal states (i.e. 1:N regimes of LA:SA activity). Our model predicts that the quantal state is dependent on the weight of connections, the probability of connections, and I_{NaP}. Specifically, increasing weight of connections and the probability of connections causes a convergence to a 1:1 regime, see Figure II-8A1, A2, B1. The weight of connections could be experimentally tested by applying an NMDA agonist to the pre-BötC. In addition, we predict that, starting with a 1:1 regime, application of a small dose of riluzole, an I_{NaP} channel blocker, would cause the emergence of MMO activity (see Figure II-9A3, B2, B3).

Finally, our results suggest that inspiratory motor outputs are driven by a group of neurons with low excitability that emerge as a cluster and recruit the rest of the network with their high spike frequency bursting. Using calcium imaging, Jeffrey Smith's lab found that a small cluster of spatially constrained neurons activates prior to the synchronized activity in the pre-BötC (unpublished data). The excitability of these neurons has not yet been characterized.

Chapter III: Late-expiratory activity: emergence and interactions with the respiratory CPG

The following section was adapted from the following accepted manuscript: Y. I. Molkov, A. P. Abdala, B. J. Bacak, J. C. Smith, J. F. R. Paton, and I. A. Rybak, “Late-expiratory activity: emergence and interactions with the respiratory CPG.,” *J. Neurophysiol.*, vol. 104, no. 5, pp. 2713–29, Nov. 2010.

A. Introduction

The respiratory rhythm and coordinated motor pattern during breathing in mammals is generated by a respiratory central pattern generator (CPG) located in the lower brain stem [3], [5], [6]. The pre-Bötzinger complex (pre-BötC), located within the medullary ventrolateral respiratory column, is considered a major source of rhythmic inspiratory activity [20], [23]–[25]. The pre-BötC, interacting with the adjacent Bötzinger complex (BötC) containing mostly expiratory neurons [3], [31]–[34] represents a core of the respiratory CPG [3], [5], [6], [16], [19], [33], [35], [36], [62], [151]. This core circuitry generates primary respiratory oscillations defined by the intrinsic biophysical properties of respiratory neurons involved, the architecture of network interactions between respiratory neural populations within and between the pre-BötC and BötC, and input drives from other brainstem compartments, including the pons, retrotrapezoid nucleus (RTN), raphé, and nucleus tractus solitarii (NTS). In addition, information on the metabolic state of the system such as levels of CO_2, O_2, pH, provided by the RTN, raphé, peripheral chemoreceptors (via

NTS), can reorganize the respiratory network and operating rhythmogenic mechanisms depending on metabolic conditions.

A distinct site of neural oscillations, the parafacial respiratory group (pFRG), putatively involved in respiratory function was initially identified *in vitro*, in the isolated neonatal rat brain stem-spinal cord preparation [37]–[39]. The pFRG seems to reside within, or to overlap with, RTN. It has been proposed that RTN/pFRG oscillations drive abdominal motor activity, expressing pre-inspiratory (or late-expiratory, late-E) or biphasic-E (with pre-inspiratory and post-inspiratory) discharges in the abdominal motor output when the system operates in the active expiration state to force exhalation [20], [41]–[43]. Several competing concepts concerning the physiological role of RTN/pFRG oscillations have been suggested and debated [20]. These include the suggestion that the pFRG represents the primary inspiratory oscillator [39], [171] and the dual oscillator concept that considers the RTN/pFRG to be an independent expiratory rhythm generator that is coupled with a distinct inspiratory rhythm generator in the pre-BötC [42], [172]. However, the exact physiological role of pFRG oscillations, the specific conditions for their emergence, and the nature and mechanisms of the interactions between the BötC/pre-BötC and RTN/pFRG oscillators are not yet known. New mechanistic insights in this regard would represent a significant step in understanding the neural control of breathing and would have a broader impact on understanding the role of interacting neural oscillations in brain operation.

Our previous large-scale computational models of the spatially and functionally organized brain stem respiratory network [16], [19] were able to reproduce the three-phase eupneic respiratory pattern generated under normal conditions as well as its reorganization resulting from multiple experimental perturbations, such as various brainstem transections and application of specific blockers of ionic channels and inhibitory synaptic transmission. Based on these modeling studies, we have concluded that the brain stem respiratory network has rhythmogenic capabilities at multiple hierarchical levels, which allows flexible, state-dependent expression of different rhythmogenic mechanisms under different physiological and metabolic conditions and enables a wide repertoire of respiratory behaviors [16], [19], [36], [41].

Our previous modeling studies, however, did not analyze in detail interactions between the respiratory CPG circuits and RTN/pFRG oscillator. The goal of this study was to extend our previous model [16] in order to investigate: (i) the metabolic state-dependent conditions for the emergence of RTN/pFRG oscillations, (ii) the neural mechanisms involved in the interactions between BötC/pre-BötC and RTN/pFRG oscillators, and (iii) the role of these interactions in shaping the coordinated pattern of respiratory motor outputs under different conditions, which may reveal the physiological role of RTN/pFRG activity.

To this end, we analyzed further our previous results [41] and some new experimental data providing additional evidence for the location of the source of abdominal late-E oscillations in RTN/pFRG, the dependence of these oscillations on the persistent sodium current, the metabolic conditions for the emergence of these oscillations, and their role in coordination of phrenic and hypoglossal motor outputs. We specifically investigated some critical regimes of coupling between RTN/pFRG and BötC/pre-BötC oscillations including a regime of quantal acceleration of late-E oscillations with the development of hypercapnia.

The modeling part of our study is presented in two consecutive aims. In this first paper, we describe an extended large-scale model and perform a series of key simulations to reproduce (and predict) experimentally observed behaviors. In Chapter IV I present a reduced model that maintains the essential features and architecture of the extended large-scale model, but allowed us to use methods of dynamical systems theory, such as bifurcation and phase plane analyses, to elucidate the mechanisms and dynamics of synchronization between the RTN/pFRG and BötC/pre-BötC oscillations. The presented combination of experimental and modeling studies provides new theoretical insights into the state-dependency of RTN/pFRG oscillations, the nature of their coupling with BötC/pre-BötC oscillations and their impact on respiratory pattern generation under different metabolic and physiological conditions.

B. Methods

B-1. Experimental data

The majority of the data used herein were taken from a recently published study [41] conducted in the *in situ* arterially perfused brainstem-spinal cord of juvenile rats. New experimental results presented here included the effects of riluzole, the persistent sodium current blocker, on the abdominal and phrenic motor activities during hypercapnia, and the effect of local blockade of GABAergic synaptic inhibition within the RTN/pFRG on late-E abdominal activity during normocapnia. Procedures for applying riluzole (5–10 μM) to the perfusate in the *in situ* preparations with recording of multi-nerve activities to study the role of this current in respiratory pattern generation *in situ* have been described in detail in [16]. The procedures used here for local, bilateral injection of bicuculline (10 μM) into the

RTN/pFRG, including histological documentation of injection sites, were identical to those described in [41] for focal injection of pharmacological agents perturbing GABAergic synaptic transmission in the RTN/pFRG. For all other experimental details, including electrophysiological methods for recording abdominal nerve (AbN) activity simultaneously with activity of cervical vagus (cVN) and hypoglossal (HN) cranial nerves and phrenic (PN) nerve, refer also to [41].

.

B-2. Data processing and analysis

We measured parameters of motor or neuronal unit activity (cycle period/frequency, inspiratory/expiratory phase durations and amplitudes) across at least 50 respiratory cycles. For time-series analysis of different outputs we used signals simultaneously recorded from nerves and neuronal units digitally acquired (5 kHz sampling rate) by means of Spike2 (Cambridge Electronics Design) software. For detection of nerve bursting activity, these signals were DC removed, rectified and integrated (50 ms time constant). An appropriate threshold was chosen and the time points of successive intersections of the integrated activity with the threshold were registered. The time intervals between the onsets or offsets of two successive bursts of nerve activity (referred to as periods) were computed. Processing of digitized data was performed using the software package TISEAN and custom written C++ programs.

B-3. Modeling and simulations

The model was developed based on, and as an extension of, the previous model described by [16]. All neurons were modeled in the Hodgkin-Huxley style (single-compartment models) and incorporated known biophysical properties and channel kinetics characterized in respiratory neurons *in vitro*. Each neuronal type was represented by a population of 50 neurons. Heterogeneity of neurons within each population was set by a random distribution of some parameters and the initial conditions for values of membrane potential, calcium concentrations, and channel conductances. A full description of the previous model and model parameters used can be found in [16]. All new (additional), and altered (relative to [16]) model parameters are indicated in Table III-1.

All simulations were performed with a simulation package NSM 3.0, developed at Drexel University by S. N. Markin, I. A. Rybak, and N. A. Shevtsova. Differential equations were solved using the exponential Euler integration method with a step of 0.1 ms. Other details of the modeling and simulation methods can be found in [16], [19].

Table III-1. Weights of synaptic connections. Values in brackets represent relative weights of synaptic inputs from the corresponding source populations (w_{ji}) or drives (w_{dmi}). * indicates populations not present in the model of Smith et al. (2007) and weights of connections adjusted in the present model relative to that model.

Target population (location)	**Excitatory drive {weight of synaptic input} or source population {weight of synaptic input from single neuron}**
bulbospinal E* (cVRG)	early-I(2) {-2}*; late-E {0.02}*.
ramp-I (rVRG)	drive(pons) {2.0}; early-I(2) {-0.3}*; pre-I /I{0.06}; aug-E{-0.1}*; post-I {-2.0}*.
early-I(2) (rVRG)	drive(pons) {2.5}*; aug-E {-0.25}; post-I {-0.25}*; late-E {0.1}*.
pre-I/I (pre-BötC)	drive(raphe) {0.3}; drive(RTN) {0.22}*; drive(pons) {0.65}*; pre-I /I {0.03}; aug-E {-0.06}*; post-I {-0.16}*; late-E {0.02}*.
late-E* (RTN/pFRG)	early-I(1) {-0.025}*; post-I {-0.0225}*; late-E {0.03}*;

early-I(1) (pre-BötC)	drive(RTN) {1}*; drive(pons) {1.1}; pre-I /I {0.1};* aug-E {-0.265}* ; post-I {-0.45}*.
aug-E (BötC)	drive(RTN) {2.1}*; drive(pons) {0.6}*; early-I(1) {-0.115}*; post-I {-0.32}; late-E {0.03}*.
post-I (BötC)	drive(RTN) {0.05}*; drive(pons) {1.65}*; early-I(1) {-0.025}*; aug-E {-0.01}.
post-I (e) (BötC)	drive(pons) {0.05}*; early-I(1) {-0.2}; aug-E {-0.2}*.

C. Results

In this section we present results from new analyses of our previously published data [41] as well as new experimental observations that form the basis for developing an extended computational model of the brainstem respiratory network described in the following section.

C-1. Emergence and quantal acceleration of late-E abdominal activity with hypercapnia

Under baseline metabolic conditions (95% O_2, 5% CO_2) the abdominal motor output (AbN) recorded in the *in situ* arterially perfused rat brainstem-spinal cord preparations typically exhibits a low-amplitude post-inspiratory activity as described in [41]. Switching to hypercapnic (7–10% CO_2) and/or hypoxic conditions evokes large amplitude late-expiratory (late–E, also called pre-inspiratory, pre-I) bursts in AbN. A representative example is shown in Figure III-1 where the late-E discharges emerge in AbN at 7% CO_2 (Figure III-1A2,B) followed by a progressive increase in their frequency (decrease in the burst period) as the CO_2 concentration is incremented to 10%. Importantly, although the frequency of late-E bursts increases with CO_2, these bursts remain coupled (phase-locked) with the bursts in the PN, cVN and HN (Figure III-1A2-A4, see also Figure III-2A1,A3, and Figure III-4A1,A2,B). With the development of hypercapnia, the ratio of late-E burst frequency to the PN burst frequency shows a step-wise or *quantal* increase from 1:5 and 1:4 (seen in Figure III-1B) to 1:3, 1:2, and, finally, to 1:1 (Figure III-1A2-A4 and B; see also Figure III-4A1,B below). On returning CO_2 to the control levels the ratio showed a step-wise reversal (see in Figure III-4B). Similar hypercapnia-evoked AbN late-E discharges phase-locked to PN with a step-wise increase of their frequency with increasing CO_2 levels has been demonstrated previously *in vivo* by Iizuka and Fregosi 2007. We call this process *quantal acceleration* of late-E activity with development of hypercapnia.

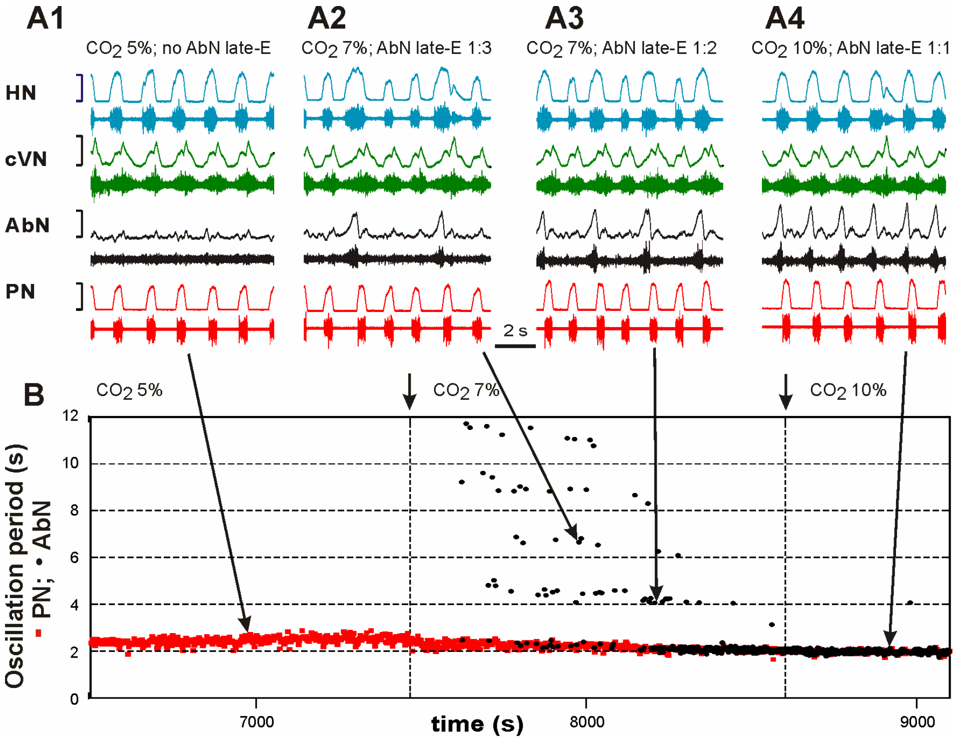

Figure III-1. Quantal acceleration of AbN late-E activity with the development of hypercapnia. (A1-A4) Simultaneously recoded activity of (bottom-up) PN (red), AbN (black), cVN (green), and HN (blue). Activity of each nerve is represented by two traces: raw recording (lower trace) and integrated activity (upper trace). (A1) Normocapnia (5% CO_2): late-E activity is absent in the AbN. (A2-A4) Quantal acceleration of AbN activity:

with the development of hypercapnia, the ratio between the AbN and PN frequencies goes through step-wise changes from 1:3 and 1:2 (A2 and A3, 7% CO_2) to 1:1 (A4, 10% CO_2). (B) Time-series representation of the entire experimental epoch with the oscillation periods in the PN (red squares) and AbN (black circles) plotted continuously vs. time. The AbN late-E bursts were synchronized with the PN bursts with a ratio increasing quantally from 1:5 to 1:1. The content of CO_2 in the perfusate of this preparation was changed at times indicated by short arrows and vertical dashed lines. Large arrows indicate times corresponding to the episodes shown in A1-A4.

C-2. Dependence of late-E abdominal bursting on RTN/pFRG

Abdala et al., 2009 showed that pharmacological suppression of the RTN/pFRG region by local microinjection of isoguvacine, a $GABA_A$ receptor agonist, abolished reversibly the hypercapnia-evoked late-E bursting in the AbN. Figure III-2 shows a time series of the oscillation periods of PN and AbN constructed for a representative preparation from the original data set for three sequential activity epochs. During the first epoch, 10% CO_2 was applied to the perfusate, which evoked a quantal distribution of late-E AbN discharge (Figure III-2A1, black circles). As shown in the second epoch (Figure III-2A2), bilateral microinjections of isoguvacine made in the RTN/pFRG caused transient apnea followed by recovery of PN discharge to the baseline frequency and subsequently blocked late-E AbN bursting during systemic application of 10% CO_2 in the perfusate (no black circles). The third epoch (Figure III-2A3) shows recovery of hypercapnia-induced AbN discharge after isoguvacine washout. Based on these experimental data and in agreement with the previous suggestions of others (see [20], [42]) we hypothesized in our model that the source of hypercapnia-evoked late-E oscillations in AbN is located within RTN/pFRG and that AbN oscillation may be considered as an indicator of the corresponding RTN/pFRG oscillations.

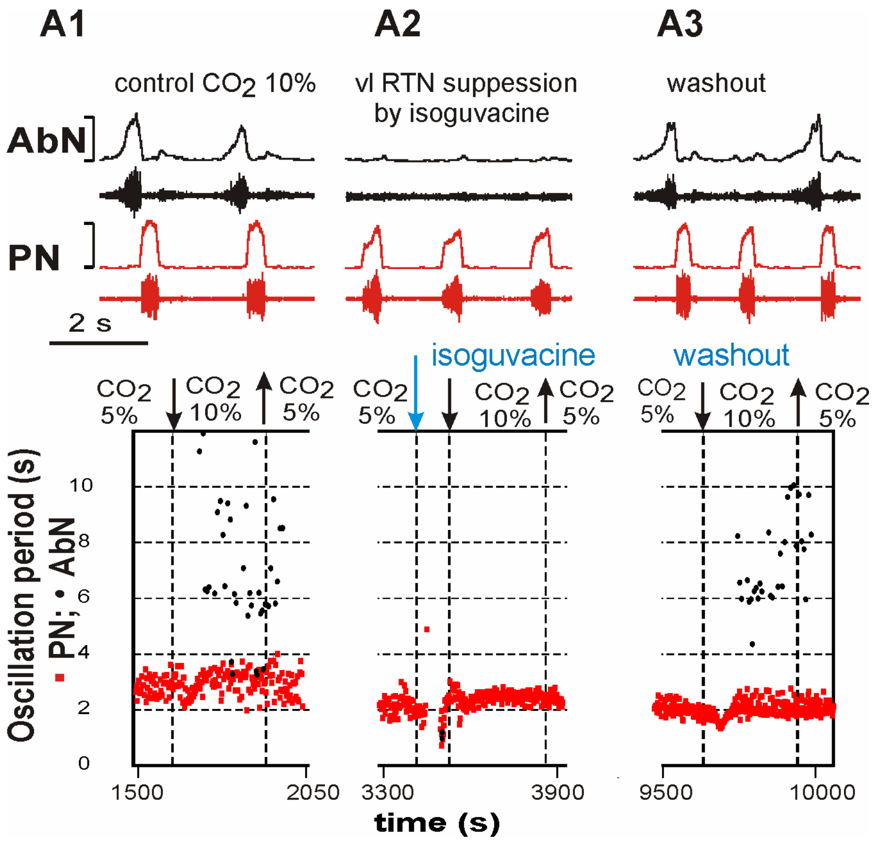

Figure III-2. The effect of RTN/pFRG suppression on hypercapnia-evoked late-E activity in AbN. The vl RTN/pFRG region was inactivated by local bilateral microinjection of isoguvacine, a $GABA_A$ receptor agonist. (A1), (A2), and (A3) columns represent three epochs from the same experiment. In each column, the top diagram shows the raw recording and integrated activity of PN (bottom traces, red) and AbN (upper traces, black), and the bottom diagram shows the changes in the oscillation periods in the PN and AbN nerves with time. In column A1, hypercapnia (10% CO_2) evoked quantally dispersed late-E bursts in AbN (see nerve recordings at the top and black circles in the bottom diagram). Note that the time interval was not sufficient to allow development of 1:1 ratio of AbN:PN frequencies. In A2 column, injection of isoguacine fully blocked late-E AbN bursting that would be expected at 10% CO_2 (no black circles). In column A3, hypercapnia (10% CO_2) again evoked late-E discharges in AbN discharge after isoguvacine washout.

C-3. Correlated CO_2-evoked late-E neuron bursting in RTN/pFRG and AbN bursting

Our previous extracellular recordings of single neuron activity in RTN/pFRG indicate that the ventrolateral (vl) part of RTN/pFRG contains a population of CO_2-sensitive neurons that exhibit bursting synchronized with the AbN late-E activity during hypercapnia.

Moreover, at 7% CO_2 such neuronal bursts are skipped whenever AbN late-E bursts are skipped, reflecting their relationships (Figure III-3A,B). Analysis of the bursting behavior of a set of neurons recorded previously shows that the CO_2-evoked RTN/pFRG neuronal and AbN late-E bursting are highly correlated during hypercapnia. The average probability of simultaneous AbN and RTN/pFRG neuron activity from a group of these neurons (n = 5) was 0.92, computed from an average recording epoch of 280 s duration (average number of 141 bursts analyzed per epoch). Accordingly, we have included in the model a CO_2-sensitive, rhythmically bursting population of neurons in the RTN/pFRG that is postulated to represent a source of late-E AbN bursting.

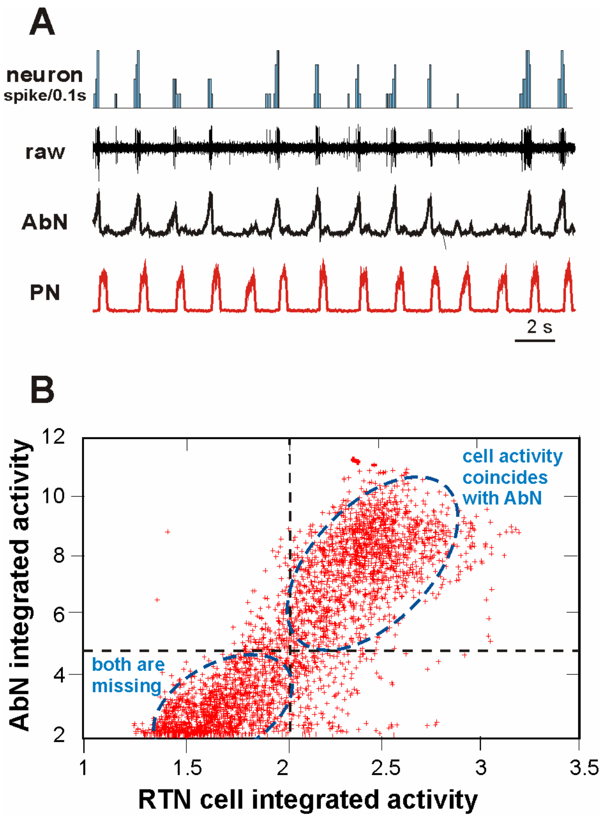

Figure III-3. An example of extracellular recording of a single neuron within vl part of RTN/pFRG during hypercapnia (7% CO_2) whose activity correlated with the AbN late-E bursts. (A) The two bottom traces show integrated activities of PN (red) and AbN (black);

the second trace shows raw activity of the RTN/pFRG neuron, and the top trace shows the corresponding spike-frequency histogram of this neuron activity (bin = 0.1 s). Note that the neuronal bursts were skipped whenever AbN bursts were skipped, reflecting their synchrony. (B) Interdependence between the RTN neuron discharges (shown in A) and AbN late-E bursts. Integrated activities of AbN and RTN neuron are calculated during a 300s epoch with sampling frequency of 100Hz (30000 points in total) and plotted against each other (red crosses). Dashed lines representing thresholds split the space into four quadrants. The top right quadrant represents cases where both cell activity and AbN late-E bursts were present (indicated by blue dashed ellipse); the bottom left quadrant represents cases where both cell and AbN late-E discharges were missing (indicated by another blue dashed ellipse) and only background activity is represented.

C-4. Dependence of late-E AbN bursting on persistent sodium current (I_{NaP})

Recent modeling studies [41], [174] have suggested an intrinsic, cellular, I_{NaP}-dependent mechanism for RTN/pFRG bursting. This previous suggestion is consistent with recent observations in the embryonic parafacial neuronal population (e-pF) that the I_{NaP} blocker, riluzole abolishes rhythmic e-pF neuron activity [175], [176]. Our new experiments (n = 5), illustrated in Figure III-4A3 and Figure III-4B (right part of the plot), show that riluzole (5 μM in the experiment shown) abolished the AbN late-E activity evoked by hypercapnia (10% CO_2) in the juvenile rat *in situ*. It is important to note that the administration of riluzole in these experiments (5-10 μM) suppressed the AbN late-E activity but did not abolish rhythmic respiratory activity although the amplitudes of all motor discharges were reduced (Figure III-4A3) as noted previously [16]. This is fully consistent with our previous *in vivo* and *in situ* studies [16], [19] showing that respiratory rhythm generation in the intact brainstem under normal conditions is not critically dependent on I_{NaP}.

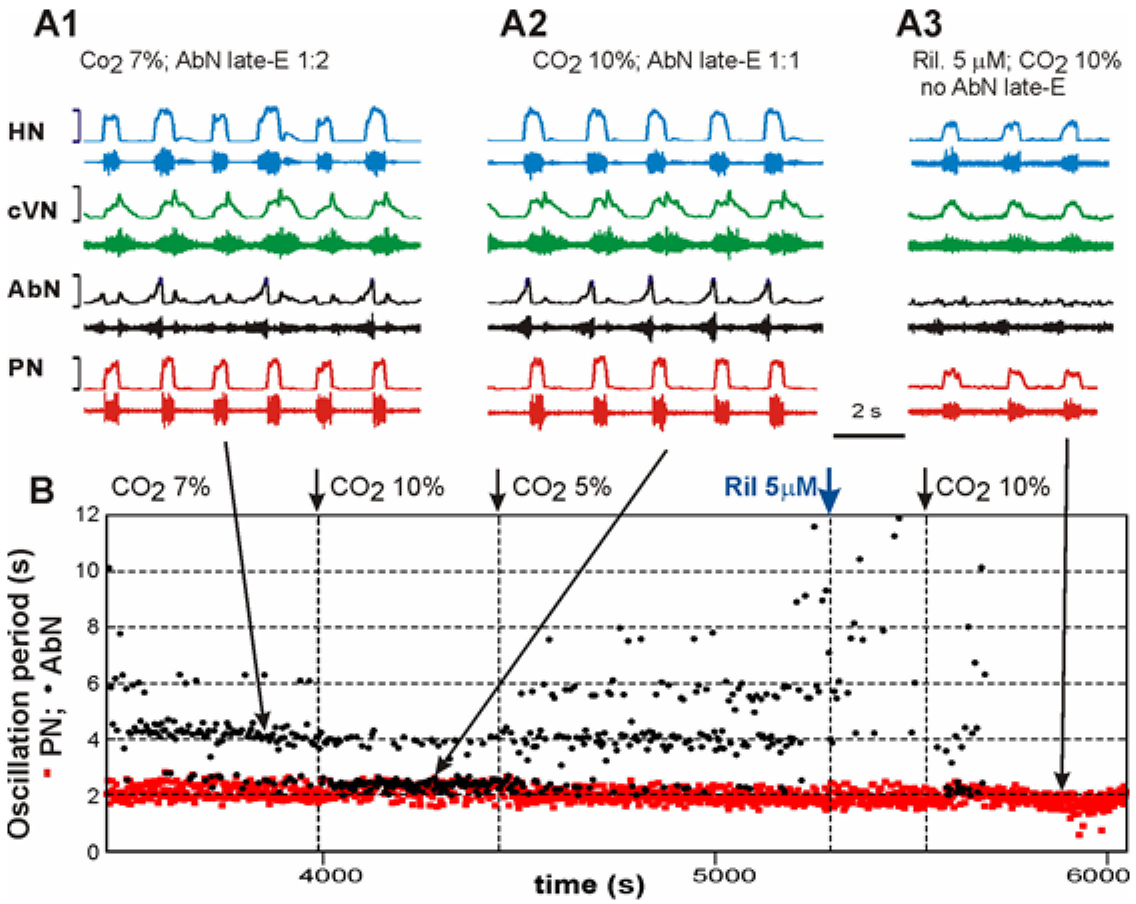

Figure III-4. Effects of hypercapnia and riluzole on the hypercapnia-induced AbN late-E activity. (A1-A3) Simultaneously recoded activity of (bottom-up) PN (red), AbN (black), cVN (green), and HN (blue). (B) Representation of the entire experimental epoch by plotting the oscillation periods in PN (red squares) and AbN (black circles) vs. time. A1-A2 and the corresponding parts of the diagram in B (indicated by large arrows) show quantal acceleration of the AbN late-E activity with the development of hypercapnia from 7% CO_2 (see in left part of B and A1 showing a 1:2 ratio between AbN and PN frequencies) to 10% CO_2 (see in B after first small arrow indicating changing CO_2 to 10% and in A2 where the ratio of frequencies is 1:1). The level of CO_2 then was returned back to 5% (see second small arrow in B) and the frequency of AbN started quantally reducing. Then riluzole (5 µM), the persistent sodium current blocker, was added to the pefusate (indicated in B by blue arrow). The right arrow in B indicates the moment when CO_2 was increased to 10% in the presence of riluzole. A3 and the right part of B show that riluzole abolished the hypercapnia-evoked AbN late-E activity while only reducing the amplitude (and frequency) of discharges in other nerves (seen in A4).

C-5. Late-E activity and temporal relationships between PN and HN discharges

The onset of the PN inspiratory bursts under normal conditions is usually delayed (by ~100 ms) relative to the HN bursts [16], [19], [177]–[179]. Interestingly, this delay has been shown to increase during hypercapnia [178]. In Figure III-5, we show temporal relationships between the onsets of HN and PN bursts during intermittent AbN bursting, extending our original analysis to illustrate in more detail the distributions of delays between HN and PN burst onsets for cases when ABN bursts are present and when they are missed from a representative preparation. The most striking result is that the presence of late-E bursts in the AbN coincides with an increase in the delay between the onsets of HN and the PN bursts (see Figure III-5A,B) to approximately 500 ms (Figure III-5B). This suggests that AbN late-E discharge is associated with an enhancement and early onset of HN bursts accompanied by a delay and shortening of PN bursts (see also [41]). In our modeling we incorporate RTN/pFRG interactions with the CPG circuitry that can reproduce these temporal features of the motor outputs.

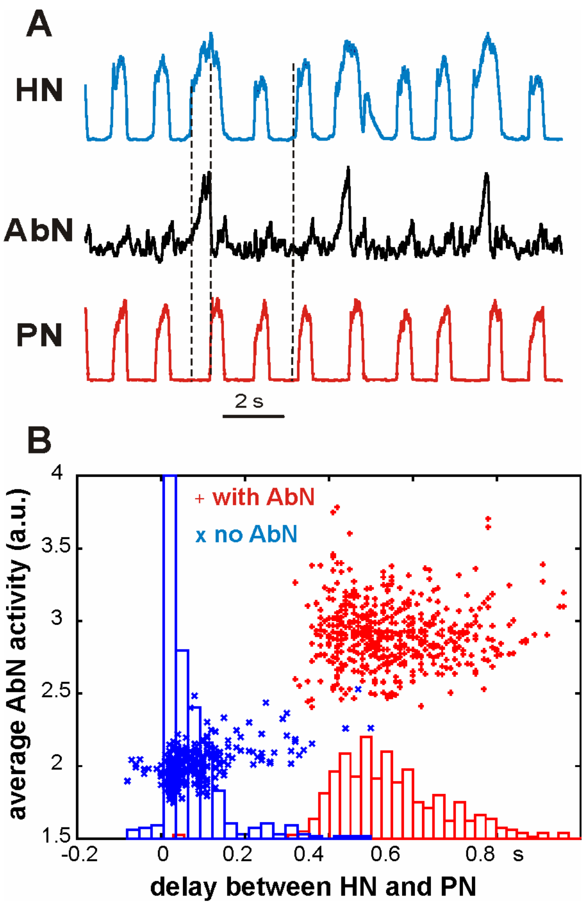

Figure III-5. Effect of late-E activity on the temporal relationships between PN and HN bursts. (A) Integrated activities of phrenic (PN, lower trace, red), abdominal (AbN, middle trace, black), and hypoglossal (HN, upper trace, blue) nerves during hypercapnic (7% CO_2) regime corresponding to a 1:3 ratio between AbN and PN frequencies. The delay between onsets of PN and HN bursts is substantially longer when late-E bursts are present in AbN than when they are missing (shown by dashed vertical lines). The earlier onset of HN discharges coincides with AbN late-E bursts and the delayed onset of PN bursts coincides with the termination AbN late-E discharges. (B) The delays between onsets of HN and PN bursts are indicated by small red pluses in the presence of AbN activity and by small blue crosses in the absence of AbN bursts. The corresponding histograms show the distributions of delays between HN and PN onsets for the two cases, when ABN bursts are present (red) and when they are missed (blue).

C-6. Patterns of AbN discharge: late-E vs. biphasic-E

In contrast to late-E AbN bursting, biphasic-E activity, consisting of pre-I (late-E) and post-I bursts has been recorded from the abdominal motor output in decerebrate neonatal rats [42], [43]. This activity pattern is similar to that of single neurons recorded from the RTN/pFRG region of the *in vitro* isolated brainstem-spinal cord preparation of neonatal rats that show a biphasic-E pattern consisting of a short pre-I discharge and a post-inspiratory (rebound) component [37], [38], [171], [174], [180]. The issue of whether the biphasic-E pattern (in both RTN/pFRG and AbN) is a specific characteristic of neonates which transforms to late-E during development or is a characteristic of the specific metabolic conditions of the *in vitro* preparation (e.g., hypercapnic hypoxia or anoxia) remains unresolved [87], [174], [181], [182]. In the *in situ* preparations AbN biphasic-E activity was more readily evoked in neonates than in juvenile animals [87]. We have found that in more mature animals transient biphasic-E discharges can be evoked under specific conditions, including hypercapnic anoxia (7% CO_2, 93% N_2) or recovery from anoxia-induced central apnea. In the analysis shown in Figure III-6, we illustrate the consistent finding that transformation of the AbN late-E bursting to a biphasic-E bursting pattern during hypercapnic anoxia is accompanied by a corresponding reduction/suppression of post-I activity recorded in the cVN. Thus lack of post-I activity appears essential for the expression of the post-I component of the biphasic-E AbN discharge pattern.

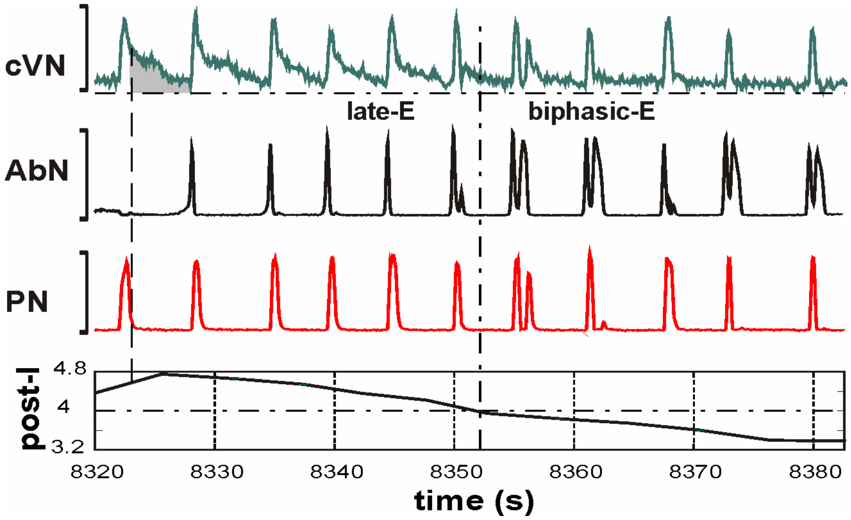

Figure III-6. Transformation of the pattern of AbN activity from late-E (pre-I) bursting to biphasic-E discharge during hypercapnic anoxia (7% CO_2, 93% N_2). The top tree traces show integrated activity of cVN, AbN and PN. The bottom trace represents the index of post-I activity calculated as an averaged activity in cVN during the expiratory phase in each cycle (shown as the gray area in the cVN trace); the expiratory phase was defined by the PN trace (vertical dashed line indicates the onset of expiration). In the first half of the recorded episode, only late-E bursts were present in AbN. The post-I component of cVN was progressively reducing. The transition of AbN bursts to a biphasic-E discharge pattern (with pre-I and post-I components) occurred after a significant suppression of the cVN post-I activity (indicated by vertical and horizontal dash-dotted lines).

C-7. Construction of the extended model and validation

The experimental findings described above provide the necessary prerequisites for extending our large-scale computational model of the brain stem respiratory network [16]. This model describes interactions between the respiratory neuron populations spatially organized within brain stem compartments (Figure III-7A). The brain stem populations include (right-to-left): bulbospinal premotor expiratory (bulbospinal E or bs-E) population of the caudal ventral respiratory group (cVRG); ramp-inspiratory (ramp-I) population of premotor bulbospinal inspiratory neurons and inhibitory early-inspiratory (early-I(2)) population located in the rostral ventral respiratory group (rVRG); pre-inspiratory/inspiratory (pre-I/I) and inhibitory early-inspiratory (early-I(1)) populations of the pre-BötC; inhibitory augmenting-expiratory (aug-E) and post-inspiratory (post-I) populations and excitatory pre-motor post-I(e) populations in the BötC; late-E population representing pFRG and located in RTN/pFRG. The latter population along with the bs-E population represents an extension (and the only difference) in the current model structure (Figure III-7A) relative to the model described in [16]. The BötC and pre-BötC populations represent together the core circuitry of the respiratory CPG. In addition, multiple drives from other brain stem components, including the pons, RTN/pFRG and raphé nuclei, provide inputs that regulate the dynamic behavior of this core circuitry, as well as activity of premotor neuron populations in the rVRG and cVRG and motor outputs.

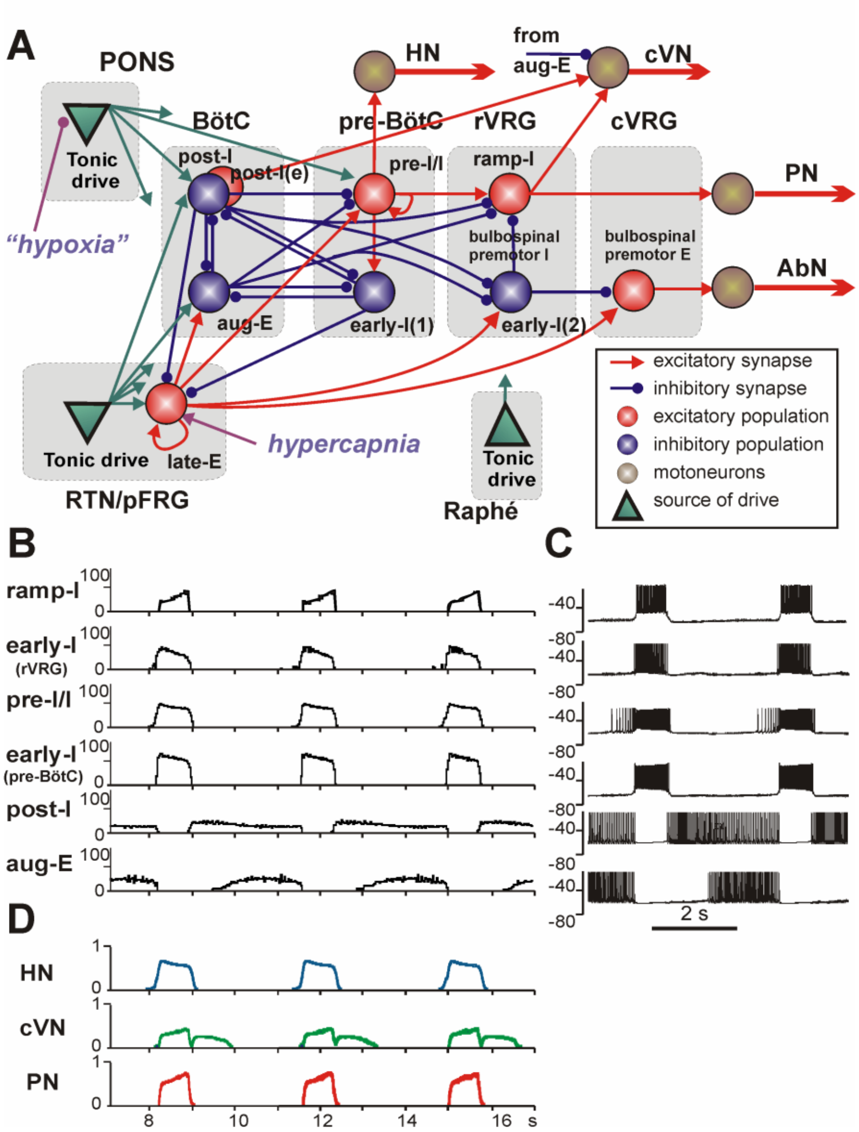

Figure III-7. The extended model of the brain stem respiratory network. (A) Schematic of the extended model showing interactions between different populations of respiratory neurons within major brain stem compartments involved in the control of breathing (pons, RTN/pFRG, BötC, pre-BötC, rVRG, and cVRG). Each population (shown as a sphere) consists of 50 neurons described in the Hodgkin-Huxley style. In comparison with the previous model (Smith et al. 2007), this model additionally incorporates the population of bulbospinal premotor expiratory (E) neurons in cVRG, representing the source of AbN activity, and the late-E population in the RTN/pFRG compartment (see text for details), serving as a source of RTN/pFRG oscillations. The model includes three sources of tonic drives: pons, RTN, and raphé (not all connections from these drive sources are shown). Justification for all interconnections used in the basic models can be found (with the corresponding references) in our previous papers [16], [19], [35]. Justification of interconnections involving the late-E population is in the text. The late-E population receives an additional external drive simulating the effect of hypercapnia; the pontine drive is considered to be hypoxia/anoxia dependent and was reduced in simulation of hypoxic conditions. (B) Model performance under normal conditions. The activity of major neural populations in the model are represented by average histograms of activity of all neurons in each population; bin=30 ms). The late-E population and the AbN output under normal conditions are silent. (C) Traces of membrane potentials of single neurons (randomly selected from each population). (D) The dynamics of the model's motor outputs: HN (blue trace); cVN (green trace) and PN (red trace).

The bulbospinal-E population of cVRG was included in the model to generate the expiratory motor output. The neurons of this population were identical to these in the ramp-I population and contained only a minimal set of ionic currents necessary for spiking activity. The late-E population of RTN/pFRG was identical to the pre-I/I-population and consisted of neurons containing I_{NaP} and having mutual excitatory interactions within the population. This was based on the hypothesis that AbN late-E bursting activity originates in the RTN/pFRG and that its generation is critically dependent on I_{NaP}, as suggested by our experimental observations.

Previous theoretical studies have demonstrated that such a population with an I_{NaP}-dependent busting mechanism can operate in the population-bursting mode (at lower excitability or drive) and in the regime of asynchronous sustained activity (when the excitability exceeds a certain threshold) [125], [136], [156]. Importantly, although the pre-I/I and late-E populations were identical in the model, their behavior was different because of the different excitability of these populations. Specifically, under normal conditions, the pre-I/I population received a strong total excitatory drive that kept this population in the state of sustained activity independent of I_{NaP} until phasic external inhibition terminated its activity (see [16], [19], [136], [156]). In contrast, a relatively weak "hypercapnic" drive could evoke I_{NaP}-dependent bursting in the late-E population.

The following connections between the late-E population and other neural populations were incorporated in the model (Figure III-7A):

(1) Excitatory connection from the late-E to the excitatory pre-I/I population of pre-BötC, allowing entrainment of the pre-BötC oscillations by the late-E oscillations;

(2) Inhibitory connection from the inhibitory inspiratory population (early-I(1) of pre-BötC) to the late-E to provide inhibition of late-E neurons during inspiration (Fig 7A). These two connections have been suggested in many previous experimental and modeling studies [20], [37]–[39], [42], [43], [87], [171], [174], [180], [181], [183];

(3) Excitatory connection from the late-E to the AbN motor output (see Figure III-7A), which was based on the previous suggestions [20], [42], [43] and our results with local inhibition suggesting that late-E AbN activity originates in the RTN/pFRG;

(4) Excitatory connections from the late-E to the inhibitory populations aug-E (of BötC) and early-I(2) (of rVRG), which both inhibit the premotor ramp-I population (see Figure III-7A). These connections were hypothesized to produce an additional delay in the onset of PN discharge by the preceding late-E burst shown in our analysis (Figure III-5);

(5) Inhibitory connection from the post-I population of BötC to the late-E population. This connection was necessary to reproduce the experimental observations described in Chapter III: C-1. The existence of this connection represents one of the key hypotheses of this study.

The performance of the model under simulated normal metabolic conditions (i.e. when the late-E population in the RTN/pFRG is not active) is shown in Figure III-7B-D. Panel B shows the integrated activities of key respiratory populations, panel C exhibits the traces of membrane potential of the corresponding single respiratory neurons (randomly selected from each population), and panel D shows the dynamics of motor outputs (PN, cVN, and HN). The model generates the three-phase eupneic-like respiratory pattern similar to that observed in the *in situ* preparations under normal conditions. In this state the respiratory oscillations emerge from the core circuitry due to dynamic interactions between (i) the excitatory neural population in pre-BötC active during inspiration (pre-I/I), (ii) the inhibitory population in pre-BötC that provides inspiratory inhibition within the network (early-I(1) of pre-BötC); and (iii) inhibitory populations in the BötC generating expiratory inhibition (post-I and aug-E).

The performance of the model under specific metabolic conditions when the late-E population is active is described below. Our simulations focused on the three following behaviors: (a) emergence and quantal acceleration of abdominal late-E activity during hypercapnia; (b) transformation of the late-E bursts to a biphasic-E activity during hypercapnic hypoxia or anoxia, and (c) quantal slowing of BötC/pre-BötC and PN oscillations with the progressive suppression of the BötC excitability.

C-8. Emergence and quantal acceleration of late-E abdominal activity during hypercapnia

In our model, the late-E population in RTN/pFRG is considered a population of central chemoreceptors, whose excitability is most sensitive to hypercapnia (an increase in the level of CO_2 in the brain stem). The behavior of the model during hypercapnia is shown in Figure III-8. The progressive hypercapnia was simulated as a linear increase of a “hypercapnic” excitatory drive to the late-E population (see Figure III-7A and Figures III-8A1-A3,B). The behavior of late-E neurons depends on: (a) their intrinsic properties, namely on the voltage-dependent dynamics of I_{NaP} activation and slow inactivation, (b) the phasic inhibition that these neurons receive from the post-I population of BötC during expiration and from the early-I(1) population of pre-BötC during inspiration, and (c) the hypercapnic excitatory drive. As a result, the late-E population begins generating bursts when hypercapnic drive exceeds some threshold (see Figure III-8B), which is mostly defined by the post-I inhibition. This post-I inhibition (being reduced during expiration) allows the late-E bursts to appear only close to end of expiration. The post-I inhibition of late-E together with late-E excitation of pre-BötC pre-I/I neurons provide coupling of RTN/pFRG (late-E) and BötC/pre-BötC oscillations.

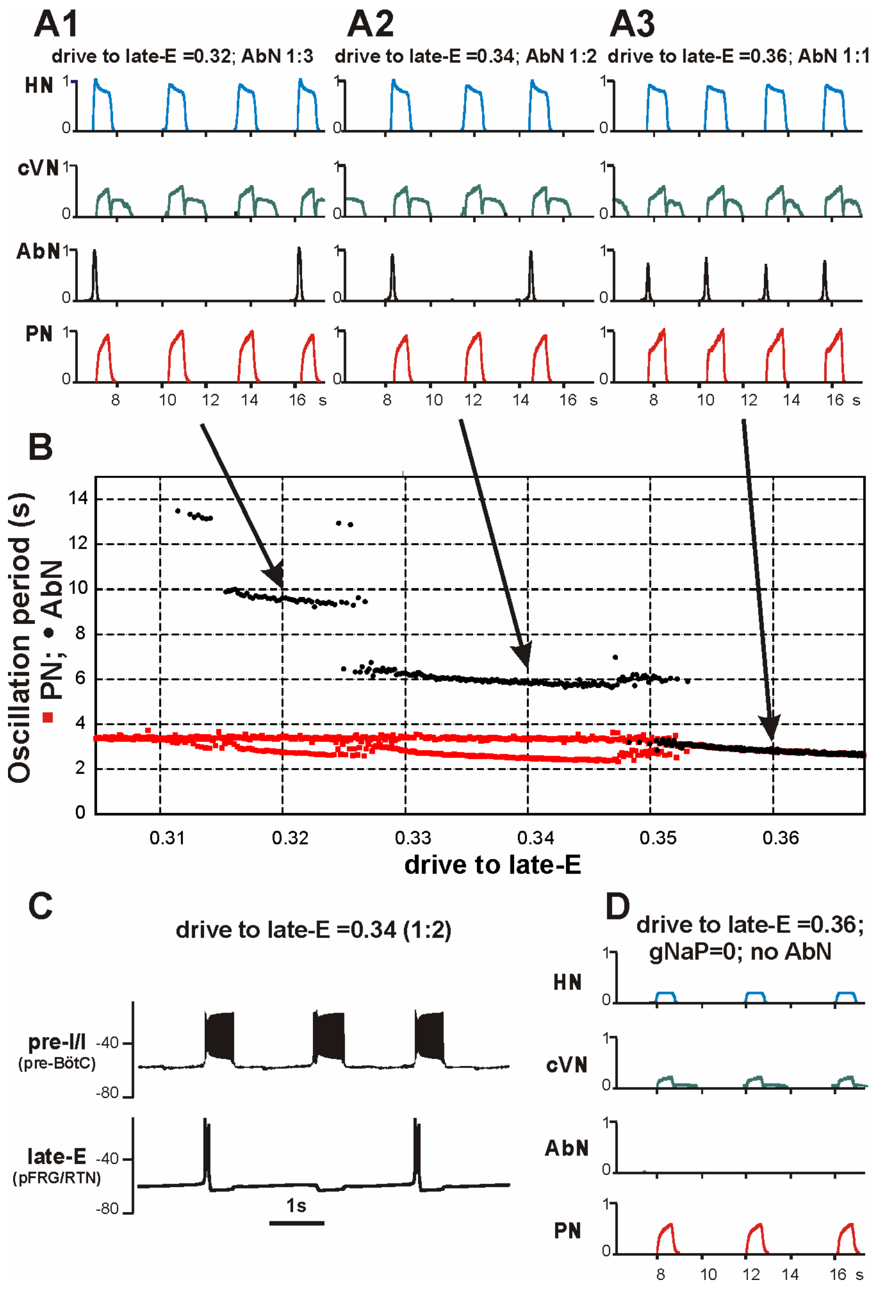

Figure III-8. Modeling the effects of progressive hypercapnia and I_{NaP} blockade. (A1-A3) The activity of motor outputs in the model during simulated hypercapnia. The late-E bursts in the AbN were always phase-locked with PN bursts and the ratio between AbN and PN frequencies quantally increased through 1:3 (A1) to 1:2 (A2) and to 1:1 (A3) as “hypercapnic” drive to the late-E population of pFRG/RTN gradually increased to simulate progressive hypercapnia. (B) The dependence of oscillation periods in AbN (black circles) and PN (red squares) on the hypercapnic drive (horizontal axis). This simulation shows a quantal acceleration of AbN activity during a gradual increase in the simulated hypercapnic drive. The ratio between AbN and PN frequencies sequentially jumped from 1:4 to 1:3 (as in A1), then to 1:2 (as in A2), and finally to 1:1 (as in A3). See Fig. 1 for comparison. With quantal acceleration of AbN activity (after it emerges at 0.31 and before it reaches 1:1 ratio at 0.35) PN periods alternate between two red branches depending on the presence or absence of an AbN burst during corresponding breathing cycle. (C) Membrane potential traces of single neurons from the pre-I/I population of pre-BötC (bottom trace) and the late-E population of RTN/pFRG (upper trace) corresponding to the regime of 1:2 coupling between AbN and PN bursts (A2). (D) Simulation of the effect of I_{NaP} blockade. Model output motor activities shown correspond to the regime of 1:1 coupling shown in A3. The blockade of I_{NaP} was simulated by setting its maximal conductance to zero in all neurons of the model. This led to a full suppression of AbN activity and a reduction in amplitude and frequency of other simulated motor outputs (compare with Figure III-4A3).

Similar to the experimental results with progressive hypercapnia (Figure III-1 and Figure III-4, and also [173], the progressive increase of hypercapnic drive in the model evokes quantal acceleration, i.e. step-wise increase in AbN burst frequency with a ratio to PN burst frequency sequentially jumping from 1:4 to 1:3, then to 1:2 and, finally, to 1:1 (see Figure III-8A1-A3, B and compare with Figure III-1A2-A4,B). Figure III-8C shows the activity of a single pre-I/I neuron of pre-BötC and a single late-E neuron of RTN/pFRG when the ratio of late-E:pre-I/I discharge frequencies is equal to 1:2. A more detailed analysis of quantal acceleration behavior using dynamical systems theory methods applied to a simplified mathematical model can be found in the following chapter.

Figure III-8D shows the result of modeling of the effect of riluzole, the I_{NaP} blocker, on the system behavior during hypercapnia. The effect of riluzole was simulated by reducing the I_{NaP} maximal conductance to zero in all neurons of the network (late-E and pre-I/I). Similar to our experimental finding (Figure III-5), the suppression of I_{NaP} during hypercapnia (1:1 coupling regime) fully silenced the late-E AbN (and RTN/pFRG late-E neuron) activity but did not abolish BötC/pre-BötC and PN oscillations. This reflects the differences in tonic drive and hence level of excitation of the late-E vs. the pre-I/I neuron populations as described earlier.

Our simulations also show that the late-E bursts when present delay the onset of PN activity and increase the delay between the onsets of HN and PN bursts (Figure III-9). This delay in the model results from (a) an advance activation of pre-I/I population (projecting to the HN output) by the late-E burst and (b) an additional inhibition of the ramp-I population (projecting to the PN output) by the early-I(2) and aug-E populations excited by the late-E (see Figure III-7). These simulation results are fully consistent with the experimental data described above (Figure III-5) and previously by [87].

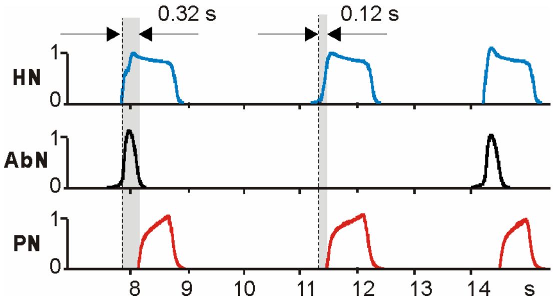

Figure III-9. The effect of late-E activity on the delay between onsets of HN and PN bursts in the model. Three motor outputs of the model are shown (HN, blue; AbN, black, and PN, red) during the hypercapnic regime corresponding to 1:2 ratio between AbN and PN frequencies. The late-E bursts when present increased the delay between onsets of the corresponding HN and PN bursts (indicated by gray bars).

C-9. Transformation of the late-E to a biphasic-E activity

As shown in Figure III-6, transformation of AbN late-E bursts to a biphasic-E activity is accompanied by a reduction of the post-I activity. Such a reduction of the post-I activity has been also observed during strong hypoxia or anoxia. As shown previously, the expression of post-I activity strongly depends on pontine input [18], [184]. Based on these observations, we suggest that metabolic conditions similar to hypercapnic anoxia can be simulated with our model by applying the “hypercapnic” drive to the late-E population and progressive reduction of the pontine drive to the network (see Figure III-7A).

The results of these simulations are shown in Figure III-10A. In the simulation shown, the value of drive to the late-E population was initially set to produce 1:1 coupling between late-E and PN activities. Then the pontine drive was progressively reduced from the initial value to zero (bottom trace in Figure III-10A). As seen in Figure III-10A, reducing the pontine drive produced significant changes in network dynamics. Specifically the post-I component in the cVN output was progressively reduced and the pattern of AbN activity changed from the late-E to a biphasic-E pattern, consisting of a short late-E (pre-I) burst and a stronger post-inhibitory rebound. The results of this simulation qualitatively reproduce the experimental results shown in Figure III-6. Interestingly, the transformation from the late-E to a biphasic-E pattern in our simulation went through an intermediate stage in which the PN (and late-E population) activity exhibited only post-I activity without the late-E (pre-I) burst. Figure III-10B-D shows the activity of a single pre-I/I neuron of pre-BötC and a single late-E neuron of RTN/pFRG for all three regimes described. A more detailed analysis of the above late-E pattern transformation can be in Chapter IV.

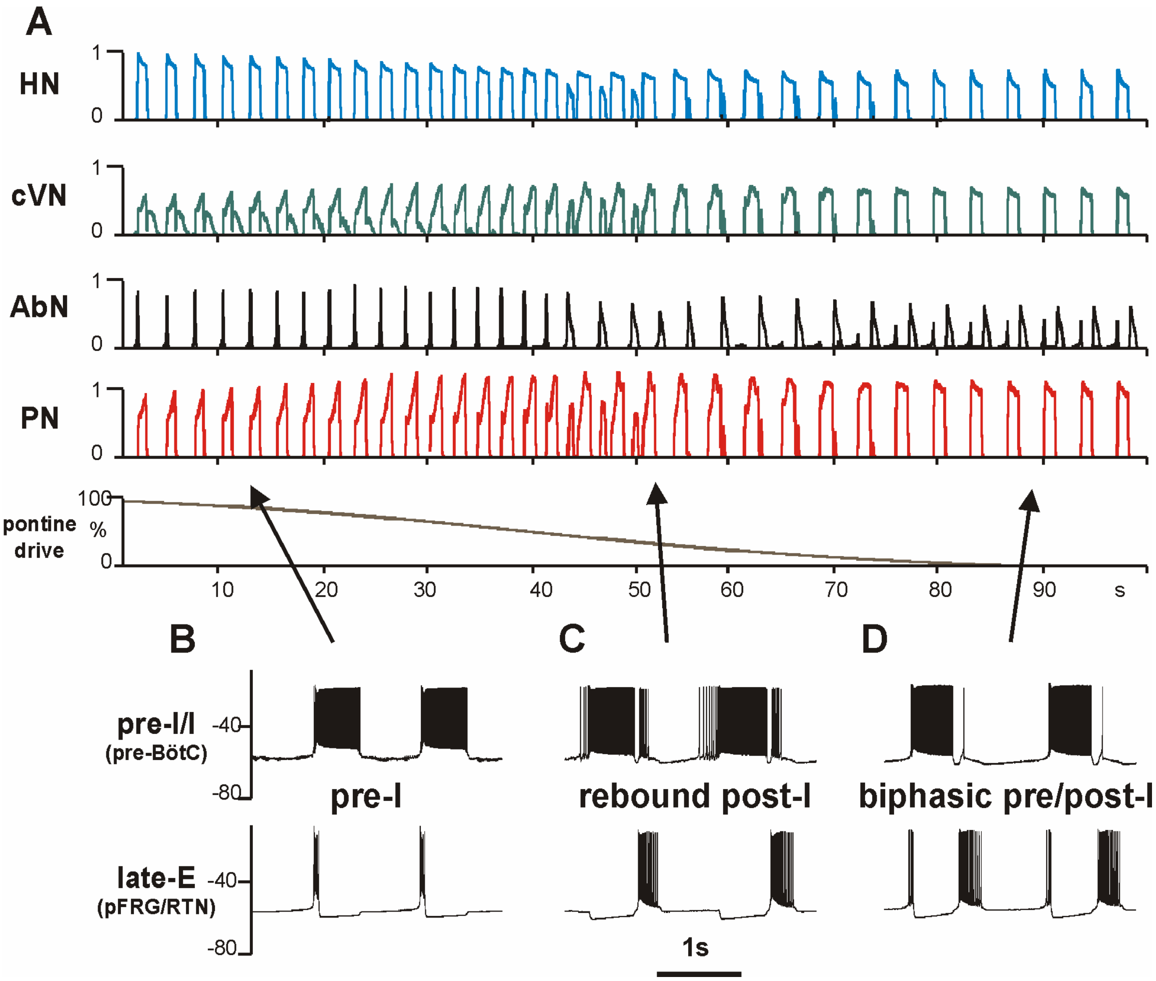

Figure III-10. Transformation of the late-E to a biphasic-E activity with the development of simulated hypoxia. (A) In this simulation, the value of drive to the late-E population was set to 0.36 to produce 1:1 coupling between the late-E and PN activities (see Figure III-8A3). A gradual reduction of pontine drive (bottom trace) was used to produce a progressive reduction of post-I activity during development of hypoxia/anoxia (see cVN trace). During this reduction of pontine drive, the AbN pattern sequentially transformed from late-E (pre-I) bursting (see 0-40 s), to a rebound post-I type bursting pattern (40-70 s), and then to a biphasic-E pattern (with pre-I and post-I components (70-100 s). (B-D) Membrane potential traces of single neurons from the pre-I/I population of pre-BötC (bottom traces) and the late-E population of RTN/pFRG (upper traces) corresponding to the AbN late-E (pre-I) pattern (B), post-I pattern (C) and the biphasic-E pattern (D), indicated by arrows.

C-10. Quantal slowing of the BötC/pre-BötC and PN activities

The quantal slowing of the pre-BötC and/or PN oscillations has been previously demonstrated with administration of opioid agonists in the *in vitro* isolated brainstem-spinal cord preparation and *in vivo* [42], [43], [172]. Previous attempts to simulate this effect were made by several groups [87], [174], [183].

This quantal slowing consists of a step-wise reduction in the frequency of pre-BötC (and/or PN) oscillations resulting from deletion (missing) of a single or a series of inspiratory bursts in the output activity recorded. Although the exact pharmacological effect of opioids is unknown, the general assumption has been that opioids reduce the excitability of pre-BötC neurons either directly or indirectly (via the suppression of excitatory synaptic transmission within the pre-BötC).

To simulate quantal slowing with our model, we first set the hypercapnic drive to the late-E population to produce 1:1 coupling between AbN late-E and PN bursts and then reduced the pontine drive to zero. As a result, both the late-E population and the AbN output in the model exhibited the biphasic-E activity profile with 1:1 coupling to the inspiratory bursts in the pre-BötC and PN (see Figure III-11A,B, left parts in both panels).

To produce quantal slowing, the excitatory synaptic conductances within the pre-BötC (in both pre-I and early-I(1) populations) were scaled by a linearly decreasing control function (see Figure III-11A, bottom trace). With the gradual decrease of these conductances, the simulated period of BötC/pre-BötC (and PN) oscillations increased in a step-wise manner (see Figure III-11B) until these oscillations completely stopped. The frequency of PN (and BötC) oscillations correspondingly decreased, so that the ratio between late-E and PN oscillation frequencies sequentially jumped from 1:1 to 2:1, and then to 4:1, until the full termination of PN bursting.

It is important to note that rhythmic activity in the late-E population of RTN/pFRG and in AbN persisted, but the profile of their bursts changed from biphasic-E to a monophasic burst whenever the PN burst was missing (Figure III-11A). This is also seen in the activities of single pre-I/I and late-E neurons shown in Figure III-11C. These modeling results are consistent with the previously published experimental data [42], [43], [172].

A more detailed analysis of quantal slowing behavior by dynamical systems theory methods applied to a simplified mathematical model can be found in Chapter IV.

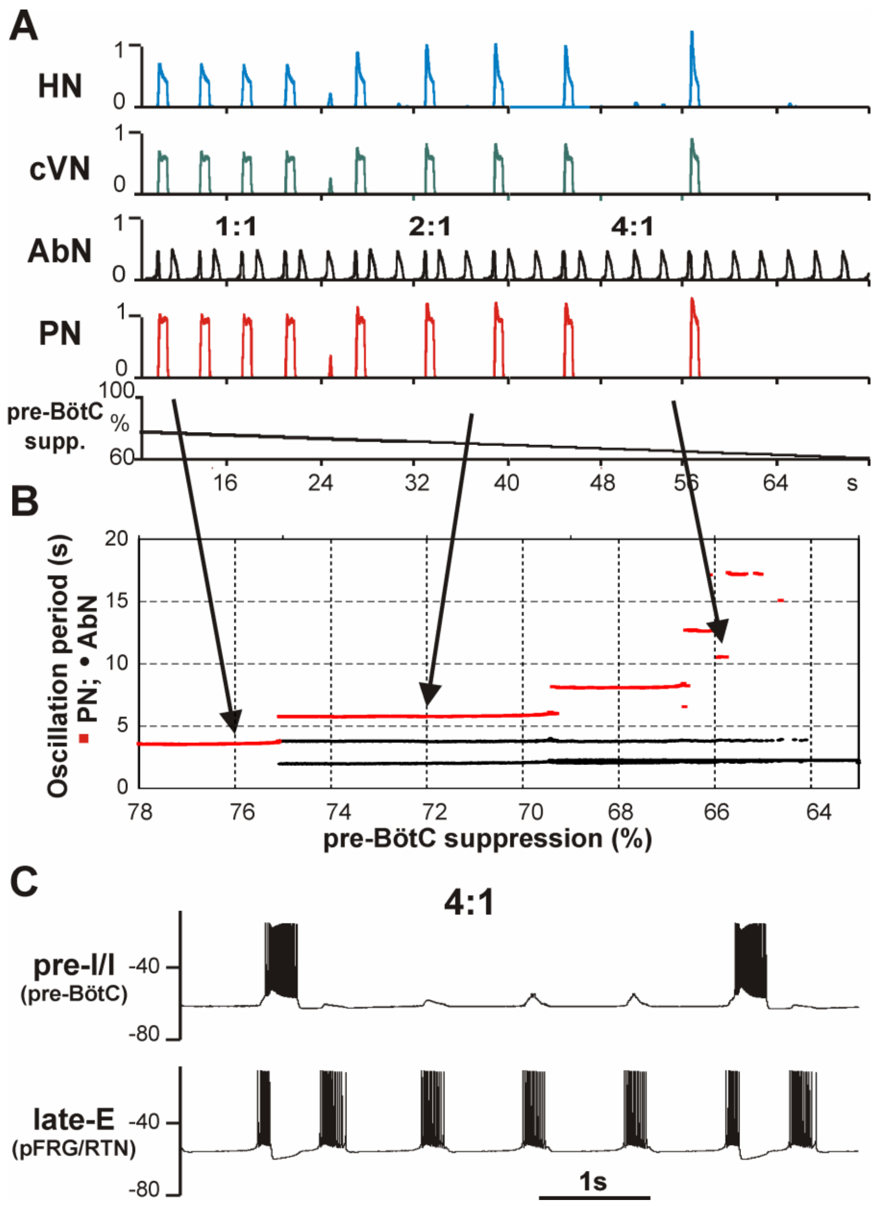

Figure III-11. Simulation of quantal slowing of PN activity**.** (A) To simulate quantal slowing of PN activity we first set the value of drive to late-E to 0.36 and the value of pontine drive to zero. This regime corresponded to the end of the simulation shown in Fig. 10 with a biphasic-E pattern of AbN activity. Then the excitability of the pre-BötC neurons (in both the pre-I/I and early-I(1) populations) was linearly decreased by a proportional reduction of all weights of excitatory synapses to pre-I/I and early-I(1) neurons (“pre-BötC suppression”, see lower trace., starting with 78% of the basic value and reducing this to zero). During progressive reduction of pre-BötC neuronal excitability, the frequency of PN (and HN and cVN) bursts was quantally reduced with the ratio to AbN frequency jumping from 1:1 to 1:2 and so on (see red steps in B), until the activity of all nerves except AbN was abolished. (B) This diagram demonstrates a step-wise dependence of AbN (black circles) and PN (red squares) periods on the pre-BötC’s synaptic depression. After the first step in PN period (around 75% of normal synaptic weights), two different periods of AbN activity were observed. The longer periods correspond to AbN cycles accompanied by PN bursts and the shorter periods correspond to AbN oscillations with PN silent. (C) Membrane potential traces of single neurons from the pre-I/I population of pre-BötC (bottom traces) and the late-E population of RTN/pFRG (upper traces), corresponding to the regime 4:1. Note that the profile of AbN bursts in A and late-E bursts in C changed from the biphasic-E activity to a monophasic burst whenever the PN bursts were missing.

C-11. Suppression of RTN/pFRG oscillations by inhibition and release by disinhibition

As noted above, our model suggests that during normal conditions the BötC/pre-BötC kernel inhibits RTN/pFRG oscillations. Therefore, we predict that blocking of inhibitory transmission within RTN/pFRG should evoke (release) oscillations in the RTN/pFRG and AbN at normal metabolic conditions. To investgate this possibility with the model, we kept a small (subthreshold) drive to the late-E population and set to zero the weights of inhibitory connections from BötC/pre-BötC (from both eatly-I(1) and post-I populations) to late-E population in RTN/pFRG. The result of this simulation is shown in Figure III-12A: the suppression of inhibition to the late-E population evoked bursing activity in both the RTN/pRFG late-E population (not shown) and in AbN. As soon as the inhibition was restored the AbN activity disappeared (Figure III-12A).

To verify this prediction experimentally, a small experimental series (on 2 juvenile rat *in situ* perfused preparations) was performed experimentally. In these experiments, GABAergic synaptic transmission was blocked/attenuated bilaterally within the vl RTN/pFRG by microinjection of the GABA antagonist bicuculline (10 μM) under normal metabolic conditions (5% CO_2). In both experiments, microinjection of bicuculline evoked a low-amplitude late-E activity, which then disappeared with washout. The results of one experiment are shown in Figure III-12B,C, which are qualitatively similar to our simulation (Figure III-12A). These results are consistent with the previously published data showing that RTN/pFRG oscillations can be produced by RTN/pFRG disinhibition [185].

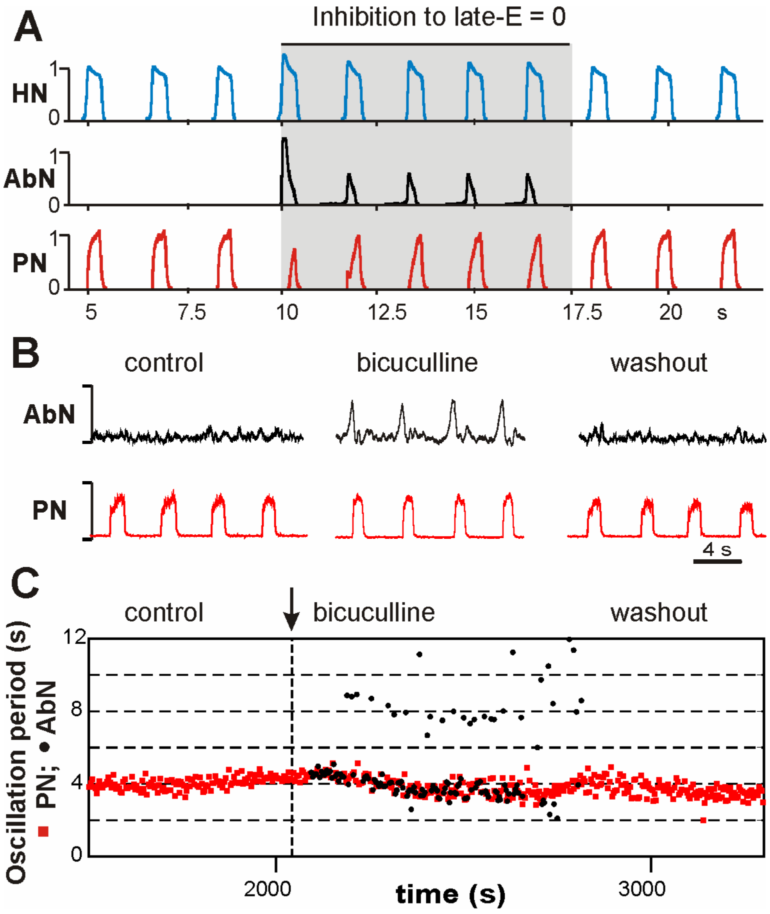

Figure III-12. Release of the AbN late-E busting under normal conditions by suppressing inhibition in RTN/pFRG. (A) Simulation results. The traces of motor outputs PN, AbN and HN generated by the model are shown. Drive to late-E was set to 0.3, below the threshold for late-E population activation (see Figure III-8B). To simulate the blockade of inhibition within RTN/pFRG, the weights of inhibitory synapses in late-E neurons were set to zero during the time interval between 10 and 17.5 s (indicated by gray area). Removing inhibition evoked late-E oscillations in both the late-E population in the RTN/pFRG (not shown) and in the model's AbN output. The bursts generated were phase-locked to PN oscillations. After inhibition returned to the previous level (at 17.5 s) AbN activity disappears. (B), (C) Experimental testing of the above modeling prediction. The experiment shown was performed at normal metabolic conditions with 5% CO_2 in the perfusate. Under control conditions there was no late-E bursting activity in AbN (see AbN activity in B, left column, and a lack of black circles in C under “control”). Bicuculline (10 μM), a blocker of $GABA_A$ inhibition, was bilaterally microinjected in vl RTN/pFRG at the moment shown in B by the vertical dashed line. As seen in B (middle column) and C (black circles), the application of bicuculline evoked rhythmic late-E activity in AbN phase-locked with PN bursts. The AbN activity evoked by disinhibition then disappeared with the drug washout (see right column in B and lack of black circles in C, right part).

D. Discussion

This study was based on and actually promotes the concept that the kernel of the respiratory CPG resides in the pre-BötC and BötC compartments within the medullary ventral respiratory column and that the respiratory rhythm is generated due to dynamic interactions between neural populations within and between these compartments [3], [5], [6], [16], [19], [31]–[36], [41], [87], [127], [186].

The other source of respiratory-related oscillations, originally found in the brainstem-spinal cord preparation of the neonatal rat [37], [38], was suggested to reside in the RTN/pFRG region and perform the function of an independent generator of pre-inspiratory/expiratory activity [20], [42], [43]**.** In the present study, we performed new analyses of experimental data and computational modeling to consider the possible conditions and mechanisms for the emergence of pFRG/RTN and abdominal late-expiratory oscillations, as well as the possible interactions between the pFRG/RTN oscillations and the respiratory CPG.

D-1. Source of late-E oscillations, conditions for their emergence, and the role of I_{NaP}

Experimental data analyzed herein have shown that the high amplitude late-E activity is not usually expressed in the AbN at the normal metabolic conditions but could be evoked by hypercapnia and other metabolic perturbations. We show that the hypercapnia-evoked late-E bursts in AbN is abolished by pharmacological suppression of the vl RTN/pFRG region (Figure III-2 and [41]) and we could find single neurons within the RTN/pFRG whose hypercapnia-evoked rhythmic activity was strongly correlated with the AbN late-E activity (Figure III-3 and [41]). These findings provide support although indirect for the previous suggestions that the generator of late-E oscillations resides in the RTN/pFRG region and is the source of the AbN late-E activity [20], [42], [43]**.**

At the same time, our results (have clearly demonstrated that late-E oscillations in the AbN (and probably in the RTN/pFRG) are not generated under normal metabolic conditions but emerge during metabolic challenges, such as hypercapnia or hypercapnic hypoxia/anoxia, at least in the mature animals. Therefore, in our opinion, the RTN/pFRG oscillator should not be considered as a fundamental component of the respiratory CPG operating during normocapnia, at least in the mature respiratory system. Our data, however, do not allow inferences about a different, e.g. a more dominant or leading, role of the RTN/pFRG oscillations at the embryonic stage or in neonatal animals, which has been widely discussed in the literature [20], [42], [171], [174]–[176].

We also showed that the hypercapnia-evoked late-E activity monitored via the AbN was abolished in the mature rat *in situ* by systemically applied riluzole, an I_{NaP} blocker. The critical role of I_{NaP} in the generation of rhythmic activity in the embryonic parafacial population (e-pF) has been previously demonstrated by administration of riluzole, which abolished the e-pF rhythmic activity [175], [176]. Our finding is consistent with this data and represents indirect evidence that the generation of rhythmic activity in the RTN/pFRG of the mature animal may also critically depend on I_{NaP}.

D-2. Interactions between the RTN/pFRG oscillator and the respiratory CPG

Before discussing the possible connections between the RTN/pFRG oscillator and the core CPG circuitry, we would like to emphasize the important difference between our concept and model and the dual oscillator concept [42], [172]. The latter considers the normal neural machinery for respiratory rhythm and inspiratory pattern generation to reside within the pre-BötC *inspiratory generator* whose rhythmic activity is fully defined by the intrinsic (or group-pacemaker) properties and excitatory interconnections within this region. In our opinion, this concept undervalues the role of other brain stem compartments, such as the BötC and pons, and interactions between them (including inhibitory interactions) in the generation of respiratory rhythm and pattern. In contrast, in our concept and the model, the respiratory rhythm is generated because of the dynamic interactions within and between the pre-BötC and BötC, representing the core of the CPG, under control of other brain stem compartments including the pons, RTN, and raphé [16], [19], [36], [87]. Therefore, concerning interactions between the RTN/pFRG oscillator and the respiratory CPG, these interactions in our opinion also involve interactions with other critical components of the CPG, including the BötC and rVRG.

A schematic of interactions between the RTN/pFRG oscillator and the respiratory CPG (with BötC/pre-BötC kernel) predicted by our model is shown in Figure III-13. These important interactions include (a) excitation of the BötC/pre-BötC oscillator (specifically the excitatory pre-I inspiratory neurons of the pre-BötC, see Figure III-7A) by the RTN/pFRG oscillations and (b) inhibition of the RTN/pFRG oscillations by the BötC/pre-BötC oscillator during inspiration (by early-I(1) population of the pre-BötC, see Figure III-7A). These two interactions have been suggested and justified in many previous experimental and modeling studies [20], [37]–[39], [42], [43], [87], [171], [174], [180], [181], [183].

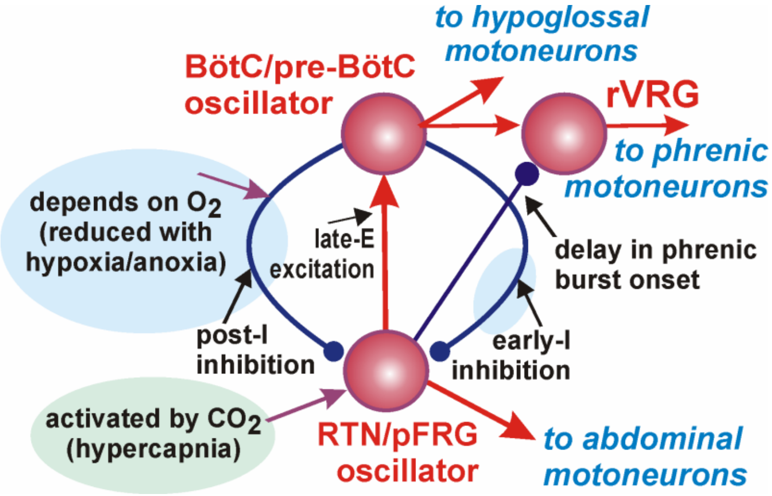

Figure III-13. Proposed interactions between BötC/pre-BötC and pFRG/RTN oscillators in the adult mammals *in vivo*. Red arrows represent excitatory influence; blue lines terminated with circles indicate inhibitory influence; violet arrows indicate metabolic dependence. Under normal metabolic conditions, the RTN/pFRG oscillator is inhibited by the BötC/pre-BötC oscillator (the core of the respiratory CPG) during both inspiration (by the inhibitory early-I neurons of pre-BötC) and expiration (by the post-I neurons of BötC) and remains silent. The normal expression of post-I inhibition requires excitatory drive from the pons (not shown). The RTN/pFRG oscillator can be activated either by hypercapnia, which directly excites RTN/pFRG neurons, or by hypoxia/anoxia (or pontine suppression), which reduces RTN/pFRG inhibition by the BötC/pre-BötC oscillator, or by both the above. When activated, the BötC/pre-BötC oscillator provides both excitation of the BötC/pre-BötC oscillator and inhibition of rVRG premotor neurons, hence increasing the delay between hypoglossal and phrenic discharges.

In addition to the above interactions, we hypothesize an inhibitory connection (direct or indirect) from the RTN/pFRG to the premotor inspiratory neurons of rVRG (Figure III-13) (e.g. via the aug-E and/or early-I(2) population, see Figure III-7A). This hypothesized connection provides a reasonable explanation for the additional delay between the hypoglossal (HN) and phrenic (PN) motor outputs associated with the late-E bursts in the abdominal motor output (Figure III-5 and Figure III-9), as well as for an increase of this delay generally observed during hypercapnia [178].

The other connection hypothesized in our study is the inhibitory connection from the BötC/pre-BötC kernel (specifically from post-I neurons of the BötC, see Figure III-7A) to the RTN/pFRG oscillator (Figure III-13). This connection provides a decreasing inhibition of RTN/pFRG during expiration. Based on our modeling studies, we hypothecize that this connection performs three important functions. First, it significantly contributes to the coupling between RTN/pFRG late-E and pre-BötC bursts by not allowing late-E RTN/pFRG bursting to occur before the end of expiration. Second, this expiratory inhibition together with the inspiratory inhibition (see above) may keep RTN/pFRG oscillations inhibited during normal conditions. Third, this inhibition may suppess the second rebound burst of AbN (and, probably, RTN/pFRG).

Based on the suggested schematic of interactions between the RTN/pFRG and BötC/pre-BötC kernel (Figure III-7A and Figure III-13) we conclude that RTN/pFRG activity is strongly controlled by BötC/pre-BötC inhibition during both inspiration and expiration which fits to the general schematic of interactions between RTN and the CPG proposed by the Guyenet group [96], [187]–[189]. Moreover, based on our simulation, we suggest that the activity of RTN/pFRG is actually more strongly controlled by the BötC/pre-BötC activity than the activity of BötC/pre-BötC is controlled by RTN/pFRG oscillations. This control of RTN/pFRG activity by the BötC/pre-BötC circuits includes control of the emergence of RTN/pFRG oscillations, their frequency and coupling to BötC/pre-BötC oscillations, which is clearly demonstrated by the regime of quanal acceleration of late-E activity with the development of hypercapnia (Figure III-1, Figure III-4, and Figure III-8).

As stated above, our model suggests that during normal conditions the BötC/pre-BötC kernel inhibits RTN/pFRG oscillations, and our simulation results demonstrated that blocking of fast inhibitory synaptic transmission within RTN/pFRG in the model should evoke (release) oscillations in the RTN/pFRG and AbN at normal metabolic conditions. We then verified this prediction experimentally, although in our experiments, we cannot fully exclude a possibility that this inhibition of RTN/pFRG is produced by sources other than the BötC post-I population. This issue requires further experimental investigations.

D-3. Effects of hypercapnia and hypoxia on RTN/pFRG activity

Our studies (previous and herein) show that the late-E activity in AbN (and probably in RTN/pFRG) is usually not generated under normal metabolic conditions. At the same time, the excitability of the late-E population in RTN/pFRG is highly sensitive to hypercapnia. Therefore, the progressive hypercapnia producing depolarization of late-E neurons can overcome the inhibition by BötC/pre-BötC and initiate late-E rhythmic activity that goes through several stages described herein as quantal acceleration until the late-E activity reaches 1:1 coupling with the BötC/pre-BötC oscillations (see Figure III-1 and Figure III-8). In contrast, strong hypoxia or anoxia can affect the RTN/pFRG oscillations through reduction of inhibition, specifically post-I inhibition (see Figure III-13) and produce an effect similar to hypercapnia by shifting a balance between inhibition and excitation at the RTN/pFRG late-E neurons.

In summary, we suggest that the emergence of RTN/pFRG and abdominal (late-E) oscillations is defined by two major factors (Figure III-13): (a) general RTN/pFRG excitability, which rises with CO_2 level (hypercapnia), and (b) post-I inhibition from the BötC/pre-BötC oscillator, which depends on the level of O_2 (hypoxia). The same factors define the pattern of RTN/pFRG and abdominal discharges. With the progressive development of hypoxia under the hypercapnic conditions the patterns transforms from a late-E (pre-I) to a post-I rebound and then to biphasic pre/post-I burst profile.

D-4. The extended model and its validation

In this study, we used and extended our previous computational model [16], [19]. This model was able to reproduce the three-phase eupneic respiratory pattern generated under normal conditions as well as the reorganization of this pattern caused by multiple experimental perturbations, such as various brainstem transections and application of specific blockers of ionic channels and inhibitory synaptic transmission. It is interesting to note that since the first publications of the basic version of our model [16], [19], [35], several modeling predictions have been (directly or indirectly) confirmed by experimental studies. For example, our model suggested that the pre-BötC compartment should contain a population of inhibitory neurons (early-I(1) in Figure III-7A) that provides inspiratory inhibition in the network. In agreement with this suggestion, Winter et al., 2009 have recently found a population of glycinergic inspiratory neurons within the pre-BötC that can "make important contribution to generation and maintenance of the respiratory rhythm". The critical role of inhibitory neurons in the BötC for rhythm generation suggested by our model have been indirectly confirmed by Abbott et al., 2009, who found that microinjections of galanin into the BötC causes severe dysrhythmia or persistent apnea [191]. Also, Bongianni et al., 2010 have demonstrated that blockade of $GABA_A$ receptors in the BötC (of rabbit) by bicuculline or gabazine induces strong depression of respiratory activity up to apnea [192]. These new results provide additional indirect support for the importance of the mutual inhibitory interactions between the BötC and pre-BötC for respiratory rhythm generation as proposed by our model.

Morgado-Valle et al., 2010 has recently found *in vitro* a sub-population of glycinergic inhibitory neurons with pacemaker-like properties within the pre-BötC [193]. These authors suggest that this finding challenges our network models, which in their opinion critically depend on excitatory pacemaker neurons within the pre-BötC. In this connection, we emphasize that: (1) our previous models [16], [18], [19], [35] and the model described herein always included an inhibitory population of pre-BötC neurons (see early-I(1) in Figure III-7); and (2) the generation of respiratory rhythm in these models under normal conditions is not critically dependent on excitatory pacemaker neuron activity, which was demonstrated with full suppression of I_{NaP} that does not disrupt rhythm generation experimentally and in these models (see [16], [19], [186], and Figure III-8D herein). We suggest that the inhibitory neuron pacemaker properties described by [193] cannot represent a basis for population bursting, because such neurons cannot excite each other to generate coherent inspiratory bursting. Moreover, in contrast to other suggestions based on reduced *in vitro* preparations (e.g. see [194]), we propose that the role of intrinsic pacemaker or group-pacemaker mechanisms is significantly reduced in the more intact network under *in situ*/*in vivo* conditions, at least in mature animals, and that network interactions as depicted in Figure III-7 play a dominant role in rhythmogenesis *per se* as well as in the control of phase durations and respiratory pattern expressed by the network.

Our current study focused on the interactions between the BötC/pre-BötC kernel of the CPG and the RTN/pFRG oscillations that emerge under specific metabolic conditions. In order to study these interactions we extended the previous model by incorporating the late-E population with I_{NaP}-dependent bursting properties in the RTN/pFRG compartment and proposed specific connections between the BötC/pre-BötC kernel and this late-E population generating RTN/pFRG oscillations. These hypothesized connections allow the model to reproduce and explain several key behaviors including the emergence and quantal acceleration of abdominal late-E activity during hypercapnia, transformation of the late-E bursts to a biphasic-E activity during hypercapnic hypoxia or anoxia, and quantal slowing of BötC/pre-BötC and PN oscillations with the progressive suppression of pre-BötC excitability. A more detailed analysis of these behaviors by dynamical systems theory methods applied to a simplified mathematical model can be found in Chapter IV showing that the same behaviors can be reproduced, suggesting that the models are robust. The ability of the extended model to reproduce these behaviors provides additional validation for the model *per se* and for the hypothesized interactions between the RTN/pFRG and the respiratory CPG. Several important predictions have been made that require further experimental testing. Our model provides a framework and tool for further experimental-theoretical studies.

E. Summary of predictions

Subcellular level predictions: A dependency on I_{NaP}, for intrinsic rhythmicity was predicted by our model. This model utilized the I_{NaP} current in both the pre-BötC and RTN/pFRG populations. Our model predicted that application of riluzole, an I_{NaP} channel blocker, locally to the RTN/pFRG would cause a cessation of AbN bursts during high metabolic load, when 1:1 AbN:RTN/pFRG bursts are expected, see Figure III-14.

System level predictions: Our model has several populations of connected neurons. A particular area of focus was the interactions between the medulla and the RTN/pFRG. Specifically, our model predicted inhibitory connections from post-I neurons of the BötC and early-I of the pre-BötC to the RTN/pFRG Figure III-15A. Moreover, the nature of this inhibition had to be asymmetric, with inhibition from post-I being the weaker of the two. Inhibition from the post-I neurons was supported by the application of a $GABA_A$ antagonist to the RTN/pFRG, see Figure III-16B, C. This caused an emergence of AbN activity at the end of the expiratory phase, without hypercapnic conditions. The timing of AbN emergence indicates that the inhibition from the early-I may in fact be stronger than inhibition from the post-I as no AbN activity was observed during the inspiratory phase.

Additional findings and predictions regarding the interaction between the RTN/pFRG and medullary neurons are discussed in the following chapter.

Chapter IV: Interacting oscillations in neural control of breathing: modeling and qualitative analysis

The following section was adapted from the following accepted manuscript: J. E. Rubin, B. J. Bacak, Y. I. Molkov, N. A. Shevtsova, J. C. Smith, and I. A. Rybak, “Interacting oscillations in neural control of breathing: modeling and qualitative analysis.,” *J. Comput. Neurosci.*, vol. 30, no. 3, pp. 607–32, Jun. 2011.

A. Introduction

Neural oscillations with various temporal and spatial patterns have been shown to play fundamental roles in brain operation, including sensory processing (in the visual [195], somatosensory [196], olfactory [197], and other sensory systems), central brain mechanisms [198], [199], and neural control of movements [200], [201]. Revealing the rhythmogenic mechanisms underlying these oscillations and characterizing the nature of interactions between different oscillations would have a broad impact on understanding the general principles of how the brain functions.

This study focuses on the interactions between two neural oscillators involved in the control of breathing in mammals. The first “oscillator” is the respiratory central pattern generator (CPG) that generates primary respiratory oscillations driving phrenic nerve motor output and controlling lung ventilation. The rhythm-generating core of this CPG has been hypothesized to include several interacting populations of respiratory neurons located in the pre-Bötzinger (pre-BötC) and Bötzinger (BötC) complexes within the ventral respiratory column of the medulla[3], [5], [16], [18], [19], [23], [35], [36], [186], [202],

[203]. The second “oscillator”, referred to as the parafacial respiratory group (pFRG), appears to reside within, or overlap with, the retrotrapezoid nucleus (RTN) [39], [42]. Recent data suggests that, with increasing metabolic demands, e.g. with increased level of CO_2 (hypercapnia) and/or decreased level of O_2 (hypoxia) [41], the RTN/pFRG oscillator starts generating a rhythmic late-expiratory (late-E, sometimes referred to as pre-inspiratory or pre-I) activity that interacts with the BötC/pre-BötC oscillations and drives an enhanced late-E rhythmic activity in the motor output controlling abdominal muscles [20], [36], [41], [42], [87].

A large-scale computational model of the respiratory CPG was previously developed to reproduce multiple experimental data obtained in the arterially perfused brainstem-spinal cord rat preparation with brain stem transections that sequentially removed rostral components of the respiratory network [16], [19]. The results of these experimental and modeling studies suggest that the core neural circuitry of the respiratory CPG resides within the BötC and pre-BötC compartments and that the primary respiratory oscillations are generated due to dynamic interactions between (i) excitatory neural populations in the pre-BötC that are active during inspiration, (ii) inhibitory populations in the pre-BötC providing inspiratory inhibition within the network; and (iii) inhibitory populations in the BötC generating expiratory inhibition [16], [19]. It has also been proposed that these network interactions form a hierarchy of multiple oscillatory mechanisms whose expression is controlled by multiple drives from several brain stem compartments, including the RTN and pons, some of which depend on and reflect current metabolic conditions (e.g. levels of CO_2, O_2 and pH) [16], [19].

To allow investigation of interactions between the BötC/pre-BötC and RTN/pFRG oscillations, the above large-scale model was extended by incorporating an additional late-E population of the RTN/pFRG that consisted of neurons with intrinsic rhythmogenic properties defined by the persistent sodium current, I_{NaP} [41]. Interactions between the late-E and other neural populations were suggested based on experimental studies [41] to reproduce the specific relationships between phrenic activity and abdominal oscillations observed in nerve recordings during various metabolic conditions. The extended large-scale model [41] was successful in reproducing several operating regimes featuring specific relationships between the above oscillations. However, the complexity of that model, based on explicit simulation of populations of neurons modeled in the Hodgkin-Huxley (HH) style, does not allow implementation of dynamical systems methods for theoretical investigation of the possible states and oscillatory regimes in the system. We have recently gained insight by simplifying such large-scale models using activity-based (non-spiking) single neuron models to represent populations of spiking neurons. Specifically, this approach was successfully applied for theoretical investigation of the core of the respiratory CPG, namely its BötC/pre-BötC kernel [35].

The model proposed herein is based on and extends the network model from this previous work [35]. An additional late-E neuron with I_{NaP}-dependent rhythmogenic properties (representing a hypothetical late-E population in the RTN/pFRG) was included in the model and interconnected with other neurons according to the connection scheme proposed in the corresponding large-scale model [41]. Our objective in this study was to develop a relatively simple model, which maintains the essential features and architecture of the large-scale model, and to harness this reduced model to theoretically investigate the oscillatory patterns and mechanisms of coupling between the BötC/pre-BötC and RTN/pFRG oscillations in the functional regimes corresponding to different metabolic conditions.

Our analysis focused on the following three scenarios studied experimentally: (1) the emergence and "quantal acceleration" of the (RTN/pFRG) late-E oscillations, and their interactions with the BötC/pre-BötC oscillations, with the progressive increase of external drive to the late-E population, simulating hypercapnic conditions, (2) transition of the late-E (pre-I) activity pattern to a biphasic-E (pre-I/post-I) pattern with changing external drives, simulating hypercapnic hypoxia conditions, and (3) "quantal slowing" of BötC/pre-BötC oscillations with progressive suppression of pre-BötC neurons, simulating the effect of opioids. These behaviors represent the typical regimes of synchronization between the BötC/pre-BötC and RTN/pFRG oscillators. Using numerical simulations in combination with bifurcation analysis and fast-slow decomposition techniques, we show and explain how gradual variation of external drives or other model parameters, associated with specific metabolic and/or physiological conditions, can produce particular BötC/pre-BötC and RTN/pFRG outputs and change the functional role of coupling between these oscillators. In addition to characterizing the phase plane conditions associated with each regime, our theoretical analysis explains certain features observed in simulations. Specifically, we show why the inspiratory period remains constant even as late-E activity emerges on progressively larger proportions of cycles in quantal acceleration, why late-E rebound activity is seen before a complete switch to biphasic-E activity emerges in hypercapnic hypoxia, and what determines pre-BötC burst times, as well as why late-E activity remains biphasic precisely on those cycles in which pre-BötC neurons activate, in quantal slowing. The results of this work provide theoretical insights into the key features and dynamics of synchronization between BötC/pre-BötC and RTN/pFRG oscillators under different physiological conditions.

B. Methods

B-1. Model description

The schematic of the respiratory network model considered herein is shown in Figure IV-1A. This model is a reduced version of the large-scale model by [41]. On the other hand, this model represents an extension of the previous reduced model of the core of the respiratory CPG [35]. The latter was extended by incorporating an additional late-expiratory (late-E) neuron that represents a hypothetical neural population within RTN/pFRG, serving as a source of late-E oscillations.

The rhythmic activity in the RTN/pFRG appears to be critically dependent on I_{NaP}, since a suppression of this current by riluzole, a specific I_{NaP} blocker, abolishes this rhythmic activity, as shown in rat embryos [175], [176] and in mature rat *in situ* preparations [17]. Therefore the late-E neuron of the RTN/pFRG added to the present model contains I_{NaP} and hence (similar to the pre-inspiratory/inspiratory (pre-I/I) neuron of the pre-BötC) is able to intrinsically generate I_{NaP}-dependent bursting under certain conditions [174], [204].

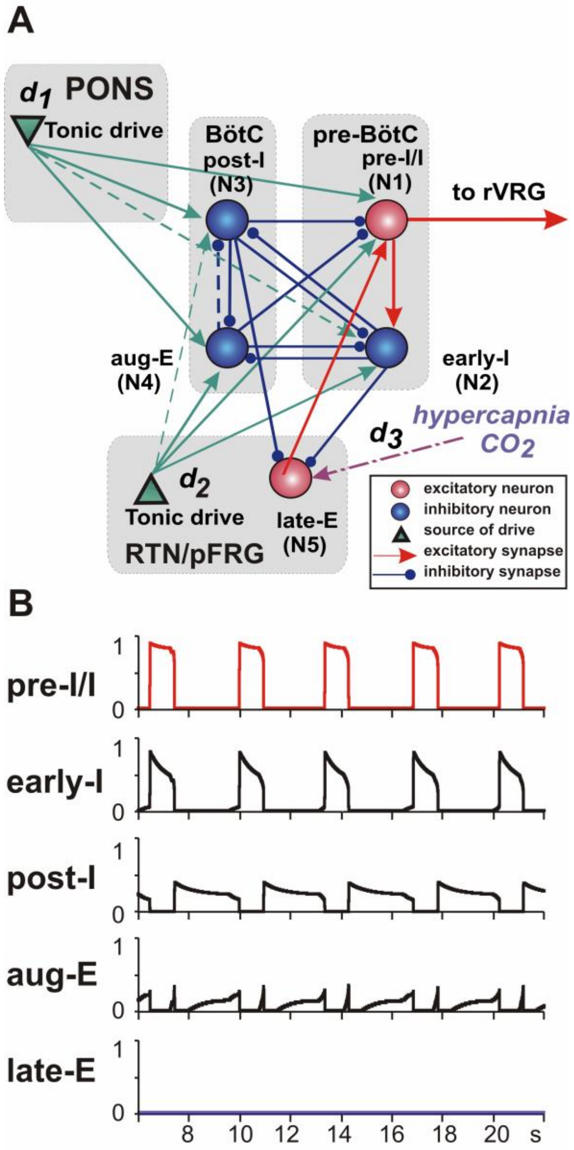

Figure IV-1. Reduced model of pre-BötC, BötC, and RTN/pFRG. (A) Model schematic. Spheres represent neurons (excitatory– red; inhibitory– blue); green triangles represent sources of tonic excitatory drives (in pons, RTN) to different neural populations. Excitatory and inhibitory synaptic connections are indicated by red or green arrows and small blue circles, respectively. (B) Model performance: output activity of all neurons is shown when “hypercapnic” drive to the late-E neuron (d_3) is set to zero. The periods of elevated activity of pre-BötC neurons define the inspiratory phases (top two traces), while the BötC neurons (post-I and aug-E) are active during expiration. Although the post-I neuron inhibits the aug-E neuron early in expiration, adaptation in the post-I neuron causes a decrease in the inhibition to aug-E and thus allows the second phase of expiration, characterized by aug-E activity, to begin.

The synaptic interactions between the core BötC/pre-BötC neurons of the CPG shown in Figure IV-1A were described in detail and justified in our previous papers [16], [19], [35]. The interactions between the late-E neuron of RTN/pFRG incorpotated in new model and the core BötC/pre-BötC neurons include (see Figure IV-1A): (a) excitation of the pre-I/I inspiratory neuron of BötC by the late-E neuron and inhibition of the late-E neuron by (b) the early-inspiratory (early-I) neuron of pre-BötC during inspiration and (c) the post-inspiratory (post-I) neuron of BötC during expiration. The first two connections (a and b) have been proposed and justified in many previous studies [20], [37]–[39], [41]–[43], [174], [181], [183], [204]. The third connection (the inhibitory one, from post-I to late-E) has been previously hypothesized [41] as the natural mechanism to prevent late-E bursting from occurring in the initial part of expiration and, together with the inspiratory inhibition (from early-I), to suppress late-E oscillations during normal conditions.

The model consists of five neurons ($i = 1,\ldots,5$), each representing one of the key populations of neurons in the preceding large-scale model [41]. The first four neurons include the excitatory pre-I/I neuron of the pre-BötC ($i = 1$), the inhibitory early-I neuron of the pre-BötC ($i = 2$), and two inhibitory neurons of the BötC, the post-I ($i = 3$) and the augmenting-expiratory (aug-E, $i = 4$) neurons. These neurons represent the core circuitry of the respiratory CPG [16], [19], [35]. The fifth neuron is the late-E neuron of the RTN/pFRG ($i = 5$, see above). These neurons interact according to the schematic shown in Figure IV-1A and receive excitatory drives from two sources: the pons (d_1) and RTN (d_2). An additional excitatory drive to late-E (d_3) is included to simulate the effect of hypercapnia.

Each neuron in the model represents a specific neural population and is described by an activity-based model in which the dependent variable V_i represents an average voltage for that (i-th) population and each output $f(V_i)$ ($0 \le f(V_i) \le 1$) represents an averaged or integrated population activity. Because we consider regimes in which neurons within each population are synchronized, we assume that the dynamics of the average voltages in the model can be represented by a conductance-based framework [35].

Specifically, the pre-I/I and late-E ($i \in \{1,5\}$) neurons are excitatory, with intrinsic oscillatory properties defined by the persistent (slowly inactivating) sodium current I_{NaP}. The membrane potentials of these neurons, V_i, thus obey the following differential equation:

$$C \cdot \dot{V}_i = -I_{NaPi} - I_{Ki} - I_{Li} - I_{SynEi} - I_{SynIi}. \qquad (IV\text{-}1)$$

The other three neurons ($i \in \{2,3,4\}$) are adaptive neurons (with adaptation defined by an outward potassium current, $I_{AD\,i}$) whose membrane potentials V_i evolve as follows:

$$C \cdot \dot{V}_i = -I_{ADi} - I_{L\,i} - I_{SynE\,i} - I_{SynI\,i}. \qquad (IV\text{-}2)$$

In equations (1) and (2), C is the neuronal capacitance, I_{Ki} represents the potassium delayed rectifier current, $I_{L\,i}$ is the leakage current, and $I_{SynE\,i}$ and $I_{SynI\,i}$ are the excitatory and inhibitory synaptic currents, respectively. The currents are described as follows:

$$I_{NaPi} = \bar{g}_{NaP} \cdot m_{NaP}(V_i) \cdot h_{NaP}(V_i) \cdot (V_i - E_{Na}),\ for\ i \in \{1,2\}; \qquad (IV\text{-}3)$$

$$I_{Ki} = \bar{g}_K \cdot m_K^4(V_i) \cdot (V_i - E_K),\ for\ i \in \{1,2\}; \qquad (IV\text{-}4)$$

$$I_{ADi} = \bar{g}_{AD} \cdot m_{ADi} \cdot (V_i - E_K),\ for\ i \in \{3,4,5\}; \qquad (IV\text{-}5)$$

$$I_{Li} = \bar{g}_L \cdot (V_i - E_{Li}),\ for \in \{1,\ldots,5\}; \qquad (IV\text{-}6)$$

$$I_{SynE1} = \bar{g}_{SynE} \cdot (V_1 - E_{SynE}) \cdot (a_{51} \cdot f(V_5) + c_{11} \cdot d_1 + c_{21} \cdot d_2)\,; \qquad (IV\text{-}7)$$

$$I_{SynE2} = \bar{g}_{SynE} \cdot (V_2 - E_{SynE}) \cdot (a_{12} \cdot f(V_1) + c_{12} \cdot d_1 + c_{22} \cdot d_2)\,; \qquad (IV\text{-}8)$$

$$I_{SynEi} = \bar{g}_{SynE} \cdot (V_i - E_{SynE}) \cdot (c_{1i} \cdot d_1 + c_{2i} \cdot d_2),\ for\ i \in \{3,4\}\,; \qquad (IV\text{-}9)$$

$$I_{SynE5} = \bar{g}_{SynE} \cdot (V_5 - E_{SynE}) \cdot c_{35} \cdot d_3\,; \qquad (IV\text{-}10)$$

$$I_{SynIi} = \bar{g}_{SynI} \cdot (V_i - E_{SynI}) \cdot \sum_{j=2;\ j \neq i}^{4} b_{ji} \cdot f(V_j),\ for\ i \in \{1,...,5\}, \qquad (IV\text{-}11)$$

where $\bar{g}_{NaPi}, \bar{g}_K, \bar{g}_{AD}, \bar{g}_L, \bar{g}_{SynEi},$ and $\bar{g}_{SynIi}$ are the maximal conductances of the corresponding ionic channels; $E_{Na}, E_K, E_{Li}, E_{SynE},$ and E_{SynI} are the corresponding reversal potentials; a_{12} and a_{51} define the weights of the excitatory synaptic input from the pre-I/I to the early-I neuron and from the late-E to the pre-I/I neuron, respectively (see Figure IV-1A); b_{ji} defines the weight of the inhibitory input from neuron *j* to neuron *i* ($j \in \{2,3,4\}$; $i \in \{1,...,5\}$); and c_{ki} defines the weight of the excitatory synaptic input to neuron *i* from drive *k* (d_k, $k \in \{1,2,3\}$).

The neuronal membrane potential is converted to the neuron output by the piecewise linear function:

$$f(V) = \begin{cases} 0,\ if\ V < V_{\min} \\ (V - V_{\min})/(V_{\max} - V_{\min}),\ if\ V_{\min} \le V < V_{\max} \\ 1,\ if\ V \ge V_{\max} \end{cases} \qquad (IV\text{-}12)$$

where $V_{\min}$ and $V_{\max}$ define the “threshold” and “saturation” voltages, respectively.

There are two types of slow variables in the model. One type represents the slow inactivation of the persistent sodium current (h_{NaPi}, $i \in \{1,5\}$; see [125]) in the pre-I/I and late-E neurons; the other variables ($m_{ADi}, i \in \{2,3,4\}$) denote adaptation in the other three neurons (each with fixed time constant τ_{AD} and maximal adaptation k_{AD}):

$$\tau_{hNaP}(V_i) \cdot \dot{h}_{NaPi} = h_{\infty NaP}(V_i) - h_{NaPi}, \quad i \in \{1,5\}; \qquad (IV\text{-}13)$$

$$\tau_{AD} \cdot \dot{m}_{ADi} = k_{AD} \cdot f(V_i) - m_{ADi}, \quad i \in \{2,3,4\} \ . \qquad (IV\text{-}14)$$

Voltage dependent activation and inactivation variables and time constants for the persistent sodium and potassium rectifier channels in the pre-I/I and late-E neurons ($i \in \{1,5\}$) are described as follows:

$$m_{NaP}(V_i) = \left(1 + \exp\left\{(V_i - V_{mNaP}) / k_{mNaP}\right\}\right)^{-1}; \qquad (IV\text{-}15)$$

$$h_{\infty NaP}(V_i) = \left(1 + \exp\left\{(V_i - V_{hNaP}) / k_{hNaP}\right\}\right)^{-1}; \qquad (IV\text{-}16)$$

$$\tau_{hNaP}(V_i) = \tau_{hNaP\max} / \cosh\left\{(V_i - V_{\tau hNaP}) / k_{\tau hNaP}\right\}; \qquad (IV\text{-}17)$$

$$m_K(V_i) = \left(1 + \exp\left\{(V_i - V_{mK}) / k_{mK}\right\}\right)^{-1}. \qquad (IV\text{-}18)$$

The architecture of network interconnections between the neurons follows that in the large-scale model in the previous chapter and is based on the existing direct and indirect experimental data and our current assumptions. The connection weights were adjusted so that, on one hand, the model reproduced the dynamics of the BötC/pre-BötC and late-E (RTN/pFRG) oscillators in all regimes considered herein and, at the same time, maintained all the features and behavior described previously [35].

B-2. Model parameters

The following default values of parameters were used (except where it is indicated in the text that some parameter values were varied in particular simulations):

Table IV-1. Parameters for reduced model of RTN/pFRG and BötC/pre-BötC interactions.

Membrane capacitance (pF):	C= 20.
Maximal conductances (nS):	$\bar{g}_{NaP}$ = 5, $\bar{g}_K$ = 5, $\bar{g}_{AD}$ = 10, $\bar{g}_L$ = 2.8, $\bar{g}_{SynE}$ = 10, $\bar{g}_{SynI}$ = 60.
Reversal potentials (mV):	E_{Na} = 50, E_K = -85, E_{SynE} = 0, E_{SynI} = -75, E_{Li} = -60 ($i \in \{1,...,4\}$), E_{L5} =-64.
Synaptic weights:	a_{12} = 0.35, a_{51} = 0.35, b_{21} = 0, b_{23} = 0.2, b_{24} = 0.25, b_{25} = 0.035, b_{31} = 0.8, b_{32} = 0.15, b_{34} = 0.5, b_{35} = 0.05, b_{41} = 0.22, b_{42} = 0.15, b_{43} = 0, b_{45} =0, c_{11} = 0.35, c_{12} = 0, c_{13} = 0.33, c_{14} = 0.05, c_{21} = 0.16, c_{22} = 0.25, c_{23} = 0, c_{24} = 0.4, c_{35} = 1.
Parameters of $f(V_i)$ functions (mV):	$V_{\min}$ = -50, $V_{\max}$ = -20.
Parameters for I_{NaP} and I_K (mV):	V_{mNaP} = -40, k_{mNaP} = -6, V_{hNaP} = -55, k_{hNaP} = 10, V_{mK} = -30, k_{mK} = -4.
Time constants (ms):	$\tau_{hNaP\max}$ = 4000, τ_{AD} =2000.
External drives:	d_1 varied from 1 (default value) to 0, d_2 =1, d_3 varied from 0 (default value) to 1. Other parameters: k_{AD} = 1.

This baseline parameter tuning, with d_1 = 1 and d_3 = 0, yielded a respiratory rhythm shown in Fig. 1B, which is representative of baseline conditions. In particular, the value d_3= 0 was assumed to represent to a normocapnic (normal CO_2) state. Changing metabolic and physiological conditions were simulated by changing external drives or other model parameters. Specifically, progressive hypercapnia (an increase in the CO_2 level) was simulated by a gradual increase of "hypercapnic" drive (d_3) to the late-E neuron, representing a population of central chemoreceptors located in RTN/pFRG, whose activity is believed to increase with the level of CO_2 [48], [92], [205]. Hypercapnic hypoxia was modeled via the reduction of post-I activity, i.e. as a progressive decrease in the pontine drive, d_1, from the baseline value $d_1 = 1$ to zero, at a particular level of hypercapnia (i.e., d_3 value). To reproduce “quantal slowing” of pre-BötC activity [42], the excitability of pre-BötC neurons was progressively suppressed by a reduction of the excitatory synaptic conductance $\overline{g}_{SynE}$ in both pre-I/I and early-I neurons.

B-3. Bifurcation analysis

For the analysis of changes in qualitative behavior of the system with variation of external drives or other model parameters we used a technique based on the construction of Poincaré sections [206]. This technique involves choosing a surface, called a Poincaré section, that is transverse to the flow in the phase space and finding the successive intersections of the model trajectory with that surface. The Poincaré section was defined by choosing a threshold and finding the time moments when the output neuron activity, $f(V)$, intersects the threshold in a fixed direction. The time interval between two successive phase transitions (referred to as period) was used to build bifurcation diagrams for each of the three scenarios of interest. In 2D bifurcation diagrams, the periods of pre-BötC and late-E active phases were plotted as functions of a parameter whose variation was used to simulate the corresponding change in the metabolic state. The variation of such a parameter was implemented using a slowly changing linear function of time, and a continuous calculation of the corresponding periods of pre-BötC (early-I neuron) and late-E oscillations was performed. In the resulting bifurcation diagrams, most qualitative changes (bifurcations) in system behavior were clearly evident as discontinuities, the appearance of new solution branches, and the emergence of clouds of points.

Some bifurcation diagrams were generated by changing two parameters independently. At each point in the corresponding 2D parametric plane, the mean value of the period was represented by color. This type of diagram shows bifurcation curves as boundaries between areas with different colors, corresponding to qualitatively different behaviors.

Bifurcation diagrams were constructed using a TISEAN software package [207] and custom written C++ programs.

B-4. Phase-plane analysis

Phase plane analysis involved the evolution of variables describing voltage (V_5) and I_{NaP} inactivation (h_5) in the late-E neuron, adaptation of early-I (m_2) or post-I (m_3) neurons, and input currents and conductances. Each neuron model includes a fast voltage variable (V_i) and a second slow variable, corresponding to persistent sodium inactivation (h_1, h_5) or adaptation (m_1, m_2, m_3). Thus, the voltage equation for each neuron, with its slow variable treated as a parameter, forms a one-dimensional fast subsystem for that neuron (assuming that other neurons' voltages are fixed). Correspondingly, when we refer to critical points of the fast subsystem for a neuron, we mean points for which the right hand side of equation (*IV-1*) (for the pre-I/I and late-E neurons) or (*IV-2*) (for all other neurons) is equal to zero. We consider some standard phase plane diagrams with a voltage variable on the horizontal axis and the associated slow variable on the vertical axis. We also consider diagrams with a slow variable on the horizontal axis and a variable representing the level of input to the corresponding neuron on the vertical axis. All synaptic inputs to neurons 3,4, and 5 are inhibitory, with the same reversal potential, and we define input variables inh_i, $i = 3,4,5$, to neuron *i* as the sum $\sum_{j \neq i} b_{ji} f(V_j)$. Neurons 1 and 2 each receive both excitatory and inhibitory inputs, and we define the variables *input*$_1$ and *input*$_2$ as the sum of synaptic currents to these neurons, excluding drives d_i. For consistency with the use of *inh* > 0, we adopted the convention that positive and negative values of input denote inhibition and excitation, respectively.

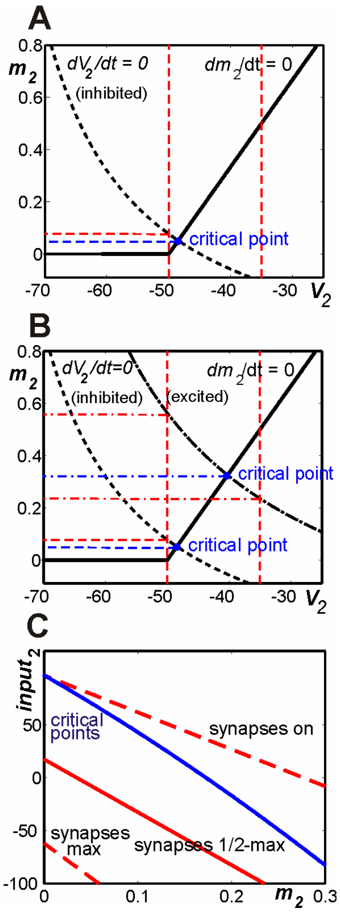

Figure IV-2. Construction of diagram for use in analysis. (A) Standard phase plane for model neuron 2, subject to a fixed level of inhibitory input ($input_2$>0). There is a critical point (blue) where model nullclines (V_2, dashed and m_2, solid) intersect. The m_2 coordinate is read off of this point (blue dashed line). The vertical red dashed lines label V_2 values at which the synaptic output from neuron 2 turns on (-50) and reaches a half-maximal level (-35). When they are positive, the m_2 coordinates of these intersections are also recorded (horizontal red dashed line). (B) The same nullclines and intersections from (A) are shown along with additional nullclines and intersections (dash-dotted curve and lines) corresponding to a different level of input to neuron 2 that is excitatory ($input_2<0$). C: Curves of critical points (blue) and intersection points with key V_2 values (red dashed and solid) in the $input_2$ versus m_2 plane.

The construction of a diagram with $input_2$ versus m_2 is illustrated in Figure IV-2A-B, with the diagram itself shown in Figure IV-2C. In Figure IV-2A, the V_2 (dashed) and m_2 (solid) nullclines, corresponding to a fixed level of input to cell 2 ($input_2$) that is positive, since it is inhibitory, intersect in a critical point. The V_2 nullcline also intersects the line $\{V_2 = V_{min} = -50\}$, at which synaptic outputs from cell 2 turn on (equation (*IV-12)*), at a positive value of m_2. We can search for such critical points and points of intersection with the line $V_2 = -50$, as well as with the lines $V_2 = -35$, corresponding to half-maximal activation of synaptic outputs, and $V_2 = V_{max} = -20$, corresponding to maximal activation of synaptic outputs, for each fixed value of $input_2$; this is done, for example, in Figure IV-2B for a level of $input_2$ corresponding to excitatory input to cell 2. From this process, we obtain a curve of m_2 values at critical points, parameterized by $input_2$, along with similar curves from the other intersections. These curves are plotted together in a single diagram showing $input_2$ versus m_2. An example is given in Figure IV-2C.

All phase plane diagrams were constructed in Matlab 7.5.0. Simulations were performed using XPPAUT, available at http://www.pitt.edu/~phase [208].

C. Results

C-1. Model performance under normal conditions

It appears that late-E oscillations are not observed under normal metabolic conditions (see [41], see also Figure IV-3A1 and B at 5% of CO_2). Similarly, the late-E neuron in the model under "normal" conditions does not receive a strong "hypercapnic" drive (d_3) and is inhibited by the early-I neuron during inspiration and by the post-I neuron during expiration (Figure IV-1A,B). In this case, the behavior of the current model is equivalent to that of the model described in detail by [35] and the model demonstrates all the regimes simulated and investigated in that paper. The output activity of all neurons of the model, in a regime corresponding to breathing under baseline conditions, is shown in Figure IV-1B. During expiration, the post-I neuron output is elevated and demonstrates adapting (decrementing) activity that is defined by the dynamic increase in its adaptation variable m_{AD3} (see equation (*IV-5*)). The resulting decline in inhibition from the post-I neuron shapes the augmenting profile of aug-E activity. This reduction in post-I inhibition also produces a slow depolarization of pre-I/I and early-I neurons. In addition, the pre-I/I neuron depolarizes further because of the slow deinactivation of I_{NaP} (slow increase of h_{NaP}, see equation (*IV-13*)). Finally, at some moment during expiration, the pre-I/I neuron rapidly activates, providing excitation of early-I. The latter inhibits both post-I and aug-E, completing the switch from expiration to inspiration (Figure IV-1B). During inspiration, the pre-I/I and early-I outputs are elevated, and the inspiratory neuron outputs settle towards a corresponding equilibrium state. In particular, the early-I neuron demonstrates adapting (decrementing) activity (Figure IV-1B), defined by the dynamic increase in its adaptation variable m_{AD2} (see equation (*IV-5*)). The decline in inhibition from this neuron produces a slow depolarization of the post-I and aug-E neurons. Eventually, the system reaches a moment at which the post-I neuron rapidly activates and inhibits both inspiratory neurons (pre-I/I and early-I) and the aug-E neuron (initially), producing the switch from inspiration back to expiration (Figure IV-1B).

C-2. Emergence and quantum acceleration of late-E oscillations with progressive hypercapnia

It has been suggested that when late-E oscillations emerge within the RTN/pFRG, they project to and drive late-E bursts in the abdominal motor output [20], [42], [43] that can be seen in the abdominal nerve, AbN. Neurons whose activity clearly correlated with the AbN late-E discharges (including simultaneous burst missing) were found in the RTN/pFRG region, and a pharmacological inactivation of the RTN/pFRG abolished the AbN late-E activity [41]. Thus the AbN late-E discharges can be considered as an indicator of the corresponding oscillations in the RTN/pFRG [20], [41]–[43].

Figure IV-3 shows the integrated activities of phrenic (PN, active during inspiration), cervical vagus (cVN) and abdominal (AbN) nerves recorded from the *in situ* arterially perfused rat brainstem-spinal cord preparation with the progressive development of hypercapnia (increasing CO_2 concentration in the perfusate) (data are taken from [41]). Under baseline metabolic conditions (95% O_2, 5% CO_2) the AbN typically exhibits a low-amplitude post-inspiratory activity (Figure IV-3A and left part of B). Switching to hypercapnic (7–10% CO_2) conditions evokes large amplitude late-E (i.e., occurring at the very end of expiration) AbN bursts (indicating the emergence of RTN/pFRG oscillations, see above). Figure 3 shows that the late-E discharges emerge in AbN at 7% CO_2 (Figure

IV-3A2,B) followed by a progressive increase in the burst frequency as the CO_2 concentration is incremented to 10%. Importantly, although the frequency of late-E AbN bursts increases with CO_2, these bursts remain coupled (phase-locked) with the bursts in the PN and cVN (Figure IV-3A2-A4). With the development of hypercapnia, the ratio of late-E AbN burst frequency to the PN burst frequency shows a step-wise or *quantal* increase from 1:5 and 1:4 (seen in Figure IV-3B) to 1:3, 1:2, and, finally, to 1:1 (Figure IV-3A2-A4 and B). On returning CO_2 to the control levels, the ratio showed a step-wise reversal. Similar hypercapnia-evoked late-E AbN discharges phase-locked to PN, with a step-wise increase of their frequency with increasing CO_2 levels, have been demonstrated previously *in vivo* [173]. We call this process *quantal acceleration* of late-E AbN activity with development of hypercapnia.

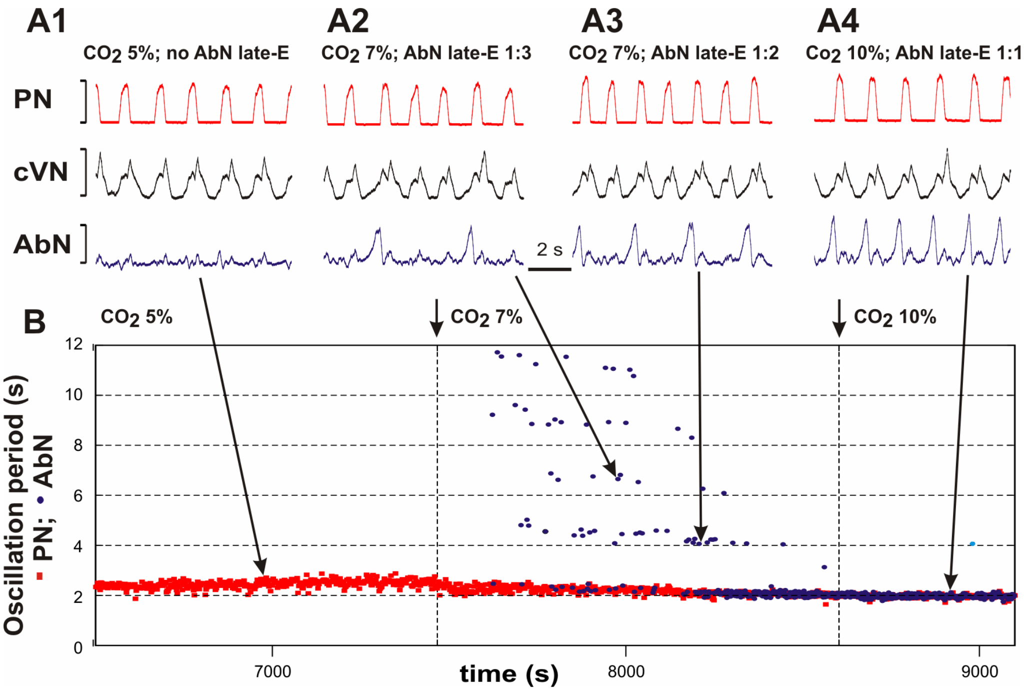

Figure IV-3. Quantal acceleration of AbN late-E activity with the development of hypercapnia in the *in situ* arterially perfused brainstem-spinal cord of juvenile rat (data from [41]). (A1-A4) Integrated activity of simultaneously recoded (top-down) phrenic nerve (PN, red), cervical vagus nerve (cVN, black) and abdominal nerve (AbN, blue). A1: Normocapnia (5% CO_2): late-E activity is absent in the AbN. A2-A4: Quantal acceleration of AbN activity: with the development of hypercapnia, the ratio between the AbN and PN frequencies goes through step-wise changes from 1:3 and 1:2 (A2 and A3, 7% CO_2) to 1:1 (A4, 10% CO_2). (B) Time-series representation of the entire experimental epoch with the oscillation periods in the PN (red squares) and AbN (blue circles) plotted continuously vs. time. The AbN late-E bursts were synchronized with the PN bursts with a ratio increasing quantally from 1:5 to 1:1. The content of CO_2 in the perfusate of this preparation was changed at times indicated by short arrows and vertical dashed lines. Large arrows indicate times corresponding to the episodes shown in A1-A4.

To simulate progressive increase of hypercapnia using our model, the excitatory "hypercapnic" drive d_3 to the late-E neuron (see Figure IV-1A) was progressively increased from $d_3 = 0$ (representing normocapnic conditions) to higher values ($d_3 \geq 1$) (Figure IV-4). The late-E neuron is a conditional burster, whose intrinsic rhythmogenic properties are defined by slowly inactivating I_{NaP} (see equation (*IV-16*)). If this neuron is isolated from the others, then with a progressive increase in excitatory drive its behavior evolves from a silent state to bursting, and then to tonic activity [125]–[127], [136]. In our model, the bursting activity in the late-E neuron is shaped by the excitatory drive to this neuron (d_3, simulating the effect of hypercapnia), the inhibitory synaptic inputs from the adapting early-I and post-I neurons (see Figure IV-1A), and the dynamics of I_{NaP} inactivation (h_5). The complex net effect of these factors is a step-wise decrease of the late-E bursting period with the progressive increase of hypercapnic drive to this neuron (d_3). Specifically, late-E bursts become 1:N synchronized with pre-BötC (pre-I/I and early-I) bursts, and a quantal increase in the ratio of late-E burst frequency to pre-BötC frequency (decrease in N) occurs as hypercapnic drive increases (see Figure IV-4A1-A3, B). Once the late-E neuron is activated, it excites the pre-I/I neuron which in turn excites early-I (Figure IV-1A). This cascade ends when the early-I neuron inhibits both expiratory neurons in the BötC and ultimately terminates the late-E burst.

The dependencies of the periods of late-E and pre-BötC oscillations on the "hypercapnic" drive to the late-E neuron are shown in the bifurcation diagram in Figure IV-4B. The late-E oscillation period changes in a stair-like manner with progressive increases in the drive to the late-E neuron. The late-E oscillations emerge at a particular drive to the late-E neuron near point **a** in Figure IV-4B. To the right from this point, the ratio of late-E to pre-BötC burst frequencies is 1:5. A further increase of the drive causes a quantal acceleration of the late-E frequency (with a 1:4 ratio to the pre-BötC frequency between points **b** and **c**; 1:3 between points **c** and **d**; 1:2 between points **d** and **e**) until a steady 1:1 synchronization with the pre-BötC oscillations is achieved (to the right from point **e**).

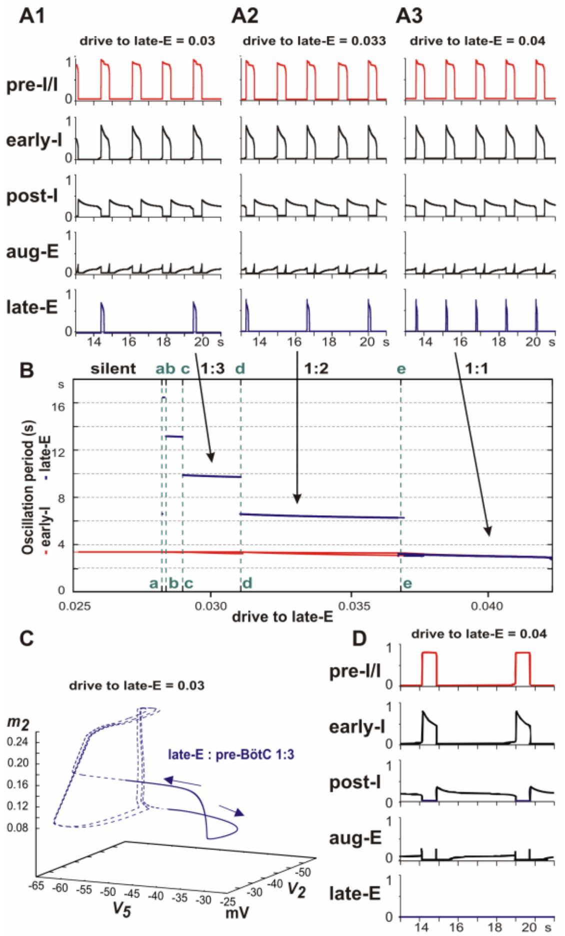

Figure IV-4. Increasing drive (d3) to the late-E neuron, applied to simulate “progressive hypercapnia”, results in the emergence and “quantal acceleration” of late-E oscillations in RTN/pFRG. (A1-A3) The frequency of late-E activity proceeds through synchronization regimes with ratio of 1:3 (A1), 1:2 (A2), and 1:1 (A3) relative to the pre-BötC/BötC frequency. (B) Bifurcation diagrams of late-E (blue) and pre-BötC (red) periods as functions of drive to late-E. The late-E period quantally decreases through a series of jumps; the drives to late-E at which the jumps occur are denoted by vertical green dashed lines, marked with the letters a through e. Drives below point a are not high enough to produce late-E neuron activity. Between points a and e late-E activity accelerates from 1:5 (one late-E burst per five pre-BötC bursts) to 1:1. (C) The trajectory of the network model projected to the (V_5, V_2, m_2) phase subspace during hypercapnia in the 1:3 regime (shown in A1). Subthreshold late-E neuron activity (dashed blue line) occurs when V_5 is below -50mV. Superthreshold late-E neuron activity (solid blue line) corresponds to bursts of the late-E seen in A1 (when d3=0.03). Cyclical subthreshold movement in (V_2, m_2) indicates two periods of early-I activity during which the late-E neuron fails to burst (see text for more details). (D) Simulation of the effect of blocking the persistent sodium current in the model. After 1:1 synchronization is achieved (as in A3), $\bar{g}_{NaP}$ is set to zero. Expiration increases in duration, pre-I activity decreases in amplitude, and the late-E neuron falls silent.

The dynamics of sub-threshold and supra-threshold changes in the membrane potential of the late-E neuron (V_5) corresponding to the 1:3 regime of synchronization (d_3 = 0.3, same as in Figure IV-4A1) is shown in Figure IV-4C as a trajectory in the (V_5, V_2, m_2) phase space. After the initial activation of the late-E neuron (supra-threshold V_5), V_2 quickly increases due to the cascading excitation from late-E to pre-I/I and from pre-I/I to early-I (rightward arrow in Figure IV-4C). As V_2 exceeds the threshold, the early-I neuron is activated and m_2 begins gradually increasing. When V_2 becomes sufficiently elevated, the early-I neuron inhibits the late-E neuron, sending V_5 to a sub-threshold state (leftward arrow in Figure IV-4C).

Simulation results demonstrating the effect of I_{NaP} suppression on the late-E and BötC/pre-BötC oscillations during hypercapnia are shown in Figure IV-4D. All parameters in this simulation are the same as in Figure IV-4A3, but $\bar{g}_{NaP}$ is set to zero in both pre-I/I and late-E neurons. One can see that the suppression of I_{NaP} in the network fully abolishes the late-E oscillations, which are critically dependent on this current in our model, but does not stop the network BötC/pre-BötC oscillations. The latter persist with a reduced frequency and slightly reduced amplitude.

Figure IV-5A-D illustrates and explains the mechanisms providing the above quantal acceleration of late-E oscillations and their synchronization with the BötC/pre-BötC oscillations. In Figure IV-5A, the state of the late-E neuron is considered in the (V_5, h_5) plane. Two pairs of V_5 nullclines are drawn. We use these nullclines to give a preliminary illustration of how hypothetical changes in the level of inhibition and drive (d_3) to the late-E neuron can shape the model activity. For this demonstration, we simulate the late-E neuron in isolation and manipulate the synaptic inhibition artificially. The solid pair of nullclines is representative of relatively low d_3 values, while raising d_3 lowers the nullclines, as illustrated by the dashed pair. If the inhibition to the late-E neuron is on, then the V_5 nullcline is elevated, as represented by the nullcline at higher h_5 values within each pair. If this inhibition is instantaneously reduced to zero, then the V_5 nullcline assumes a new, lower, position in the space, as illustrated by the nullcline at lower h_5 values within each pair. Note that three of the V_5 nullclines shown have cubic shapes, each consisting of a left branch (LB) and a middle branch (MB) that meet in a point, which we call the left knee (LK), and a right branch (RB), which meets MB at the right knee (RK). Importantly, the positions of the knees depend on the levels of drive and inhibition to the late-E neuron, as is evident in Figure IV-5A.

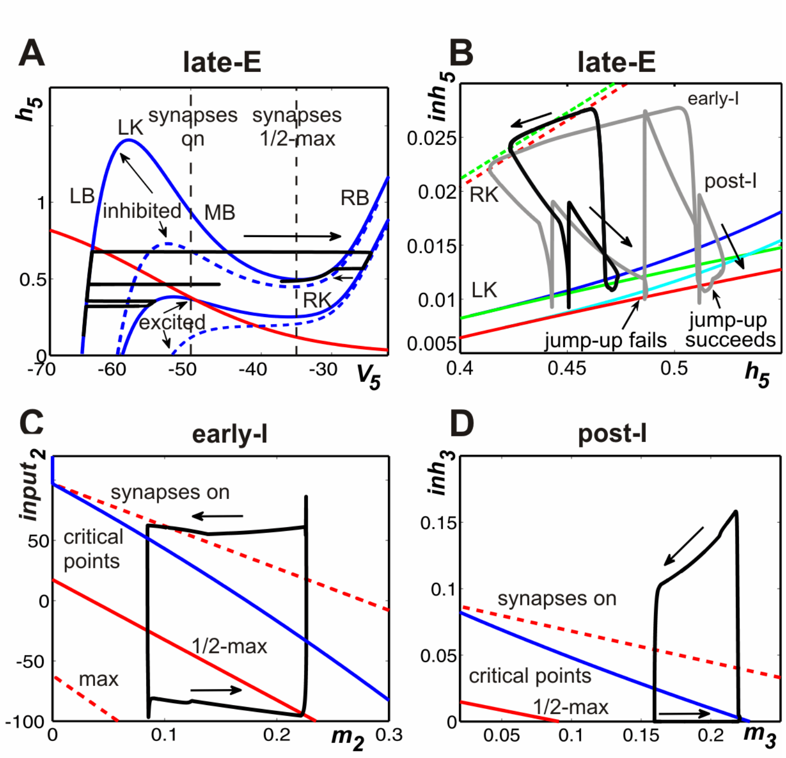

Figure IV-5. Phase plane analysis of model performance during "hypercapnia." (A) Projection of model trajectory to the (V_5, h_5) phase plane together with V_5 nullclines corresponding to intermediate and high values of d_3 (solid and dashed blue curves, respectively) and the nullcline for the slow variable, h_5 (red curve). The upper V_5 nullclines correspond to higher inhibition than do the lower ones. The trajectory shown undergoes three excursions, namely a failed burst (lowest h_5), a successful burst that is prematurely terminated by the return of inhibition (middle h_5), and a successful burst that temporarily survives the return of inhibition (highest h_5). Vertical dashed black line marked "synapses on" shows the lower threshold of the voltage-to-activity function *f(V)* defined by equation (*IV-12*). (B) Trajectories during 1:1 and 2:1 activity regimes (black and grey curves, respectively) projected to the (h_5, inh_5) plane, together with curves for the right (dashed) and left (solid) knees of the V_5 nullcline. Different curves of knees correspond to d_3 values that produce 2:1 (red) and 1:1 (green) regimes. As shown in A, increasing inhibition moves the nullcline to lower voltages and makes the cubic-like shape more pronounced, thus raising the value of h_5 at each knee. A trajectory must cross the curve of left knees for the late-E neuron to become active. Curves of critical points of the (V_5, h_5) equations on the left branch of the V_5 nullcline are shown in blue (1:1 regime) and light blue (2:1 regime). (C), (D): Trajectories projected to show early-I (C) and post-I (D) dynamics, along with curves of critical points of the (V_2, m_2) and (V_3, m_3) equations (blue) and synaptic thresholds (red). The synaptic thresholds represent the values of $input_2$ and m_2 or inh_3 and m_3 at which each neuron will reach voltages of -50 ("on", upper dashed), -35 ("half max", solid red), and -20 ("max", lower dashed, not shown in D) if it evolves on its voltage nullcline. Each m variable increases while the corresponding neuron is active (rightward arrows) and decreases while the neuron is silent (leftward arrows).

A trajectory of the model solution with the lower level of d_3 (solid nullclines), starting at the initial condition $(V_5, h_5) \approx (-65,0.15)$, is shown in black in Figure IV-5A. In this example, we manipulate the level of inhibition to the late-E neuron, purely to illustrate the effects that changes in inhibition can have on late-E neuron dynamics. As time advances from zero, h_5 increases, corresponding to deinactivation of I_{NaP}. In this particular simulation, when $h_5 \approx 0.35$, we turned off the inhibition to the late-E neuron and the trajectory jumped to the lower solid V_5 nullcline. The position of this nullcline prevents V_5 from crossing the synaptic activation threshold (-50 mV; "synapses on" in Figure IV-5A) and exciting the pre-I neuron. We subsequently restored inhibition, which caused the trajectory to return to the elevated V_5 nullcline. A second withdrawal and return of inhibition was imposed with $h_5 \approx 0.45$. The trajectory could not reach the RB of the V_5 nullcline, even though it was above the LK, because the inhibition was restored too quickly. With a still higher value of h_5, namely $h_5 \approx 0.6$, a third removal of inhibition was performed and the trajectory reached the right branch of the V_5 nullcline, corresponding to full late-E neuron activation. Furthermore, when inhibition was subsequently restored again, the late-E neuron remained active (on a RB) for some additional time, as illustrated by the trajectory segment on the far right of Figure IV-5A (leftward arrow), due to the relative nullcline positions. This same mechanism is the reason why the activation of the early-I neuron does not immediately terminate late-E activity in the network rhythm (e.g. Figure IV-4), even though early-I inhibits late-E. Ultimately, the late-E activity is terminated when h_5 reaches the RK of a V_5 nullcline, causing a decrease in V_5 that returns the late-E neuron to a sub-threshold state on the LB.

In summary, we see that because of the significant difference in rates of evolution of V_5 and h_5, the late-E cell will head toward the synaptic activation thresholds if the solution trajectory in the (V_5, h_5) phase plane lies above the LK corresponding to the levels of drive and inhibition that it is receiving, although it may fail to reach them if inhibition increases sufficiently fast. As inhibition decreases, the LK moves to lower values of h_5, making it easier for the late-E cell to activate, and the RK moves lower as well. Increases in inhibition have the opposite effects, but an abrupt increase in inhibition will not terminate late-E activity if it arrives after the late-E neuron is on the RB and the trajectory remains above the resulting RK.

This discussion makes clear that it is the frequency with which the solution trajectory can rise above the left knee of the V_5 nullcline in the (V_5, h_5) plane that determines which of the 3:1, 2:1, and 1:1 (pre-BötC:late-E) synchronization regimes occurs in Figure IV-4. Figure IV-5B illustrates the qualitative differences between the 2:1 and 1:1 regimes in the (h_5, inh_5) plane. This diagram includes LK curves, RK curves, and curves of critical points for each of the two regimes. Indeed, since the inhibition to the late-E neuron varies continuously, it is not so useful to show a small number of particular nullclines in the (V_5, h_5) plane, as in Figure IV-5A. Since the knee positions depend on the level of inhibition to the late-E neuron, and V_5 is fixed as a function of (h_5, inh_5) at each knee, it is useful to generate curves of knees, indicating how the h_5 coordinates of LK and RK depend on inh_5, in the (h_5, inh_5) plane. These curves are shown as solid (LK) and dashed (RK) red (2:1 regime) and green (1:1 regime) curves in Figure IV-5B. Similarly, the critical point where the V_5 and h_5 nullclines intersect varies with inh_5 (e.g., Figure IV-5A). This critical point may lie on the LB or MB of the V_5 nullcline and moves from the LB to the MB as inhibition decreases or drive increases. The light (2:1 regime) and dark (1:1 regime) blue curves in Figure IV-5B show the relationships between the h_5 coordinates of the critical point and inh_5 for those values of inh_5 that are large enough such that the critical point lies on the LB. Two trajectories (black and grey) are plotted along with the LK, RK, and critical point curves. The trajectory shapes reflect an asymmetry present in the inhibition to the late-E neuron: smaller values of inh_5 arise during periods of post-I inhibition, and larger values correspond to periods of early-I inhibition. As noted previously, for a fixed value of inh_5, the h_5 coordinate of a trajectory must exceed the $h_5$value at the LK of the V_5 nullcline for the trajectory to reach elevated V_5 values, corresponding to late-E activation. In Figure IV-5B, since h_5 is on the horizontal axis, jump-up requires the trajectory to move to the right of the relevant (solid) LK curve.

Now, we are ready to consider the regime of 1:1 synchronization between the late-E and pre-I/early-I neurons, as illustrated by the black trajectory in Figure IV-5B. The upper part of this trajectory, labeled by the leftward arrow, corresponds to a period when the late-E neuron is active and excitation from late-E to pre-I has allowed the pre-I and early-I neurons to become active as well, inducing a large inh_5. When the late-E neuron reaches the RK (dashed green curve), it jumps to the LB and becomes inactive, and thus h_5 starts to increase, while inh_5 slowly decreases due to adaptation of early-I. When the early-I neuron becomes inactive, inh_5 sharply decreases and the trajectory is able to cross the LK curve (lower left spike in the black trajectory in Figure IV-5B crosses the solid green curve) but the post-I neuron activates and inhibits the late-E neuron before the late-E can activate, just as in Figure IV-5A (middle spike in trajectory). This leads to the post-I phase, corresponding to the part of the black trajectory labeled with the downward right arrow.

During this phase, h_5 continues to increase and the post-I neuron adapts, causing inh_5 to drift down again. This time, the late-E neuron can cross the LK curve and activate (loop structure in the lower part of the black trajectory in Figure IV-5B). Activation of late-E is quickly followed by early-I activation, resulting in a sharp increase in inh_5, and the 1:1 cycle repeats.

The grey trajectory in Figure IV-5B is similar to the black one but corresponds to the 2:1 regime. The key difference between the two cases is labeled “jump-up fails”. There, we see that the 2:1 trajectory reaches the LK (red solid) curve during expiration but is hit with a strong inhibition (increase in inh_5) due to a second activation of the pre-I/early-I neurons, which prevents the late-E neuron from becoming active. The end of the second pre-I/early-I phase is followed by post-I activation as previously (rightmost down-up spike along the grey trajectory) and subsequent post-I adaptation (downward arrow along grey trajectory), after which the late-E neuron finally crosses the LK curve and activates near the label “jump-up succeeds” in Figure IV-5B. Interestingly, we note that the value of h_5 when late-E activation fails in the 2:1 regime is greater than the value when it succeeds in the 1:1 regime. Indeed, an increase in drive to late-E hampers I_{NaP} deinactivation (lowers h_5), but it can promote late-E activation nonetheless because of how it lowers the LK curve, decreasing the level of I_{NaP} required for late-E to cross it. Moreover, the failure of the late-E neuron to activate on particular cycles occurs because the pre-I/early-I neurons activate first, not because the late-E is insufficiently excitable. This observation yields the prediction that a decrease in pre-I and early-I excitability would be sufficient to prevent or reduce late-E cycle skipping.

So far, our analysis has illustrated how late-E activity is determined by its phase plane structures. We can also use this type of analysis to explain why the early-I oscillation period remains roughly constant as the drive to the late-E neuron is varied (Figure IV-4B). A key point is that transitions between phases can occur through distinct mechanisms known as escape and release (see also [35], [209]–[211]). It turns out that even under hypercapnic conditions, the early-I activity in the model is initiated primarily by escape, such that the excitation it receives from pre-I, and by extension the excitation from late-E to pre-I, has little effect on the timing of inspiration onset. This point is illustrated in Figure IV-5C. There, the trajectory shown approaches the blue curve of critical points in the direction of increasing m_2 while the early-I neuron is active, and hence adapting (rightward arrow; recall that negative $input_2$ corresponds to excitation from pre-I), and from the direction of decreasing m_2 while the early-I neuron is silent, and hence recovering from adaptation (leftward arrow; positive $input_2$ corresponds to inhibition from post-I and aug-E). The red curves show the places where the early-I voltage hits the synaptic thresholds V_{min} (synapses start to activate, upper dashed red curve), V_{max} (synapses reach maximum strength, lower dashed red curve), and $(V_{min} + V_{max})/2$ (solid red curve) from equation (*IV-12*), assuming that the projection of the trajectory to the (V_2, m_2) plane lies on the V_2 nullcline, which is true except during fast voltage excursions at phase transitions. While the early-I neuron is silent, the trajectory reaches the V_{min} curve at a high $input_2$ value, corresponding to strong inhibition. Indeed, even as the post-I neuron adapts (Figure IV-5D, bottom trajectory segment/rightward arrow), the aug-E activity ramps up, yielding a roughly constant inhibition to the early-I neuron. The crossing of the V_{min} curve by the early-I neuron allows the early-I neuron to start inhibiting the expiratory neurons, which quickly suppresses their activity (e.g., Figure IV-5D, rightmost vertical trajectory segment). Thus, the early-I neuron escapes from the silent phase to the active phase, while the expiratory neurons become silent. This escape is independent of the activation of the late-E neuron and hence a constant early-I neuron period is maintained as d_3 is varied. Importantly, this invariance of period is also maintained if the model is tuned such that it is pre-I escape, rather than early-I escape, that initiates the inspiratory phase.

Activation of the post-I neuron occurs in a different manner than that described above, namely by release from early-I inhibition. Indeed, while the post-I neuron is silent, the inhibition it receives from the early-I neuron (inh_5) gradually decreases (Figure IV-5D, upper trajectory segment/leftward arrow) as m_2 increases and V_2 decreases correspondingly (Figure IV-5C, bottom trajectory segment). This release allows the post-I neuron eventually to cross the synaptic activation threshold and inhibit the early-I and pre-I neurons. Interestingly, the late-E neuron is gradually released from inhibition in parallel with the release of the post-I neuron. This common release provides a shared window of opportunity for post-I and late-E activation. In the hypercapnic parameter regimes that we simulated, post-I always activates first and suppresses the late-E neuron, but it is possible that in other regimes, corresponding for example to different experimental contexts, an earlier late-E activation could occur.

C-3. Transforming the late-E pattern to biphasic-E activity with development of hypoxia

Abdominal motor activity with a biphasic-E profile, consisting of late-E (pre-I) and post-I components, was recorded *in vivo* from decerebrate neonatal rats [20], [42]. This abdominal activity pattern was similar to the pattern of single neuron activity recorded from the RTN/pFRG region of the *in vitro* isolated brainstem-spinal cord preparation of neonatal rats [37], [38]. The issue of whether the biphasic-E pattern (in both RTN/pFRG and AbN) is a specific characteristic of neonates which transforms to late-E during development or is a characteristic of the specific metabolic conditions of the *in vitro* preparation (e.g., hypercapnic hypoxia or anoxia) remains unresolved [41], [174], [181], [182], [212], [213]. In the *in situ* preparations, the biphasic-E AbN activity was more readily evoked in neonates than in juvenile animals [41]. However, transient biphasic-E AbN discharges can be evoked *in situ* under specific conditions, such as hypercapnic anoxia (7% CO_2, 93% N_2) or recovery from anoxia-induced central apnea [41]. Exposing the system to hypoxia (low O_2) or anoxia (no O_2) results in suppression of post-I activity [214]. In the experimental results shown in Figure IV-6, we illustrate the consistent finding that transformation of the late-E AbN bursting to a biphasic-E bursting pattern during hypercapnic anoxia is accompanied by a corresponding reduction/suppression of post-inspiratory activity in the cVN. We suggest that the lack of post-I activity elsewhere in the network appears essential for the expression of the post-I component of the biphasic-E AbN discharge pattern.

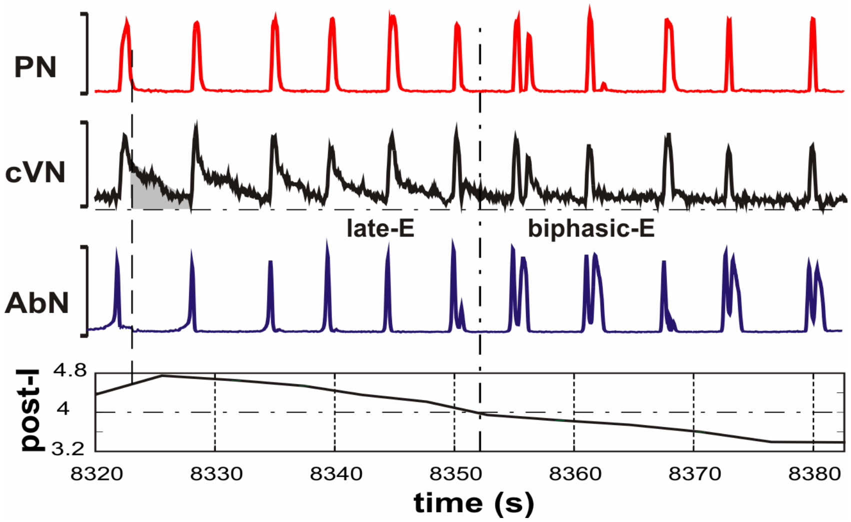

Figure IV-6. Transformation of the pattern of AbN activity from late-E (pre-I) bursting to biphasic-E discharge during hypercapnic anoxia (7% CO_2, 93% N_2, 0% O_2). The top tree traces show integrated activity of PN, cVN and AbN. The bottom trace represents the index of post-I activity calculated as an averaged activity in cVN during the expiratory phase in each cycle (an example is shown as the gray area in the cVN trace); the expiratory phase was defined by the absence of activity in the PN trace (the vertical dashed line across the first cycle of integrated activity indicates the onset of expiration for the first cycle shown in this example). In the first half of the recorded episode, only late-E bursts were present in AbN. The post-I component of cVN gradually decreased. The transition of AbN bursts to a biphasic-E discharge pattern (with pre-I and post-I components) occurred after a significant suppression of the cVN post-I activity (indicated by vertical and horizontal dash-dotted lines).

It was suggested that the post-I component of the biphasic-E activity pattern represents a post-inhibitory rebound resulting from the abrupt termination of inspiration and a corresponding rapid release of late-E neurons from inspiratory inhibition [174], which is normally suppressed by post-I neurons.

The activity of post-I neurons has been shown to depend on the pontine input or drive [18], [184]. Thus, to simulate hypercapnic hypoxia conditions, we set d_3 =0.04 (producing 1:1 coupling between late-E and pre-BötC oscillations during hypercapnia, see Figure IV-4A3,B) and decreased pontine drive from d_1 =1 to zero linearly over time. Figure

IV-7A shows the result of our simulation. With the linear decrease of pontine drive, the late-expiratory burst of the late-E neuron is transformed first to a rebound post-I burst and then to a biphasic-E activity with late-E and post-I components. Simultaneously, a reduction and, finally, a full suppression of activity of the post-I neuron occurs (Figure IV-7A).

Figure IV-7B shows the bifurcation diagram representing the periods of late-E and pre-BötC oscillations as functions of pontine drive. To generate this diagram, we reduced d_1 in a sequence of steps (left to right) from d_1=1 to d_1=0 and simulated the model dynamics for each fixed value of d_1. The red and blue bifurcation curves show the time intervals between successive activations of the early-I and late-E neurons, respectively. When the pontine drive is strong enough (prior to point **a** in Figure IV-7B), late-E neuron activity occurs in a single burst at the end of expiration (late-E or pre-I) with a 1:1 coupling to the pre-BötC activity. The system then proceeds through a series of bifurcations until point **d**, when late-E neuron activity settles into a post-I pattern. At point **a,** a bifurcation happens that splits (doubles) the period curves but bursts by late-E and pre-BötC neurons remain phase-locked (1:1). In the region between points **b** and **d,** the timing of bursts of late-E neuron activity varies between pre-I (i.e., just before the early-I phase) and post-I, with post-I

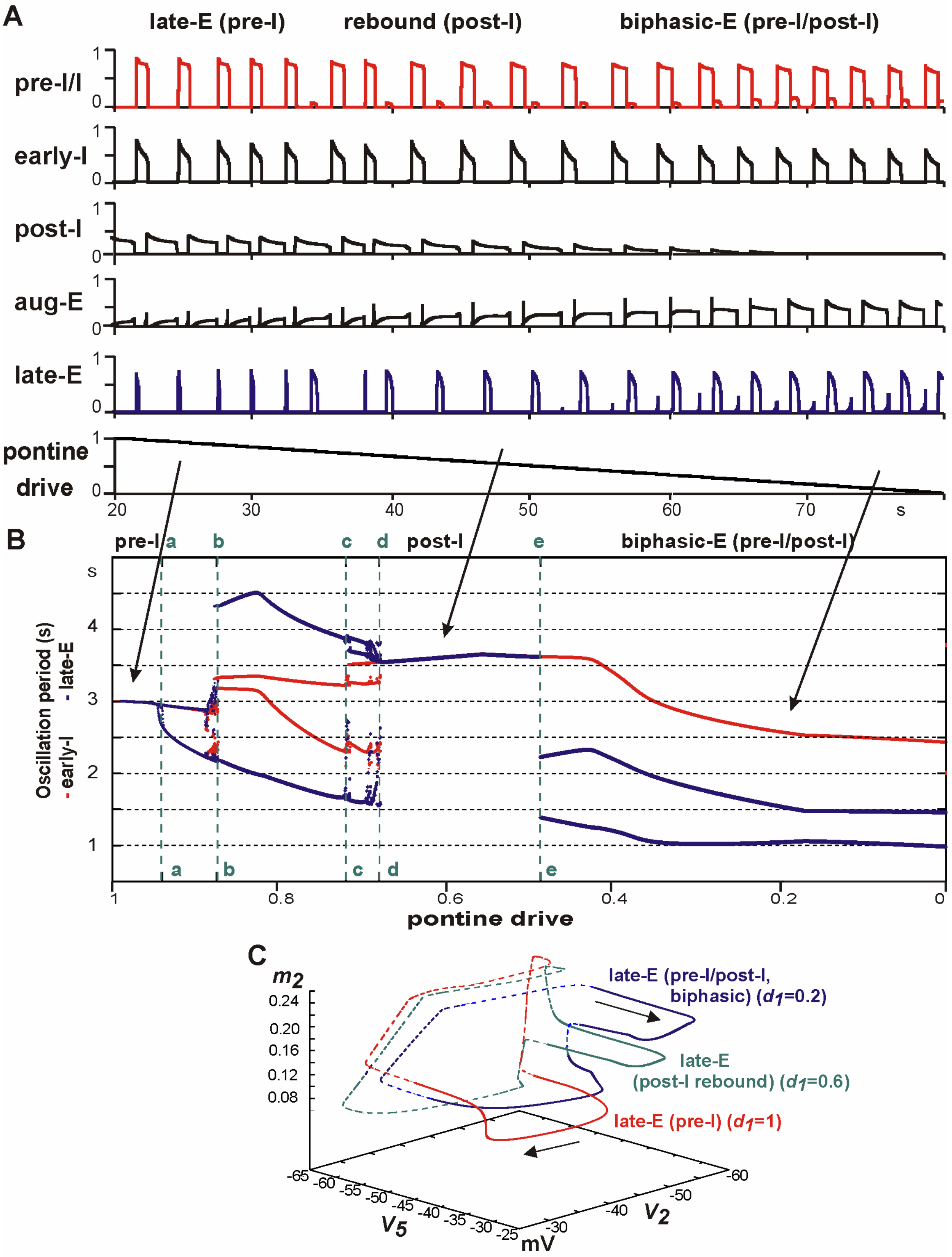

Figure IV-7. Simulation of “hypercapnic hypoxia” conditions. The “hypercapnic” drive was set to d_3=0.04 (producing 1:1 coupling between late-E and pre-BötC oscillations, see

Figure IV-4 A3,B). (A) Changing model performance with a linear reduction of pontine drive from d_1 =1 to zero (lower trace) applied to simulate the development of ”hypoxia”. With the reduction of pontine drive, the activity of the post-I neuron weakens and, finally, becomes fully suppressed by inhibition from the aug-E neuron. Simultaneously, the late-expiratory burst of the late-E neuron is transformed first to a rebound post-I burst and then to a biphasic-E activity pattern with pre-I and post-I components. (B) Bifurcation diagram showing the periods of late-E neuron and early-I neuron oscillations as functions of pontine drive d_1 (indicated on the bottom axis). The diagram shows that with the progressive reduction of pontine drive, the system proceeds through a series of bifurcations indicated by points **a** – **e** and the vertical dashed green lines (see details in the text). (C) Trajectories in the (V_5, V_2, m_2) subspace at three levels of pontine drive: unsuppressed (d_1 =1, red), reduced to 60% (d_1 =0.6, green), and reduced to 20% (d_1 =0.2, blue) of the initial value, while the hypercapnic drive to the late-E neuron is held constant (d_3 =0.04, hypercapnia).

becoming more common as pontine drive increases. Specifically, in the (**b**,**c**) interval, late-E neuron bursts alternate between pre-I and post-I. Then, to the right from **c**, two out of every three late-E bursts occur during the post-I phase, and so on. This sequence converges at point **d**. The transitions between these regimes likely occur through chaotic behavior (note the spread in periods in the vicinity of the points **b**, **c** and **d**). The period of the pre-BötC neurons does not undergo any further jumps as late-E neuron activity transitions from a post-I type to a biphasic-E response (point **e**). At point **e,** the post-I activity becomes weak enough to allow for the emergence of second late-E neuron bursts in the pre-inspiratory phase. This converts the shape of late-E neuron activity to a biphasic-E (pre-I/post-I) discharge.

Figure IV-7C shows projections of typical trajectories to the (V_5, V_2, m_2) subspace, corresponding to three levels of pontine drive (unsuppressed pontine drive, d_1 =1, red; 40% suppression, d_1=0.6, green; and 80% suppression, d_1=0.2, blue), while the hypercapnic drive to the late-E neuron is held constant (d_3=0.04, hypercapnia). Periods of sub- and supra-threshold late-E neuron activity are distinguished by dashed and solid lines, respectively. When d_1=1, a 1:1 late-E to pre-I/I and early-I synchronization is observed, and therefore all instances of supra-threshold V_2 activity are preceded by supra-threshold V_5 activity. Once supra-threshold V_2 activity is achieved, m_2 begins to increase, and soon thereafter, V_5 rapidly drops due to inhibition from the early-I. After termination of late-E neuron activity, m_2 continues to increase and causes a gradual decrease in V_2, until the post-I neuron is released and early-I neuron activity ends (Figure IV-7C-D). Finally, after V_2 has decreased to a minimum, there is a small decrease in V_5 as inhibition from the post-I neuron takes over and expiration begins. During expiration, m_2 resets to its initial value before the late-E neuron bursts again and restarts the cycle. For d_1=0.6 (green trajectory), the periods when V_2 and V_5 are supra-threshold have become separate. At the end of inspiration, m_2 begins to decrease and a V_5 rebound emerges. During the rebound, V_2 remains unchanged and no supra-threshold activity is observed until m_2 reaches its minimum, well after V_5 activity has ended. The inspiratory phase, marked by an increase in V_2, begins after m_2 reaches its minimum; this phase then terminates similarly to the trajectory corresponding to d_1=1. When the pontine drive is further suppressed (d_1=0.2, blue) a biphasic-E pattern is observed. Following the termination of inspiration, an immediate increase in V_5 to supra-threshold activity is observed. This rebounding activity occurs while m_2 is still quite elevated and terminates earlier in the expiratory phase than it does when d_1=0.6. After V_5 returns to its sub-threshold state, m_2 continues to decrease and a second increase in V_5 precedes the emergence of supra-threshold V_2 activity. V_2 begins its increase with a larger value of m_2 than in the other cases, presumably due to excitation received from the late-E neuron, which allows it to overcome some residual adaptation. V_5 then begins to decrease as V_2 and m_2 increase, and inspiration ensues as previously.

Figure IV-8A-D illustrates and explains the mechanisms providing the transformation in the pattern of late-E neuron activation. In Figure IV-8A-C, the behavior of the late-E neuron is considered in the (V_5, h_5) plane for the regimes shown in Figure IV-7C. The positions of the V_5 nullclines in this plane are crucial for determining the late-E behavior. The uppermost nullcline in each plane arises when the late-E neuron is maximally inhibited by the early-I neuron. The next nullcline down arises at the onset of post-I neuron activity. As d_1 is decreased, the peak in post-I neuron activity is reduced and hence the inhibition from the post-I to the late-E neuron weakens, changing the position that the V_5 nullcline takes during post-I neuron activity. Finally, post-I inhibition gradually decreases during expiration, causing the V_5 nullcline to move progressively lower, and certain examples of resulting nullcline positions, occurring at important moments in the evolution of each solution, are also shown.

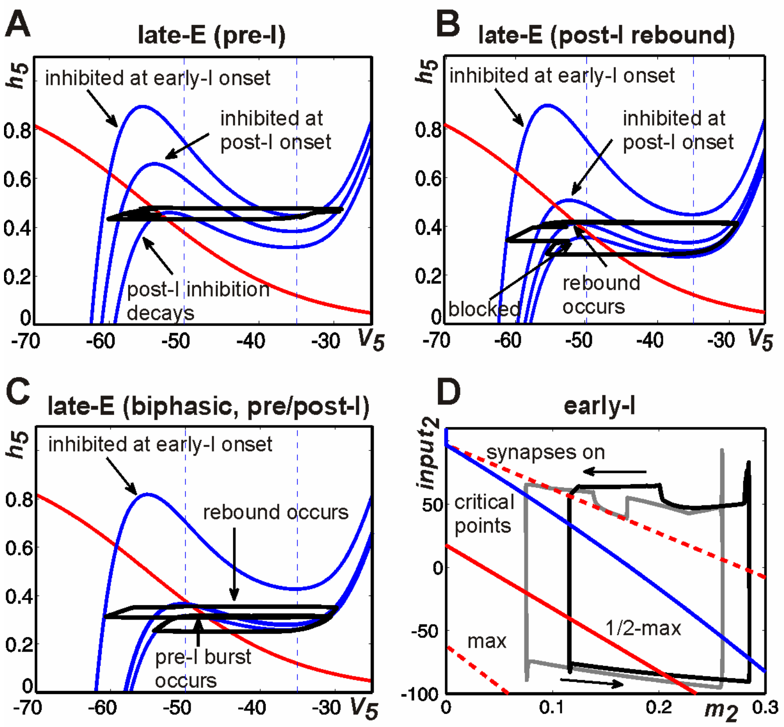

Figure IV-8. Phase plane analysis in case of hypercapnic hypoxia. (A)-(C) Blue curves show V_5 nullclines for various levels of inhibition to the late-E neuron while red curves show the h_5 nullcline. (A) For d_1=1, V_5 nullclines shown correspond to the inhibition to the late-E neuron at the start of early-I activity (top), at the start of post-I activity (middle), and at the moment when late-E activates (bottom). (B) When pontine drive is reduced to 60% of the default value (d_1=0.6), the late-E neuron exhibits only "rebound" bursts during the post-I phase. The top three V_5 nullclines shown are analogous to those in A, although the positions of the middle and lower of these three differ due to different levels of post-I activation. The lowermost V_5 nullcline corresponds to the level of inhibition to the late-E neuron at the onset of early-I activity. (C) When pontine drive is reduced to 20% (d_1=0.2), biphasic late-E neuron activity occurs. The V_5 nullclines shown correspond to the inhibition to the late-E neuron at the start of early-I activity (top), at the start of post-I activity (middle), and just before the onset of early-I activity (bottom). The nullcline corresponding to the moment when the late-E neuron undergoes rebound activation (analogous to the bottom nullcline in A) is omitted due to its proximity to the middle nullcline shown. (D) Projection of model trajectories to the ($input_2$, m_2) plane at pontine drive reduced to 60% (d_1=0.6, grey, rebound regime) and to 20% (d_1=0.2, black, biphasic regime), along with curve of critical points (blue) and synaptic threshold curves (red; as in Figure IV-5). In the both regimes, the dip in the trajectory at high $input_2$ occurs when rebound activation of the late-E neuron happens, because the pre-I neuron is slightly activated and hence a small excitation to the early-I neuron (decrease in $input_2$) results (see text for further details).

When d_1= 1, the mechanism for the pre-I activation of the late-E neuron is rather straightforward. As the post-I neuron adapts and its inhibition to the late-E neuron weakens, the LK of the V_5 nullcline eventually dips below the trajectory in the (V_5, h_5) plane, which allows the late-E neuron to jump to high voltage (Figure IV-8A). As discussed with respect to Figure IV-5A and Figure IV-6C, by the time this happens, the early-I neuron is ready to activate on its own, such that the late-E neuron's activity ends up occurring just before the onset of inspiration, and the pre-I regime of late-E neuron activation results.

When the pontine drive is reduced, the post-I neuron achieves a lower level of activity and thus the inhibition to the late-E neuron during the post-I phase is weaker than in the case of full drive. Thus, the V_5 nullcline drops below the trajectory, allowing late-E activation earlier in the post-I phase, which we call post-I rebound (Figure IV-8B). This activation of late-E could potentially recruit the early-I neuron but in fact fails to do so. Indeed, we observe that the pre-I neuron cannot strongly activate in response to this earlier late-E activation, because it has not had enough time to recover and overcome the inhibition it receives from the post-I and aug-E neurons (Figure IV-7A). The weak activation of the pre-I neuron is insufficient to activate the early-I neuron (Figure IV-7A; Figure IV-8D, grey trajectory: note that the dip in the upper part remains just above the dashed synaptic threshold curve). Since it does not immediately precede inspiratory activity, the activation of the late-E neuron cannot be labeled as pre-inspiratory in this case. Indeed, it is likely that the various, possibly chaotic regimes arising between the pre-I and post-I rebound cases as d_1 is reduced (Figure IV-7B) involve shifts in the timing of late-E neuron activation relative to the onset of pre-I/early-I neuron activity. Finally, although the late-E neuron's activity ends before pre-I/early-I neuron activity starts, and the trajectory in the (V_5, h_5)

plane returns back to the LB of the V_5 nullcline, this trajectory lies below the knee of the relevant V_5 nullclines, determined by the inhibition from the post-I neuron to the late-E neuron, until the early-I neuron activates and strongly inhibits the late-E neuron, pushing the trajectory back to the upper V_5 nullcline (Figure IV-8B, "blocked").

When the pontine drive becomes lower still, this last observation no longer holds. The late-E neuron's post-I rebound occurs earlier in the post-I phase (also evident in the early-I neuron's dynamics as the dip in the top part of the black trajectory in Figure IV-8D), so that h_5 has more time to recover before the early-I neuron activates, and furthermore, the LK of the V_5 nullcline is lower throughout the post-I phase because the post-I neuron's activity is weaker. Thus, the trajectory is able to climb above the knee of the V_5 nullcline and activate the late-E neuron a second time before the early-I neuron becomes active (Figure IV-8C, "pre-I burst occurs"). This second late-E activation yields enough activation to pull the early-I neuron into the active phase before it reaches the synaptic threshold on its own. The fact that excitatory input plays a role in recruiting the early-I neuron can be seen from the fact that the black trajectory in Figure IV-8D lies above the top dashed ("synapses on") curve when it suddenly undergoes a near-vertical drop, corresponding to synaptic excitation of the early-I neuron (via excitation of the pre-I neuron by the late-E neuron) and resulting in the onset of the inspiratory phase.

The recruitment of the early-I neuron by the late-E neuron in the biphasic regime, which we have identified using phase plane analysis, explains the decrease in early-I oscillation period that occurs as pontine drive decreases in the biphasic-E regime, as shown in Figure IV-7B. Interestingly, this decrease occurs despite the increase in the aug-E activity level and, correspondingly, in the level of inhibition that the aug-E neuron sends to the pre-I and early-I neurons. In addition to explaining this aspect of how period changes with pontine drive, our analysis makes a clear prediction that post-I rebound occurs as a natural intermediate state between regimes in which late-E neuron activation is a pre-I event and those in which late-E neuron activation is biphasic: in the model, as post-I neuron activity weakens, late-E neuron activity can emerge earlier in the respiratory period via rebound, but only with additional post-I weakening can the late-E neuron activate a second time before the pre-I/early-I neurons are activated and suppress the late-E neuron.

C-4. Quantal slowing of pre-BötC oscillations

“Quantal slowing” of breathing is a phenomenon in which the average breathing frequency is reduced as a result of the skipping of output bursts in the pre-BötC or phrenic motor output while RTN/pFRG or related abdominal oscillations are maintained [42], [172]. Experimentally, this phenomenon was demonstrated by administration of μ-opioid agonists, such as DAMGO or fentanyl, which was suggested to suppress excitability of pre-BötC neurons [42], [172].

To simulate quantal slowing in the model, we started from conditions of “hypercapnic hypoxia”, established by increasing the “hypercapnic” drive to d_3=0.04 and reducing pontine drive to d_1=0.4, so that the late-E neuron expressed biphasic-E busts with 1:1 coupling to the pre-BötC oscillations (see Figure IV-7A, Figure *IV*-9A). Pre-BötC depression was simulated by a progressive reduction of the maximal conductance of excitatory synaptic inputs ($\overline{g}_{SynE},\ i \in \{1,2\}$; the default value is 10 nS) in both pre-BötC neurons (pre-I/I and early-I). The results of the quantal slowing simulation are shown in Fig. 9A, where $\overline{g}_{SynE}$ in the pre-I/I and early-I neurons is reduced linearly over time from

80% of the default value to 64%, at which point the ratio of the late-E to pre-BötC oscillation frequencies becomes 5:1, and then kept constant.

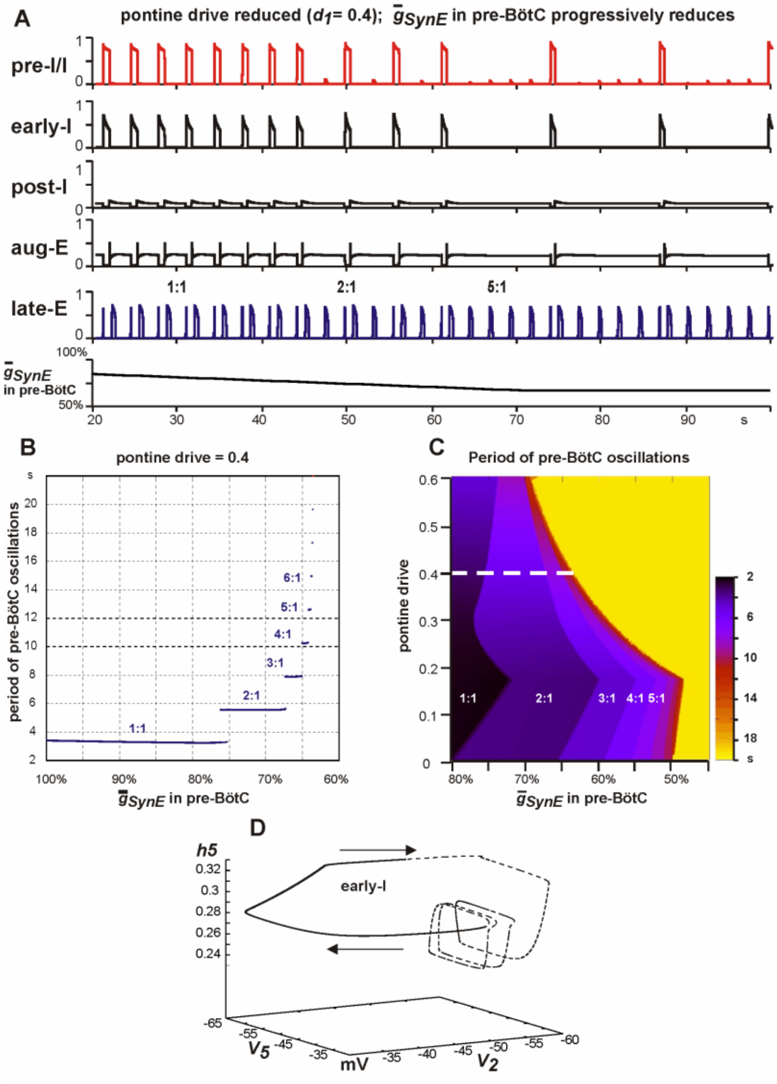

Figure IV-9. "Quantal slowing" in a reduced model of the medullary VRC. (A) Simulation of "quantal slowing" of pre-BötC oscillations. "Hypercapnic hypoxia" conditions were set by fixing "hypercapnic" drive at d_3=0.04 and reducing pontine drive to d_1=0.4, so that the late-E neuron expressed biphasic-E busts with 1:1 coupling to the pre-BötC oscillations (see the text and Figure IV-7A). Pre-BötC depression was simulated by a progressive reduction of the maximal conductance of excitatory synaptic inputs in both pre-BötC neurons (the default value is 10 nS). $\bar{g}_{SynE}$ in the pre-I /I and early-I neurons was linearly reduced from 80% of the default value to 64%, where the ratio of the late-E neuron to pre-

BötC neuron oscillation frequencies becomes 5:1, and then kept constant. (B) Bifurcation diagram of the period of pre-BötC oscillations as a function of $\overline{g}_{synE}$ in pre-BötC neurons (pre-I/I and early-I). $\overline{g}_{synE}$ defines the excitability of these neurons and is reduced from its default value (on the left) to 60% of the default value (to the right). The late-E neuron's period remains relatively constant as the pre-BötC neuron's period proceeds through a series of jumps in duration. Each jump represents a quantal change of the ratio of the pre-BötC oscillation frequency to the late-E frequency. (C) Two-parameter bifurcation diagram that shows the period of pre-BötC oscillations as a function of pontine drive and $\overline{g}_{synE}$. Darker colors indicate shorter periods of pre-BötC activity (see palette on the right). The yellow area indicates no activity in the pre-BötC neurons. Areas of different regimes are labeled by the ratio of the late-E frequency to the pre-BötC frequency (from 1:1 to 5:1). The dashed white line indicates the level of pontine drive corresponding panels A and B. (D) A trajectory in the (V_5, V_2, h_2) subspace generated with the pontine drive reduced to 40% (d_1=0.4) and $\overline{g}_{synE}$ reduced to 65% of baseline, representing the 4:1 synchronization regime. The part of the trajectory for which early-I neuron activity is sub-threshold (below -50 mV) is dashed and the part with supra-threshold early-I activity is solid.

The suppression of excitability of the pre-BötC neurons compromises their ability to activate via escape from the inhibition of the BötC neurons. When pre-BötC neurons are unable to escape, expiration increases in duration. Late-E neuron activity remains biphasic precisely on those cycles on which pre-BötC neurons fire (Figure IV-9A). Consistent with cycle skipping, the bifurcation diagram in Figure IV-9B, created by simulating the model for each of a sequence of fixed $\overline{g}_{SynE}$ values between 100% and 60% of the default value, shows that the period of the pre-BötC oscillations increases as the suppression of pre-BötC excitability progresses. The gradual decrease of pre-BötC excitability causes the pre-BötC to move through a series of regimes with increased periods of pre-BötC oscillations (quantal slowing), arising as ratios (1:1, 2:1, etc.) of the late-E frequency to the pre-BötC frequency. The existence of such regimes depends on the pontine drive suppression, reflecting the level of "hypoxia". The two-parameter bifurcation diagram in Figure IV-9C illustrates this relationship. A reduction of pontine drive changes the levels of pre-BötC excitability at which the “steps” between regimes of synchronization, with different frequency ratios between the late-E and pre-BötC oscillations, occur. Figure IV-9D shows a trajectory in (V_5, V_2, h_5) at d_1=0.4 and $\bar{g}_{synE}$ reduced to 65%, corresponding to the 4:1 regime (see Figure IV-9A,B). Three cycles of late-E neuron activation and deactivation occur without any supra-threshold early-I neuron activity. After the fourth late-E neuron activation, V_2 increases above the synaptic threshold and early-I neuron activity ensues. The activation of the early-I neuron causes a decrease in V_5 (silencing the late-E neuron). Finally, V_2 proceeds back to a sub-threshold value, and the late-E neuron’s bursts resume.

Using phase plane analysis, we can explain why late-E neuron activity is biphasic precisely on those cycles where inspiratory activation occurs. On “rebound cycles” that lack supra-threshold early-I activity, the projection of the trajectory to the (V_5, h_5) plane reaches the LK of the appropriate V_5 nullcline and the late-E neuron activates (Figure IV-10A), and then the trajectory travels down the RB of the V_5 nullcline, hits the RK, and returns to the LB of the V_5 nullcline. This late-E neuron activation, however, fails to elicit early-I neuron activation and the associated increase in inhibition (inh_5) of the late-E neuron. Over successive rebound cycles, post-I and aug-E activity levels, and hence the level of inh_5, quickly equilibrate. Figure IV-10B shows another view of these cycles as part of a full 2:1 trajectory, projected to the (h_5, inh_5) plane. This image includes LK (solid) and RK (dashed) curves. Each late-E neuron activation cycle corresponds to an excursion from the LK curve to the RK curve and a return to the LK curve. On pure rebound cycles, since inh_5 is approximately constant, the trajectory is roughly horizontal (Figure IV-10B, pure rebound). Eventually, a cycle is reached on which late-E neuron activation does lead to early-I neuron activity (Figure IV-10B, pre-I), with a corresponding rapid rise in inh_5. The inhibition to the late-E neuron elicited by the activation of the early-I neuron causes the V_5 nullcline to move to a high position in the (V_5, h_5) plane (Figure IV-10A; also Figure IV-8C). In particular, the right knee of the V_5 nullcline has an h_5-coordinate that significantly exceeds the h_5 value on the solution trajectory at the onset of early-I activity (Figure IV-10B; note that the h_5 value at the point of highest inh_5 along the trajectory is much smaller than the h_5 value at the red, dashed RK curve for that inh_5). Thus, the late-E neuron quickly returns to the silent phase when early-I neuron activity starts (as illustrated in Figure IV-5A, middle excursion, as well). This rapid return prevents significant inactivation of I_{NaP} in the late-E neuron, such that h_5 remains relatively high, and h_5 continues to increase while the late-E neuron is inhibited by the early-I neuron throughout the inspiratory phase (Figure IV-10B, inspiration). When inspiration ends and this inhibition is removed, the high value of h_5 relative to the LK of the V_5 nullcline (Figure IV-10B; note that the part of the trajectory with lowest inh_5 and $h_5 > 0.35$ has h_5 well above the solid, red LK curve for that inh_5) allows the late-E neuron to undergo rebound activation, resulting in a biphasic late-E activity profile (Figure IV-10B, post-I rebound; note that the post-I neuron also activates at that time, causing inh_5 to become nonzero along the post-I rebound part of the trajectory).

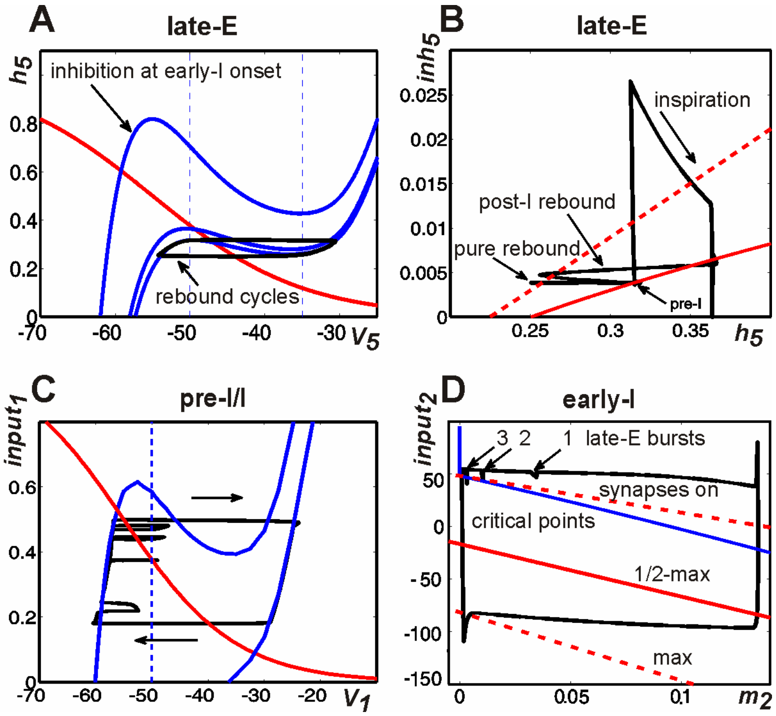

Figure IV-10. Phase plane analysis in the case of suppression of pre-BötC excitability. (A) Cycling of late-E activity during expiration. V_5 nullclines are shown as solid blue curves; the upper nullcline corresponds to the onset of inhibition from the early-I neuron and the middle and lower nullclines to the onset and steady-state levels of inhibition from the post-I neuron, respectively. The black trajectory represents a series of late-E neuron activation cycles occurring during expiration that are not followed by pre-I/early-I activity. (B) Trajectory for an oscillation with a 2:1 late-E:early-I oscillation frequency ratio, in the (h_5, inh_5) plane. Included with the trajectory are curves of left knees (solid red) and right knees (dashed red). The horizontal parts of the trajectory correspond to periods when the late-E neuron is active; the post-I rebound immediately follows inspiration while the pure rebound occurs without inspiratory activity. The segment of the trajectory labeled pre-I corresponds to the time of activation of the late-E neuron just prior to inspiration, which is followed by the activation of the pre-I/early-I neurons, the sharp rise in inh5, and the subsequent inspiration phase. (C), (D) Projections of the trajectory for a 4:1 late-E:early-I solution. (C) (V_1, h_1) plane for the pre-I neuron. The trajectory is superimposed on the h_1 (red) and V_1 nullclines (blue) corresponding to the steady-state level of inhibition from the post-I/aug-E neurons (upper) and to the absence of inhibition (lower). The threshold for the turn-on of synaptic output from the pre-I neuron is also shown (dashed blue). Time increases in a clockwise direction along the trajectory. Note that there are five, not four, excursions in V_1 away from the LB in this image due to the fact that the late-E neuron, which excites the pre-I neuron, exhibits one cycle of biphasic activation. (D) (m_2, $input_2$) plane for the early-I neuron. The trajectory is superimposed on the curves corresponding to the onset of early-I synaptic activity (upper dashed red), half-maximal (solid red), and maximal (lower dashed red) early-I synaptic activity. The blue curve is a curve of critical points, which becomes vertical at m_2=0. Time increases in a counterclockwise direction along the trajectory, with the top corresponding to expiration and the bottom to inspiration.

It is not surprising that a reduced pre-BötC excitability causes the pre-BötC neurons to skip cycles. Exactly which cycles will be skipped is determined by the evolution of the variables for these neurons in the model network, relative to the synaptic activation threshold, which reflects the level of inhibition that they receive. More precisely, the pre-I neuron receives synaptic excitation when the late-E neuron activates. This excitation may push V_1 above the synaptic activation threshold of -50 mV (Figure IV-10C), but it will not induce full pre-I neuron activation if the trajectory does not reach the RB of the V_1 nullcline. The weak crossing of the synaptic activation threshold by the pre-I neuron results in a weak excitation of the early-I neuron, which either fails to turn on the early-I neuron's synaptic outputs (Figure IV-10D; note that excursions 1 and 2 lie above the "synapses on" curve) or turns them on only very weakly (Figure IV-10D, excursion 3), such that the early-I neuron cannot terminate post-I/aug-E activity and take over. In the example shown in Figure IV-10D, the m_2-coordinate of the trajectory approaches a minimum value very close to 0 while the early-I neuron is inactive until finally, a fourth activation of the late-E neuron pulls the trajectory across the early-I synaptic activation curve (by decreasing $input_2$) and causes the onset of inspiration.

We emphasize that, in contrast to hypercapnic simulations, the activation of the early-I neuron in the case of quantal slowing results not from escape but from recruitment by the late-E neuron. Thus, the burst times of the pre-BötC neurons are set by the RTN/pFRG period in this regime, which stands as a prediction of the model, along with the prediction that biphasic late-E neuron activation occurs exactly on those cycles on which early-I neuron activation occurs.

D. Discussion

We have analyzed a reduced model based on a proposed network of interactions [41] between two oscillators involved in the neural control of breathing: a BötC/pre-BötC oscillator that is considered a rhythmogenic kernel of the respiratory CPG, and a RTN/pFRG late-E oscillator that is activated with increasing metabolic demands and, when activated, generates late-E (or pre-inspiratory) oscillations. Using simulations and bifurcation analysis, we have explored how changes in drives within the network shift output patterns from a baseline state of late-E neuron quiescence, through a regime of late-E neuron quantal acceleration featuring 1:N phase-locking between late-E and BötC/pre-BötC activation, through an evolution of late-E neuron output patterns culminating in biphasic activation, to a regime of quantal slowing featuring N:1 phase-locking between late-E and BötC/pre-BötC activation. Using phase plane analysis, we have explained the mechanisms for transitions between regimes and have also elucidated why recruitment of late-E activity in quantal acceleration does not affect BötC/pre-BötC period, why a regime of post-I rebound late-E neuron activation arises before biphasic late-E neuron activation and why BötC/pre-BötC period decreases as pontine drive in the model is reduced, and why biphasic late-E activation persists precisely on cycles featuring BötC/pre-BötC activation in quantal slowing. These features of model dynamics all stand as predictions for subsequent experimental testing, and inasmuch as our analysis shows how particular model components affect these features, we can also predict the effects of experimental manipulations, such as changes in excitability of particular respiratory neuron populations, on network outputs.

D-1. Two oscillators involved in respiratory rhythm generation

The longstanding view has been that the generation of the respiratory rhythm and (inspiratory-expiratory) motor pattern involves network interactions, mostly inhibitory, between different populations of respiratory neurons located within, or distributed over, multiple brain stem compartments [3], [5], [203]. From the time of its discovery [23], the pre-BötC has been shown to play an essential role in respiratory rhythm generation (reviewed in [20]). However, the pre-BötC alone (without interactions with other brain stem compartments, e.g., with the BötC) is not sufficient for generating the normal respiratory rhythm and pattern (eupnea). Recent experimental studies, based on a series of brain stem transections *in situ*, and the corresponding modeling studies suggest that the network interactions within and between the pre-BötC and BötC, along with the intrinsic rhythmogenic properties of pre-BötC neurons, form a hierarchy of multiple oscillatory mechanisms [16], [19], [36], [186]. The functional expression of these mechanisms is controlled by drives from other brain stem components, including the RTN and pons, which regulate the dynamic behavior of the core circuitry and may re-organize it with changes in physiological or metabolic conditions [16], [19], [36], [186]. The important role of the BötC and other brain stem regions for respiratory rhythm generation has been experimentally re-confirmed by several studies [191], [202], [215].

Alternatively, the current dual oscillator concept suggests that there are two distinct rhythm generators driving breathing when the RTN/pFRG is active: one located in the pre-

BötC and considered to be an *inspiratory* rhythm generator, and another located in the RTN/pFRG and considered as an *expiratory* rhythm generator [42], [172]. This contrasts with our suggestion that the first oscillator represents a core network of the *respiratory* CPG that generates coordinated *respiratory* (i.e., inspiratory, post-inspiratory and expiratory) oscillations, particularly due to the network interactions within the CPG kernel (BötC/pre-BötC) that in turn are controlled by inputs from other brain stem compartments (RTN, pons). Indeed, the essential feature of our model, distinguishing it from other related models, is that rhythm generation in this oscillator relies on the network interactions within the pre-BötC/BötC circuitry and generates not just *inspiratory* oscillations but a coordinated *inspiratory-expiratory* oscillatory pattern. In particular, this circuitry generates its own expiratory activity (provided by post-I and aug-E neurons of the BötC), which also contributes to the specific interactions between the CPG kernel and the RTN/pFRG oscillator.

D-2. Modeling the interactions between the oscillators

Three relatively simple computational models have been proposed previously to simulate coupling between pre-BötC and RTN/pFRG oscillators and to suggest possible mechanisms that govern their interactions. Joseph and Butera, 2005 used an abstract canonical model composed of two identical phase oscillators [183]. Wittmeier et al., 2008 simulated both oscillators as single neurons with I_{NaP}-dependent bursting properties described previously [125], and Lal et al., 2011 considered interacting populations of such neurons [204]. The connections between the oscillators proposed in all these models were: (a) an excitatory input from the RTN/pFRG oscillator to the pre-BötC oscillator, providing the entrainment of the latter by the former, and (b) an inhibitory input from the pre-BötC oscillator to the RTN/pFRG one, providing inhibition of the latter during inspiration. These connections were sufficient to reproduce regimes of quantal slowing of the pre-BötC oscillator with the phase relationships observed experimentally under conditions of reduced excitability of pre-BötC neurons, which was considered as a test for these models. The same two connections have been included in our model (Figure IV-1A), which also produced a realistic simulation of quantal slowing behavior (see Figure IV-9), without requiring any decrease of pre-BötC activation amplitude, as was needed in an earlier study [204]. Note, however, that while these two connections are sufficient for reproducing quantal slowing behavior, the RTN/pFRG oscillator has a much stronger effect on pre-BötC oscillations than the pre-BötC has on the RTN/pFRG oscillator.

In our more complete model, this imbalance arises specifically in the regime of quantal slowing (see Chapter III: C-4). In contrast to the dual oscillator concept [42], [172] and the previous models [174], [183], [204], in which the pre-BötC oscillator is only active and able to affect the RTN/pFRG oscillator during inspiration, our model incorporates an additional third connection, namely the inhibitory connection from the post-I neuron of the BötC to the late-E neuron of the RTN/pFRG. Our analysis shows that this connection is critical for reproducing and explaining the regime of quantal acceleration of RTN/pFRG oscillations [41], [87], [173], [212]. Moreover, we showed that the reduction/suppression of this inhibitory input is critical for the transformation of the late-E activity to the biphasic-E pattern during simulated hypercapnic hypoxia/anoxia (Figures IV-6, IV-7, and IV-8; see also [212].

The existence of (presumably post-I) inhibition of RTN/pFRG activity during expiration is consistent with previously proposed inhibition of RTN chemosensitive neurons by the medullary CPG circuits during both inspiration and expiration [47], [92], [182] and is indirectly confirmed by the experimental finding that blockade of inhibition within RTN/pFRG can produce (release) and accelerate the RTN/pFRG and/or abdominal oscillations in normal metabolic conditions [185], [216].

D-3. Coupling between the BötC/pre-BötC and pFRG/RTN oscillators

Within the framework of synchronization, the BötC/pre-BötC and RTN/pFRG generators can be considered as a system of coupled oscillators. The dynamics of each oscillator may be represented by a stable limit cycle in some phase space. The phase space of a system of two oscillators is a Cartesian product of the phase spaces of each oscillator. The corresponding limit set is a 2D invariant torus and the behavior of this system is represented by a trajectory on this torus (Figure IV-11A1,A2; see also [217]). If the ratio of oscillation frequencies of the two oscillators is rational (i.e. equal to N/M, for some integers N and M), then this trajectory is closed, indicating N:M synchronization between oscillators, where the numbers N and M represent topological invariants, namely the numbers of rotations around two orthogonal circles that together span the torus (e.g., large and small circles as illustrated in Figure IV-11A1,A2).

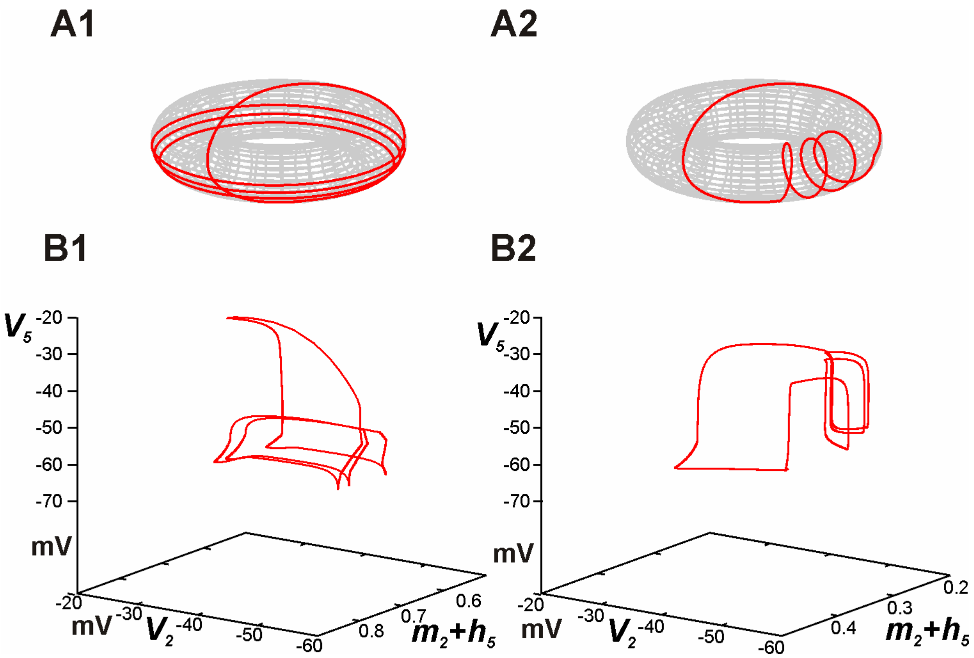

Figure IV-11. Illustration of coupling between two oscillators with different ratios of frequencies represented by the trajectories on a 2D torus. (A) In A1 the system makes 4 “large” cycles during 1 “small” cycle (1:4 synchronization regime). In A2 the system makes 4 “small” cycles during 1 “large” cycle (4:1 synchronization regime). (B1), (B2) The corresponding examples from the current model with different ratios between the late-E (pFRG/RTN) and BötC/pre-BötC oscillations shown in (V_2, m_2+h_5, V_5) sub-space. The trajectory in B1 corresponds to a “weak hypercapnia” 1:3 synchronization regime, in which one cycle of late-E corresponds to 3 rotations of early-I. In B2, the excitability of pre-BötC neurons is suppressed, producing the 4:1 synchronization regime. The oscillators switch their roles. Late-E traverses 4 cycles while early-I rotates only once.

With changing conditions, the system of coupled oscillators can proceed through regimes characterized by different relations between oscillation frequencies and phase relationships. In this context, the specific interactions between the oscillators perform two functions. First, they help select the particular (N,M) pairs for which stable synchronized oscillations occur, and second, they constrain the phase relationships between the oscillators within these oscillations. The regimes considered in this study can be interpreted based on this concept.

Interestingly, our analysis reveals that a sequence of shifts in the functional coupling between the BötC/pre-BötC and RTN/pFRG oscillators occurs across the regimes that we have simulated. Our simulation of progressive hypercapnia (Figure IV-4) is based on a gradual increase of RTN/pFRG excitability that results in a quantal increase in the frequency of RTN/pFRG oscillations, as seen in abdominal motor output [41], [87], [173]. With a progressive increase of RTN/pFRG excitability (as could be defined by the CO_2 level), these oscillations emerge then accelerate and proceed through a series of phase-locked resonances with 1:N ratios between the RTN/pFRG and BötC/pre-BötC frequencies, with N decreasing from an initial higher value to 1 (see Figure IV-11B1). Given the tuning of our model to reproduce experimentally observed regimes of activity, a feature that arises is that by the time post-I inhibition decays enough to allow late-E activation, the early-I neuron has already reached the synaptic activation curve and is thus able to escape (despite roughly constant inhibition from post-I plus aug-E) and become active on its own, without the excitatory input triggered by the late-E neuron (Figure IV-5C). In this regime, late-E neuron activation is also independent of BötC/pre-BötC activity, such that the two oscillators are effectively uncoupled. Moreover, although the late-E neuron activates first on cycles in which it does become active, it does not entrain inspiratory activity and hence the frequency of the RTN/pFRG oscillations approaches the frequency of the BötC/pre-BötC oscillator, which remains essentially constant, as N decreases. The maintenance of a steady oscillation frequency in hypercapnia, despite the appearance and acceleration of late-E activity, represents a prediction of this model, although this may be specific to particular experimental settings that lack additional feedback signals (e.g. from lung stretch receptors) not present in the model. Furthermore, since post-I neuron activation occurs through release from inhibition from the early-I neuron, and this inhibition is shared by the late-E neuron as well, our model suggests the theoretical possibility that the timing of late-E activity could switch from pre-I to post-I or even biphasic under strong hypercapnic conditions.

In simulated hypercapnic hypoxia (Figure IV-7), the system can exhibit phase-locked regimes with different phase shifts depending on pontine drive, which controls the expression of post-I neuron activity and hence the inhibition from the post-I neuron to the late-E and pre-BötC neurons. If late-E neuron activity entrained pre-BötC activity in the regime when late-E neuron activation directly precedes pre-BötC activity, then a decrease in post-I inhibition would be expected to maintain and accelerate the regime of pre-inspiratory late-E neuron activation (pre-I regime). Instead, a switch to the rebound regime, in which late-E activity occurs during expiration but is not associated with a switch to inspiration, occurs. In the rebound regime, the late-E neuron would be able to generate repetitive oscillations on its own under the reduced level of post-I inhibition, especially as that inhibition decayed during expiration. The inhibition that the late-E neuron receives from the early-I neuron during inspiration, however, suppresses its activity, setting up a certain phase relationship between inspiration and late-E activation (Figure IV-8B). After this inhibition is removed, the late-E neuron can break free from post-I inhibition more easily than it could in the purely hypercapnic regime. But the excitation of the pre-BötC that ensues from an earlier late-E activation cannot cause early-I activation (Figure IV-8D). Thus, the RTN/pFRG/pre-BötC network switches from being effectively decoupled in the pre-I regime to having an effectively one-way coupling, from pre-BötC to RTN/pFRG, in the rebound regime. We note that the transitions between these regimes occur through aperiodic, possibly chaotic, behaviors (see Figure IV-7B), corresponding to a form of asynchronous dynamics as the oscillators cannot settle into a phase-locked regime.

As pontine drive is progressively lowered, the rebound regime gives way to the biphasic regime when the late-E neuron recovers enough, due to its intrinsic dynamics and the further weakened post-I inhibition, to activate a second time during expiration. In contrast to the pre-I regime observed in pure hypercapnia, this second activation does recruit the pre-BötC neurons (Figure IV-8D). Pre-BötC neuron activity suppresses late-E neuron activity, but as a result the persistent sodium current for the late-E neuron shows little inactivation and the late-E neuron can rebound immediately following the end of inspiration (Figure IV-8C), yielding the biphasic activity profile. Thus, the biphasic regime reflects two-way coupling between the RTN/pFRG and BötC/pre-BötC oscillators. A decrease in oscillation period in this regime arises because less I_{NaP} deinactivation is required for the late-E neuron to escape from the weaker post-I inhibition and the late-E neuron is able to entrain the pre-BötC neurons, despite the increase in aug-E activity and the associated inhibition. A subtle point is that, because the late-E rebound occurs earlier than in the pure rebound regime, the resulting excitation does not interfere as much with recovery of the pre-I pre-BötC neurons (through deinactivation of I_{NaP}) as its later rebound does.

In summary, our model offers a possible explanation of why, under gradual suppression of pontine drive, the timing of late-E activation progresses from late-E activation to rebound activation and finally to biphasic activation. This hypothesis yields the prediction that recordings featuring biphasic late-E activity represent states of low pontine drive or high pontine suppression or states in which some other factor limits post-I activation.

Finally, in addition to effects of hypercapnia and reduced pontine drive, we have considered progressive suppression of pre-BötC excitability (e.g., by opioid agonists), which leads to quantal slowing of pre-BötC activity [42], [43], [172]. In this regime in our model, the network interactions between the oscillators (specifically the excitatory connection from the RTN/pFRG to pre-BötC) provide phase locking. Due to their decreased excitability, the pre-BötC neurons depend on recruitment by the late-E neuron to activate. Thus, the pre-BötC frequency is quantally reduced through a series of resonances with M:1 ratios between the RTN/pFRG and BötC/pre-BötC frequencies with M increasing from 1 to higher values (see Figure IV-11B2). The pre-BötC to RTN/pFRG connection becomes less important in this regime than in the others. This connection does yield the biphasic late-E neuron activity profiles seen in oscillation cycles that feature pre-BötC activity (Figure IV-10B). However, the time interval between late-E neuron activations does not differ noticeably between these cycles and cycles of pre-BötC skipping (Figure IV-9 A) and the late-E neuron controls oscillatory period. The mechanisms responsible for the precise shapes of the curves delineating transitions between regimes as pontine drive and pre-BötC excitability vary (Figure IV-9 C), and the full characterization of the dynamics of the model network presented here, remain for further investigation.

D-4. Modeling issues

We have used a reduced model in this paper. This reduction includes the omission of various currents present in biological neurons and imposes certain characteristics on the model’s outputs. In particular, the model aug-E neuron exhibits a brief surge of activity at the start of the post-I phase in our simulated solutions. This surge is a figment of the model aug-E neuron’s monotone nullclines. With such a simplified model structure, the rapid cessation of inhibition from the early-I neuron causes the aug-E voltage nullcline to quickly move to elevated voltages, and a corresponding rise in the aug-E neuron’s voltage results. Post-I activation quickly tamps out the aug-E surge, and this feature is not necessary in the model rhythms. Similarly, there is little distinction between the timing of activation of the pre-I and early-I neurons in the model. We claim that our insights about the relationship of late-E and pre-BotC activity in different regimes will carry over to activity patterns with a more realistic time shift between pre-I and early-I phases. In particular, the idea that pre-BotC activity need not be entrained by late-E in hypercapnia would hold if the early-I escape from inhibition were replaced by a pre-I escape and subsequent recruitment of the early-I neuron.

Our models for the pre-I/I neuron in the pre-BotC and the late-E neuron in the RTN/pFRG include persistent sodium current. It remains for future work to incorporate additional factors that may contribute to pre-BötC dynamics (see [35] and references therein) into a respiratory network setting. Similarly, although the persistent sodium current is prevalent in respiratory neurons and appears to be significant in late-E dynamics, it is important to note that equivalent dynamics can be achieved by other inward, slowly inactivating or outward, slowly activating currents [218].

By means of the qualitative analysis presented in this study we have shown that the proposed model closely reproduces several behaviors observed experimentally. This agreement supports the proposed connectivity between the RTN/pFRG and pre-BötC/BötC circuits and changes in model parameters used for simulating the experimentally applied changes in metabolic or physiological conditions. Our simulation results suggest that the functional roles of the synaptic connections between possible pre-BötC and RTN/pFRG oscillator networks change under variations in respiratory demand, with suppression of RTN/pFRG, relative independence, each direction of one-way effective coupling, and two-way effective coupling each emerging in specific situations and resulting in particular activity profiles, as discussed in the previous section. Thus, this coupled oscillator network embodies an inherent flexibility that likely enhances the capacity of the CPG to respond dynamically to changing conditions.

E. Summary of predictions

Sub-cellular level predictions: Same as previous chapter.

System level predictions: Same as previous chapter.

Qualitative analysis of the reduced model indicated that the transition from expiration to inspiration is governed by the early-I neuron's "escape" from post-I inhibition (escape was defined by the adaptive variable reaching a threshold and causing activation, see [167]). This mechanism differs from release, i.e. reduced inhibition to a neuron allowing the emergence of that neuron, which governs the transition from inspiration to expiration. This predicted mechanism is supported by the shortening of expiration with no appreciable change in the inspiratory phase, following RTN/pFRG emergence. This finding suggests that the respiratory network is constructed to provide robust durations of inspiration at the expense of the expiratory phase's variability.

Chapter V: Control of breathing by interacting pontine and pulmonary feedback loops

The following section was adapted from the following accepted manuscript: Y. I. Molkov, B. J. Bacak, T. E. Dick, and I. A. Rybak, “Control of breathing by interacting pontine and pulmonary feedback loops.,” *Front. Neural Circuits*, vol. 7, p. 16, Jan. 2013.

A. Introduction

As in other CPGs, afferent feedbacks are involved in the control of the mammalian respiratory CPG and the generation and shaping of the breathing pattern. Many peripheral mechano- and chemo-sensory afferents, including those from the lungs, tracheobronchial tree and carotid bifurcation, provide feedback signals involving in the homeodynamic control of breathing, cardiovascular function, and different types of motor behaviors coordinated with breathing, such as coughing (see [219], for review). The NTS is the major integrative site of these afferent inputs. The present study focuses on the mechanoreceptor feedback mediated by pulmonary stretch receptors (PSRs). These mechanoreceptors respond to mechanical deformations of the lungs, trachea, and bronchi, and produce a burst of action potentials during each breath, thereby providing the central nervous system with feedback regarding rate and depth of breathing (see [12], for review). Activation of PSRs elicits reflex effects including inspiratory inhibition or expiratory facilitation (representing the so-called Hering-Breuer reflex), enhancement of early inspiratory effort, bronchodilatation, and tachycardia. PSR axons travel within the vagus nerve, and form excitatory synapses in NTS pump cells [10]–[12], [220]–[222]. Pharmacological microinjection and lesion studies [12]–[15], [223] suggest that NTS pump cells mediate the Hering-Breuer reflex (lung-inflation induced termination of inspiration). Through pump cells, PSR-originating information alters the activity of CPG neurons in manners consistent with their proposed roles in rhythm generation.

The other feedback loop, important for the respiratory CPG operation, involves multiple pontine-medullary interactions. The pons (Kölliker-Fuse nucleus, parabrachial nucleus, A5 area, etc.) contains neurons expressing inspiratory (I)-, inspiratory- expiratory (IE)-, or expiratory (E)-modulated activity, especially in vagotomized animals [3], [64], [68], [73], [75], [82], [224]–[229]. This modulation is probably based on reciprocal connections between medullary and pontine respiratory regions which were described in a series of morphological studies [3], [225], [229]–[233]. The principal source of pontine influence on the medulla is thought to be the Kölliker-Fuse region in the dorsolateral pons, although other areas, including those from the ventrolateral pons, are also involved [18], [58], [60], [64], [68], [75], [78], [184], [225], [227], [234], [235]. Pontine activity contributes to the regulation of phase duration as demonstrated by stimulation and lesion studies [60], [64], [74], [75], [78], [127], [184], [236]. Stimulation of the Kölliker-Fuse or medial parabrachial nuclei induced a premature termination of inspiration (I-E transition) and extended expiratory phase. These effects were similar to the effects of vagal stimulation [3]. Also, the effects of both vagal and pontine stimulation appear to be mediated by the same medullary circuits that control onset and termination of inspiration [60], [64], [127], [236], [237]. Finally, the respiratory pattern in vagotomized animals with an intact pons is similar to that in animals without the pons and vagi intact. The above observations support the idea that the pontine nuclei mediate a function similar to that of the Hering-Breuer reflex.

Bilateral injections of NMDA antagonists (MK-801 and AP-5) into the rostral pons reversibly increase the duration of inspi-ration in vagotomized rats, and this increase is dose-dependent [58]. This suggests that the rostral pons contains neurons with NMDA-receptors participating in the inspiratory off-switch mechanism. Morrison et al., 1994 showed that lesions of the parabrachial nuclei in the decerebrate, vagotomized, unanesthetized rat produced a significant (4-fold) increase in the duration of inspiration and a doubling of the duration of expiration, supporting a role for this pontine area in the regulation of the timing of the phases of respiration [238]. This abnormal breathing pattern is known as apneusis. Administration of MK-801 into the rostral dorsolateral pons was shown to induce apneusis in vagotomized ground squirrels [239]. Systemic injection of MK-801 increases the inspiratory duration or results in an apneustic-like breathing in vagotomized and artificially ventilated rats. Similarly, Jodkowski et al., 1994 showed that electrical and chemical lesions in the ventrolateral pons produced apneustic breathing in vagotomized rats [75]. At the same time, apneustic breathing is not usually developed if the vagi remained intact and can be reversed by vagal stimulation, suggesting that NMDA receptors are not involved in the pulmonary (vagal) feedback mechanism. Feldman et al. recorded cells in the rostral pons that exhibited respiratory modulation only when lung inflation, via a cycle-triggered pump, was stopped [73]. The emergence of this respiratory-modulated activity suggests that afferent vagal input may have an inhibitory effect on the respiratory modulated cells in the pons (see also [71]). In the same work, it was noticed that this activity had no apparent influence on the tonic discharge of pontine neurons, suggesting that this inhibition might be presynaptic. Dick et al., 2008 recorded several hundred cells in the dorsolateral pons of decerebrate cats, artificially ventilated by a cycle-triggered pump before and after vagotomy. In their experiments, vagotomy led to either an emergence or facilitation of respiratory modulation in the pons. Sustained electrical stimulation of the vagus nerve elicited the classic Hering-Breuer reflex. Systemic or local blockade of NMDA receptors can result in an apneustic breathing pattern [58], [237], [240]–[244] similar to that demonstrated by pontine lesions or transections.

The specifics of feedback control in the brainstem respiratory CPG is that the latter operates under control of two control loops (pulmonary and pontine ones), which both regulate key neural interactions within the CPG, thereby affecting the respiratory rate, respiratory phase durations and breathing pattern, and, at the same time, interact with each other so that each of them may dominate in the control of breathing depending on the conditions and/or the state of the system. Such feedback interactions and a state-dependent feedback control of the CPG may have broader implication in other CPGs in vertebrates and/or invertebrates.

Specifically, our study focuses on the following major feedback loops involved in the control of breathing (Figure V-1A): (1) the peripheral, pulmonary (vagal) loop that controls the medullary rhythm-generating kernel via afferent inputs from PSRs mediated by the NTS circuits, and (2) the pontine control loop, that provides pontine control of the respiratory rhythm and pattern. Our central hypothesis is that both the peripheral afferent and pontine-medullary loops control the respiratory frequency and phase durations via key medullary circuits responsible for the respiratory phase transitions (onset of inspiration, E-I, and inspiratory off-switch, I-E, see Figure V-1A). In addition, these loops interact changing, balancing, and adjusting their control gain via interaction between NTS and VRC and pontine circuits. To investigate the involvement and potential roles of these feedback loops and their interactions with the medullary respiratory circuits we simulated the effects of suppression/elimination of each and both these feedbacks on the respiratory pattern and respiratory phase durations. The results of simulations were compared with the related experimental data and showed good qualitative correspondence hence providing important insights into feedback control of breathing.

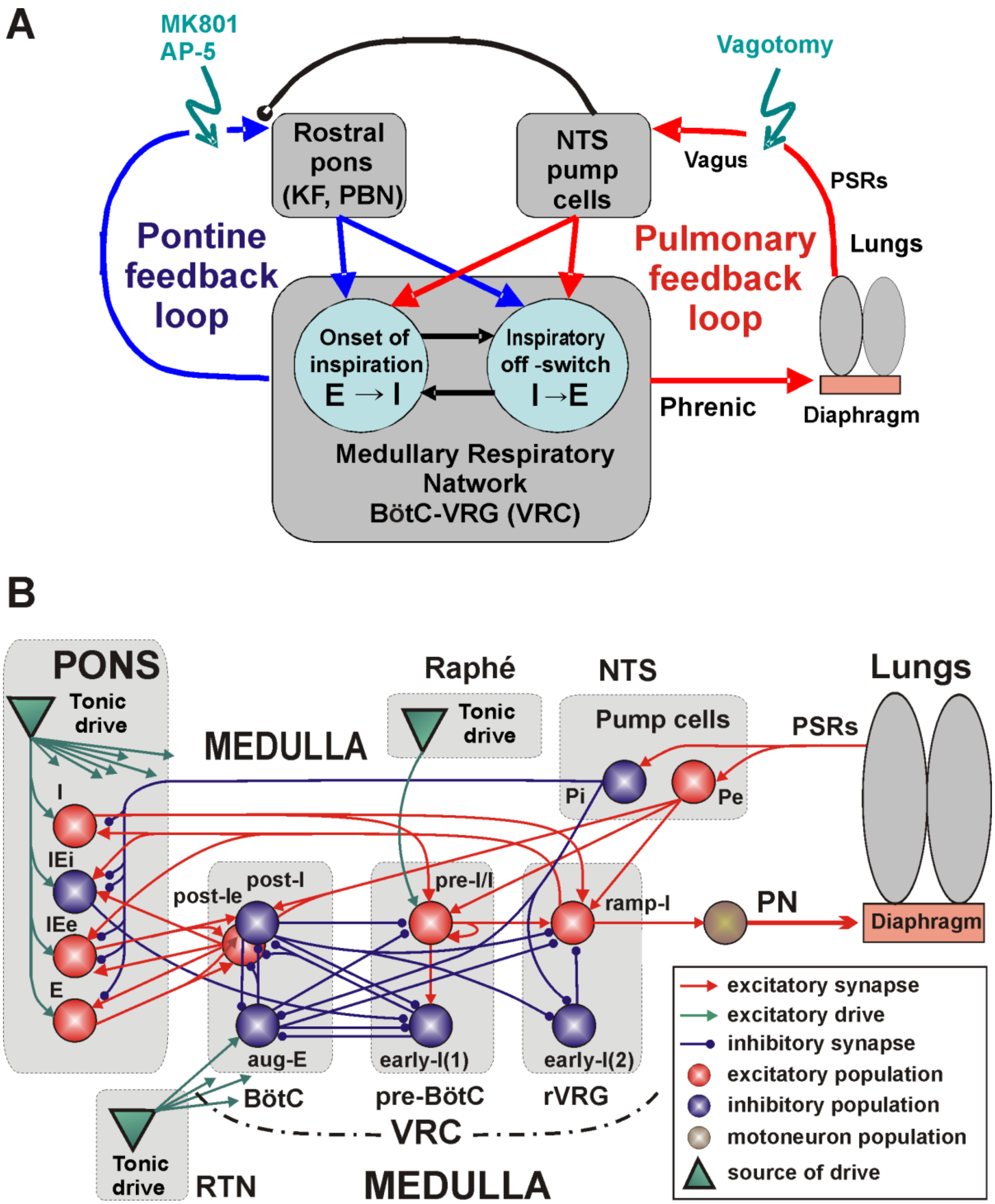

Figure V-1. The medullary respiratory network with pulmonary and pontine feedbacks. (A) A general schematic diagram representing the respiratory network with two interacting feedback. See text for details.(B) The detailing model schematic showing interactions between different populations of respiratory neurons within major brainstem compartments involved in the control of breathing (pons, BötC, pre-BötC, and rVRG) and the organization of pulmonary and pontine feedbacks. Each neural population (shown as a sphere) consists of 50 single-compartment neurons described in the Hodgkin-Huxley style.

The model includes 3 sources of tonic excitatory drive located in the pons, RTN, and raphé—all shown as green triangles. These drives, project to multiple neural populations in the model (green arrows; the particular connections to target populations are not shown for simplicity, but are specified in Table A3 in the Appendix). See text for details. Abbreviations: AP-5, amino-5-phosphonovaleric acid, NMDA receptor antagonist; BötC, Bötzinger complex; e, excitatory; E, expiratory or expiration; i, inhibitory; I, inspiratory or inspiration; IE, inspiratory-expiratory; KF, Kölliker-Fuse nucleus; MK801, dizocilpine maleate, NMDA receptor antagonist; NTS, Nucleus Tractus Solitarii; P, pump cells; PBN, ParaBrachial Nucleus; PN, Phrenic Nerve; pre-BötC, pre-Bötzinger Complex; PSRs, pulmonary stretch receptors; RTN, retrotrapezoid nucleus; r, rostral; VRC, ventral respiratory column; VRG, ventral respiratory group.

B. Methods

B-1. Simulation Package

All simulations in this study were performed using a neural simulation package NSM-3.0 developed at Drexel by Drs. Markin, Shevtsova, and Rybak and ported to the high-performance computer cluster systems running OpenMPI by Dr. Molkov. This simulation environment has been specifically developed and used for multiscale modeling and computational analysis of cross-level integration of: (a) the intrinsic biophysical properties of single respiratory neurons (at the level of ionic channel kinetics, dynamics of ion concentrations, synaptic processes, etc.); (b) population properties (synaptic interactions between neurons within and between populations with random distributions of neuronal parameters); (c) network properties (connectivity strength and type of synaptic interactions, with user-defined or random distribution of connections), (d) morpho-physiological structure (organization of interacting modules/compartments) (see [16]–[19], [89], [136], [245], [246]. NSM-3.0 has special tools for simulation of various *in vivo* and *in vitro* experimental approaches, including suppression of specific ionic channels or synaptic transmission systems, various lesions/transections, application of various pharmacological, electrical and other stimuli to particular neurons or neural populations, etc.

B-2. Modeling basis: Neuronal parameters and ionic channel kinetics

The model presented in this paper continues a previously published series of models of neural control of respiration [16]–[19], [89], [136], [245], [246] and, specifically, represents an extension of the Smith et al., 2007 model [16]. Following that model, each neuron type in the present model was represented by a population of 20–50 neurons. Each neuron was modeled as a single-compartment neuron described in the Hodgkin-Huxley (HH) style. These neuron models incorporated the currently available data on ionic channels in the medullary neurons and their characteristics. Specifically, the kinetic and voltage-gated and characteristics of fast (Na) and persistent (NaP) sodium channels in the respiratory brainstem were based on the studies of the isolated pre-BötC neurons in rats [156]. The kinetics and steady-state characteristics of activation and inactivation of high-voltage activated (CaL) calcium channels were based on the earlier studies performed *in vitro* [247] and *in vivo* [237]. Temporal characteristics of intracellular calcium kinetics in respiratory neurons were drawn from studies of Frermann et al., 1999 [248]. Other descriptions of channel kinetics were derived from previous models [16], [19].

Heterogeneity of neurons within each population was set by a random distribution of some neuronal parameters and initial conditions to produce physiological variations of baseline membrane potential levels, calcium concentrations, and channel conductances. All simulations were performed using the simulation package NSM 3.0 (see above). Differential equations were solved using the exponential Euler integration method with a step of 0.1 ms. We utilized the high-performance computational capabilities of the Biowulf Linux cluster at the National Institutes of Health, Bethesda, MD (http://biowulf.nih.gov).

B-3. Single Neuron Model

All neurons were modeled in the Hodgkin-Huxley style as single-compartment models:

$$C \cdot \frac{dV}{dt} = -I_{Na} - I_{NaP} - I_{K} - I_{CaL} - I_{K,Ca} - I_{L} - I_{SynE} - I_{SynI}\,, \qquad (V\text{-}1)$$

where V is the membrane potential, C is the membrane capacitance, and t is time. The terms in the right part of this equation represent ionic currents: I_{Na} - fast sodium (with maximal conductance $\bar{g}_{Na}$); I_{NaP} - persistent (slow inactivating) sodium (with maximal conductance $\bar{g}_{NaP}$); I_K - delayed rectifier potassium (with maximal conductance $\bar{g}_{K}$); $I_{Ca,L}$ - high voltage activated calcium (with maximal conductance $\bar{g}_{Ca,L}$); $I_{K,Ca}$ - calcium-dependent potassium (with maximal conductance $\bar{g}_{K,Ca}$), I_L - leakage (with constant conductance $\bar{g}_{L}$); I_{SynE} (with conductance $\bar{g}_{SynE}$) and I_{SynI} (with conductance $\bar{g}_{SynI}$) - excitatory and inhibitory synaptic currents, respectively.

Currents are described as follows:

$$I_{Na} = \bar{g}_{Na} \cdot m_{Na}^{3} \cdot h_{Na} \cdot (V - E_{Na})\,; \qquad (V\text{-}2)$$

$$I_{NaP} = \bar{g}_{NaP} \cdot m_{NaP} \cdot h_{NaP} \cdot (V - E_{Na})\,; \qquad (V\text{-}3)$$

$$I_{K} = \bar{g}_{K} \cdot m_{K}^{4} \cdot (V - E_{K})\,; \qquad (V\text{-}4)$$

$$I_{CaL} = \bar{g}_{CaL} \cdot m_{CaL} \cdot h_{CaL} \cdot (V - E_{Ca})\,; \qquad (V\text{-}5)$$

$$I_{K,Ca} = \bar{g}_{K,Ca} \cdot m_{K,Ca}^{2} \cdot (V - E_{K})\,; \qquad (V\text{-}6)$$

$$I_{L} = g_{L} \cdot (V - E_{L})\,; \qquad (V\text{-}7)$$

$$I_{SynE} = g_{SynE} \cdot (V - E_{SynE})\,; \tag{V-8}$$

$$I_{SynI} = g_{SynI} \cdot (V - E_{SynI})\,, \tag{V-9}$$

where E_{Na}, E_K , E_{Ca}, E_L, E_{SynE}, and E_{SynI} are the reversal potentials for the corresponding channels. Variables m_i and h_i with indexes indicating ionic currents represent, respectively, the activation and inactivation variables of the corresponding ionic channels. Kinetics of activation and inactivation variables is described as follows:

$$\tau_{mi}(V) \cdot \frac{dm_i}{dt} = m_{\infty i}(V) - m_i\,; \tag{V-10}$$

$$\tau_{hi}(V) \cdot \frac{dh_i}{dt} = h_{\infty i}(V) - h_i\,. \tag{V-11}$$

The expressions for steady state activation and inactivation variables and time constants are shown in Table V-1. The value of maximal conductances for all neuron types are shown in Table V-2.

The kinetics of intracellular calcium concentration Ca is described as follows [134].

$$\frac{dCa}{dt} = -k_{Ca} \cdot I_{Ca,L} \cdot (1 - P_B) + (Ca_0 - Ca) / \tau_{Ca}\,, \tag{V-12}$$

where the first term constitutes influx (with the coefficient k_{Ca}) and buffering (with the probability P_B), and the second term describes pump kinetics with resting level of calcium concentration Ca_0 and time constant τ_{Ca}.

$$P_B = B/(Ca + B + K)\,, \tag{V-13}$$

where B is the total buffer concentration and K is the rate parameter. The calcium reversal potential is considered a variable and is a function of Ca: $E_{Ca} = 13.27 \cdot \ln(4/Ca)$, *(at rest* $Ca = Ca_0 = 5 \times 10^{-5}$ *mM and* $E_{Ca} = 150mV$*).*

The excitatory (g_{SynE}) and inhibitory synaptic (g_{SynI}) conductances are equal to zero at rest and may be activated (opened) by the excitatory or inhibitory inputs respectively:

$$g_{SynEi}(t) = \bar{g}_E \cdot F_i^{presyn} \cdot \sum_j S\{w_{ji}\} \cdot \sum_{t_{kj}<t} \exp\left(-\left(t - t_{kj}\right)/\tau_{SynE}\right) + \bar{g}_{Ed} \cdot \sum_m S\{w_{dmi}\} \cdot d_{mi}; \qquad (V\text{-}14)$$

$$g_{SynIi}(t) = \bar{g}_I \cdot \sum_j S\{-w_{ji}\} \cdot \sum_{t_{kj}<t} \exp\left(-\left(t - t_{kj}\right)/\tau_{SynI}\right) + \bar{g}_{Id} \cdot \sum_m S\{w_{dmi}\} \cdot d_{mi}, \qquad (V\text{-}15)$$

where the function $S\{x\} = x$, *if* $x \geq 0$, *and* 0 *if* $x < 0$. In equations (*V-14*) and (V-15), each of the excitatory and inhibitory synaptic conductances has two terms. The first term describes the integrated effect of inputs from other neurons in the network (excitatory or inhibitory). The second term describes the integrated effect of inputs from external drives d_{mi}. Each spike arriving to neuron i from neuron j at time t_{kj} increases the excitatory synaptic conductance by $\bar{g}_E \cdot w_{ji}$ if the synaptic weight $w_{ji} > 0$, or increases the inhibitory synaptic conductance by $-\bar{g}_I \cdot w_{ji}$ if the synaptic weight $w_{ji} < 0$. $\bar{g}_E$ and $\bar{g}_I$ are the parameters defining an increase in the excitatory or inhibitory synaptic conductance, respectively, produced by one arriving spike at $|w_{ji}| = 1$. τ_{SynE} and τ_{SynE} are the decay time constants for the excitatory and inhibitory conductances, respectively. In the second terms of equations (*V-15*) and (*V-16*), $\bar{g}_{Ed}$ and $\bar{g}_{Id}$ are the parameters defining the increase in the excitatory or inhibitory synaptic conductance, respectively, produced by external input drive $d_{mi} = 1$ with a synaptic weight of $|w_{dmi}| = 1$. All drives were set to 1.

Presynaptic inhibition is simulated as an attenuator of excitatory synapses by means of a factor $F_i^{presyn} \leq 1$. This factor is calculated according to the following equation:

$$F_i^{presyn} = \left(1 + \sum_j S\left\{-w_{ji}^p\right\} \cdot \sum_{t_{kj}<t} \exp\left(-\left(t - t_{kj}\right)/\tau_{SynI}\right)\right)^{-1}, \qquad (V\text{-}16)$$

where $w_{ji}^p \leq 0$ is the weight of presynaptic inhibitory connection that synapse *i* receives from neuron *j*. If a synapse *i* does not receive any presynaptic inhibition, then $w_{ji}^p = 0$ for and hence for this synapse $F_i^{presyn} = 1$.

The relative weights of synaptic connections (w_{ji}, w_{ji}^p, and w_{dmi}) are shown in Table V-3. The following neuronal and synaptic parameters were used: C = 36 pF; E_{Na} = 55 mV; E_K = −94 mV; E_{SynE} = −10 mV; E_{SynI} = E_{Cl} = −75 mV; $g_E = g_I = g_{Ed} = g_{Id}$ = 1.0 nS; τ_{SynE} = 5 ms; τ_{SynI} = 15 ms; Ca_0 = 5 × 10−5 mM; k_{Ca} = 2 × 10−5 mM/C; τ_{Ca} = 250 ms; B = 0.030 mM; K = 0.001 mM.

Table V-1. Steady state activation and inactivation variables and time constants for different ionic channels.

Ionic Channels	$m_\infty(V)$, V in mV; $\tau_m(V)$, ms; $h_\infty(V)$, V in mV; $\tau_h(V)$, ms;
Fast Sodium (*Na*)	$m_{\infty Na} = 1/(1+\exp(-(V+43.8)/6)$; $\tau_{mNa} = 0.252/\cosh((V+43.8)/14)$; $h_{\infty Na} = 1/(1+\exp(-(V+67.5)/10.8)$; $\tau_{hNa} = 8.456/\cosh((V+67.5)/12.8)$,
Persistent Sodium (*NaP*)	$m_{\infty NaP} = 1/(1+\exp(-(V+47.1)/3.1)$; $\tau_{mNaP} = 1/\cosh((V+47.1)/6.2)$; $h_{\infty NaP} = 1/(1+\exp(-(V+60)/9)$; $\tau_{hNaP} = 5000/\cosh((V+60)/9)$,

Delayed rectifier potassium (*K*)	$\alpha_{\infty K} = 0.01 \cdot (V+44)/(1-\exp(-(V+44)/5))$; $\beta_{\infty K} = 0.17 \cdot \exp(-(V+49)/40))$; $m_{\infty K} = \alpha_{\infty K} / \left(\alpha_{\infty K} + \beta_{\infty K}\right)$; $\tau_{mK} = 1/\left(\alpha_{\infty K} + \beta_{\infty K}\right)$,
High-voltage activated calcium (*Ca_L*)	$m_{\infty CaL} = 1/(1+\exp(-(V+27.4)/5.7))$; $\tau_{mCaL} = 0.5$; $h_{\infty CaL} = 1/(1+\exp(-(V+52.4)/5.2)$; $\tau_{hCaL} = 18$,
Calcium-dependent potassium $K(Ca^{++})$	$\alpha_{\infty K,Ca} = 1.25 \cdot 10^8 \cdot [Ca]_j^2, \beta_{\infty K,Ca} = 2.5$; $m_{\infty K,Ca} = \alpha_{\infty K,Ca} / \left(\alpha_{\infty K,Ca} + \beta_{\infty K,Ca}\right)$; $\tau_{mK,Ca} = -3000 / \left(\alpha_{\infty K,Ca} + \beta_{\infty K,Ca}\right)$

Table V-2. Maximal conductances of ionic channels in different neuron types

Neuron type	$\bar{g}_{Na}$, **nS**	$\bar{g}_{NaP}$, **nS**	$\bar{g}_{K}$, **nS**	$\bar{g}_{CaL}$, **nS**	$\bar{g}_{K,Ca}$, **nS**	g_L, **nS**
Pre-I	170	5.0	180			2.5
Post-I, post-I(e)	400		250	0.1	6.0	6.0
Aug-E	400		250	0.1	3.0	6.0
Early-I(1)	400		250	0.1	3.5	6.0
Early-I(2)	400		250	0.1	11.0	6.0
All others	400		250			6.0

Table V-3. Weights of synaptic connections in the network.

Target population (location)	**Excitatory drive (weight of synaptic input from this drive) or source population (from single neuron)**
ramp-I (rVRG)	drive(Pons) (0.7); post-I (−1.0); aug-E(−0.15); pre-I /I (0.06); early-I(2); pontine I (0.2); Pe (0.115)
early-I(2) (rVRG)	drive(Pons) (2); post-I (−0.5); Pi (−0.15)
pre-I/I (pre-BötC)	drive(Pons) (0.03); drive(Raphe) (0.3); drive(RTN) (0.2); post-I (−0.1625); aug-E (−0.0275); pre-I /I (0.03); pontine I (0.2); Pe (0.025)
early-I(1) (pre-BötC)	drive(Pons) (0.75); drive(RTN) (2.03); post-I (−0.4); aug-E (−0.2); pre-I /I (0.04); pontine IEi (−0.15)
aug-E (BötC)	drive(Pons) (0.6); drive(RTN) (1.25); post-I (−0.09); early-I(1) (−0.135); Pi (−0.075)
post-I and post-Ie (BötC)	drive(Pons) (0.5); aug-E (−0.025); early-I(1) (−0.15); pontine IEe (0.35); pontine E (0.075); Pe (0.275)
pontine I (Pons)	drive(Pons) (0.25) (only to tonic subpopulation); ramp-I (0.025); Pi (−0.5p)
pontine IEe and IEi (Pons)	drive(Pons) (0.2) (only to tonic subpopulations); ramp-I (0.03); post-Ie (0.05); Pi (−0.5p)
pontine E	drive(Pons) (0.3) (only to tonic subpopulations);

(Pons)	post-Ie (0.05); Pi (−5.0p)
Pe and Pi (NTS)	PSRs (1.0)
Phrenic Nerve (PN)	ramp-I (0.065)
Lungs	PN (12)
PSRs	Lungs (3.0)

B-4. Modeling neural populations

Each functional type of neuron in the model was represented by a population of 50 neurons. Connections between the populations were established so that, if a population A was assigned to receive an excitatory or inhibitory input from a population B or external drive D, then each neuron of population A received the corresponding excitatory or inhibitory synaptic input from each neuron of population B or from drive D, respectively. The pontine I, IEi, IEe, and E population represent an exception: only half of each population (the tonic subpopulation) receives tonic drive (see in the section "Pontine Feedback Loop"). To provide heterogeneity of neurons within neural populations, the value of E_L was randomly assigned from normal distributions using average value ± SD. Leakage reversal potential for all neurons (except for the pre-I ones) was $E_L = -60 \pm 1.2$ mV; for pre-I neurons $E_L = -68 \pm 1.36$ mV.

B-5. Modeling of lungs, PN, and PSR

The phrenic motoneuron population and phrenic nerve (PN) were not modeled. Integrated activity of the ramp-I population were considered as PN motor output. An increase in lung volume (lung inflation) V was modeled as a low-pass filter of PN activity:

$$\tau_V \cdot \frac{dV}{dt} = -V + w_{PN \to V} \cdot PN \qquad (V\text{-}17)$$

where τ_V = 100 ms is a lung time constant. The PSR output was considered proportional to the lung inflation V.

C. Results

C-1. Model architecture and operation in normal conditions

The main objective of this study was to investigate the mechanisms underlying control of the mammalian breathing pattern that is generated in the respiratory CPG circuits in the medulla and modulated by two major feedback loops, one involving interactions of medullary respiratory circuits with the lungs, and the other resulting from interactions of these circuits with the pontine circuits contributing to control of breathing (Figure V-1A). We used an explicit computational modeling approach and focused on investigating the anticipated changes in the motor output (activity of the phrenic nerve, PN), specifically the changes in the duration of the inspiratory and expiratory phases under conditions of removal or suppression of the above feedback interactions (Figure V-1A). The full schematic of our model is shown in Figure V-1. While developing this model, we used as a basis and extended the well-known large-scale computational model of the brainstem respiratory network developed by [16]. This basic model focused on the interactions among respiratory neuron populations within the medullary VRC. Similar to that model, the medullary respiratory populations in the present model (see Figure V-1B) include (right-to-left): a ramp-inspiratory (ramp-I) population of pre-motor bulbospinal inspiratory neurons and an inhibitory early-inspiratory [early-I(2)] population—both in the rostral ventral respiratory group (rVRG); a pre-inspiratory/inspiratory (pre-I/I) and an inhibitory early-inspiratory [early-I(1)] populations of the pre-BötC; and an inhibitory augmenting-expiratory (aug-E) and inhibitory (post-I) and excitatory (post-Ie) post-inspiratory populations in the BötC. As suggested in the previous modeling studies [16], [18], [19], these populations interact within and between the pre-BötC and BötC compartments and form a core circuitry of the respiratory CPG. In addition, multiple inputs and drives from other brainstem components, including the pons, RTN, NTS, and raphé affect interactions within this core circuitry and regulate its dynamic behavior and the motor output expressed in the activity of phrenic nerve (PN).

Respiratory oscillations in the basic and present models emerge within the BötC/pre-BötC core due to the dynamic interactions among: (1) the excitatory neural population, located in the pre-BötC and active during inspiration (pre-I/I); (2) the inhibitory population in the pre-BötC providing inspiratory inhibition within the network [early-I(1)]; and (3) the inhibitory populations in the BötC generating expiratory inhibition (post-I and aug-E). A full description of these interactions leading to the generation of the respiratory pattern can be found in previous publications [16], [18], [19]. Specifically, during expiration the activity of the inhibitory post-I neurons in BötC decreases because of their intrinsic adaptation properties (defined by the high-threshold calcium and calcium-dependent potassium currents) and augmenting inhibition from the aug-E neurons Figure V-1B and Figure V-2A,B). At some moment, the pre-I/I neurons of pre-BötC release from the deceasing post-I inhibition and start firing (Figure V-2) providing excitation to the inhibitory early-I(1) population of pre-BötC and the premotor excitatory ramp-I populations of rVRG (Figure V-1B). The early-I(1) population inhibits all post-inspiratory and expiratory activity in the BötC leading to the disinhibition of all inspiratory populations including the ramp-I hence completing the onset of inspiration (E-I transition). During inspiration early-I(1) inhibition of BötC expiratory neurons decreases due to intrinsic adaptation properties defined by the high-threshold calcium and calcium-dependent potassium currents (Figure V-2). This decrease of inspiratory inhibition leads to the onset of expiration and termination of inspiration (inspiratory off-switch) (Figure V-2). In the rVRG, the premotor ramp-I neurons receive excitation from the pre-I/I neurons and drive phrenic motoneurons and PN activity. The early-I(2) population shapes augmenting pattern of ramp-I neurons and PN. The PN projects to the diaphragm (Figure V-1B) hence controlling changes in the lung volume (inflation/deflation) providing breathing.

The architecture of network interactions within the medullary VRC column (i.e., within and between the BötC, pre-BötC and rVRG compartments) in the present model is the same as in the preceding model of [16]. The extension of the basic model in the present study includes: (1) a more detailed simulation of the pontine compartment (in the Smith et al. model, the pontine compartment did not have neuron populations but simply provided tonic drive to medullary respiratory populations), (2) incorporation of suggested interactions between the pontine and medullary populations that form the pontine control loop in the model (Figure V-1), and (3) incorporation of the pulmonary (vagal) control loop that included models of the lungs and pump cells in the NTS (Figure V-1).

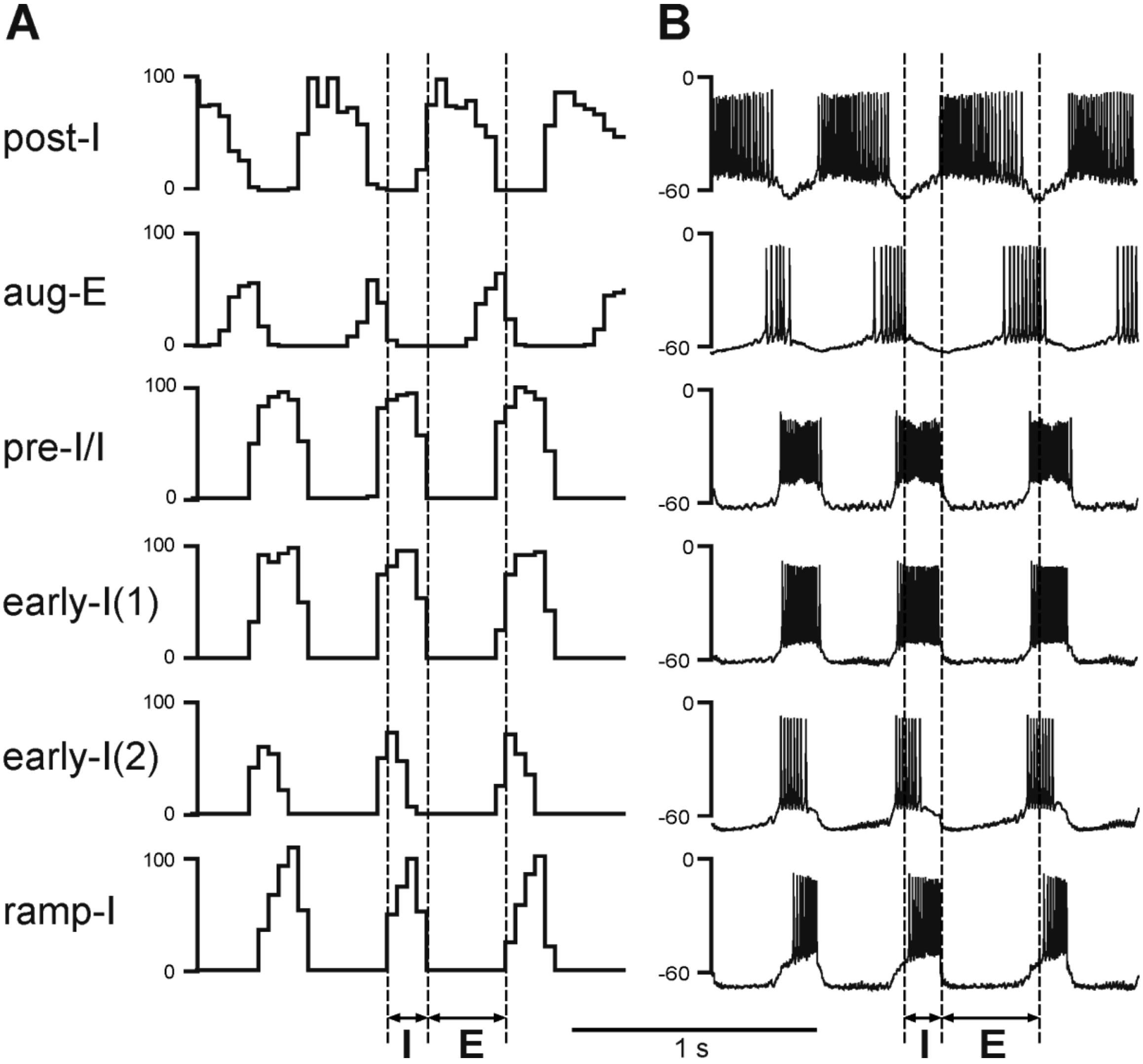

Figure V-2. Performance of the core medullary network under normal conditions (with both feedbacks intact). (A) The activity of main neural populations of the core respiratory network under normal conditions. The shown population activities include (top–down): post-inspiratory (post-I) and augmenting expiratory (aug-E) (both in BötC); pre-inspiratory/ inspiratory (pre-I/I) and early-inspiratory [early-I(1)] (both in pre-BötC); early-inspiratory [early-I(2)] and ramp-inspiratory (ramp-I) (both in rVRG).The activity of each population is represented by the histogram of neuronal firing in the population (spikes/s; bin = 30 ms). (B) Traces of membrane potentials of the corresponding single neurons (randomly selected from each population). Vertical dashed line indicate the inspiratory (I) and expiratory (E) phases.

C-2. Pontine feedback loop

As shown in multiple studies in cats and rats, many pontine neurons (including those in the Kölliker-Fuse and parabrachial nuclei) exhibit respiratory modulated activity, specifically with I-, IE-, E-, or EI-related activity [3], [64], [67], [68], [73], [82], [224]–[229]. These neurons may have respiratory modulated activity summarized with background tonic firing or may express a pure phasic respiratory activity (especially in rats, e.g., see [82], [233]). These pontine respiratory-modulated activities are probably based on specific axonal projections and synaptic inputs from the corresponding medullary respiratory neurons [3], [225], [229]–[233]. In turn, pontine neurons (including those in the Kölliker-Fuse and parabrachial nuclei) project back to the medullary respiratory neurons contributing to the control of the respiratory phase durations and phase switching [18], [60], [64], [74], [184], [236]. These mutual interactions between pontine and medullary respiratory neurons form what we refer to as a pontine (or pontine-medullary) control loop.

To simulate the pontine feedback loop, we incorporated in the pontine compartment of the model the following populations (see Figure V-1B): the excitatory populations of neurons with inspiratory-modulated (I), inspiratory-expiratory-modulated (IEe) and expiratory-modulated (E) activities, and the inhibitory population of neurons with an inspiratory- expiratory-modulated (IEi) activity. As described above, pontine neurons with such types of modulated activity were found in both rat and cat. However, the existing experimental data on intrapontine and pontine-medullary interactions are insufficient and do not provide exact information on the specific connections between these neuron types; they only suggest general ideas and principles for organization of these interactions, such as the possible reciprocal interconnections between the pontine and medullary neurons with similar respiratory-related patterns (see references in the previous paragraph) and the existence of pontine projections to key medullary neurons involved in the respiratory phase switching (such as post-I, see references above). Therefore in the model, respiratory modulation of neuronal activity in pontine populations was provided by excitatory inputs from the medullary respiratory neurons with the corresponding phases of activity within the respiratory cycle. Specifically, the inspiratory modulation activity in the pontine I population was provided by excitatory inputs from the medullary ramp-I population, the IE modulation in the pontine IEe and IEi populations resulted from excitatory inputs from the medullary ramp-I and post-Ie populations, and the expiratory-modulation in the pontine E population was provided by inputs from the medullary post-Ie population. In addition, to simulate the presence of neurons with respiratory modulated phasic and tonic activities, each of the above four population was split into two equal subpopulations with neurons having the same properties and neuronal connections, but differed by tonic drive, which was received only by tonically active subpopulations (not shown in Figure V-1B).

In turn, the pontine feedback in the model included (see Figure V-1B): (1) excitatory inputs from the pontine I neurons (from both tonic and phasic subpopulations) to the medullary pre-I/I and ramp-I populations; (2) excitatory inputs from the pontine IEe neurons (both tonic and phasic subpopulations) to the medullary post-I population; (3) inhibitory inputs from the pontine IEi neurons (again both subpopulations) to the medullary early-I(1) population; and (4) excitatory inputs from the pontine E neurons (both subpopulations) to the medullary post-I, post-Ie, and aug-E populations. These neuronal connections from pons to medulla (especially pontine inputs to the medullary post-I and pre-I/I populations) allowed the pontine feedback to control operation of the respiratory network in the BötC/pre-BötC core and specifically to control the durations of the respiratory phases and phase switching. Specifically, the connection weights in the model were tuned so that (a) the durations of inspiration (T_I) and expiration (T_E) in the model without vagal feedback would be within the corresponding physiological ranges for the vagotomized rat *in vivo* (T_I = 0.2–0.55 s and T_E = 0.8–1.7 s, e.g., see [241], [249]) and (b) after full suppression or removal of the pons, the value of T_I would dramatically increase (3–4 times or more) to be consistent with apneusis [58], [75], [227].

C-3. Pulmonary (Vagal) feedback loop

The busting activity of phrenic motoneurons produces rhythmic inflation/deflation of the lungs, which in turn causes rhythmic activation of PSRs projecting back to the medullary respiratory network within the vagus nerve and hence providing pulmonary (vagal) feedback. The activity of pulmonary afferents in the medulla is relayed by the NTS pump (P) cells. To simulate pulmonary feedback loop, we incorporated simplified models of the lungs and PSRs, so that changes in the lung volume were driven by the activity of PN (see Figure V-1A,B). The resultant lung inflation activates PSRs that projected back activating the excitatory (Pe) and inhibitory (Pi) pump cells populations in the NTS. The latter finally projected to the VRC and pons (Figure V-1B). Hence in the model, both Pe and Pi populations were involved in the Hering-Breuer reflex preventing over-inflation of the lungs. Specifically (Figure V-1B), the Pe population excited the post-I population, which was based on the previous experimental data that both lung inflation and electrical stimulation of the vagus nerve produced an additional activation of decrementing expiratory neurons [250]. Following the previous model [18] we suggested that vagal feedback inhibits the early-I(1) population (in this model, via the Pi population). Both these interactions produced a premature termination of inspiration with switching to expiration and a prolongation of expiration.

C-4. Interactions between the loops

As mentioned in the section “Introduction,” the respiratory-modulated activity in the pons is usually much stronger in the absence of lung inflation and in vagotomized animals (e.g., see [72], [228]). One explanation for these effects is that the respiratory-modulated activity in the pons is suppressed by vagal afferents via NTS neurons projecting to the pons. There is indirect evidence that this suppression is based on presynaptic inhibition [73], [228]. Therefore in our model, this presynaptic inhibition is provided by the Pi population of NTS and affects all excitatory synaptic inputs from medullary to pontine neural populations (Figure V-1B). Therefore, this presynaptic inhibition suppresses the respiratory modulation in the activities of pontine neurons and reduces the influence of pontine feedback on the medullary respiratory network operation and the respiratory pattern generated. Because of the lack of specific data, the synaptic weighs of connections from both pump cell populations (Pe and Pi) were set so that (a) significantly reduce the respiratory modulation in all types of pontine neurons and (b) keep the durations of inspiration and expiration in simulations with vagal feedback intact within their physiological ranges for the rat *in vivo* (T_I = 0.17–0.3s and T_E = 0.3–0.5 s, e.g., see [241]).

C-5. Simulation of vagotomy (pulmonary feedback removal)

Under normal conditions the “intact” model generated the respiratory pattern with the duration of inspiration T_I = 0.189 ± 0.046 s and the duration of expiration T_E = 0.388 ± 0.064 s (Figure V-2, Figure V-3A, Figure V-4A, Figure V-5A). “Vagotomy” was simulated by breaking the pulmonary feedback, specifically by a removal of afferent inputs from PSRs to the pump cells in the NTS (Figure V-1A). The resultant changes in the activity of different neural populations and in the output respiratory pattern in the model after simulated vagotomy are shown in Figure V-3B and Figure V-4B. As a result of vagotomy the pump cells (Pi and Pe populations) become silent (only the activity of Pi is shown in Figure V-3B and Figure V-4B; the activity of Pe population is similar, i.e., it also becomes silent). This eliminates the excitatory effect of lung inflation (PSR) on the post-I population (and post-Ie, pre-I/I, and ramp-I), mediated by Pe, and its inhibitory effect on the aug-E population, provided by Pi (Figure V-1B). This also eliminates the pulmonary (vagal) control of respiratory phase switching and phase durations. However, this breaking of the pulmonary feedback also removes the presynaptic inhibition of all medullary inputs to pontine neural populations (provided in the intact case by the NTS’s Pi population) hence increasing respiratory-modulated activities in the pontine neurons involved in the feedback control of the respiratory network operation (Figure V-1A,B). This therefore increases the gain of pontine feedback and its role in the control of respiratory phase switching and phase durations. Figure V-3 shows that the vagotomy resulted in increases in the respiratory-modulated activity of pontine populations, a prolongation of inspiration (T_I = 0.277 ± 0.108 s), and a dramatic increase in the expiratory phase duration (T_E = 0.938 ± 0.065 s). Figure V-4 shows that the applied vagotomy produced a significant increase of inspiratory (I), inspiratory-expiratory (IE), and expiratory (E) modulation in the activity of the corresponding pontine neurons with tonic activity and releases the corresponding firing in pontine neurons with phasic I, IE, and E activities not active in the intact case.

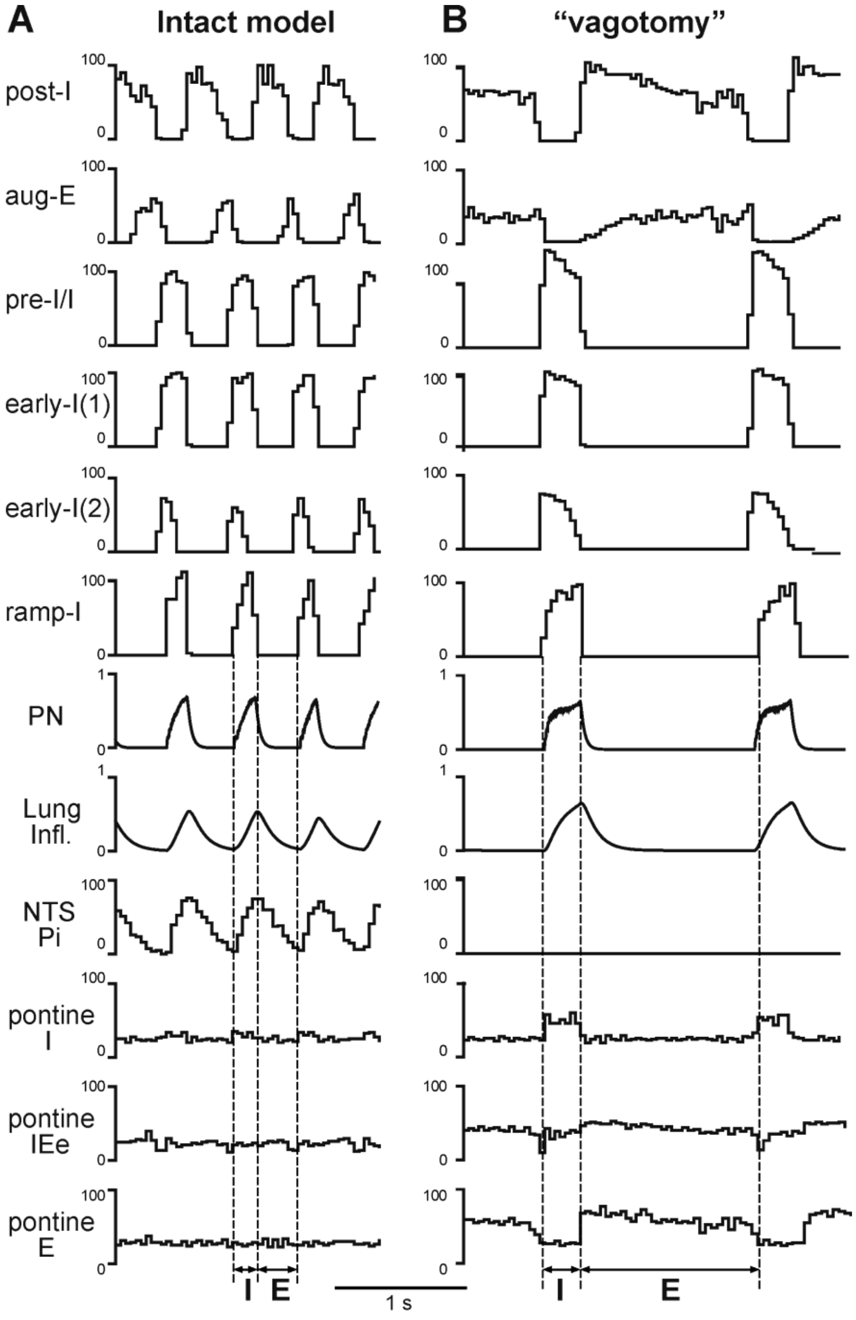

Figure V-3. Simulated vagotomy (removal of the pulmonary feedback). Activity of major VRC (post-I, aug-E, early-I(1), pre-I/I, early-I(1), early-I(2), and ramp-I), NTS (Pi) and pontine (I, IEe, and E) neural populations, lung inflation and PN activity before (A) and after (B) simulated vagotomy. Vertical dashed line indicate the inspiratory (I) and expiratory (E) phases. See text for details.

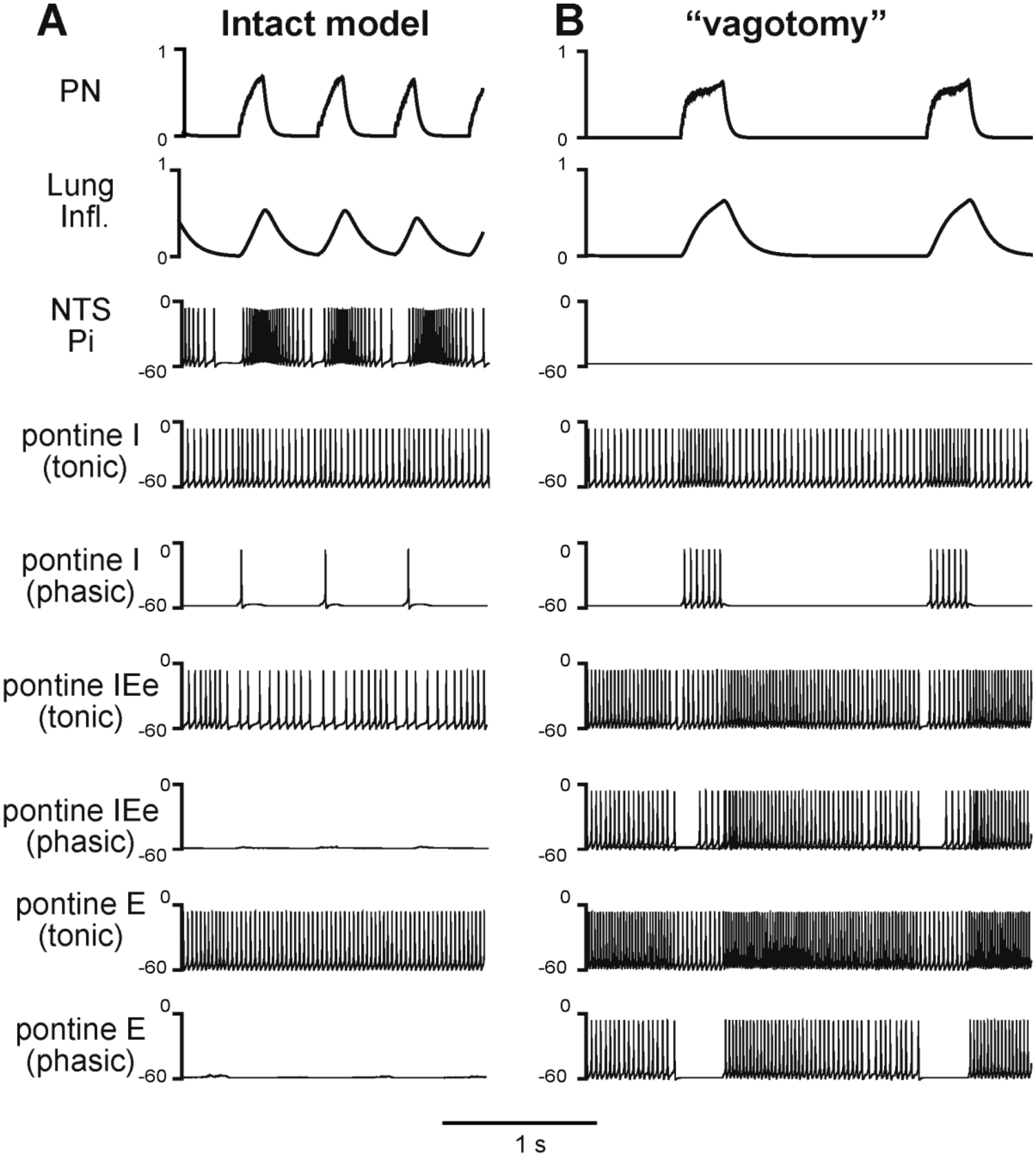

Figure V-4. Respiratory modulation in the activity of pontine neurons before (A) and after (B) simulated vagotomy. The changes of phrenic activity (PN) and the lung inflation are shown at the top. Below these graphs, membrane potentials traces of representative single neurons from the Pi and pontine populations (tonic and phasic subpopulations) are shown. See text for details.

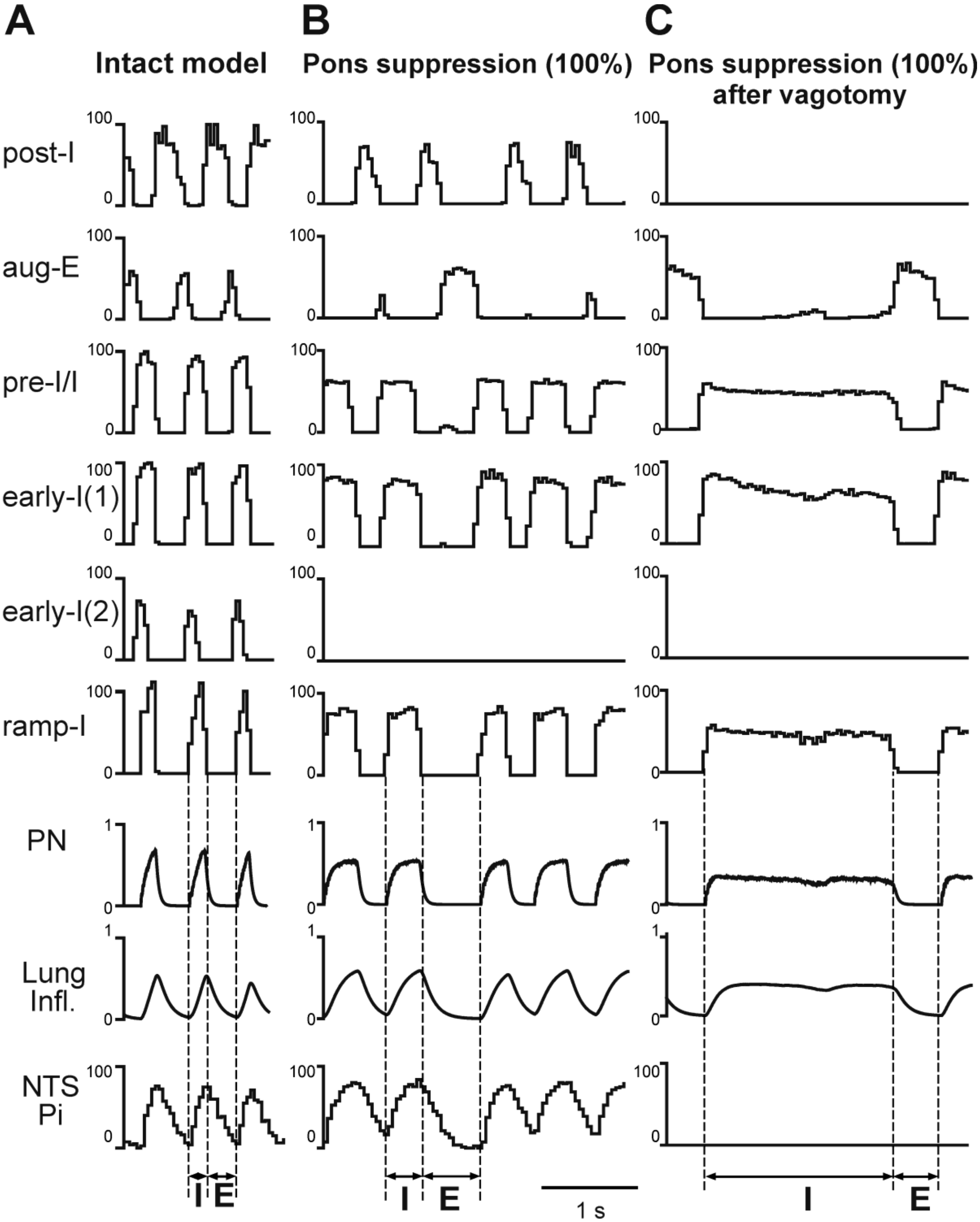

Figure V-5. The effects of pontine suppression before and after simulated vagotomy. Activity of major medullary [post-I, aug-E, early-I(1), pre-I/I, early-I(1), early-I(2), and ramp-I], NTS (Pi) and pontine (I, IEe, and E) neural opulations, lung inflation and PN activity under control conditions. (A) and following the 100% suppression of pontine activity before (B) and after (C) simulated vagotomy. The activity pattern shown in (C) represents typical apneusis. Vertical dashed line indicate the inspiratory (I) and expiratory (E) phases. See text for details.

C-6. Simulation of pontine feedback suppression with and without pulmonary feedback

A complete removal of the pons (i.e., a removal of pontine feedback) in the model with an intact pulmonary feedback produced a prolongation of inspiration (T_I = 0.337 ± 0.052 s) and a slightly reduced in average (in comparison to the intact model) but highly variable expiratory duration (T_E = 0.353 ± 0.159 s) characterized by occasional deletions of aug-E bursts (see Figure V-5B and Figure V-6A). To compare our simulations with the existing experimental data on the effects of pontine suppression by local injections of MK801, a blocker of NMDA receptors, that might not completely suppress the excitatory synaptic transmission in the pontine neurons and their activity, we also simulated a partial suppression of excitatory synaptic weights in the pontine compartment (e.g., by 25% see Figure V-6A). Such partial suppression produced a visible prolongation of inspiration (T_I = 0.262 ± 0.028 s with T_E = 0.297 ± 0.028 s at 25% suppression, Figure 6A).

In contrast to pontine suppression with the intact pulmonary feedback, the same procedures after vagotomy led to a dramatic increase in the average duration of inspiration (making the inspiratory duration highly variable) at relatively constant duration of expiration (Figure V-5C and Figure V-6A). This prolongation of inspiration after vagotomy increased with the degree of pontine suppression (reducing the weights of excitatory synaptic inputs to pontine neurons) (Figure V-6A) and accompanied by a suppression or full elimination of post-I activity and reduced amplitude of integrated PN (Figure V-5C). Both these features are typical for apneusis [3], [75], [227], [251]. The durations of inspiration and expiration after vagotomy at different degrees of pontine suppression were the following: T_I = 0.437 ± 0.143 s with T_E = 0.433 ± 0.030 s at 25% suppression; T_I = 0.885 ± 0.339 s with T_E = 0.417 ± 0.004 s at 75% suppression; and T_I = 571 ± 0.310 s with T_E = 0.431 ± 0.003 s at 100% suppression.

The results of our simulations reflecting changes in T_I and T_E following different combinations of vagotomy with pontine suppression at different degrees are shown together in Figure V-6A. Our general conclusions made from these simulations are the following. (1) A suppression of pontine activity with the intact pulmonary feedback leads to a moderate prolongation of inspiration, slight shortening of expiration, and an increase in variability of T_E (with 100% pontine suppression). (2) The simulated vagotomy (with the intact pontine-medullary interactions) causes a moderate prolongation of inspiration with an increase in variability of T_I and a strong prolongation of expiration. (3) Combination of both perturbations does not produce visible effects on T_E , but leads to a significant prolongation of inspiration (increasing with the degree of pontine suppression), increasing of T_I variability, and other typical characteristics of apneusis (suppressed post-I activity and reduced PN amplitude).

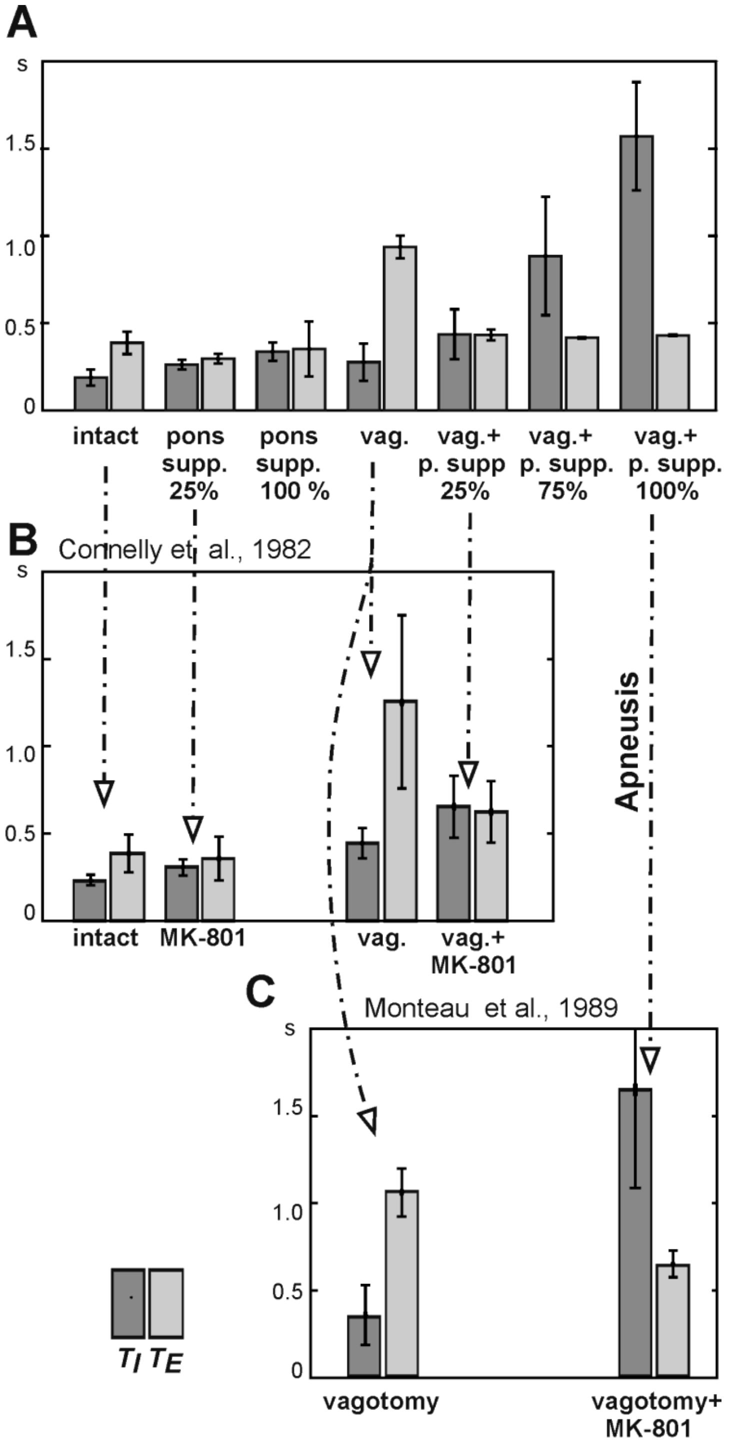

Figure V-6. Changes in the durations of inspiration (T_I) and expiration (T_E) following pontine suppression and/or vagotomy. (A) Changes in T_I and T_E following the simulated pontine suppression at different degrees (25%, 75%, and 100%) before and after (vag. +) vagotomy. (B) Changes in T_I and T_E in the study of Connelly et al. (1992): diagrams are built for spontaneously breathing Wistar rats under control conditions and after administration of NMDA blocker MK-801 before and after vagotomy. (C) Changes in T_I

and T_E in the study of Monteau et al. 1990 performed in anaesthetized vagotomized rats using MK-801 administration.

C-7. Comparison with experimental data

To test our model, we performed simulation with 25%, 75%, and 100% suppression of the pontine control loop before and after simulated vagotomy (removal of the pulmonary feedback). The resultant changes in T_I and T_E are shown in Figure V-6A. To compare these simulation results with the related experimental data, we built similar diagrams from the early study of Connelly et al., 1992 [241], which examined spontaneously breathing in Wistar rats during the administration of NMDA blocker MK-801 before and after vagotomy (Figure V-6B). In this study, the experiments on Wistar rats (in contrast to the Sprague-Dawley strain) did not end with apneusis, due to (in our opinion) an insufficient suppression of the pontine feedback by the performed MK-801 injections. Nevertheless, the effects of vagotomy and MK-801 administration on T_I and T_E before and after vagotomy reported in Connelly et al. study are qualitatively similar to our simulations with 25% suppression of pontine feedback (see Figure V-6A,B). Specifically, the 25% pontine suppression in our simulations and the administration of MK-801 in Connelly et al. experiments result in an increase of T_I and slight reduction of T_E before vagotomy and in a significant prolongation of inspiration after vagotomy. In addition, vagotomy alone without other perturbations in both cases results in an increase of T_I and significant prolongation of T_E (see Figure V-6A,B). Moreover, the changes in the respiratory frequency and the shape and amplitude of integrated phrenic activity after vagotomy and/or pontine suppression in our model are similar to that in the experimental studies with MK-801 administration (Figure V-7). The other comparison of our simulations was made with the experimental study of Monteau et al., 1990 [249] performed in anaesthetized vagotomized rats by using MK-801 administration, which results are summarized in Figure V-6C. This study did demonstrate that MK-801 application after vagotomy produced switching from a normal breathing pattern to the typical apneusis. The relationships between T_I and T_E in our simulation after vagotomy and their changes following 100% pontine suppression (apneusis) are similar to these in the Monteau et al. study (see Figure V-6A,C).

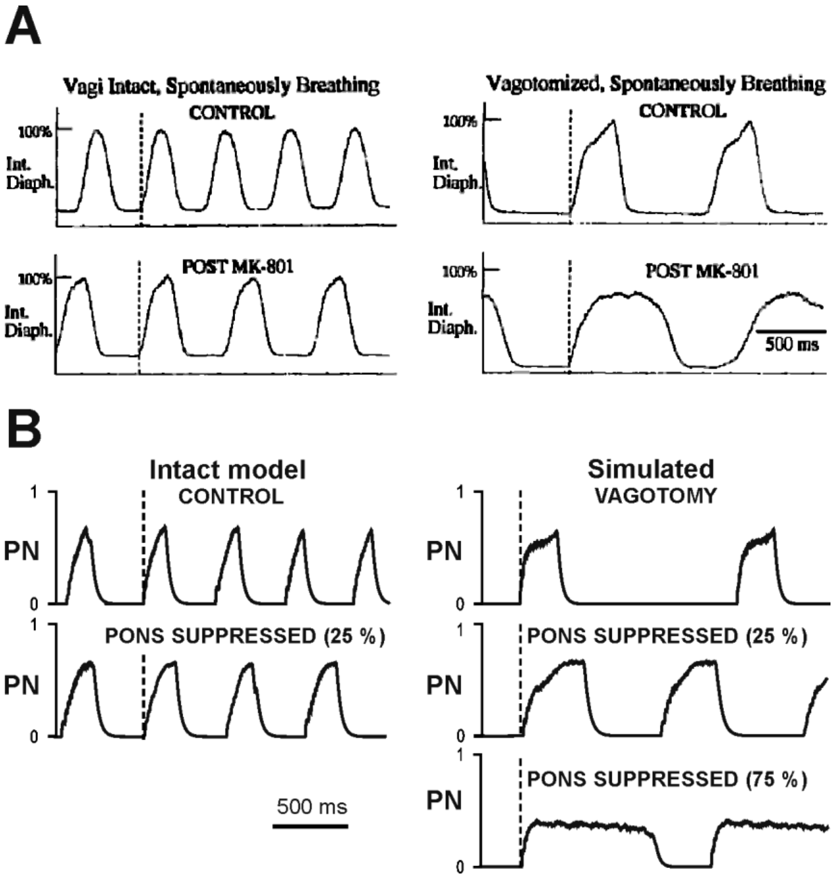

Figure V-7. Changes in the breathing pattern (phrenic activity, PN) following MK-801 application (pontine suppression in the model) before and after vagotomy. (A) Changes in integrated phrenic nerve activity (Int. Diaph.) from spontaneously breathing Wistar rats before (top traces) and after (bottom traces) NMDA channel blockade, before (left diagrams) and after (right diagrams) vagotomy (from Connelly et al., 1992) (B) Changes in integrated phrenic nerve activity (PN) in our simulations before (top traces) and after (bottom traces) simulated pontine suppression, before (left diagrams) and after (right diagrams) simulated vagotomy.

D. Discussion

The results of our simulations promote the concept that both pulmonary and pontine feedback loops contribute to the control of the respiratory pattern and, specifically, the durations of inspiration (T_I) and expiration (T_E). Furthermore, our modeling results are consistent with the previous suggestion of specific interactions between these feedback loops, in particular that the PSR afferents involved in the pulmonary control of T_I and T_E attenuate the gain of the pontine control of these phase durations (via the presynaptic inhibition of excitatory inputs from medullary to pontine populations) [3], [60], [71]–[73]. Nevertheless, according to our simulations, pontine activity still plays a role in the control of inspiration and expiration even when the pulmonary feedback is intact, although the gain of this pontine control is significantly reduced by the presynaptic inhibition. This presynaptic inhibition is expected to suppress the respiratory modulation in the activity of pontine neurons expressing either tonic or phasic firing patterns [3], [67], [68], [71]–[73], [82], [226]–[229], which is reproduced by our model (Figure V-4). Also, the model offers a plausible mechanistic explanation for the previous experimental findings that injection of NMDA antagonists in the dorsolateral pons (specifically in the Kölliker-Fuse area) leads to a prolongation of inspiration and to apneusis in the case of a lack of pulmonary feedback [5], [58], [227], [237], [240], [241], [243], [244].

In contrast to previous suggestions and models [18], [60], [64], [74], [184], [236], the mechanisms of action of the two feedbacks considered in the current model are not exactly symmetric. Excitatory inputs from both these feedbacks (from PSRs via the NTS's

Pe cells, and from the pontine I, IEe, and E populations) activate the ramp-I, pre-I/I, post-Ie, and post-I medullary populations (see Figure V-1B). The majority of these excitatory connections are the ones activating the inhibitory post-I population that controls the inspiratory off-switching, i.e., the timing of inspiratory phase termination and T_I, and those activating the excitatory pre-I/I population which, in a balance with the inputs to post-I, control the onset of inspiration (and T_E). However the effect of these excitatory inputs from the two feedbacks on the medullary circuitry is not identical and depends on the particular synaptic weights and the activity pattern of the inhibitory NTS's Pi cells providing presynaptic inhibition of medullary inputs to the pontine neurons (Figure V-1B). The organization of inhibitory inputs of these feedbacks to the medullary populations in the model is different. While the pulmonary feedback inhibits the aug-E population (via PSRs and Pi cells) causing a complex effect on the respiratory pattern, the pontine IEi population inhibits the early-I(1) population hence promoting expiration, which is clearly seen after vagotomy (Figure V-1B).

It is important to mention that the current model of the medullary core respiratory circuits in the VRC (including the BötC, pre-BötC, and rVRG) used in our model was derived from the model of Smith et al. 2007 without significant changes. Starting with that first publication, this basic model (with necessary additions) was able to reproduce multiple experimental results, including the characteristic changes of the respiratory pattern following a series of pontine and medullary transections and effect of riluzole (persistent sodium current blocker) on the intact and sequentially reduced *in situ* preparation [16], [19], the emergence of the additional late-expiratory oscillations in the RTN/parafacial respiratory group (RTN/pFRG) during hypercapnia and interactions between the BötC/pre-

BötC and RTN/pFRG oscillators [17], [41], [88], the effects of baroreceptor stimulation and the respiratory-sympathetic coupling including this following the intermittent hypoxia [245], [246], etc. The extended model described here was also able to reproduce the above behaviors, including the biologically plausible changes of membrane potentials and firing patterns of different respiratory neurons (Figure V-2B). The ability of the extended model to reproduce the experimentally observed effects of the two feedback loops provides an additional support for the model of the core respiratory circuits used in all these previous models.

The exact mechanisms of pontine control of breathing are not well-understood and the pontine-medullary connections incorporated in the model are currently speculative. However, the general importance of the pons in the control of the respiratory pattern is well-recognized (see [64], for review). Studies utilizing the classic neurophysiological approaches of lesioning, stimulating and recording neurons have established that the lateral pons influences not only phase duration, phrenic amplitude, and response to afferent stimulation, but also the dynamic changes in respiratory pattern associated with persistent stimuli. For instance, blocking neural activity in the dorsolateral pons not only prolongs inspiration but also blocks the adaptation to vagal stimulation [252], and the shortening of expiration associated with repeated lung inflation [60]. Thus, the pons is not only intimately involved in the initial response to various stimuli, but also in the complex processes of accommodation and habituation. In the cardiovascular control system, parabrachial stimulation attenuates the NTS response to carotid sinus nerve stimulation by inhibition of NTS neurons receiving these inputs [253].

With normally operating pontine-medullary interactions, the simulated vagotomy results in a prolongation of inspiration and significant increase of the expiratory duration (Figure V-3B and Figure V-6A). However, despite these changes, the breathing pattern after vagotomy remains similar to that in eupnea (Figure V-3). This maintenance of the eupneic breathing pattern occurs because the control performed by the pulmonary loop is now partly mimicked by the pontine loop, whose gain is increasing after vagotomy, as the latter removes the presynaptic inhibition of medullary inputs to pontine neurons (Figure V-1B). Our model suggests that the pulmonary feedback yet performs the major function in the control of respiratory phase transitions and phase durations, and that a removal of this control loop places the full responsibility for this control on the pontine feedback loop.

The complementary role of the pontine and pulmonary feedbacks in control of phase duration (especially T_I) in our model is consistent with the classical interpretation of their function in respiratory control (see [64], for review). In particular, a premature termination of inspiration and switching to expiration can be elicited by stimulation of either the rostral pons or the pulmonary afferents [3], [18], [184], [224], [227], [236]. This observation was explained by their common excitatory input on the post-inspiratory neurons in the medullary VRC which are critically involved in this phase transition [18], [60], [184], [236].

Alternatively, our results suggest that the pontine-medullary feedback does not simply function as an “internal pulmonary feedback,” performing a redundant function and compensating for the potential loss of vagal input. The specific increase in the variability of T_E with the suppression pontine activity and the significant prolongation of T_E after vagotomy (Figure V-6A) indicate that the pontine and pulmonary feedbacks differ in the control of T_E. Indeed, our modeling results show that these control loops may complement each other in differential control of phase duration and breathing pattern variability. For example, an increase of T_E variability with pontine suppression, as seen in Figure V-5B and Figure V-6A, may be the case during various breathing disorders, such as sleep apnea or ventilator weaning [254]. In this connection, the stability of T_E can be critically important and is primarily being controlled by the pons. Moreover, the Kölliker-Fuse area of the dorsolateral pons was explicitly identified to contribute to breathing disorders in a mouse model for a neurodevelopmental disease called Rett-syndrome [255], [256].

Consistent with the many earlier and recent experimental data from cats and rats [3], [50], [75], [227], our simulations show that a strong pontine suppression (e.g., 75%) or its removal after vagotomy leads to apneusis, characterized by a significant increase of inspiratory duration and its variability (Figure V-5C and Figure V-6A). The other specific characteristics of apneusis are a lack of post-inspiratory activity and a reduction of phrenic amplitude during inspiration [3], [50], [75], [227], which were reproduced in our simulations (Figure V-5C).

Our understanding of interactions between individual components of complex systems is often insufficient to explain emergent properties of these systems. The present study elucidates the important role of two major feedback loops and interactions between them in regulation of the respiratory rate and breathing pattern allowing the brainstem respiratory network to maintain system's homeostasis and adjust breathing to various metabolic and physiologic demands.

E. Summary of predictions

System level predictions: The main topic of this work concerned the inspiratory off switch (IOS) that was governed by the pulmonary and pontine feedback loops. Our model predicted that the IOS mechanism of both loops operated via excitation of the post-I neurons in the pre-BötC. Moreover, we predict that, under intact conditions, i.e. present pulmonary and pontine feedback loops, the pulmonary feedback loop provides the main source of inspiratory termination. However, when the pulmonary feedback loop is removed (analogous to vagotomy), phasic pontine activity emerges and assumes control of the IOS. Our results suggest that: (i) the pons assumes control of the IOS when the pulmonary feedback loop fails and (ii) the pons minimizes variability of the expiratory phase duration.

Excitation of the post-I neurons for the IOS builds on the conclusion that the “release” mechanism, and not “escape,” causes the inspiration to expiration transition. In the previous chapter, we showed that the escape mechanism appears to increase the robustness of phase duration relative to the release mechanism. Future work in this area could use phase plane analysis to determine if the IOS exploits the escape/release framework. However, it would be consistent with our findings if the transition from inspiration to expiration is governed by escape and release when the feedback loops are present and absent, respectively.

Chapter VI: Summary

The work presented in this dissertation is the result of several, related projects completed since joining the Rybak lab in May 2009. The overarching goal was to create a progressively more extensive model of the respiratory CPG network that would offer insights into the mechanisms underlying the neural control of respiration in mammals. However, my secondary goal was to make computational neuroscience, and applied mathematics in general, more accessible to experimentalists and the public at large. Software for several models presented in this dissertation are readily available from our lab's webpage.

My first specific aim was to address the existence of mixed mode oscillations in the pre-Bötzinger complex (pre-BötC) of inspiratory neurons. I used a large-scale model of 100 spiking neurons with sparse connectivity and heterogenous values of baseline excitability (set by distributing the reversal potential of the leak current, E_L). When connection weights were varied, mixed mode oscillations emerged for a broad range of parameter sets. Careful observation of the participating neurons showed that small amplitude bursts were comprised of mostly high excitability neurons, and large amplitude bursts only occurred when low excitability neurons participated. A reduced model was then constructed to demonstrate that the slow recovery of the low excitability neurons determined the timing of large amplitude population bursts. This study indicates the critical nature of a core sub-group of low excitability neurons in the pre-BötC that ultimately determine the timing of motor outputs needed for inspiration. This model predicts the emergence of MMOs when I_{NaP} is attenuated, a specific finding that is under investigation by researchers in Jeff Smith's lab at NIH/NINDS.

My second and third specific aims addressed the interactions between the pre-BötC, BötC, RTN/pFRG, and the pontine regions of the VRC. A similar pre-BötC population from Aim 1 was used in this model, although mixed mode oscillations were not a concern. The interactions studied in Aims 2 and 3 involved the emergence of RTN/pFRG activity during conditions with elevated CO_2 (hypercapnia). Experimental evidence demonstrated that the abdominal nerve activates just before inspiration in quantal (i.e. integer ratios) increments relative to the main inspiratory motor nerves (phrenic and hypoglossal nerves), and approaches a 1:1 ratio when carbon dioxide is at a maximum. Moreover, this abdominal nerve activity was likely caused by pre-motor activity of the RTN/pFRG as inhibition of the RTN/pFRG caused silencing of the abdominal nerve. Experimental evidence also indicated a transformation to a biphasic (late-expiratory, early-inspiratory) pattern of RTN/pFRG (and abdominal nerve) activity when O_2 was reduced (hypoxic conditions). Moreover, application of opioids caused a quantal slowing of the BötC/pre-BötC relative to the RTN/pFRG.

In Aim 2, I used a large-scale model to fully recreate the experimental evidence and in Aim 3 I used a reduced model to understand the dynamics of the large-scale model from a dynamical systems perspective. These models made several assumptions that were ultimately model predictions: (i) the RTN/pFRG had to have intrinsic rhythmicity, in this case rhythmicity came from the persistent sodium current; (ii) the RTN/pFRG received inhibition from the post-I neurons of the BötC, thus restricting the onset of RTN/pFRG activity to the end of the expiratory phase; (iii) the RTN/pFRG projected to the pre-motor neurons of the pre-BötC and excited these inspiratory neurons, facilitating the onset of the inspiratory phase; (iv) the RTN/pFRG either has intrinsic chemosensitivity or receives a tonic drive from chemosensitive regions; (v) the pons is particularly sensitive to hypoxia and reducing pontine involvement caused a reduction of post-I activity in the BötC, leading to less inhibition of the RTN/pFRG during expiration, ultimately enabling the biphasic-E pattern; (vi) application of opioids caused a decrease in the strength of excitatory connection between respiratory neurons, particularly in the pre-BötC, and this led to a quantal slowing of the BötC/pre-BötC with respect to the RTN/pFRG. The work done in these modeling studies increased our understanding of the connectivity architecture of the brainstem respiratory network and the intrinsic properties of neurons in the RTN/pFRG region of the medulla.

In Aim 4 I incorporated several elements of the models in Aims 1-3 to model not only the interactions of the VRC, but also lung inflation and its effect on neurons in the NTS. The interactions between the BötC/pre-BötC, pons, and NTS are not well understood, and this modeling study provided several specific predictions regarding these interactions. Namely, (i) excitatory pump cells in the NTS project to neurons in the BötC, facilitating the termination of inspiration and the onset of expiration; (ii) inhibitory pump cells presynaptically neurons in the pons, reducing their phasic modulation; (iii) vagotomy eliminates NTS activity and allows the pons, which is now disinhibited, to function as an inspiratory off switch. This modeling study built on the work presented in Aims 1-3 to further increase our understanding of the connectivity between key parts of the brainstem respiratory network.

The multi-scale, hierarchal approach presented in this thesis enabled me to analyze interactions in complex systems in a logical fashion. I started with a single population (the pre-BötC) and studied particular features of that population, then incorporated more populations (BötC, RTN/pFRG, and the pons) to understand how the larger respiratory network functioned, finally I incorporated a model of the lungs and the NTS to further understand the dynamics of this system. That said, the work presented in this dissertation is far from a complete understanding of the neural control of respiration. However, several models presented in this dissertation have been expanded for use in other computational studies [245], [246], [257]–[260], that have continued to increase our understanding of the generation and control of respiration. It is my hope that work of the type presented here, i.e. collaborative efforts between experimentalists and computational modelers, continues to further our understanding of many basic processes and clinical interventions.

Bibliography

[1] K. E. Barrett, S. M. Barman, S. Boitano, and H. L. Brooks, “Introduction to Pulmonary Structure & Mechanics,” in *Ganong’s Review of Medical Physiology, 25e*, New York, NY: McGraw-Hill Education, 2016.

[2] W. M. Panneton and A. J. Lechner, “Central and Peripheral Neural Controls of Respiration,” in *Respiratory: An Integrated Approach to Disease*, A. J. Lechner, G. M. Matuschak, and D. S. Brink, Eds. New York, NY: McGraw-Hill Education, 2015.

[3] M. I. Cohen, “Neurogenesis of respiratory rhythm in the mammal.,” *Physiol. Rev.*, vol. 59, no. 4, pp. 1105–73, Oct. 1979.

[4] D. Richter and J. C. Smith, “Respiratory rhythm generation in vivo.,” *Physiology (Bethesda).*, vol. 29, no. 1, pp. 58–71, 2014.

[5] A. L. Bianchi, M. Denavit-Saubie, and J. Champagnat, “Central control of breathing in mammals: neuronal circuitry, membrane properties, and neurotransmitters.,” *Physiol. Rev.*, vol. 75, no. 1, pp. 1–45, 1995.

[6] D. D. W. Richter and K. M. Spyer, “Studying rhythmogenesis of breathing: Comparison of in vivo and in vitro models,” *Trends in Neurosciences*, vol. 24, no. 8. pp. 464–472, 2001.

[7] R. Von Baumgarten and E. Kanzow, “The interaction of two types of inspiratory neurons in the region of the tractus solitarius of the cat,” *Archives Italiennes de Biologie*, vol. 96, no. 4. pp. 361 – 373, 11-Jan-1958.

[8] M. G. Levitzky, “Chapter 9. Control of Breathing,” in *Pulmonary Physiology, 8e*, New York, NY: The McGraw-Hill Companies, 2013.

[9] M. I. Cohen, “Synchronization of discharge, spontaneous and evoked, between inspiratory neurons.,” *Acta Neurobiol. Exp. (Wars).*, vol. 33, no. 1, pp. 189–218, 1973.

[10] D. B. Averill, W. E. Cameron, and A. J. Berger, “Monosynaptic excitation of dorsal medullary respiratory neurons by slowly adapting pulmonary stretch receptors.,” *J. Neurophysiol.*, vol. 52, no. 4, pp. 771–785, 1984.

[11] S. B. Backman, C. Anders, D. Ballantyne, N. Röhrig, H. Camerer, S. Mifflin, D. Jordan, H. Dickhaus, K. M. Spyer, and D. Richter, “Evidence for a monosynaptic connection between slowly adapting pulmonary stretch receptor afferents and inspiratory beta neurones,” *Pflügers Arch. Eur. J. Physiol.*, vol. 402, no. 2, pp. 129–136, 1984.

[12] L. Kubin, G. F. Alheid, E. J. Zuperku, and D. McCrimmon, “Central pathways of pulmonary and lower airway vagal afferents.,” *J. Appl. Physiol.*, vol. 101, no. 2, pp. 618–627, 2006.

[13] D. McCrimmon, D. F. Speck, and J. L. Feldman, “Role of the ventrolateral region of the nucleus of the tractus solitarius in processing respiratory afferent input from vagus and superior laryngeal nerves,” *Exp. Brain Res.*, vol. 67, no. 3, pp. 449–459, 1987.

[14] K. Ezure, K. Otake, J. Lipski, and R. B. Wong She, “Efferent projections of pulmonary rapidly adapting receptor relay neurons in the cat,” *Brain Res.*, vol. 564, no. 2, pp. 268–278, 1991.

[15] K. Ezure, I. Tanaka, and M. Miyazaki, “Inspiratory inhibition of pulmonary rapidly adapting receptor relay neurons in the rat.,” *Neurosci. Lett.*, vol. 258, no. 1, pp. 49–52, 1998.

[16] J. C. Smith, A. P. Abdala, H. Koizumi, I. A. Rybak, and J. F. R. Paton, “Spatial and functional architecture of the mammalian brain stem respiratory network: a hierarchy of three oscillatory mechanisms.,” *J. Neurophysiol.*, vol. 98, no. 6, pp. 3370–87, Dec. 2007.

[17] Y. I. Molkov, A. P. Abdala, B. J. Bacak, J. C. Smith, J. F. R. Paton, and I. A. Rybak, “Late-expiratory activity: emergence and interactions with the respiratory CpG.,” *J. Neurophysiol.*, vol. 104, no. 5, pp. 2713–29, Nov. 2010.

[18] I. A. Rybak, N. A. Shevtsova, J. F. R. Paton, T. E. Dick, W. M. St-John, M. Mörschel, and M. Dutschmann, “Modeling the ponto-medullary respiratory network,” *Respiratory Physiology and Neurobiology*, vol. 143, no. 2–3. pp. 307–319, 2004.

[19] I. A. Rybak, A. P. Abdala, S. Markin, J. F. R. Paton, and J. C. Smith, “Spatial organization and state-dependent mechanisms for respiratory rhythm and pattern generation,” *Prog. Brain Res.*, vol. 165, pp. 201–20, Jan. 2007.

[20] J. L. Feldman and C. a. Del Negro, “Looking for inspiration: new perspectives on respiratory rhythm.,” *Nat. Rev. Neurosci.*, vol. 7, no. 3, pp. 232–242, 2006.

[21] H. Koizumi, C. G. Wilson, S. Wong, T. Yamanishi, N. Koshiya, and J. C. Smith, “Functional imaging, spatial reconstruction, and biophysical analysis of a respiratory motor circuit isolated in vitro.,” *J. Neurosci.*, vol. 28, no. 10, pp. 2353–2365, 2008.

[22] J. L. Feldman, G. S. Mitchell, and E. E. Nattie, “Breathing : Rhythmicity , plasticity , chemosensitivity,” *Annu. Rev. Neurosci.*, no. 26, pp. 239–266, 2003.

[23] J. C. Smith, H. H. Ellenberger, K. Ballanyi, D. Richter, and J. L. Feldman, “Pre-Bötzinger complex: a brainstem region that may generate respiratory rhythm in mammals.,” *Science*, vol. 254, no. 5032, pp. 726–729, 1991.

[24] J. C. Rekling and J. L. Feldman, “PreBötzinger complex and pacemaker neurons: hypothesized site and kernel for respiratory rhythm generation.,” *Annu. Rev. Physiol.*, vol. 60, pp. 385–405, 1998.

[25] N. Koshiya and J. C. Smith, “Neuronal pacemaker for breathing visualized in vitro.,” *Nature*, vol. 400, no. 6742, pp. 360–363, 1999.

[26] S. M. Johnson, N. Koshiya, and J. C. Smith, “Isolation of the kernel for respiratory rhythm generation in a novel preparation: the pre-Bötzinger complex ‘island’.,” *J. Neurophysiol.*, vol. 85, no. 4, pp. 1772–1776, 2001.

[27] S. M. Johnson, J. C. Smith, G. D. Funk, and J. L. Feldman, “Pacemaker behavior of respiratory neurons in medullary slices from neonatal rat.,” *J. Neurophysiol.*, vol. 72, no. 6, pp. 2598–2608, 1994.

[28] M. Thoby-Brisson and J.-M. M. Ramirez, “Identification of two types of inspiratory pacemaker neurons in the isolated respiratory neural network of mice.,” *J. Neurophysiol.*, vol. 86, no. 1, pp. 104–112, 2001.

[29] X. M. Shao and J. L. Feldman, “Respiratory rhythm generation and synaptic inhibition of expiratory neurons in pre-Bötzinger complex: differential roles of glycinergic and GABAergic neural transmission.,” *J. Neurophysiol.*, vol. 77, no. 4, pp. 1853–1860, 1997.

[30] C. a. Del Negro, S. M. Johnson, R. J. Butera, and J. C. Smith, “Models of respiratory rhythm generation in the pre-Bötzinger complex. III. Experimental tests of model predictions.,” *J. Neurophysiol.*, vol. 86, no. 1, pp. 59–74, 2001.

[31] K. Ezure, “Synaptic connections between medullary respiratory neurons and considerations on the genesis of respiratory rhythm,” *Progress in Neurobiology*, vol. 35, no. 6. pp. 429–450, 1990.

[32] C. Jiang and J. Lipski, “Extensive monosynaptic inhibition of ventral respiratory group neurons by augmenting neurons in the Botzinger complex in the cat,” *Exp. Brain Res.*, vol. 81, no. 3, pp. 639–648, 1990.

[33] G. F. Tian, J. H. Peever, and J. Duffin, “Botzinger-complex, bulbospinal expiratory neurones monosynaptically inhibit ventral-group respiratory neurones in the decerebrate rat,” *Exp. Brain Res.*, vol. 124, no. 2, pp. 173–180, 1999.

[34] K. Ezure, I. Tanaka, and Y. Saito, “Brainstem and spinal projections of augmenting expiratory neurons in the rat.,” *Neurosci. Res.*, vol. 45, no. 1, pp. 41–51, Jan. 2003.

[35] J. E. Rubin, N. A. Shevtsova, B. Ermentrout, J. C. Smith, and I. A. Rybak, "Multiple rhythmic states in a model of the respiratory central pattern generator.," *J. Neurophysiol.*, vol. 101, no. 4, pp. 2146–65, Apr. 2009.

[36] J. C. Smith, A. P. Abdala, I. A. Rybak, and J. F. R. Paton, "Structural and functional architecture of respiratory networks in the mammalian brainstem.," *Philos. Trans. R. Soc. Lond. B. Biol. Sci.*, vol. 364, no. 1529, pp. 2577–87, Sep. 2009.

[37] H. Onimaru, A. Arata, and I. Homma, "Primary respiratory rhythm generator in the medulla of brainstem-spinal cord preparation from newborn rat.," *Brain Res.*, vol. 445, no. 2, pp. 314–24, Apr. 1988.

[38] H. Onimaru and I. Homma, "Respiratory rhythm generator neurons in medulla of brainstem-spinal cord preparation from newborn rat.," *Brain Res.*, vol. 403, no. 2, pp. 380–384, 1987.

[39] H. Onimaru and I. Homma, "A novel functional neuron group for respiratory rhythm generation in the ventral medulla.," *J. Neurosci.*, vol. 23, no. 4, pp. 1478–1486, 2003.

[40] J. C. Smith, D. E. Morrison, H. H. Ellenberger, M. R. Otto, and J. L. Feldman, "Brainstem projections to the major respiratory neuron populations in the medulla of the cat.," *J. Comp. Neurol.*, vol. 281, no. 1, pp. 69–96, 1989.

[41] A. P. Abdala, I. A. Rybak, J. C. Smith, and J. F. R. Paton, "Abdominal expiratory activity in the rat brainstem-spinal cord in situ: patterns, origins and implications for respiratory rhythm generation.," *J. Physiol.*, vol. 587, no. Pt 14, pp. 3539–3559, 2009.

[42] W. a Janczewski and J. L. Feldman, "Distinct rhythm generators for inspiration and expiration in the juvenile rat.," *J. Physiol.*, vol. 570, no. Pt 2, pp. 407–420, 2006.

[43] W. A. Janczewski, H. Onimaru, I. Homma, and J. L. Feldman, "Opioid-resistant respiratory pathway from the preinspiratory neurones to abdominal muscles: in vivo and in vitro study in the newborn rat.," *J. Physiol.*, vol. 545, no. Pt 3, pp. 1017–26, Dec. 2002.

[44] G. Nattie and A. Li, "Multiple central chemoreceptor sites: Cell types and function in vivo," in *Advances in Experimental Medicine and Biology*, 2008, vol. 605, pp. 343–347.

[45] E. Nattie and A. Li, "Central chemoreception 2005: A brief review," *Autonomic Neuroscience: Basic and Clinical*, vol. 126–127. pp. 332–338, 2006.

[46] E. Nattie and A. Li, “Central chemoreceptors: Locations and functions,” *Compr. Physiol.*, vol. 2, no. 1, pp. 221–254, 2012.

[47] P. G. Guyenet, R. L. Stornetta, D. a Bayliss, and D. K. Mulkey, “Retrotrapezoid nucleus: a litmus test for the identification of central chemoreceptors.,” *Exp. Physiol.*, vol. 90, no. 3, pp. 247–53; discussion 253–7, 2005.

[48] P. G. Guyenet, D. a. Bayliss, R. L. Stornetta, M. G. Fortuna, S. B. G. Abbott, and S. D. DePuy, “Retrotrapezoid nucleus, respiratory chemosensitivity and breathing automaticity.,” *Respir. Physiol. Neurobiol.*, vol. 168, no. 1–2, pp. 59–68, Aug. 2009.

[49] M. Marckwald, *Die Athembewegungen und deren Innervation beim Kaninchen*. [München] ;;[Leipzig]: [Oldenbourg], 1887.

[50] T. Lumsden, “Observations on the respiratory centres in the cat.,” *J. Physiol.*, vol. 57, no. l, pp. 153–160, 1923.

[51] H. Gautier and F. Bertrand, “Respiratory effects of pneumotaxic center lesions and subsequent vagotomy in chronic cats,” *Respir. Physiol.*, vol. 23, no. 1, pp. 71–85, 1975.

[52] W. M. S. John, R. L. Glasser, and K. Richard A., “Apneustic breathing after vagotomy in cats with chronic pneumotaxic center lesions,” *Respir. Physiol.*, vol. 12, no. 2, pp. 239–250, 1971.

[53] W. M. S. John, R. L. Glasser, and R. A. King, “Rhythmic respiration in awake vagotomized cats with chronic pneumotaxic area lesions,” *Respir. Physiol.*, vol. 15, no. 2, pp. 233–244, 1972.

[54] W. M. S. T. John, “Differing responses to hypercapnia and hypoxia following pneumotaxic center ablation,” *Respir. Physiol.*, vol. 23, no. 1, pp. 1–9, 1975.

[55] W. M. St. John and S. C. Wang, “Alteration from apneusis to more regular rhythmic respiration in decerebrate Cats,” *Respir. Physiol.*, vol. 31, no. 1, pp. 91–106, 1977.

[56] A. H. Ropper, M. A. Samuels, and J. P. Klein, “Chapter 26. Disorders of the Autonomic Nervous System, Respiration, and Swallowing,” in *Adams and Victor’s Principles of Neurology, 10e*, New York, NY: The McGraw-Hill Companies, 2014.

[57] T. E. Dick and S. K. Coles, “Ventrolateral pons mediates short-term depression of respiratory frequency after brief hypoxia,” *Respiration Physiology*, vol. 121, no. 2–3. pp. 87–100, 2000.

[58] M. L. Fung and W. M. St-John, “Separation of multiple functions in ventilatory control of pneumotaxic mechanisms.,” *Respir. Physiol.*, vol. 96, no. 1, pp. 83–98, 1994.

[59] A. J. Garcia, S. Zanella, H. Koch, A. Doi, and J.-M. Ramirez, “Chapter 3--networks within networks: the neuronal control of breathing.,” *Prog. Brain Res.*, vol. 188, pp. 31–50, Jan. 2011.

[60] M. Mörschel and M. Dutschmann, “Pontine respiratory activity involved in inspiratory/expiratory phase transition.,” *Philos. Trans. R. Soc. Lond. B. Biol. Sci.*, vol. 364, no. 1529, pp. 2517–26, Sep. 2009.

[61] I. A. Rybak, J. F. R. J. F. Paton, J. S. Schwaber, S. JS, and J. S. Schwaber, “Modeling neural mechanisms for genesis of respiratory rhythm and pattern. II. Network models of the central respiratory pattern generator.,” *2Journal Neurophysiol.*, vol. 77, no. 4, pp. 2007–26, Apr. 1997.

[62] I. A. Rybak, N. A. Shevtsova, J. F. R. Paton, O. Pierrefiche, W. M. St-John, and A. Haji, “Modelling respiratory rhythmogenesis: focus on phase switching mechanisms.,” *Adv. Exp. Med. Biol.*, vol. 551, pp. 189–194, 2004.

[63] Y. I. Molkov, B. J. Bacak, T. E. Dick, and I. A. Rybak, “Control of breathing by interacting pontine and pulmonary feedback loops.,” *Front. Neural Circuits*, vol. 7, p. 16, Jan. 2013.

[64] M. Dutschmann and T. E. Dick, “Pontine mechanisms of respiratory control.,” *Compr. Physiol.*, vol. 2, no. 4, pp. 2443–69, Oct. 2012.

[65] M. Andrzejewski, K. Mückenhoff, P. Scheid, and D. Ballantyne, “Synchronized rhythms in chemosensitive neurons of the locus coeruleus in the absence of chemical synaptic transmission,” in *Respiration Physiology*, 2001, vol. 129, no. 1–2, pp. 123–140.

[66] D. Ballantyne, M. Andrzejewski, K. Mückenhoff, and P. Scheid, “Rhythms, synchrony and electrical coupling in the Locus coeruleus,” *Respir. Physiol. Neurobiol.*, vol. 143, no. 2–3, pp. 199–214, 2004.

[67] C. F. Shaw, M. I. Cohen, and R. Barnhardt, “Inspiratory-modulated neurons of the rostrolateral pons: effects of pulmonary afferent input,” *Brain Res.*, vol. 485, no. 1, pp. 179–184, 1989.

[68] T. E. Dick, M. C. Bellingham, and D. W. Richter, “Pontine respiratory neurons in anesthetized cats,” *Brain Res.*, vol. 636, no. 2, pp. 259–269, 1994.

[69] C. von Euler, “On the central pattern generator for the basic breathing rhythmicity.,” *J. Appl. Physiol.*, vol. 55, no. 6, pp. 1647–1659, 1983.

[70] C. von Euler, I. Marttila, J. E. Remmers, and T. Trippenbach, “Effects of lesions in the parabrachial nucleus on the mechanisms for central and reflex termination of inspiration in the cat.,” *Acta Physiol. Scand.*, vol. 96, no. 3, pp. 324–37, Mar. 1976.

[71] M. I. Cohen and J. L. Feldman, “Models of respiratory phase-switching,” *Fed. Proc.*, vol. 36, no. 10, pp. 2367–2374, 1977.

[72] J. L. Feldman, M. I. Cohen, and P. Wolotsky, “Powerful inhibition of pontine respiratory neurons by pulmonary afferent activity,” *Brain Res.*, vol. 104, no. 2, pp. 341–346, 1976.

[73] J. L. Feldman and H. Gautier, “Interaction of pulmonary afferents and pneumotaxic center in control of respiratory pattern in cats.,” *J. Neurophysiol.*, vol. 39, no. 1, pp. 31–44, 1976.

[74] M. I. Cohen and C. F. Shaw, “Role in the inspiratory off-switch of vagal inputs to rostral pontine inspiratory-modulated neurons,” *Respir. Physiol. Neurobiol.*, vol. 143, no. 2–3, pp. 127–140, 2004.

[75] J. S. Jodkowski, S. K. Coles, and T. E. Dick, “A ‘pneumotaxic centre’ in rats,” *Neurosci. Lett.*, vol. 172, no. 1–2, pp. 67–72, 1994.

[76] M. I. Cohen, M. F. Piercey, P. M. Gootman, and P. Wolotsky, “Respiratory rhythmicity in the cat,” *Fed. Proc.*, vol. 35, no. 9, pp. 1967–1974, 1976.

[77] P. G. Guyenet, N. Koshiya, D. Huangfu, A. J. Verberne, and T. A. Riley, “Central respiratory control of A5 and A6 pontine noradrenergic neurons.,” *Am J Physiol*, vol. 264, no. 6 Pt 2, pp. R1035–44, 1993.

[78] J. S. Jodkowski, S. K. Coles, and T. E. Dick, “Prolongation in expiration evoked from ventrolateral pons of adult rats.,” *J. Appl. Physiol.*, vol. 82, no. 2, pp. 377–81, 1997.

[79] G. F. Alheid and D. R. McCrimmon, “The chemical neuroanatomy of breathing,” *Respiratory Physiology and Neurobiology*, vol. 164, no. 1–2. pp. 3–11, 2008.

[80] G. F. Alheid, W. K. Milsom, and D. R. McCrimmon, “Pontine influences on breathing: An overview,” *Respiratory Physiology and Neurobiology*, vol. 143, no. 2–3. pp. 105–114, 2004.

[81] G. F. Alheid, P. A. Gray, M. C. Jiang, J. L. Feldman, and D. R. McCrimmon, “Parvalbumin in respiratory neurons of the ventrolateral medulla of the adult rat.,” *J. Neurocytol.*, vol. 31, no. 8–9, pp. 693–717, Jan. 2002.

[82] G. Song, Y. Yu, and C.-S. Poon, "Cytoarchitecture of pneumotaxic integration of respiratory and nonrespiratory information in the rat.," *J. Neurosci.*, vol. 26, no. 1, pp. 300–310, 2006.

[83] H. Koizumi, N. Koshiya, J. X. Chia, F. Cao, J. Nugent, R. Zhang, and J. C. Smith, "Structural-functional properties of identified excitatory and inhibitory interneurons within pre-Botzinger complex respiratory microcircuits.," *J. Neurosci.*, vol. 33, no. 7, pp. 2994–3009, 2013.

[84] W. Tan, S. Pagliardini, P. Yang, W. A. Janczewski, and J. L. Feldman, "Projections of preBötzinger complex neurons in adult rats.," *J. Comp. Neurol.*, vol. 518, no. 10, pp. 1862–78, May 2010.

[85] G. Song, P. Yu, and L. Liu, "Projections from pontine pneumotaxic center to medullary Bötzinger complex in cats," *Sheng Li Xue Bao*, vol. 48, no. 1, pp. 59–64, 1996.

[86] B. G. Lindsey, Y. M. Hernandez, K. F. Morris, R. Shannon, and G. L. Gerstein, "Respiratory-related neural assemblies in the brain stem midline," *J Neurophysiol*, vol. 67, no. 4, pp. 905–922, 1992.

[87] A. P. Abdala, I. A. Rybak, J. C. Smith, D. B. Zoccal, B. H. Machado, W. M. St-John, and J. F. Paton, "Multiple pontomedullary mechanisms of respiratory rhythmogenesis.," *Respir. Physiol. Neurobiol.*, vol. 168, no. 1–2, pp. 19–25, 2009.

[88] J. E. Rubin, B. J. Bacak, Y. I. Molkov, N. A. Shevtsova, J. C. Smith, and I. A. Rybak, "Interacting oscillations in neural control of breathing: modeling and qualitative analysis.," *J. Comput. Neurosci.*, vol. 30, no. 3, pp. 607–32, Jun. 2011.

[89] B. G. Lindsey, I. a. Rybak, and J. C. Smith, "Computational Models and Emergent Properties of Respiratory Neural Networks," in *Comprehensive Physiology*, vol. 2, no. 3, 2012, pp. 1619–1670.

[90] J. B. Dean, D. A. Bayliss, J. T. Erickson, W. L. Lawing, and D. E. Millhorn, "Depolarization and stimulation of neurons in nucleus tractus solitarii by carbon dioxide does not require chemical synaptic input," *Neuroscience*, vol. 36, no. 1, pp. 207–216, 1990.

[91] P. G. Guyenet, R. L. Stornetta, D. A. Bayliss, D. K. Mulkey, and G. B. Richerson, "Re: Homing in on the specific phenotype(s) of central respiratory chemoreceptors. Commentary," *Experimental Physiology*, vol. 90, no. 3. pp. 266–269, 2005.

[92] P. G. Guyenet, R. L. Stornetta, and D. a. Bayliss, "Retrotrapezoid nucleus and central chemoreception," *J. Physiol.*, vol. 586, no. 8, pp. 2043–2048, 2008.

[93] a Kawai, D. Ballantyne, K. Mückenhoff, and P. Scheid, “Chemosensitive medullary neurones in the brainstem--spinal cord preparation of the neonatal rat.,” *J. Physiol.*, vol. 492 (Pt 1, no. 1996, pp. 277–92, 1996.

[94] I. C. Solomon, N. H. Edelman, and J. A. Neubauer, “Pre-Bötzinger complex functions as a central hypoxia chemosensor for respiration in vivo.,” *J. Neurophysiol.*, vol. 83, no. 5, pp. 2854–68, May 2000.

[95] E. E. Nattie and A. Li, “Central chemoreception in the region of the ventral respiratory group in the rat.,” *J. Appl. Physiol.*, vol. 81, no. 5, pp. 1987–95, Nov. 1996.

[96] P. G. Guyenet, “The 2008 Carl Ludwig Lecture: retrotrapezoid nucleus, CO2 homeostasis, and breathing automaticity.,” *J. Appl. Physiol.*, vol. 105, no. 2, pp. 404–416, 2008.

[97] B. J. Canning, “Anatomy and neurophysiology of the cough reflex: ACCP evidence-based clinical practice guidelines.,” *Chest*, vol. 129, no. 1 Suppl, p. 33S–47S, Jan. 2006.

[98] B. J. Canning and A. Fischer, “Neural regulation of airway smooth muscle tone.,” *Respir. Physiol.*, vol. 125, no. 1–2, pp. 113–27, Mar. 2001.

[99] M. J. Carr and B. J. Undem, “Bronchopulmonary afferent nerves.,” *Respirology*, vol. 8, no. 3, pp. 291–301, Sep. 2003.

[100] R. O. Davies, L. Kubin, and A. I. Pack, “Pulmonary stretch receptor relay neurones of the cat: location and contralateral medullary projections.,” *J. Physiol.*, vol. 383, no. 1, pp. 571–585, 1987.

[101] S. Donoghue, M. Garcia, D. Jordan, and K. M. Spyer, “The brain-stem projections of pulmonary stretch afferent neurones in cats and rabbits.,” *J. Physiol.*, vol. 322, no. 1982, pp. 353–363, 1982.

[102] S. Donoghue, M. Garcia, D. Jordan, and K. M. Spyer, “Identification and brain-stem projections of aortic baroreceptor afferent neurones in nodose ganglia of cats and rabbits.,” *J. Physiol.*, vol. 322, pp. 337–52, 1982.

[103] H. M. Coleridge, J. C. Coleridge, and H. D. Schultz, “Afferent pathways involved in reflex regulation of airway smooth muscle.,” *Pharmacol. Ther.*, vol. 42, no. 1, pp. 1–63, Jan. 1989.

[104] L.-Y. Lee, Y. Shuei Lin, Q. Gu, E. Chung, and C.-Y. Ho, “Functional morphology and physiological properties of bronchopulmonary C-fiber afferents.,” *Anat. Rec. A. Discov. Mol. Cell. Evol. Biol.*, vol. 270, no. 1, pp. 17–24, 2003.

[105] L. Y. Lee and T. E. Pisarri, “Afferent properties and reflex functions of bronchopulmonary C-fibers,” *Respir. Physiol.*, vol. 125, no. 1–2, pp. 47–65, 2001.

[106] J. Widdicombe, “Airway receptors.,” *Respir. Physiol.*, vol. 125, no. 1–2, pp. 3–15, Mar. 2001.

[107] K. Ezure and I. Tanaka, “Identification of deflation-sensitive inspiratory neurons in the dorsal respiratory group of the rat,” *Brain Res.*, vol. 883, no. 1, pp. 22–30, 2000.

[108] E. Hering, “Die Selbststeuerung der Athmung durch den Nervus vagus,” *Math. Cl.*, vol. 57, no. 2, pp. 672–677, 1868.

[109] J. Breuer, “Die Selbststeuerung der Athmung durch den Nervus vagus,” *Math. Classe1*, vol. 58, no. 2, pp. 909–937, 1868.

[110] M. Kalia and M. M. Mesulam, “Brain stem projections of sensory and motor components of the vagus complex in the cat: II. Laryngeal, tracheobronchial, pulmonary, cardiac, and gastrointestinal branches.,” *J. Comp. Neurol.*, vol. 193, pp. 467–508, 1980.

[111] M. Kalia and M. M. Mesulam, “Brain stem projections of sensory and motor components of the vagus complex in the cat: I. The cervical vagus and nodose ganglion.,” *J. Comp. Neurol.*, vol. 193, no. 2, pp. 435–65, 1980.

[112] M. Kalia and J. M. Sullivan, “Brainstem projections of sensory and motor components of the vagus nerve in the rat.,” *J. Comp. Neurol.*, vol. 211, pp. 248–265, 1982.

[113] M. Kalia and D. Richter, “Morphology of physiologically identified slowly adapting lung stretch receptor afferents stained with intra-axonal horseradish peroxidase in the nucleus of the tractus solitarius of the cat. II. An ultrastructural analysis.,” *J. Comp. Neurol.*, vol. 241, no. 4, pp. 521–35, Nov. 1985.

[114] A. J. Berger, “Dorsal respiratory group neurons in the medulla of cat: Spinal projections, responses to lung inflation and superior laryngeal nerve stimulation,” *Brain Res.*, vol. 135, no. 2, pp. 231–254, 1977.

[115] A. C. Bonham and D. R. McCrimmon, “Neurones in a discrete region of the nucleus tractus solitarius are required for the Breuer-Hering reflex in rat.,” *J. Physiol.*, vol. 427, pp. 261–280, 1990.

[116] M. Cohen and J. Feldman, “Discharge properties of dorsal medullary inspiratory neurons: relation to pulmonary afferent and phrenic efferent discharge,” *J. Neurophysiol.*, vol. 51, no. 4, pp. 753–776, 1984.

[117] R. A. Wilson and F. C. Keil, *The MIT Encyclopedia of The Cognitive Sciences*, vol. 26, no. 2. 1999.

[118] L. Abbott and P. Dayan, “Theoretical Neuroscience,” *Comput. Math. Model. Neural …*, vol. 60, no. 3, pp. 489–95, 2001.

[119] Nrets, “Equivalent electrical circuit for the Hodgkin–Huxley model of the action potential.,” *http://www.wikiwand.com*, 2011. .

[120] L. F. Abbott, “Lapicque’s introduction of the integrate-and-fire model neuron (1907),” *Brain Res. Bull.*, vol. 50, no. 5–6, pp. 303–304, 1999.

[121] R. FitzHugh, “Mathematical models of threshold phenomena in the nerve membrane,” *Bull. Math. Biophys.*, vol. 17, no. 4, pp. 257–278, 1955.

[122] J. Nagumo, S. Arimoto, and S. Yoshizawa, “An Active Pulse Transmission Line Simulating Nerve Axon*,” *Proc. IRE*, vol. 50, no. 10, pp. 2061–2070, 1962.

[123] A. L. Hodgkin and A. F. Huxley, “The dual effect of membrane potential on sodium conductance in the giant axon of Loligo.,” *J. Physiol.*, vol. 116, no. 4, pp. 497–506, Apr. 1952.

[124] A. L. Hodgkin and A. F. Huxley, “The components of membrane conductance in the giant axon of Loligo.,” *J. Physiol.*, vol. 116, no. 4, pp. 473–96, Apr. 1952.

[125] R. J. Butera, J. Rinzel, and J. C. Smith, “Models of respiratory rhythm generation in the pre-Bötzinger complex. I. Bursting pacemaker neurons.,” *J. Neurophysiol.*, vol. 82, pp. 382–397, 1999.

[126] R. J. Butera, J. Rinzel, and J. C. Smith, “Models of respiratory rhythm generation in the pre-Bötzinger complex. II. Populations Of coupled pacemaker neurons.,” *J. Neurophysiol.*, vol. 82, pp. 398–415, 1999.

[127] I. A. Rybak, N. a Shevtsova, K. Ptak, and D. McCrimmon, “Intrinsic bursting activity in the pre-Bötzinger Complex: Role of persistent sodium and potassium currents,” *Biol. Cybern.*, vol. 90, no. 1, pp. 59–74, 2004.

[128] J. R. Huguenard and D. A. McCormick, “Simulation of the currents involved in rhythmic oscillations in thalamic relay neurons,” *J Neurophysiol*, vol. 68, no. 4, pp. 1373–1383, Oct. 1992.

[129] Y. I. Molkov, B. J. Bacak, A. E. Talpalar, and I. A. Rybak, “Mechanisms of left-right coordination in Mammalian locomotor pattern generation circuits: a mathematical modeling view.,” *PLoS Comput. Biol.*, vol. 11, no. 5, p. e1004270, May 2015.

[130] J. E. Rubio, “A mathematical model of the respiratory center.,” *Bull. Math. Biophys.*, vol. 29, no. 4, pp. 718–36, Dec. 1967.

[131] J. E. Rubio, “A new mathematical model of the respiratory center,” *Bull. Math. Biophys.*, vol. 34, no. 4, pp. 467–481, Dec. 1972.

[132] S. Geman and M. Miller, “Computer simulation of brainstem respiratory activity.,” *J Appl Physiol*, vol. 41, no. 6, pp. 931–938, 1976.

[133] J. Duffin, “A model of respiratory rhythm generation.,” *Neuroreport*, vol. 2, no. 10, pp. 623–626, 1991.

[134] I. a Rybak, J. F. Paton, and J. S. Schwaber, “Modeling neural mechanisms for genesis of respiratory rhythm and pattern. I. Comparison of model performances during afferent nerve stimulation.,” *J. Neurophysiol.*, vol. 77, no. 4, pp. 2027–2039, 1997.

[135] I. A. Rybak, J. F. Paton, and J. S. Schwaber, “Modeling neural mechanisms for genesis of respiratory rhythm and pattern. III. Comparison of model performances during afferent nerve stimulation.,” *J. Neurophysiol.*, vol. 77, no. 4, pp. 2027–39, Apr. 1997.

[136] I. A. Rybak, N. A. Shevtsova, W. M. St-John, J. F. R. Paton, and O. Pierrefiche, “Endogenous rhythm generation in the pre-Botzinger complex and ionic currents: Modelling and in vitro studies,” *Eur. J. Neurosci.*, vol. 18, no. 2, pp. 239–257, 2003.

[137] H. Kantz and T. Schreiber, “Human ECG: nonlinear deterministic versus stochastic aspects,” *IEE Proc. - Sci. Meas. Technol.*, vol. 145, no. 6, pp. 279–284, 1998.

[138] R. Guttman, S. Lewis, and J. Rinzel, “Control of repetitive firing in squid axon membrane as a model for a neuroneoscillator.,” *J. Physiol.*, vol. 305, pp. 377–95, Aug. 1980.

[139] J. Rinzel, “Excitation dynamics: insights from simplified membrane models.,” *Fed. Proc.*, vol. 44, no. 15, pp. 2944–6, Dec. 1985.

[140] M. Desroches, J. Guckenheimer, B. Krauskopf, C. Kuehn, H. Osinga, and M. Wechselberger, “Mixed-mode oscillations with multiple time scales,” *SIAM Rev.*, vol. 54, no. 2, pp. 211–288, 2010.

[141] C. T. Dickson, J. Magistretti, M. H. Shalinsky, E. Fransén, M. E. Hasselmo, and A. Alonso, “Properties and role of I(h) in the pacing of subthreshold oscillations in entorhinal cortex layer II neurons.,” *J. Neurophysiol.*, vol. 83, no. 5, pp. 2562–2579, 2000.

[142] M. Yoshida and A. Alonso, “Cell-type specific modulation of intrinsic firing properties and subthreshold membrane oscillations by the M(Kv7)-current in neurons of the entorhinal cortex.,” *J. Neurophysiol.*, vol. 98, no. 5, pp. 2779–94, Nov. 2007.

[143] J. Winson, “Loss of hippocampal theta rhythm results in spatial memory deficit in the rat.,” *Science*, vol. 201, no. 4351, pp. 160–163, 1978.

[144] G. S. Medvedev and J. E. Cisternas, “Multimodal regimes in a compartmental model of the dopamine neuron,” *Phys. D Nonlinear Phenom.*, vol. 194, no. 3–4, pp. 333–356, Jul. 2004.

[145] C. a. Del Negro, C. G. Wilson, R. J. Butera, H. Rigatto, and J. C. Smith, “Periodicity, mixed-mode oscillations, and quasiperiodicity in a rhythm-generating neural network.,” *Biophys. J.*, vol. 82, no. 1 Pt 1, pp. 206–214, 2002.

[146] K. Kam, J. W. Worrell, W. a Janczewski, Y. Cui, and J. L. Feldman, “Distinct inspiratory rhythm and pattern generating mechanisms in the preBötzinger complex.,” *J. Neurosci.*, vol. 33, no. 22, pp. 9235–45, May 2013.

[147] D. Golomb, “Mechanism and Function of Mixed-Mode Oscillations in Vibrissa Motoneurons,” *PLoS One*, vol. 9, no. 10, p. e109205, 2014.

[148] C. Iglesias, C. Meunier, M. Manuel, Y. Timofeeva, N. Delestrée, and D. Zytnicki, “Mixed mode oscillations in mouse spinal motoneurons arise from a low excitability state.,” *J. Neurosci.*, vol. 31, no. 15, pp. 5829–5840, 2011.

[149] C. a. Del Negro, C. Morgado-Valle, and J. L. Feldman, “Respiratory rhythm: An emergent network property?,” *Neuron*, vol. 34, no. 5, pp. 821–830, 2002.

[150] J. C. Smith, A. P. Abdala, A. Borgmann, I. A. Rybak, and J. F. R. Paton, “Brainstem respiratory networks: Building blocks and microcircuits,” *Trends Neurosci.*, vol. 36, no. 3, pp. 152–162, 2013.

[151] J.-M. M. Ramirez, U. J. Quellmalz, and D. W. Richter, “Postnatal changes in the mammalian respiratory network as revealed by the transverse brainstem slice of mice.,” *J. Physiol.*, vol. 491 (Pt 3, pp. 799–812, 1996.

[152] S. P. Lieske, M. Thoby-Brisson, P. Telgkamp, and J.-M. Ramirez, “Reconfiguration of the neural network controlling multiple breathing patterns: eupnea, sighs and gasps [see comment],” *Nat. Neurosci.*, vol. 3, no. 6, pp. 600–607, 2000.

[153] P. E. Jasinski, Y. I. Molkov, N. A. Shevtsova, J. C. Smith, and I. A. Rybak, “Sodium and calcium mechanisms of rhythmic bursting in excitatory neural networks of the pre-Bötzinger complex: a computational modelling study.,” *Eur. J. Neurosci.*, vol. 37, no. 2, pp. 212–30, Jan. 2013.

[154] F. Peña, M. A. Parkis, A. K. Tryba, and J.-M. Ramirez, “Differential contribution of pacemaker properties to the generation of respiratory rhythms during normoxia and hypoxia,” *Neuron*, vol. 43, no. 1, pp. 105–117, 2004.

[155] H. Koizumi and J. C. Smith, “Persistent Na+ and K+-dominated leak currents contribute to respiratory rhythm generation in the pre-Bötzinger complex in vitro.,” *J. Neurosci.*, vol. 28, no. 7, pp. 1773–85, Feb. 2008.

[156] I. A. Rybak, K. Ptak, N. A. Shevtsova, and D. McCrimmon, “Sodium currents in neurons from the rostroventrolateral medulla of the rat,” *J Neurophysiol*, 2003. [Online]. Available: http://www.ncbi.nlm.nih.gov/pubmed/12761275. [Accessed: 06-Jul-2015].

[157] I. A. Rybak, Y. I. Molkov, P. E. Jasinski, N. a Shevtsova, and J. C. Smith, *Rhythmic bursting in the pre-Bötzinger complex: mechanisms and models.*, vol. 209. 2014.

[158] J. R. Dunmyre, C. a. Del Negro, and J. E. Rubin, “Interactions of persistent sodium and calcium-activated nonspecific cationic currents yield dynamically distinct bursting regimes in a model of respiratory neurons,” *J. Comput. Neurosci.*, vol. 31, no. 2, pp. 305–328, 2011.

[159] J. Rubin and D. Terman, “Synchronized Activity and Loss of Synchrony Among Heterogeneous Conditional Oscillators,” *SIAM Journal on Applied Dynamical Systems*, vol. 1, no. 1. pp. 146–174, 2002.

[160] D. Somers and N. Kopell, “Rapid synchronization through fast threshold modulation,” *Biol. Cybern.*, vol. 68, no. 5, pp. 393–407, Mar. 1993.

[161] C. a. Del Negro, N. Koshiya, R. J. Butera, and J. C. Smith, “Persistent sodium current, membrane properties and bursting behavior of pre-bötzinger complex inspiratory neurons in vitro.,” *J. Neurophysiol.*, vol. 88, no. 5, pp. 2242–2250, 2002.

[162] C. a. Del Negro, C. Morgado-Valle, J. A. Hayes, D. D. Mackay, R. W. Pace, E. A. Crowder, and J. L. Feldman, “Sodium and calcium current-mediated pacemaker neurons and respiratory rhythm generation.,” *J. Neurosci.*, vol. 25, no. 2, pp. 446–453, 2005.

[163] J. L. Feldman and K. Kam, “Facing the challenge of mammalian neural microcircuits: Taking a few breaths may help.,” *J. Physiol.*, vol. 1, pp. 3–23, Nov. 2014.

[164] O. Ekeberg, P. Wallen, A. Lansner, H. Traven, L. Brodin, and S. Grillner, “A Computer-Based Model for Realistic Simulations of Neural Networks .1. The Single Neuron and Synaptic Interaction,” *Biol. Cybern.*, vol. 65, no. 2, pp. 81–90, 1991.

[165] A. El Manira, J. Tegnér, and S. Grillner, “Calcium-dependent potassium channels play a critical role for burst termination in the locomotor network in lamprey.,” *J. Neurophysiol.*, vol. 72, no. 4, pp. 1852–61, 1994.

[166] P. Wallén, B. Robertson, L. Cangiano, P. Löw, A. Bhattacharjee, L. K. Kaczmarek, and S. Grillner, “Sodium-dependent potassium channels of a Slack-like subtype contribute to the slow afterhyperpolarization in lamprey spinal neurons.,” *J. Physiol.*, vol. 585, no. Pt 1, pp. 75–90, 2007.

[167] J. E. Rubin, J. a Hayes, J. L. Mendenhall, and C. a Del Negro, “Calcium-activated nonspecific cation current and synaptic depression promote network-dependent burst oscillations.,” *Proc. Natl. Acad. Sci. U. S. A.*, vol. 106, no. 8, pp. 2939–2944, 2009.

[168] D. Ryczko, V. Charrier, A. Ijspeert, and J.-M. Cabelguen, “Segmental oscillators in axial motor circuits of the salamander: distribution and bursting mechanisms.,” *J. Neurophysiol.*, vol. 104, no. 5, pp. 2677–92, 2010.

[169] I. A. Rybak, K. Stecina, N. A. Shevtsova, and D. A. McCrea, “Modelling spinal circuitry involved in locomotor pattern generation: insights from the effects of afferent stimulation.,” *J. Physiol.*, vol. 577, no. Pt 2, pp. 641–58, Dec. 2006.

[170] D. a McCrea and I. A. Rybak, “Organization of mammalian locomotor rhythm and pattern generation.,” *Brain Res. Rev.*, vol. 57, no. 1, pp. 134–46, Jan. 2008.

[171] H. Onimaru, Y. Kumagawa, and I. Homma, “Respiration-related rhythmic activity in the rostral medulla of newborn rats.,” *J. Neurophysiol.*, vol. 96, no. 1, pp. 55–61, 2006.

[172] N. M. Mellen, W. A. Janczewski, C. M. Bocchiaro, and J. L. Feldman, “Opioid-induced quantal slowing reveals dual networks for respiratory rhythm generation,” *Neuron*, vol. 37, no. 5, pp. 821–826, 2003.

[173] M. Iizuka and R. F. Fregosi, “Influence of hypercapnic acidosis and hypoxia on abdominal expiratory nerve activity in the rat,” *Respir. Physiol. Neurobiol.*, vol. 157, no. 2–3, pp. 196–205, 2007.

[174] S. Wittmeier, G. Song, J. Duffin, and C.-S. Poon, “Pacemakers handshake synchronization mechanism of mammalian respiratory rhythmogenesis.,” *Proc. Natl. Acad. Sci. U. S. A.*, vol. 105, no. 46, pp. 18000–18005, 2008.

[175] G. Fortin and M. Thoby-Brisson, “Embryonic emergence of the respiratory rhythm generator.,” *Respir. Physiol. Neurobiol.*, vol. 168, no. 1–2, pp. 86–91, 2009.

[176] M. Thoby-Brisson, M. Karlén, N. Wu, P. Charnay, J. Champagnat, and G. Fortin, “Genetic identification of an embryonic parafacial oscillator coupling to the preBötzinger complex.,” *Nat. Neurosci.*, vol. 12, no. 8, pp. 1028–35, 2009.

[177] J. C. Leiter and W. M. St-John, “Phrenic, vagal and hypoglossal activities in rat: pre-inspiratory, inspiratory, expiratory components.,” *Respir. Physiol. Neurobiol.*, vol. 142, no. 2–3, pp. 115–26, 2004.

[178] Y. Fukuda and Y. Honda, “Modification by chemical stimuli of temporal difference in the onset of inspiratory activity between vagal (superior laryngeal) or hypoglossal and phrenic nerves of the rat,” *Jpn. J. Physiol.*, vol. 38, no. 3, pp. 309–319, 1988.

[179] J. H. Peever, L. Shen, and J. Duffin, “Respiratory pre-motor control of hypoglossal motoneurons in the rat.,” *Neuroscience*, vol. 110, no. 4, pp. 711–22, 2002.

[180] H. Onimaru, A. Arata, and I. Homma, “Intrinsic burst generation of preinspiratory neurons in the medulla of brainstem-spinal cord preparations isolated from newborn rats.,” *Exp. brain Res.*, vol. 106, no. 1, pp. 57–68, Jan. 1995.

[181] K. Ballanyi, H. Onimaru, and I. Homma, “Respiratory network function in the isolated brainstem-spinal cord of newborn rats,” *Prog. Neurobiol.*, vol. 59, no. 6, pp. 583–634, 1999.

[182] M. G. Fortuna, G. H. West, R. L. Stornetta, and P. G. Guyenet, “Botzinger expiratory-augmenting neurons and the parafacial respiratory group.,” *J. Neurosci.*, vol. 28, pp. 2506–2515, 2008.

[183] I. M. P. Joseph and R. J. Butera, “A simple model of dynamic interactions between respiratory centers.,” *Conf. Proc. IEEE Eng. Med. Biol. Soc.*, vol. 6, pp. 5840–5842, 2005.

[184] M. Dutschmann and H. Herbert, “The Kölliker-Fuse nucleus gates the postinspiratory phase of the respiratory cycle to control inspiratory off-switch and upper airway resistance in rat.,” *Eur. J. Neurosci.*, vol. 24, no. 4, pp. 1071–84, Aug. 2006.

[185] S. Pagliardini, W. a Janczewski, W. Tan, C. T. Dickson, K. Deisseroth, and J. L. Feldman, “Active expiration induced by excitation of ventral medulla in adult anesthetized rats.,” *J. Neurosci.*, vol. 31, no. 8, pp. 2895–2905, 2011.

[186] I. A. Rybak, R. O’Connor, A. Ross, N. Shevtsova, S. C. Nuding, L. S. Segers, R. Shannon, T. E. Dick, W. L. Dunin-Barkowski, J. M. Orem, I. C. Solomon, K. F. Morris, and B. G. Lindsey, “Reconfiguration of the pontomedullary respiratory network: a computational modeling study with coordinated in vivo experiments.,” *J. Neurophysiol.*, vol. 100, no. 4, pp. 1770–1799, 2008.

[187] P. G. Guyenet, “Novel two-rhythm generator theory of breathing in mammals,” *J. Physiol.*, vol. 570, no. Pt 2, p. 207, 2006.

[188] P. G. Guyenet, “Regulation of Ventral Surface Chemoreceptors by the Central Respiratory Pattern Generator,” *J. Neurosci.*, vol. 25, no. 39, pp. 8938–8947, 2005.

[189] P. G. Guyenet, R. L. Stornetta, S. B. G. Abbott, S. D. Depuy, and R. Kanbar, “The Retrotrapezoid Nucleus and Breathing,” in *Arterial Chemoreception: From Molecules to Systems*, vol. 758, 2012, pp. 115–122.

[190] S. M. Winter, J. Fresemann, C. Schnell, Y. Oku, J. Hirrlinger, and S. Hülsmann, “Glycinergic interneurons are functionally integrated into the inspiratory network of mouse medullary slices,” *Pflugers Arch. Eur. J. Physiol.*, vol. 458, no. 3, pp. 459–469, 2009.

[191] S. B. G. Abbott, P. G. R. Burke, and P. M. Pilowsky, “Galanin microinjection into the PreBötzinger or the Bötzinger Complex terminates central inspiratory activity and reduces responses to hypoxia and hypercapnia in rat.,” *Respir. Physiol. Neurobiol.*, vol. 167, no. 3, pp. 299–306, 2009.

[192] F. Bongianni, D. Mutolo, E. Cinelli, and T. Pantaleo, “Respiratory responses induced by blockades of GABA and glycine receptors within the Bötzinger complex and the pre-Bötzinger complex of the rabbit.,” *Brain Res.*, vol. 1344, pp. 134–47, 2010.

[193] C. Morgado-Valle, S. M. Baca, and J. L. Feldman, “Glycinergic pacemaker neurons in preBötzinger complex of neonatal mouse.,” *J. Neurosci.*, vol. 30, no. 10, pp. 3634–9, 2010.

[194] C. a. Del Negro, K. Kam, J. a Hayes, and J. L. Feldman, “Asymmetric control of inspiratory and expiratory phases by excitability in the respiratory network of neonatal mice in vitro.,” *J. Physiol.*, vol. 587, pp. 1217–1231, 2009.

[195] W. Singer, “Synchronization of Cortical Activity and its Putative Role in Information Processing and Learning.,” *Annu Rev Physiol*, vol. 55, pp. 349–374, 1993.

[196] M. Bauer, R. Oostenveld, M. Peeters, and P. Fries, “Tactile spatial attention enhances gamma-band activity in somatosensory cortex and reduces low-frequency activity in parieto-occipital areas.,” *J. Neurosci.*, vol. 26, no. 2, pp. 490–501, 2006.

[197] L. M. Kay, J. Beshel, J. Brea, C. Martin, D. Rojas-Líbano, and N. Kopell, “Olfactory oscillations: the what, how and what for,” *Trends Neurosci.*, vol. 32, no. 4, pp. 207–214, 2009.

[198] M. Bazhenov, I. Timofeev, M. Steriade, and T. J. Sejnowski, “Self-sustained rhythmic activity in the thalamic reticular nucleus mediated by depolarizing GABAA receptor potentials.,” *Nat. Neurosci.*, vol. 2, no. 2, pp. 168–174, 1999.

[199] A. B. L. Tort, M. a Kramer, C. Thorn, D. J. Gibson, Y. Kubota, A. M. Graybiel, and N. J. Kopell, “Dynamic cross-frequency couplings of local field potential oscillations in rat striatum and hippocampus during performance of a T-maze task.,” *Proc. Natl. Acad. Sci. U. S. A.*, vol. 105, no. 51, pp. 20517–20522, 2008.

[200] S. N. Baker, J. M. Kilner, E. M. Pinches, and R. N. Lemon, “The role of synchrony and oscillations in the motor output,” *Exp. Brain Res.*, vol. 128, no. 1–2, pp. 109–117, 1999.

[201] S. Grillner, “Biological pattern generation: the cellular and computational logic of networks in motion.,” *Neuron*, vol. 52, no. 5, pp. 751–766, Dec. 2006.

[202] a Monnier, G. F. Alheid, and D. R. McCrimmon, “Defining ventral medullary respiratory compartments with a glutamate receptor agonist in the rat.,” *J. Physiol.*, vol. 548, no. Pt 3, pp. 859–874, 2003.

[203] D. W. Richter, “Neural Regulation of Respiration: Rhythmogenesis and Afferent Control,” in *Comprehensive Human Physiology*, 1996, pp. 2079–2095.

[204] A. Lal, Y. Oku, S. Hülsmann, Y. Okada, F. Miwakeichi, S. Kawai, Y. Tamura, and M. Ishiguro, “Dual oscillator model of the respiratory neuronal network generating quantal slowing of respiratory rhythm,” *J. Comput. Neurosci.*, vol. 30, no. 2, pp. 225–240, 2011.

[205] H. Onimaru, K. Ikeda, and K. Kawakami, “Phox2b, RTN/pFRG neurons and respiratory rhythmogenesis.,” *Respir. Physiol. Neurobiol.*, vol. 168, no. 1–2, pp. 13–8, Aug. 2009.

[206] H. Kantz and T. Schreiber, “Nonlinear Time Series Analysis,” *Technometrics*, vol. 47, no. 3, p. 369, 2004.

[207] R. Hegger, H. Kantz, and T. Schreiber, “Practical implementation of nonlinear time series methods: The TISEAN package,” *Chaos*, vol. 9, no. 413, p. 27, 1998.

[208] B. Ermentrout, “Simulating, Analyzing, and Animating Dynamical Systems: A Guide Toi Xppaut for Researchers and Students,” Mar. 2002.

[209] S. Daun, J. E. Rubin, and I. a. Rybak, “Control of oscillation periods and phase durations in half-center central pattern generators: A comparative mechanistic analysis,” *J. Comput. Neurosci.*, vol. 27, no. 1, pp. 3–36, 2009.

[210] F. K. Skinner, N. Kopell, and E. Marder, “Mechanisms for oscillation and frequency control in reciprocally inhibitory model neural networks,” *J. Comput. Neurosci.*, vol. 1, pp. 69–87, 1994.

[211] X.-J. Wang and J. Rinzel, “Alternating and Synchronous Rhythms in Reciprocally Inhibitory Model Neurons,” *Neural Comput.*, vol. 4, pp. 84–97, 1992.

[212] P. G. Guyenet and D. K. Mulkey, “Retrotrapezoid nucleus and parafacial respiratory group,” *Respir. Physiol. Neurobiol.*, vol. 173, no. 3, pp. 244–255, 2010.

[213] J. C. Smith, R. J. Butera, N. Koshiya, C. Del Negro, C. G. Wilson, and S. M. Johnson, “Respiratory rhythm generation in neonatal and adult mammals: The hybrid pacemaker-network model,” *Respir. Physiol.*, vol. 122, no. 2–3, pp. 131–147, 2000.

[214] J. F. R. Paton and M. Dutschmann, “Central control of upper airway resistance regulating respiratory airflow in mammals.,” *J. Anat.*, vol. 201, no. 4, pp. 319–23, 2002.

[215] P. G. R. Burke, S. B. G. Abbott, S. McMullan, a K. Goodchild, and P. M. Pilowsky, “Somatostatin selectively ablates post-inspiratory activity after injection into the Bötzinger complex.,” *Neuroscience*, vol. 167, no. 2, pp. 528–539, 2010.

[216] H. Onimaru, A. Arata, and I. Homma, “Inhibitory synaptic inputs to the respiratory rhythm generator in the medulla isolated from newborn rats,” *Pflügers Arch. Eur. J. Physiol.*, vol. 417, no. 4, pp. 425–432, 1990.

[217] A. Pikovsky, M. Rosenblum, J. Kurths, P. B. Chirikov, N. Budker Institute of Nuclear Physics,´ P. P. C., C. Niels Bohr Institute, P. F. Moss, S. L. University of Missouri, P. H. Swinney, and T. U. of T. at A. Center for Nonlinear Dynamics, *Synchronization: A Universal Concept in Nonlinear Sciences*. 2003.

[218] E. M. Izhikevich, *Dynamical systems in neuroscience*. 2007.

[219] I. J. Llewellyn-Smith and A. J. M. Verberne, *Central regulation of autonomic functions*. 2011.

[220] A. J. Berger and T. E. Dick, “Connectivity of slowly adapting pulmonary stretch receptors with dorsal medullary respiratory neurons.,” *J. Neurophysiol.*, vol. 58, no. 6, pp. 1259–1274, 1987.

[221] J. Bajić, E. J. Zuperku, and F. A. Hopp, “Processing of pulmonary afferent input patterns by respiratory I-beta neurons.,” *Am. J. Physiol.*, vol. 256, no. 2 Pt 2, pp. R379–R393, 1989.

[222] K. Anders, W. Ohndorf, R. Dermietzel, and D. Richter, “Synapses between slowly adapting lung stretch receptor afferents and inspiratory beta-neurons in the nucleus of the solitary tract of cats: a light and electron microscopic analysis.,” *J. Comp. Neurol.*, vol. 335, no. 2, pp. 163–172, 1993.

[223] K. Ezure and I. Tanaka, “GABA, in some cases together with glycine, is used as the inhibitory transmitter by pump cells in the Hering-Breuer reflex pathway of the rat,” *Neuroscience*, vol. 127, no. 2, pp. 409–417, 2004.

[224] F. Bertrand and A. Hugelin, “Respiratory synchronizing function of nucleus parabrachialis medialis: pneumotaxic mechanisms.,” *J. Neurophysiol.*, vol. 34, no. 2, pp. 189–207, Mar. 1971.

[225] A. L. Bianchi and W. M. St-John, “Medullary axonal projections of respiratory neurons of pontile pneumotaxic center,” *Respir. Physiol.*, vol. 48, no. 3, pp. 357–373, 1982.

[226] W. M. St-John, “Influence of pulmonary inflations on discharge of pontile respiratory neurons.,” *J. Appl. Physiol.*, vol. 63, no. 6, pp. 2231–9, Dec. 1987.

[227] W. M. St-John, “Neurogenesis of patterns of automatic ventilatory activity,” *Progress in Neurobiology*, vol. 56, no. 1. pp. 97–117, 1998.

[228] T. E. Dick, R. Shannon, B. G. Lindsey, S. C. Nuding, L. S. Segers, D. M. Baekey, and K. F. Morris, “Pontine respiratory-modulated activity before and after vagotomy in decerebrate cats.,” *J. Physiol.*, vol. 586, no. Pt 17, pp. 4265–4282, 2008.

[229] L. S. Segers, S. C. Nuding, T. E. Dick, R. Shannon, D. M. Baekey, I. C. Solomon, K. F. Morris, and B. G. Lindsey, “Functional connectivity in the pontomedullary respiratory network.,” *J. Neurophysiol.*, vol. 100, no. 4, pp. 1749–1769, 2008.

[230] P. A. Nunez-Abades, A. M. Morillo, and R. Pasaro, “Brainstem connections of the rat ventral respiratory subgroups: Afferent projections,” *J. Auton. Nerv. Syst.*, vol. 42, no. 2, pp. 99–118, 1993.

[231] S. P. Gaytán, F. Calero, P. A. Núñez-Abades, A. M. Morillo, and R. Pásaro, “Pontomedullary efferent projections of the ventral respiratory neuronal subsets of the rat,” *Brain Res. Bull.*, vol. 42, no. 4, pp. 323–334, 1997.

[232] Y. Zheng, D. Riche, J. C. Rekling, A. S. Foutz, and M. Denavit-Saubié, “Brainstem neurons projecting to the rostral ventral respiratory group (VRG) in the medulla oblongata of the rat revealed by co-application of NMDA and biocytin,” *Brain Res.*, vol. 782, no. 1–2, pp. 113–125, 1998.

[233] K. Ezure and I. Tanaka, “Distribution and medullary projection of respiratory neurons in the dorsolateral pons of the rat.,” *Neuroscience*, vol. 141, no. 2, pp. 1011–23, Aug. 2006.

[234] M. L. Fung and W. M. St-John, “Electrical stimulation of pneumotaxic center: activation of fibers and neurons.,” *Respir. Physiol.*, vol. 96, no. 1, pp. 71–82, 1994.

[235] M. L. Fung and W. M. St-John, “Neuronal activities underlying inspiratory termination by pneumotaxic mechanisms.,” *Respir. Physiol.*, vol. 98, no. 3, pp. 267–81, Jan. 1994.

[236] M. Okazaki, R. Takeda, H. Yamazaki, and A. Haji, “Synaptic mechanisms of inspiratory off-switching evoked by pontine pneumotaxic stimulation in cats,” *Neurosci. Res.*, vol. 44, no. 1, pp. 101–110, 2002.

[237] O. Pierrefiche, A. Haji, A. Bischoff, and D. W. Richter, “Calcium currents in respiratory neurons of the cat in vivo.,” *Pflugers Arch.*, vol. 438, no. 6, pp. 817–26, Nov. 1999.

[238] S. F. Morrison, S. L. Cravo, and H. M. Wilfehrt, “Pontine lesions produce apneusis in the rat,” *Brain Res.*, vol. 652, no. 1, pp. 83–86, 1994.

[239] M. B. Harris and W. K. Milsom, “Apneusis follows disruption of NMDA-type glutamate receptors in vagotomized ground squirrels,” *Respir. Physiol. Neurobiol.*, vol. 134, no. 3, pp. 191–207, 2003.

[240] A. S. Foutz, J. Champagnat, and M. Denavit-Saubié, “Involvement of N-methyl-d-aspartate (NMDA) receptors in respiratory rhythmogenesis,” *Brain Res.*, vol. 500, no. 1–2, pp. 199–208, 1989.

[241] C. A. Connelly, M. R. Otto-Smith, and J. L. Feldman, “Blockade of NMDA receptor-channels by MK-801 alters breathing in adult rats.,” *Brain Res.*, vol. 596, no. 1–2, pp. 99–110, Nov. 1992.

[242] O. Pierrefiche, A. S. Foutz, J. Champagnat, and M. Denavit-Saubié, “The bulbar network of respiratory neurons during apneusis induced by a blockade of NMDA receptors.,” *Exp. brain Res.*, vol. 89, no. 3, pp. 623–39, Jan. 1992.

[243] L. Ling, D. R. Karius, and D. F. Speck, “Role of N-methyl-D-aspartate receptors in the pontine pneumotaxic mechanism in the cat.,” *J. Appl. Physiol.*, vol. 76, no. 3, pp. 1138–43, Mar. 1994.

[244] V. Borday, A. S. Foutz, L. Nordholm, and M. Denavit-Saubi??, “Respiratory effects of glutamate receptor antagonists in neonate and adult mammals,” *Eur. J. Pharmacol.*, vol. 348, no. 2–3, pp. 235–246, 1998.

[245] D. M. Baekey, Y. I. Molkov, J. F. R. Paton, I. A. Rybak, and T. E. Dick, “Effect of baroreceptor stimulation on the respiratory pattern: insights into respiratory-sympathetic interactions.,” *Respir. Physiol. Neurobiol.*, vol. 174, no. 1–2, pp. 135–45, Nov. 2010.

[246] Y. I. Molkov, D. B. Zoccal, D. J. A. Moraes, J. F. R. Paton, B. H. Machado, and I. A. Rybak, “Intermittent hypoxia-induced sensitization of central chemoreceptors contributes to sympathetic nerve activity during late expiration in rats.,” *J. Neurophysiol.*, vol. 105, no. 6, pp. 3080–91, Jun. 2011.

[247] F. P. Elsen and J. M. Ramirez, “Calcium currents of rhythmic neurons recorded in the isolated respiratory network of neonatal mice.,” *J. Neurosci.*, vol. 18, no. 24, pp. 10652–10662, 1998.

[248] D. Frermann, B. U. Keller, and D. W. Richter, “Calcium oscillations in rhythmically active respiratory neurones in the brainstem of the mouse.,” *J. Physiol.*, vol. 515 (Pt 1, no. 1999, pp. 119–31, 1999.

[249] R. Monteau, P. Gauthier, P. Rega, and G. Hilaire, “Effects of N-methyl-d-aspartate (NMDA) antagonist MK-801 on breathing pattern in rats,” *Neurosci. Lett.*, vol. 109, no. 1–2, pp. 134–139, 1990.

[250] F. Hayashi, S. K. Coles, and D. R. McCrimmon, “Respiratory neurons mediating the Breuer-Hering reflex prolongation of expiration in rat.,” *J. Neurosci.*, vol. 16, no. 20, pp. 6526–6536, 1996.

[251] M. L. Fung and W. M. St-John, “The functional expression of a pontine pneumotaxic centre in neonatal rats.,” *J. Physiol.*, vol. 489 (Pt 2, pp. 579–591, 1995.

[252] M. S. Siniaia, D. L. Young, and C. S. Poon, “Habituation and desensitization of the Hering-Breuer reflex in rat.,” *J. Physiol.*, vol. 523 Pt 2, pp. 479–91, 2000.

[253] R. B. Felder and S. W. Mifflin, “Modulation of carotid sinus afferent input to nucleus tractus solitarius by parabrachial nucleus stimulation,” *Circ Res*, vol. 63, no. 1, pp. 35–49, 1988.

[254] M. J. Tobin, F. Laghi, and A. Jubran, “Ventilatory failure, ventilator support, and ventilator weaning.,” *Compr. Physiol.*, vol. 2, no. 4, pp. 2871–921, 2012.

[255] G. M. Stettner, P. Huppke, C. Brendel, D. W. Richter, J. Gärtner, and M. Dutschmann, “Breathing dysfunctions associated with impaired control of postinspiratory activity in Mecp2-/y knockout mice.,” *J. Physiol.*, vol. 579, no. Pt 3, pp. 863–76, Mar. 2007.

[256] A. P. L. Abdala, M. Dutschmann, J. M. Bissonnette, and J. F. R. Paton, “Correction of respiratory disorders in a mouse model of Rett syndrome.,” *Proc. Natl. Acad. Sci. U. S. A.*, vol. 107, no. 42, pp. 18208–18213, 2010.

[257] Y. I. Molkov, N. A. Shevtsova, C. Park, A. Ben-Tal, J. C. Smith, J. E. Rubin, and I. A. Rybak, “A closed-loop model of the respiratory system: focus on hypercapnia and active expiration.,” *PLoS One*, vol. 9, no. 10, p. e109894, Jan. 2014.

[258] T. E. Dick, Y. I. Molkov, G. Nieman, Y.-H. Hsieh, F. J. Jacono, J. Doyle, J. D. Scheff, S. E. Calvano, I. P. Androulakis, G. An, and Y. Vodovotz, “Linking Inflammation, Cardiorespiratory Variability, and Neural Control in Acute Inflammation via Computational Modeling.,” *Front. Physiol.*, vol. 3, p. 222, Jan. 2012.

[259] N. A. Shevtsova, D. Büsselberg, Y. I. Molkov, A. M. Bischoff, J. C. Smith, D. W. Richter, and I. A. Rybak, “Effects of glycinergic inhibition failure on respiratory rhythm and pattern generation.,” *Prog. Brain Res.*, vol. 209, pp. 25–38, Jan. 2014.

[260] Y. I. Molkov, D. B. Zoccal, D. M. Baekey, A. P. L. Abdala, B. H. Machado, T. E. Dick, J. F. R. Paton, and I. A. Rybak, “Physiological and pathophysiological interactions between the respiratory central pattern generator and the sympathetic nervous system.,” *Prog. Brain Res.*, vol. 212, pp. 1–23, Jan. 2014.

Vita

Bartholomew James Bacak was born in Bethlehem, Pennsylvania on June 4, 1987. After attending Liberty High School, Bartholomew studied Bioengineering at the University of Pittsburgh, graduating with honors in 2009. Following two years of research in the laboratory of Ilya Rybak, Bartholomew enrolled in Drexel University's MD/PhD program. From 2011-2013 he completed the first two years of his medical training prior to rejoining the Rybak lab as a PhD candidate. At the time of his successful dissertation defense in March 2016, Bartholomew had six manuscripts published in high impact journals, these include:

1. **B. J. Bacak**, T. G. Kim, J. E. Rubin, J. C. Smith, I. A., Rybak. "Mixed-mode oscillations and population bursting in the pre-Bötzinger complex," *eLife.*, vol. 5, p. e13403, March 2016.

2. **B. J. Bacak**, J. Segaran, and Y. I. Molkov, "Modeling the effects of extracellular potassium on bursting properties in pre-Bötzinger complex neurons," *J. Comput. Neurosci.*, Feb. 2016.

3. Y. I. Molkov*, **B. J. Bacak***, A. E. Talpalar, and I. A. Rybak, "Mechanisms of left-right coordination in Mammalian locomotor pattern generation circuits: a mathematical modeling view.," *PLoS Comput. Biol.*, vol. 11, no. 5, p. e1004270, May 2015. *These authors contributed equally

4. Y. I. Molkov, **B. J. Bacak**, T. E. Dick, and I. A. Rybak, "Control of breathing by interacting pontine and pulmonary feedback loops.," *Front. Neural Circuits*, vol. 7, p. 16, Jan. 2013.

5. J. E. Rubin, **B. J. Bacak**, Y. I. Molkov, N. A. Shevtsova, J. C. Smith, and I. A. Rybak, "Interacting oscillations in neural control of breathing: modeling and qualitative analysis.," *J. Comput. Neurosci.*, vol. 30, no. 3, pp. 607–32, Jun. 2011.

6. Y. I. Molkov, A. P. Abdala, **B. J. Bacak**, J. C. Smith, J. F. R. Paton, and I. A. Rybak, "Late-expiratory activity: emergence and interactions with the respiratory CpG.," *J. Neurophysiol.*, vol. 104, no. 5, pp. 2713–29, Nov. 2010

© Copyright 2016

Bartholomew J. Bacak. All Rights Reserved.